The utility of barium isotopes as a tracer of methane cycling in continental margin settings



Ethan George Petrou
University College
University of Oxford

A thesis submitted for the degree of
Doctor of Philosophy

Trinity 2024

This thesis is dedicated to
the Petrou family
with a clanship as
boundless as the sea

I must go down to the sea again,
to the lonely sea and the sky.
And all I ask is a tall ship and a
star to steer her by

— John Masefield

'Why? Why', he repeated
petulantly, 'should alpine scenery
be thought conducive to study?'

— Evelyn Waugh
Brideshead Revisited

Full fathom five thy father lies;
Of his bones are coral made;
Those are pearls that were his
eyes: Nothing of him that doth
fade, But doth suffer a sea-change
Into something rich and strange.
Sea-nymphs hourly ring his knell:
Ding-dong. Hark! now I hear
them,—ding-dong, bell.

— William Shakespeare
The Tempest

Acknowledgements

No training, neither academic nor personal, can prepare you for a DPhil. The fortitude, resilience, and flexibility the degree demands are something uniquely fostered whilst being held in the dreaming spires, set to the background of history. As such, stark differences surround my path from fledgling to flourished. I have been guided to operate independently in all academic aspects, from project conceptualisation and execution to experimental work and writing. In addition, the DPhil has pushed me personally to develop dogged tenacity and gain skills in project management, presentation, and scientific communication. All these abilities will be invaluable moving forward, and I am extremely grateful for the chance to have acquired them and the people who taught me them. Those who say a DPhil is inherently isolating are wrong; I have never felt so fulfilled.

This DPhil would never have come into fruition without the support of others. I start, as customary, with my supervisory team, without whose guidance my academic journey would not have been realised. To Professor Gideon Henderson, for proving you can do it all and whose adept leadership steered the ship of my DPhil, my utmost thanks. To Dr Luke Bridgestock, whose Herculean efforts as a supervisor, unending patience, and infallible reviews of my chapters moulded the scientist I am today. To Professor Joe Cartwright, for fostering the spirit of a research group and whose scientific passion is second to none. And finally, to Dr Martino Foschi, whose resolute temperament and guidance have shown me how to navigate the academic world, doing so with style. Thank you all for your continual dedication and academic support, and for consistently challenging me to reach my full potential as a scientist.

Guidance and support can be sought in a multitude of places at Oxford. A huge thank you to Professor Yu-Te Alan Hsieh for your unending kindness and for having me as a visiting researcher in your laboratory group at the Institute of Oceanography, National Taiwan University for Michaelmas Term 2023. My laboratory skills and thesis have greatly improved under your tutelage, and I hold my time in Taiwan and the friends I made there in high regard. I would also like to wish Dr Jane Barling my gratitude for your continual assistance and advice in the metal-free clean labs at Oxford. Next, to Nikki Sridhar for countless hours of engaging laboratory time in MFL4 and even more on TIMS troubleshooting; we made it in the end. To my academic brothers, Dr Raphael Pietzsch and Dr Tzu-Hao (David) Wang for making conferences so enjoyable and for an unforgettable post-conference geo-trip around Hawaii. Lastly, thank you to my Master's supervisor, Professor Pieter Vermeesch for initiating my geochemical journey and introducing me to the wonders of open-source software. I also extend my gratitude to fellow Master's students Michael Claydon, Matthew Simmons, and Henry Partridge, along with Dr Vanessa Vasconcelos, Dr Florence Holbrook, and Dr Abraham Lee, for their support and camaraderie.

By far the most momentous addition to my DPhil experience was being accepted as a member of the scientific party of Expedition 391: Walvis Ridge as part of the International Ocean Discovery Program (IODP) on board the R/V JOIDES Resolution. Getting the chance to work in such an international, collaborative environment on a ship steeped in history has been remarkable, and I shall cherish my moments offshore Namibia with (extended) port-calls in Cape Town with zeal. I thank the expedition co-chiefs, Professor William Sager and Professor Kaj Hoernle, and expedition project manager, Dr Tobias Hoefig, for their relentless efforts in making the expedition a reality despite all the obstacles. A special thanks to Dr Arianna Valentina Del Gaudio, along with Aaron Avery, Yusuke Kubota, Professor Claire Carvallo, and Mark Higley, for keeping ship morale so high, swapping stories like sailors, and spending many a night under the starlit sky to the sound of the surf and the spume.

Another rewarding experience during my studies was being accepted onto a UK Research and Innovation science policy internship hosted at the Royal Society in London. As a member of the Science Policy Resilient Futures team, I was able to tackle complex scientific problems regarding climate change through to space exploration from a top-down approach, the antithesis to research. I thank Dr Rupert Lewis for hosting me in the team and placing me as part of the policy briefing steering committees for Geological Carbon Storage and for Net Zero Aviation Fuels. Furthermore, my thanks go to the entire Resilient Futures team, especially Daisy Weston, Leo Marioni, Euan Casey, and James Musisi, for banishing drudgery and involving me as a valued member from the very start.

Finally, my unyielding gratitude goes to Professor Peter Flemings. Through your guidance, I had the utmost privilege of working (on two occasions) in your dynamic research group at the University of Texas at Austin on cutting-edge methane hydrate research: as a headstrong youth and as a reflective graduate student. Thank you for always believing in me and my academic journey. Participating as a scientific party member of the UT-GOM2 and UT-GOM2-2 expeditions on the Helix Q4000 vessel allowed me to foster long-lasting collaborations and learn revolutionary science direct from the source. I would also like to thank Professor Ann Cook and Professor Derek Sawyer for uncountable teaching moments offshore, along with Dr Zachary Murphy and Camila Van Der Maal for nautical fellowship and 3am cookies and corn. Being offshore, surrounded by endless water and night, evokes a profound sense of insignificance, a humbling realisation of one's infinitesimal place in the world that everyone should experience.

Whilst living in Texas, I had the joy of being a member of Pearl Street Co-operative. That institution of serenity and squalor where we revelled made up the formative years of our lives. I will always have great respect for all the Pearlies involved in helping develop the person I am today. To Tessa Morris and Sophie Mather for always being a positive force, along with Chad Williams, Walker Donnelly, Scott Willis, Abdullah

Yusuf, Amber Camilleri, Mia Goldstein, Melissa Denny, Henry Smith, Roisin O'Neill, David Plaks, Amy Andrews, Amy Buckley, Kelsey Morris, Hasan Seth, Selbi Gabolinscy, Sam Cedar, Nakul Garg, and Carly Michelakis, thank you for those moments of unbridled chaos. Lastly, my deepest appreciation to the Seth and Goldstein families for treating me as one of your own and looking after me on Thanksgivings and Hanukkahs.

Being a member of University College Oxford (Univ) and having the chance to study in a collegiate environment has been unrelentingly rewarding. The ability to collaborate and socialise with people from different academic disciplines at different stages of their academic career has been one of the most fruitful experiences during my DPhil and I am extremely grateful for the network and memories that I will take forward. In particular, I would like to thank Francesca Sollohub, Alex Swanson, Luke Coffey, Alex Benn, Dr Rebecca te Water Naudé, Dr Mohamed Baioumy, and Dr Gabija Navickaité for embodying the spirit of Univ and for endless hours of entertainment and conviviality. I thank Sir Ivor Crewe, Baroness Valerie Amos, and Angela Unsworth for their steadfast collaboration during my tenure as MCR President, which was crucial in driving the community forward, along with my stalwart committee. Moreover, I thank college for awarding me the David and Lois Sykes scholarship for travel around mainland China, an unequalled experience. Finally, I would like to extend my gratitude to the Univ Trustees of the Chalet Trust and to the members of the 2019 Univ First Party for an ephemeral yet unrivalled reading party in the French Alps, reaffirming that there is great beauty in the bucolic.

In addition to my traditional academic studies, I am extremely grateful for the musical education I have also received whilst at Oxford. A big thank you to Professor Giles Underwood and Carys Lane for helping me find my voice, teaching me how to sing, and awarding me a choral scholarship after so much tumult. Being a member of the University College Chapel Choir and St James's Piccadilly Lay Singers during my sojourn in London has been an incredible way to meet long-lasting friends against bewitching backdrops. A special thank you to Julia Sandros-Alper

for your unerring support in the music round and firebrand spirit, along with bass 1 love, and the inner sanctum.

To round off my education, I have been enrolled in Modern Greek language classes throughout the course of my studies. I am grateful to Kostas Skordyles for his suspenseful tutelage of the beautiful language. I also thank Antonia Jameson, as well as James Hua and Nathan Websdale, for our odyssey in getting to grips with the enigmatic language and its many quirks. Όσο περισσότερα μαθαίνουμε τόσο λιγότερα γνωρίζουμε.

My deepest gratitude, of course, goes to my family, whose unwavering support has been instrumental in shaping my journey. You have been there through all the eras, giving me space to take healthy risks and providing me with the stability and safety net that not everyone is fortunate enough to have. To my mother and father, Nicolette and Andreas Petrou, thank you for always promoting education in the home and providing a recuperative environment during all the intermezzo periods of my life. To my brothers Jacob Petrou, Felix Petrou, and Oscar Petrou, nothing compares to the profound bonds of brotherhood. Every day, I am grateful for the enduring moments we have shared and am continually astounded by all you achieve. Thank you to Sanne van Lieshout and Jordan Breslin for joining the fold wholeheartedly and coping with the crazy. Lastly, welcome to the family, Sophia Petrou; a whole world of adventure awaits you.

Finally, to Odysseus Archontikis. I am unaccountably better due to your kindness, support, and patience. Thank you for always maintaining a curiosity about the world around you, for your keen acumen, and for your thoughtful and emotive logic. In addition, I am profoundly thankful for you showing me Greece, its unrestrained culture, and your family's heartfelt welcome. Getting to experience the country through your eyes has been a zenith of the journey. I will greatly miss those languid Oxford days, when we truly lacked for nothing. May there always be wind in our sail as we are bound, backs borne against the burnished sun, onward to the next chapter. *Et in Arcadia ego.*

Statement of Originality

This is to certify that to the best of my knowledge, the content of this thesis is my own work. This thesis has not been submitted, either by myself or others, for any other degree requirements or for any other purpose.

I certify that the intellectual content of this thesis is the product of my own work and that all the assistance received in preparing this thesis and sources have been acknowledged.



10/10/2024

Signature *Date*

Abstract

Global warming has the potential to release large quantities of methane (CH_4), a green-house gas, stored as methane hydrate from marine sediments, representing a positive carbon cycle-climate feedback. Increased sedimentary barium (Ba) burial rates have been suggested to provide evidence of global scale CH_4 release accompanying past global warming events, but these ideas remain controversial. Interpretations of these records are however ambiguous and as such Ba isotopes ($\delta^{138/134}Ba$) could be developed to provide added constraints. As such, this study focuses on the eastern margin of the South Atlantic, a reduced margin with known CH_4 cycling. Seismic imaging techniques using high-resolution 2D and 3D data and a compilation of literature geochemical data reveal variable upward diffusive and advective fluxes of CH_4 across the margin, attributed to subsurface focused fluid flow via migratory pathways, affecting redox conditions in near surface sediments. To use $\delta^{138/134}Ba$ records to inform on Ba burial rates and thus global scale CH_4 release requires comprehensive constraints on the marine Ba isotope mass balance. Two key isotopic constraints are missing from this budget: the continental shelf benthic input and burial of authigenic Ba on margins and with current constraints, inputs appear systematically offset to heavy Ba isotope compositions relative to the main output. To investigate the final two components of the marine Ba mass balance, Ba concentration ($[Ba]$) and $\delta^{138/134}Ba$ data are presented for marine sediments and co-existing pore waters along with overlying seawater and suspended particulate samples along the Namibian continental shelf, a reduced margin where benthic inputs are expected, and Regab Pockmark, Congo Margin. The $[Ba]$ of upwelling seawater increases by 10.6% (40.6 to 44.9 $nmol/kg$) as it circulates over the Namibian shelf attributed to benthic inputs caused by the diagenetic remobilisation of barite ($BaSO_4$) driven by changes in $BaSO_4$ saturation. The isotopic data for these samples can be feasibly explained by the input of Ba with $\delta^{138/134}Ba \approx +0.31‰$, consistent with measured pore water values from underlying anoxic sediments. Consequently, the remobilised benthic Ba input becomes enriched in heavier Ba isotopes relative to the initial input from sinking particles, leading to the buried Ba reservoir evolving towards a lighter isotopic composition. The results of this study imply that large benthic Ba fluxes from continental shelves may constitute a recycling of authigenic Ba phases (e.g. $BaSO_4$), rather than an input of 'new' Ba. This has implications for how this component of the Ba cycle is considered in the marine Ba mass balance and helps to bring the current constraints on the marine input and output fluxes into balance. Conversely, Regab Pockmark cold seep benthic inputs feature $\delta^{138/134}Ba \approx$ -0.14‰. This may reflect the quantitative removal of pore water Ba by $BaSO_4$ precipitation within the upper sediments, preventing significant Ba release to the water column. This finding consequently does not support use of sedimentary $[Ba]$ and $\delta^{138/134}Ba$ records as a tracer of past CH_4 release events and that the $\delta^{138/134}Ba$ of Ba benthic inputs could vary by location.

Contents

1 Introduction **1**

2 Impact of the shallow hydrocarbon plumbing system on fluid-flow and surficial sediment redox conditions in the Lüderitz Basin **9**

2.1 Introduction 10
2.2 Data and methods 13
2.2.1 Seismic and well data 13
2.2.2 Marine sediment core data 15
2.2.3 Methods 17
2.3 Geological Setting 18
2.3.1 Geodynamic Evolution of the Namibian Margin 18
2.3.2 Seismic Stratigraphy 18
2.4 Results 24
2.4.1 Seismic interpretation of direct hydrocarbon indicators and associated fluid flow features 24
2.4.1.1 Pockmarks 24
2.4.1.2 Fluid Escape Pipes 25
2.4.1.3 Bottom Simulating Reflector (BSR) 26
2.4.1.4 Enhanced reflections (ERs) 29
2.4.2 Geochemical indicators - indirect observation on fluid flow . . 32
2.5 Discussion 34
2.5.1 Proposed Lüderitz Basin HPS model 34
2.5.2 Evidence for a Biogenic HPS 37
2.5.2.1 Production of Biogenic Methane 37
2.5.2.2 Migration pathways of biogenic methane 38
2.5.3 Evidence for a Thermogenic HPS 39
2.5.3.1 Source Rock distribution 41
2.5.3.2 Stratal Migration 41

2.5.3.3 Cross-stratal Migration 42
2.5.4 Impacts on measured marine sediment core geochemical data . 43
2.6 Conclusion 44

3 Constraints on the Ba isotope composition of benthic inputs from reduced margin sediments 47
3.1 Introduction 48
3.2 Study Area & Samples 50
3.2.1 Scientific Background of Study Area 50
3.2.2 Types of Samples Used in the Study 52
3.2.3 Sample collection methods 54
3.2.3.1 Seawater samples 54
3.2.3.2 Suspended Particulate samples 55
3.2.3.3 Marine sediment cores 56
3.3 Analytical Techniques 57
3.3.1 Sample Preparation 57
3.3.2 Measurement of elemental concentrations 58
3.3.3 Measurement of Ba isotope compositions 59
3.4 Results 60
3.4.1 Data Quality 60
3.4.2 Hydrography at the time of sampling 62
3.4.3 Pore water Fe, Mn and SO_4 results 62
3.4.4 Seawater distribution of dissolved Ba concentrations and isotope compositions 64
3.4.5 Sediment distributions of Ba concentrations and isotope compositions 65
3.5 Discussion 70
3.5.1 Pore water redox conditions at time of sampling 70
3.5.2 Evidence for the benthic input of barium from the continental shelf 72
3.5.3 The drivers of the identified benthic flux 73
3.5.4 Constraining the Ba isotopic composition of the observed benthic fluxes 75
3.5.5 Mass balance considerations on the loss of isotopically heavy Ba from reducing sediments 76
3.5.6 Implications for the global Ba mass balance 80

3.6 Conclusion 84

4 Examining the utility of barium isotopes as a tracer of large-scale seafloor methane venting 86

4.1 Introduction 87
4.2 Study area and samples 90
4.2.1 Scientific Background 90
4.2.2 Types of Samples Used in the Study 92
4.2.3 Sample collection methods 94
4.3 Analytical Techniques 94
4.4 Results 96
4.4.1 Data Quality 96
4.4.2 Seawater distribution of dissolved Ba concentrations and isotope compositions 98
4.4.3 Carbonate phase concentrations and Ba isotopic composition . 100
4.5 Discussion 103
4.5.1 Impact of CH_4 venting on the marine Ba inventory 103
4.5.2 Ba response during release from Fe-Mn phases 105
4.5.3 Incorporation of Ba isotopes into authigenic carbonates 106
4.6 Conclusion 107
4.7 Sample origin and data contribution statement 108

5 Conclusion 109

A Appendix For Chapter 2 112

A.1 3D study site stratigraphy 112
A.2 ODP site 1084 well data 116

B Appendix For Chapter 3 123

B.1 MC-ICP-MS methodology 123
B.2 Contouring of oxygen penetration depth data 132
B.3 Calculation of propagated error 156

C Appendix For Chapter 4 157

C.1 TIMS methodology 160

Bibliography 162

List of Figures

1.1 The global marine Ba cycle 6

2.1 Available datasets for the study 15
2.2 Light et al. (1993) well-tie calibration 16
2.3 Seismic Stratigraphy of the Namibian Margin 20
2.4 Seismic character of the different megasequences 21
2.5 Fluid escape pipes in 3D seismic 27
2.6 Map of the interpreted BSR and seismic expression 30
2.7 SMTZ map of core pore water sulphate data 33
2.8 2D seismic cross-section with differing surface TOC 35
2.9 Biogenic Gas Production Window 40
2.10 Seismic structure relation to SMTZ depth 45

3.1 The global marine Ba cycle 49
3.2 Map of sampling site 53
3.3 Hydrology of RGNO CTD data 63
3.4 Sediment and pore water Ba, Fe, Mn, and SO_4 concentration 64
3.5 Ba concentration and $\delta^{138/134}Ba$ data vs depth 66
3.6 Ba concentration and $\delta^{138/134}Ba$ data in upwelling water 67
3.7 Ba/Al and Ba_{excess} 68
3.8 Barite Saturation Index 74
3.9 Seawater regeneration mass balance 77
3.10 $\delta^{138/134}Ba$ offsets across the Namibian margin 79
3.11 Remobilisation mass balance 81
3.12 Marine Ba input-output $\delta^{138/134}Ba$ values 84

4.1 Extent of Regab pockmark and seawater sampling 93
4.2 Barium concentration and $\delta^{138/134}Ba$ values generated in this study . 98
4.3 Regab pockmark seawater regeneration mass balance 101
4.4 Authigenic carbonate phase Ba concentration and $\delta^{138/134}Ba$ values . 102

A.1 Pockmark expression on seismic data 118
A.2 Hydrate stability curve 119
A.3 Seismic Structures 120
A.4 Methane concentration data 121
A.5 Proposed thermogenic HPS 121
A.6 Well-tie of ODP-1084 122

B.1 DBa concentration and $\delta^{138/134}Ba$ and of pumped vs CTD collection methods 132
B.2 TIMS vs ICP-MS derived Ba concentration 133

C.1 Scanned images of carbonate samples and sampling areas 157
C.2 Authigenic carbonate phase Ba concentration instrumental variations 159

List of Tables

2.1 Sequence stratigraphy of the Lüderitz Basin 19

3.1 Fluxes and isotopic composition of marine Ba mass balance 51

A.1 3D seismic volume properties 112
A.2 References for collated 2D seismic line database 113
A.3 Literature sources of geochemical data used in this study, Chapter 2. 114

B.1 Literature oxygen data 124
B.2 Literature sulphate data 125
B.3 SRM NIST 3104a and NBS-127 data generated in Chapter 3 126
B.4 Regional concentration and $\delta^{138/134}Ba$ data 128
B.5 Measured and published CRM data 133
B.6 Ba concentration and $\delta^{138/134}Ba$ values for repeated selected samples of different sample type 134
B.7 Procedural blank data generated in Chapter 3 134
B.8 $Ba/Al_{detrital}$ reference ratios 135
B.9 Marine Ba mass balance input/output fluxes Ba concentration and $\delta^{138/134}Ba$ values 136

C.1 Geochemical data measured for Chapter 4 158
C.2 SRM NIST 3104a and NBS-127 data generated in Chapter 4 158
C.3 Procedural blank data generated in Chapter 4 160

List of Reactions

Reaction {1}: Sulphate-dependent Anaerobic Oxidation of Methane (S-AOM) 3
Reaction {2}: Barite dissolution/precipitation 3
Reaction {3}: Sulphate-dependent Anaerobic Oxidation of Methane (S-AOM) 11
Reaction {4}: Diffusive Flux calculation 32
Reaction {5}: Methanogenesis (ME) 37
Reaction {6}: Secondary methanogensis or CO_2 reduction (CR) 37
Reaction {7}: δ-notation (‰) of Ba isotope data 60
Reaction {8}: Ba_{excess} 69
Reaction {9}: $BaSO_4$ Saturation Index 73
Reaction {10}: Ba concentration mass balance 75
Reaction {11}: Regeneration mass balance 75
Reaction {12}: Ba concentration mass balance 78
Reaction {13}: Remobilisation mass balance 78
Reaction {14}: Total isotopic composition of summer input fluxes 82
Reaction {15}: Sulphate-dependent Anaerobic Oxidation of Methane (S-AOM) 88
Reaction {16}: δ-notation (‰) of Ba isotope data 96
Reaction {17}: Ba concentration mass balance 103
Reaction {18}: Regeneration mass balance 103
Reaction {19}: General formula for propagation of error 156

Chapter 1

Introduction

Global warming has the potential to release large quantities of methane (CH_4), a green-house gas, stored as methane hydrate from marine sediments, representing a positive carbon cycle-climate feedback (James et al., 2016). Unambiguous evidence of this feedback in the geological record will improve understanding of the potential risk it poses for exacerbating anthropogenic global warming. For example, climate driven sedimentary CH_4 release is one of the hypothesised mechanisms for the onset of the Paleocene-Eocene Thermal Maximum (PETM)(Dickens et al., 2003; Frieling et al., 2016; Haynes and Hönisch, 2020; Inglis et al., 2021; Berndt et al., 2023) and the early Cambrian greenhouse climate required for the Cambrian Explosion (Cheng et al., 2024). Therefore, there is a need to understand if past climate change events have led to large-scale CH_4 release from the ocean to the atmosphere and, at a more local level, to track past CH_4 cycling dynamics in specific seep sites.

The primary source of CH_4 in marine sediments is the biogenic production by methanogenic archaea occurring from near surface to as much as 4600 metres below seafloor ($mbsf$) (Clayton, 1992; Rice, 1993; Marchesi et al., 2006; Hong et al., 2014a). Organic-rich sediments, typically accumulating on continental margins, enter the biogenic gas production window (30 - 40 °C; Stolper et al. (2014); Colosimo et al. (2016)), promoting methanogenesis (Aditiawati and Pujobroto, 2013; Cokar et al., 2013a,b; Hong et al., 2013; Buan and Robinson, 2018). The factors that favour significant generation of biogenic gas are: abundant total organic carbon deposits, typically greater than 0.5% (Claypool and Kaplan, 1974); anoxic conditions (Claypool and Threlkeld, 1983); low temperature and low sulphidic environment (Rice, 1993); high sedimentation rate (50 - 200 m/My; Hong et al. (2014b); Clayton (1992)); and sufficient pore space for microbes to develop (Rice, 1993). Methane can also be derived thermogenically, produced by the thermal maturation of organic

matter (Rice, 1993; Azambuja et al., 2010). Once produced, CH_4-rich fluids can migrate via stratal and cross-stratal structures throughout sedimentary basins (Rice, 1993; Gay et al., 2006, 2007; Moss and Cartwright, 2010b; Hong et al., 2013, 2014b; Foschi and Cartwright, 2016). The upward diffusive and advective flux of CH_4 can then enter the correct pressure-temperature conditions for methane hydrate formation (Xu and Ruppel, 1999; Ben-Avraham et al., 2002; Lopez et al., 2005; Boswell et al., 2012; Wenau et al., 2015; Foschi and Cartwright, 2016; Flemings et al., 2020), be sealed by stratigraphic/structural traps (Araujo-Rodrigues and Luís-Sauer, 2015; Foschi and Cartwright, 2016; Scarselli et al., 2016; Sun et al., 2021; Pichel et al., 2023) or be released into the marine inventory (Charlou et al., 2003; Allison et al., 2008; Hustoft et al., 2009; Ho et al., 2012; Berndt et al., 2023). Warming ocean bottom waters change temperature gradients in upper sediments, and sea-level changes alter pressure gradients; together, they shift the depth range of methane hydrate stability leading to the dynamic formation and dissociation of hydrate bodies in continental margin settings (Xu and Ruppel, 1999; Hunter et al., 2013; Chen et al., 2019; Flemings et al., 2020; Kunath et al., 2020). Therefore, tracing CH_4 and its sedimentary release has implication for both the climate and the energy industry.

Over the past two decades, seismic imaging techniques using high-resolution 2D and 3D data have significantly enhanced the understanding of subsurface geometry (Cartwright et al., 2007; Judd and Hovland, 2007). This has improved the knowledge of the distribution of gas-charged sediments, subsequent CH_4 migration, and their integration into a connected hydrocarbon plumbing system (HPS)(Heggland, 2004; Berndt, 2005; Løseth et al., 2009; Andresen, 2012; Anka et al., 2012; Ostanin et al., 2013; Foschi and Cartwright, 2016; Sun et al., 2021). This is required in order to determine if focused fluid flow is impacting the distribution of CH_4 in sedimentary basins, currently lacking in frontier basins (Koch et al., 2013; Hodgson et al., 2014; Intawong et al., 2015; Eastwell et al., 2018).

Large amounts of the upward diffusive and advective flux of CH_4 is utilised during the consumption of pore water sulphate (SO_4) during the anaerobic oxidation of methane (AOM) at the sulphate-methane transition zone (SMTZ), which is an important biogeochemical sink of SO_4 in reducing environments (Dickens, 2001; Lin et al., 2012). Here SO_4 is microbially mediated to oxidise CH_4 in a 1:1 ratio to form bicarbonate (Equation 1; Borowski et al. (1996); Niewöhner et al. (1998)).

$$CH_4 + {SO_4}^{2-} \longrightarrow {HCO_3}^{-} + HS^{-} + H_2O \quad \{1\}$$

$$BaSO_{4\ (s)} \rightleftharpoons {Ba^{2+}}_{(aq)} + {SO_4}^{2-}{}_{(aq)} \quad \{2\}$$

This process promotes the dissolution of barite ($BaSO_4$) in marine sediments in continental margin settings, due to $BaSO_4$ solubility, causing $BaSO_4$ in marine sediments to become undersaturated (Equation 2). As a result, large amounts of dissolved barium (Ba) accumulate in the pore waters below the SMTZ (∼7500 - 300,000 $nmol/L$; Riedinger et al. (2006); Henkel et al. (2012)) in contrast to pore water above the SMTZ (∼217 - 7500 $nmol/L$; Dickens (2001); Henkel et al. (2012); Middleton et al. (2023a)) and overlying seawater (∼35.2 - 158 $nmol/L$; Horner et al. (2015); Bates et al. (2017); Hsieh and Henderson (2017); Bridgestock et al. (2018); Hemsing et al. (2018); Geyman et al. (2019); Cao et al. (2020); Yu et al. (2022); Middleton et al. (2023a); Zhang et al. (2023)). The dissolved Ba subsequently diffuses through the pore fluids, eventually reaching a sulphate-replete front, and either re-precipitates as diagenetic $BaSO_4$ (Rutsch et al., 1995; Dean et al., 1997; Nürnberg et al., 1997; McManus et al., 1998; Gingele et al., 1999; Dickens, 2001; Paytan and Griffith, 2007; Schenau et al., 2001; Henkel et al., 2012; Martinez-Ruiz et al., 2015; Bridgestock et al., 2019; House and Norris, 2020; Scholz et al., 2023) or diffuses into the ocean as a benthic input from continental margin settings (Torres et al., 1996a,b; Scholz et al., 2023; Zhang et al., 2023).

As such, Ba concentrations in paleo archives have been used to infer aspects on past CH_4 cycling. Diagenetic $BaSO_4$ fronts take 10^4 to 10^6 years to develop, and so sedimentary Ba records are used to assess changes in SO_4 profiles and hence the past changes in the position of the SMTZ, which is sensitive to upward CH_4 fluxes (Dickens, 2001; Snyder et al., 2007a; Bhatnagar et al., 2011). However, these records can be sensitive to remobilisation over time (Dickens, 2001; Schenau et al., 2001; Henkel et al., 2012; Martinez-Ruiz et al., 2015; Bridgestock et al., 2019; House and Norris, 2020; Scholz et al., 2023). It can also be unclear if peaks in Ba in ancient marine sediments are diagenetic fronts or if they are related to other factors such as export production (Schenau et al., 2001; Gallego-Torres et al., 2007). This makes using sedimentary Ba concentration records to distinguish between preservation and productivity effects unreliable, especially in sediments of high organic matter, which

are typically of interest (Martinez-Ruiz et al., 2015).

Several processes can also affect $BaSO_4$ and pore water Ba during early diagenesis in SO_4-replete waters above the SMTZ. Firstly, shallow pore water Ba concentrations ($< 0.3\ mbsf$, $385 \pm 25.4\ nmol/kg$ ($\pm$2SE, n = 288); Paytan and Kastner (1996); Cao et al. (2023); Middleton et al. (2023a); Scholz et al. (2023)) are typically observed to be higher than in the overlying bottom seawater ($80.59 \pm 7.04\ nmol/kg$ ($\pm$2SE, n = 11); Horner et al. (2015); Hsieh and Henderson (2017); Bridgestock et al. (2018); Zhang et al. (2023)), leading to a diffusive benthic flux of Ba into the ocean. In addition, during early diagenesis the cycling of Fe-Mn phases at the sediment water interface (SWI) can promote the release of adsorbed Ba to the dissolved pool (Bayon et al., 2011; He et al., 2021; Gäng et al., 2023). Finally, recent studies have shown that ion exchange processes between Ba in pore waters and $BaSO_4$ in marine sediments are expected (Middleton et al., 2023a,b; van Zuilen et al., 2023). The extent of how each of these processes can affect Ba are key unknowns for constraining the global Ba in the oceans.

In continental margin settings sedimentary CH_4 release is accompanied by variable rates of Ba discharge across the SWI (Torres et al., 1996a,b; Greinert et al., 2002; Aloisi et al., 2004; Castellini et al., 2006; McQuay et al., 2008; Hanor and Mercer, 2011; Feng and Roberts, 2011). Therefore, CH_4 venting from continental margin settings could be an important Ba input to the ocean, and this mechanism could be recorded by higher authigenic Ba burial rates in marine sediments. For example, enhanced Ba burial rates observed during the PETM have been interpreted as a response to climate driven sedimentary CH_4 release via the dissociation of methane hydrate bodies (Dickens et al., 2003; Frieling et al., 2019). However, this assumes that methane hydrate dissociation results in a large scale dissolved Ba input to the ocean, which in turn results in a global increase in Ba burial. Therefore, unknowns include (1) if such CH_4 release can truly affect the global marine Ba cycle in this manner, and (2) if other mechanisms could also explain such global increases in Ba burial. Barium isotopes offer novel insights into past marine Ba cycling, helping to distinguish between Ba burial mechanisms. To achieve this, a deeper understanding of the links between the CH_4 and marine Ba cycle, along with their isotopic effects, is needed. Confidence in such interpretations are hindered by an incomplete understanding of the global marine Ba cycling and its links to CH_4 cycling.

Recent studies identify large, significant Ba fluxes (17 $Gmol/yr$; Rahman et al. (2022); Whitmore et al. (2022)) from continental margin sediments though the mechanism causing them is unknown. Changes in $BaSO_4$ solubility in surficial sediments represents one possible mechanism that would build up a remobilised pool of Ba, which in turn could be linked to CH_4 cycling. However, the magnitude of any subsequent benthic input could vary due to the extent of $BaSO_4$ re-precipitation at or close to the SWI, where Ba rich pore waters encounter SO_4 rich seawater (Aloisi et al., 2004), and/or the strength of the Ba efflux (Aquilina et al., 1992; Dia et al., 1993; Torres et al., 1996b; Aloisi et al., 2004; Castellini et al., 2006; Hein et al., 2007; Snyder et al., 2007a; Canet et al., 2013; Stevens et al., 2015; Núñez-Useche et al., 2018; Bei et al., 2020; Zhou et al., 2022). Both attributes are variable at different continental margins and are difficult to constrain making it difficult to use dissolved and sediment Ba concentrations as a tracer of past CH_4 release.

Stable Ba isotope variations could be developed as a new tool to test the fidelity of Ba as a tracer of large scale CH_4 release, potentially leading to clearer geological insights into the significance of this carbon cycle-climate feedback and would overcome uncertainties in current Ba concentration based proxies for marine cycling. Recent studies have constrained the Ba isotope composition of important external components of the marine Ba cycle, including inputs from rivers (Bridgestock et al., 2021a,b; Cao et al., 2021; Zhang et al., 2023), groundwater (Mayfield et al., 2021; Rahman et al., 2022) and hydrothermal vents (Hsieh et al., 2021; Zhang et al., 2024), and output via burial in open ocean sediments (Crockford et al., 2019)(Figure 1.1). With current constraints, inputs appear systematically offset to heavy Ba isotope compositions relative to the main output (Horner and Crockford, 2021). Two key isotopic constraints are missing from this budget: the continental shelf benthic input and burial of authigenic Ba on continental margins. Constraining the remaining two isotopic compositions would aid in establishing whether the shelf sediment benthic input is an internal ('recycling') rather than an external ('new') component of the Ba cycle and would allow reassessment in whether Ba can be used as a marine proxy for marine CH_4 cycling.

Recent studies have provided updated constraints on the input and output fluxes of the marine Ba mass balance (Carter et al., 2020; Bridgestock et al., 2021b; Hayes et al., 2021; Hsieh et al., 2021; Mayfield et al., 2021; Rahman et al., 2022; Whitmore et al., 2022). Including the shelf sediment benthic input in the marine Ba mass

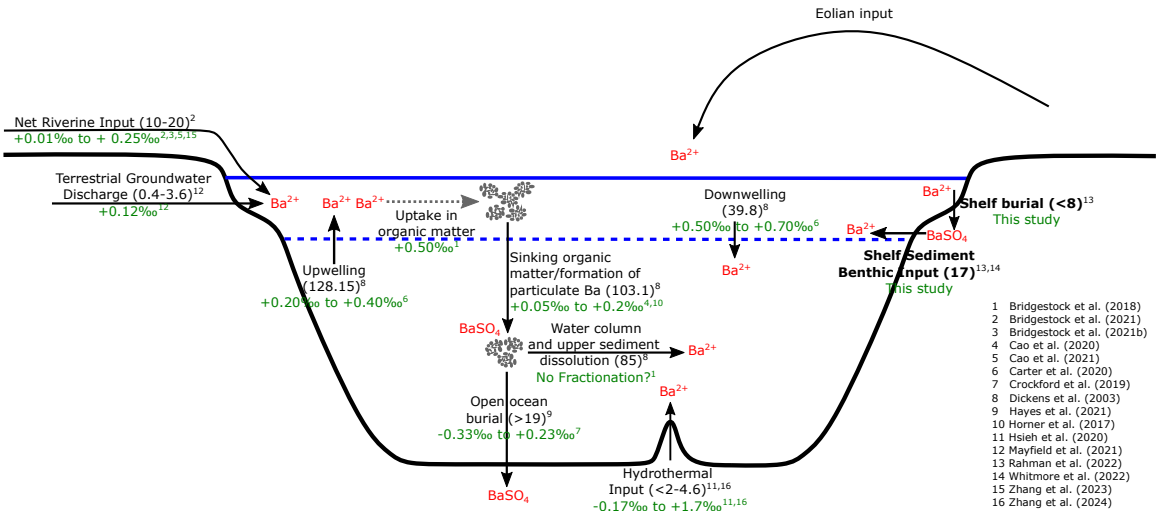

Figure 1.1: A simplified diagram of the marine Ba cycle. Direction of fluxes are shown with black arrows, with the value of the flux in parentheses (in $Gmol.yr^{-1}$). The associated phase of barium (Ba) is shown in red, with Ba^{2+} as the dissolved phase and $BaSO4$ as the solid phase. Currently the isotopic composition of the shelf sediment burial and the shelf sediment benthic input are the two remaining components to be constrained.

balance as an input causes a two-thirds imbalance between inputs and outputs (Rahman et al., 2022; Horner and Crockford, 2021). A possible explanation of this flux imbalance is that shelf benthic inputs could be an internal ('recycling') rather than an external ('new') component of the Ba cycle. This uncertainty on the role of shelf sediment benthic input needs to be resolved in order to use Ba concentration as a proxy in the marine system for CH_4 cycling.

This study aims to examine the utility of Ba isotopes as a tracer of CH_4 cycling in continental margin settings, both in the modern and geological archives. The main study area is the Benguela Upwelling System (BUS), an example of an eastern boundary upwelling system (EBUS), located along the Namibian coastal margin (García-Reyes and Largier, 2010; Santos et al., 2012; Varela et al., 2015; Wang et al., 2015; Brady et al., 2019; Seabra et al., 2019; Abrahams et al., 2021; Bograd et al., 2022). The BUS is defined as an upwelling centre that has high biological primary productivity, with an annual average rate between 580 and 1470 $gCm^{-2}a^{-1}$ (Small and Menzies, 1981; Demarcq, 2009; Barlow et al., 2009; Monteiro, 2010; Verheye et al., 2016; Emeis et al., 2018; Jacobs et al., 2020; Paparazzo et al., 2021). The high rates of productivity in turn drive the development of an oxygen minimum zone (OMZ), <50 $\mu mol/kg$, overlying the continental shelf (Chapman and Shannon, 1987;

Tyson and Pearson, 1991; Berger et al., 2002b; Brüchert et al., 2003; Pitcher et al., 2014; Schmidt and Eggert, 2016; Rixen et al., 2021; Lovecchio et al., 2022; Said et al., 2023) causing large gradients in shelf sediment redox conditions/diagenesis that are variable across the continental margin (Brüchert et al., 2003; Borchers et al., 2005; Brüchert et al., 2006; Abshire et al., 2020; Wyatt et al., 2021; Hunt et al., 2022; Liu et al., 2022; Gäng et al., 2023; Kossack et al., 2023; Chen et al., 2024b). Hence, the biogenic and thermogenic production and migration of CH_4 are well-documented across the BUS (Clemson et al., 1997; Bagguley and Prosser, 1999; Niewöhner et al., 1998; Wefer et al., 1998; Zachos et al., 2004; Hopkins, 2006; Riedinger et al., 2006; Swart, 2009; Moss, 2010; Moss and Cartwright, 2010b; Cartwright et al., 2012; Lin et al., 2012; Böning et al., 2020; Hopkins and Cartwright, 2021) and would promote the diagenetic remobilisation of $BaSO_4$ due to solubility changes (Equation 2). This would build a large remobilised pool of Ba that has the potential to enter the seawater as a benthic input making the BUS an appropriate location to: constrain the final two components of the marine Ba mass balance; determine the role of shelf sediment benthic inputs; and test whether Ba concentration and Ba isotopes can be used as a tracer of CH_4 cycling in continental margin settings.

In Chapter 2 the study first focuses on understanding the CH_4 system present in the BUS and aims to determine (1) if a hydrocarbon plumbing system (HPS) is present in the BUS, (2) the origin of CH_4 and connectivity of the HPS, and (3) the potential impact of the subsurface HPS on measured geochemical data in shallow marine sediment cores i.e. if the diagenetic remobilisation of $BaSO_4$ is ubiquitous across the BUS. To achieve this high-resolution 2D and 3D multichannel seismic reflection data are interpreted with respect to fluid flow features. Secondly, in Chapter 3 the study aims to understand the cycling of Ba between the water column and surficial sediments ($<30\ cm$ below the SWI) in the BUS, and to constrain the associated isotopic effects, specifically (1) the mechanism controlling the benthic Ba fluxes from anoxic continental margin settings and (2) the isotopic composition of these fluxes. Ergo, Ba concentration and Ba isotopes are presented for dissolved seawater, suspended particulate matter, marine sediment core and extracted pore water fraction, spanning gradients in redox conditions across the BUS. Finally, in Chapter 4 the study examines the utility of Ba isotopes as a tracer of large-scale seafloor CH_4 venting by gaining first constraints on the isotopic composition of benthic Ba fluxes associated with CH_4 cold seeps. By assessing the global importance of shelf sediment benthic inputs of Ba, and the mechanism that causes them, the final

two components of the marine Ba mass balance can be constrained, and the role of shelf sediment benthic inputs can be evaluated. This will allow re-assessment of the marine Ba mass balance and if an imbalance in input-output fluxes is still present and needs to be resolved, required in order to use Ba as a tracer for past CH_4 cycling.

Chapter 2

Impact of the shallow hydrocarbon plumbing system on fluid-flow and surficial sediment redox conditions in the Lüderitz Basin

The upward diffusive and advective flux of methane (CH_4) has the ability to alter redox conditions and drive biogeochemical cycling in surface marine sediments. However, due to the focused fluid migration, the upward diffusive and advective flux of CH_4 is variable, both spatially and in its intensity. Therefore, caution must be exercised when interpreting geochemical data of shallow sediment cores in areas of known CH_4 flux when no subsurface geophysical data are available for context. Over the past two decades, seismic imaging techniques using high-resolution 2D and 3D multichannel seismic reflection data have significantly enhanced the understanding of subsurface geometry. This has improved the knowledge of the distribution of gas-charged sediments, subsequent fluid migration, and their integration into connected hydrocarbon plumbing systems (HPS). As such, this study aims to determine (1) if a HPS is present in the Lüderitz Basin, offshore Namibia, a frontier basin with limited understanding of subsurface CH_4 flow, (2) the origin of fluids and connectivity of the HPS, and (3) the impact of the subsurface HPS on measured geochemical data in shallow marine sediment cores. To achieve this, a detailed seismic interpretational study of direct hydrocarbon indicators (DHIs), using 2D and 3D multichannel seismic reflection data was performed. Typical, distinctive types of DHIs were utilised for the interpretational framework such as (1) a bottom simulating reflection (BSR), (2) enhanced reflections (ERs), and (3) pipes. All these features are indicative of fluid migration throughout the shallow part of the Lüderitz Basin. The spatial distribution of the recorded DHIs indicate a predominantly shallow,

biogenic HPS with a small component derived from thermogenic sources is present. Focused fluid flow via migration pathways causes a variable upward CH_4 diffusive and advective flux across the Lüderitz Basin that impacts to variable degrees the redox conditions shallow marine sediment cores are subject to. As such, marine sediment cores only provide a limited view of the subsurface and erroneous conclusions may be drawn if interpreting biogeochemical data in isolation in areas of known, variable CH_4 flux.

2.1 Introduction

Hydrocarbon plumbing systems (HPS) are networks of permeable pathways facilitating the ascent of hydrocarbons, fluids, and gas to shallower reservoirs from the deeper kitchen area of a basin where they are generated. In these shallower reservoirs, hydrocarbons can accumulate in quantities that are commercially viable and therefore ascertaining whether a connected HPS is present is useful for initial exploration in frontier basins (Andresen, 2012). The pathways for any given HPS exhibit considerable variability contingent upon geological context, but typically involve a combination of stratal (along bedding) and cross-stratal (vertical) hydrocarbon migration (England et al., 1987). Further to this, it is common to observe secondary hydrocarbon accumulations in shallower parts of the basin, separated from the identified source by thousands of metres of low-permeability sediments (Aplin et al., 1999). As a result, an integrated approach has been developed to identify the diverse set of geological features that can highly focus vertical hydrocarbon migration. Seal bypass systems that aid the cross-stratal migration of fluids, such as faults, pipes and intrusions, can be identified on multichannel seismic reflection data and are common features in areas of active vertical fluid and hydrocarbon flow (Cartwright et al., 2007; Judd and Hovland, 2007). In addition, it is feasible to group various, disparate fluid flow phenomena observed on seismic data, including the bottom simulating reflection (BSR), pipes, and pockmarks, and explicitly establish their interconnection into a single united migration pathway (Heggland, 2004; Berndt, 2005; Løseth et al., 2009; Sun et al., 2021).

The upward diffusive and advective flux of fluids, in particular methane (CH_4), can aid in altering redox conditions, driving biogeochemical cycling in surface marine sediments. For CH_4, the major pathway is via the consumption of pore water sulphate

(SO_4) during the anaerobic oxidation of methane (AOM) at the sulphate-methane transition zone (SMTZ), which is an important biogeochemical sink of SO_4 in reducing environments (Dickens, 2001; Lin et al., 2012). Here SO_4 is microbially mediated to oxidise CH_4 in a 1:1 ratio to form bicarbonate (Equation 3; Borowski et al. (1996); Niewöhner et al. (1998); Jørgensen et al. (2001); Jørgensen and Kasten (2006)). Therefore, the depth of the SMTZ has been established as an inverse scale of the strength of the upwards diffusive CH_4 flux (Dickens, 2001; Davie and Buffett, 2003; Bhatnagar et al., 2008, 2011; Hu et al., 2018; Li et al., 2019).

$$\mathrm{CH_4 + {SO_4}^{2-} \longrightarrow {HCO_3}^{-} + HS^{-} + H_2O} \qquad \{3\}$$

This process promotes the dissolution of barite ($BaSO_4$) in marine sediments along continental margins, due to changes in $BaSO_4$ solubility, causing $BaSO_4$ in marine sediments to become undersaturated. As a result, large amounts of dissolved Ba accumulate in the pore waters below the SMTZ (∼7500 - 300,000 $nmol/L$; Dickens (2001); Riedinger et al. (2006); Henkel et al. (2012)) in contrast to pore water above the SMTZ (∼217 - 7500 $nmol/L$; Dickens (2001); Henkel et al. (2012); Middleton et al. (2023a)). This causes a decoupling of sedimentary barium accumulation rates from the export production of carbon and makes the use of sedimentary Ba burial rates to determine climate driven sedimentary CH_4 release potentially unreliable (Dymond et al., 1992; Dickens, 2001; Dickens et al., 2003; Riedinger et al., 2006; Carter et al., 2020; Frieling et al., 2016). Due to focused fluid migration, the upward diffusive and advective flux of CH_4 is variable, both spatially and in its intensity. Therefore, caution must be exercised when interpreting geochemical data of shallow marine sediment cores in areas of known CH_4 flux when no subsurface geophysical data are available for context.

Recently, geochemical techniques of surface hydrocarbon seeps and numerical modelling of source rock maturation have been integrated into HPS model generation, furthering the validity of potential fluid migration (Anka et al., 2012; Ostanin et al., 2013). However, in frontier basins that lack extensive and robust datasets along with previous investigation, the interpretation of a valid HPS becomes difficult. Furthermore, without subsurface context, conclusions based on the variation measured in regional geochemical marine sediment core data, becomes uncertain in their validity, potentially rendering results bias. This is becoming increasingly common with limited geophysical data being publicly available in areas where

geochemical sampling occurs.

This study aims to determine (1) if a HPS is present in the Lüderitz Basin, offshore Namibia, a frontier basin with limited understanding of subsurface CH_4 flow, (2) the origin of fluids and connectivity of the HPS, and (3) the impact of the subsurface HPS on measured geochemical data in shallow marine sediment cores. To achieve this, a detailed seismic interpretational study of direct hydrocarbon indicators (DHIs), using predominately 2D seismic reflection data was performed. DHIs are an example of anomalous seismic amplitudes that occur because of the presence of fluid, hydrocarbon or a combination of both (Sheriff, 1975). They are visible on seismic data because the varying changes of pore fluid alters the bulk rock elastic property. DHIs are a common feature in unconsolidated, relatively young sediments and are a typical feature of the Lüderitz Basin (Clemson et al., 1997; Bagguley and Prosser, 1999; Hopkins, 2006; Moss, 2010; Moss and Cartwright, 2010b; Cartwright et al., 2012; Hopkins and Cartwright, 2021). In addition, shallow marine sediment core geochemical data at centimetre scale resolution is utilised to ascertain subsurface CH_4 flow.

The study area is the Lüderitz Basin, offshore Namibia, where limited data are available, and previous research and exploration have been minimal (Clemson et al., 1997; Wefer et al., 1997; Moss and Cartwright, 2010a; Hodgson et al., 2014). The Namibian passive margin has extensive source rock and reservoir sequences that could thrust Namibia into the exploration age (Schmidt, 2004; Hodgson et al., 2014; Intawong et al., 2015; Ceraldi et al., 2017). The lack of wells and known seals increase the exploration risk for the Lüderitz Basin but the adjacent Kudu gas field and exploration successes in basins on the Brazilian conjugate margin shows promise for development of a connected HPS (Davies and der Spuy, 1990; Strozyk et al., 2017). Therefore, the distribution of DHIs and fluid flow features in the study area are grouped and analysed, to determine if their spatial relationships indicate they are associated and support a HPS (Andresen, 2012; Foschi and Cartwright, 2016). For the study area, both geochemical, marine sediment core data, and geophysical data, comprising of 2D and 3D multichannel seismic reflection data, are integrated to investigate the HPS. The distribution of DHIs and the geometry of the HPS will suggest whether a thermogenic, biogenic, or mixed source of CH_4 is probable. This is an ideal case study area in which to analyse a HPS in a frontier area lacking in robust

physical samples and wells, and to determine what impact subsurface focused fluid flow can have on redox and geochemical measurements in marine sediment cores.

2.2 Data and methods

2.2.1 Seismic and well data

The multichannel seismic reflection data used in this study is comprised of a 2D seismic survey, collated from literature (Light et al., 1993; Clemson, 1997; Bagguley and Prosser, 1999; Corner et al., 2002), along with a single exploration 3D cube provided by Serica Energy (Figure 2.1).

The 2D seismic data survey was collated from published literature sources (Table A.2 & Figure 2.1; Light et al. (1993); Clemson (1997); Bagguley and Prosser (1999); Corner et al. (2002)). Each line possesses its own acquisition parameters, orientation and spacing with varied processing parameters. The data, when not already, was converted into two-way travel time (TWT). The survey is comprised of 71 lines totalling 16,552 km and provided a regional overview across the entire Namibian margin. The combination of the 2D grids is characterized by a spacing of $\sim$10 - 90 km (Figure 2.1). The surveys are zero phased with a SEG normal polarity where an increase in acoustic impedance is represented by a positive amplitude, herein a positive reflection (Brown, 1986). The vertical seismic resolution varies across the database because of the different processing methods applied to data from various sources. However, considering an observed frequency range of 30 to 45 Hz and a velocity variation between 1600 and 1900 m/s, the vertical resolution, roughly a quarter of the dominant wavelength (Widess, 1973), falls within the range of 10 to 12 metres (m).

The Serica Energy dataset is a high-quality, 3D, pre-stack time-migrated volume, acquired by Serica Energy in 2012, that is clipped within the Cenozoic (-1s TWT below seafloor). It covers $\sim$4200 km^2, collected in $\sim$345 - 1500 m water depth, within the Lüderitz Basin, 100 km from the Lüderitz Arch. The Serica Energy dataset followed the standard method of constructing seismic data using the TWT of compressional waves (P-waves), measured during acquisition (Brown, 1986). The data was processed using a work-flow focused on multiple removal, which included surface related multiple elimination (SRME) and demultiple Radon transform. Full Kirchhoff pre-stack time migration has been applied to restore the position of the

reflections in time domain. As such, the final survey was finalised with a 4 ms interval and a 12.5 m by 12.5 m bin size (N-S in-lines and E-W cross-lines). Table A.1 provides further information on survey parameters.

Limited well information is available across the Namibian margin making well calibrations possible but with appropriate caveats (Figure 2.1). Wireline logs were collected in Ocean Drilling Programme (ODP) Leg 175 in wells ODP-1080 to ODP-1085 and multiple electrical, porosity and lithology logs are available (Wefer et al., 1999). Wireline logs were also collected for the four DSDP wells, located on Walvis Ridge, however, are less of use to this study due to lack of seismic data in this area. The ODP-1084 well is $\sim$12 km NNW of the dataset and has been used for seismic well-tie calibration. A well-tie calibration was achieved by integrating core-log-seismic data. Well log data, typically p-wave velocity, were matched with seismic reflection data and verified using lithological, porosity, density, and acoustic impedance information. Key reflectors were correlated to ensure consistency between the log and seismic data allowing a depth conversion to occur. As such the ODP-1084 well was projected onto seismic data. Further ODP-1084 well data are discussed in Appendix A.

The results from recently drilled exploration wells are not publicly available although some stratigraphic and petroleum data have been released via specific exploration company websites. The largest viable petroleum system offshore Namibia is the Kudu gas field, located 120 km SSW offshore the Namibian and South African border in water depths of $\sim$200 m (Figure 2.2c). A direct well calibration for available seismic data is possible and shows a direct link between seismic facies and sequence stratigraphy (Figure 2.2a-b; Light et al. (1993)). The reservoir gas is sweet, dry and low in CO_2 (Cartwright et al., 2012) with current gas reserves predicted between 1.3 and 3.0 trillion cubic-feet (TCF). Early Cretaceous Aeolian sands of the late syn-rift stage constitute the reservoir rock that is interbedded with volcanic rocks (Muntingh and Brown, 1993). The Kudu gas field is hosted by a stratigraphic trap with a small structural component (Jungslager, 1999; Cartwright et al., 2012). Appraisal wells have determined multiple stacked reservoirs of 50 m in thickness with a porosity of 12% (Muntingh, 1993). Other recent, extensive oil and gas discoveries have occurred and include the Mopane oil discovery west of Kudu by Galp Energia with an initial estimate of 10 - 12.5 billion barrels (Hodgson et al., 2024). The Venus, Graff, Jonker, Mangetti, La Rona, and Enigma discoveries have the potential

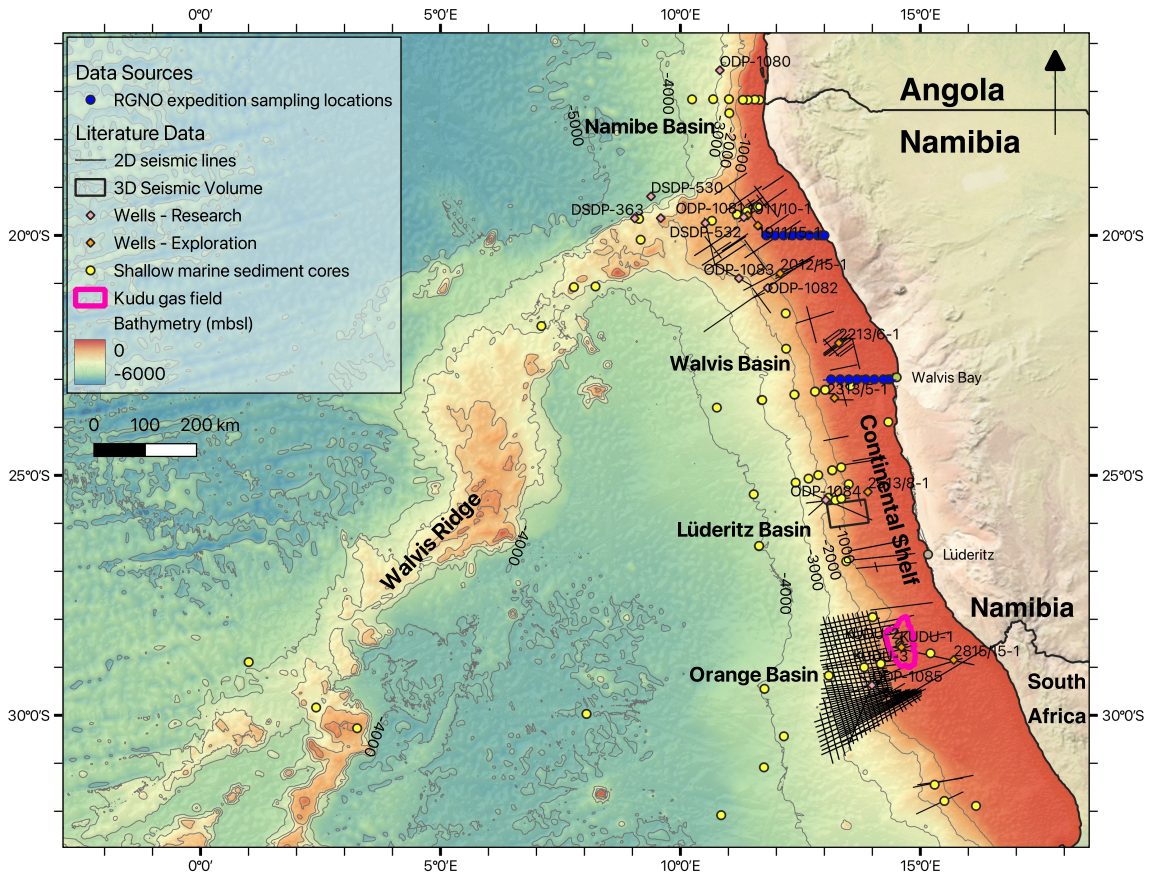

Figure 2.1: Spatial distribution of the different datasets and sources available for use in this project. Core data, seismic data and petrophysical data form the majority of the data wealth.

to be developed for extensive oil and gas recovery, though currently pose operational challenges (Heins, 2022; Hodgson et al., 2021; Rathee and Tewari, 2024).

2.2.2 Marine sediment core data

To provide more context on fluid flow in the Lüderitz Basin, porosity and marine sediment core concentration data was compiled for 53 marine sediment core samples from literature across the Namibian margin to capture varied redox zones (Figure 2.1 & Table A.3; Gingele (1992); Hensen (1996); Hensen et al. (1997); Wefer et al. (1997); Haese et al. (1998); Niewöhner et al. (1998); Heuer (2002); Müller (2003); Hensen et al. (2003); Müller (2004); Zachos et al. (2004); Riedinger et al. (2006); Lin et al. (2012); Goldhammer et al. (2011); Ashe (2018); Böning et al. (2020)).

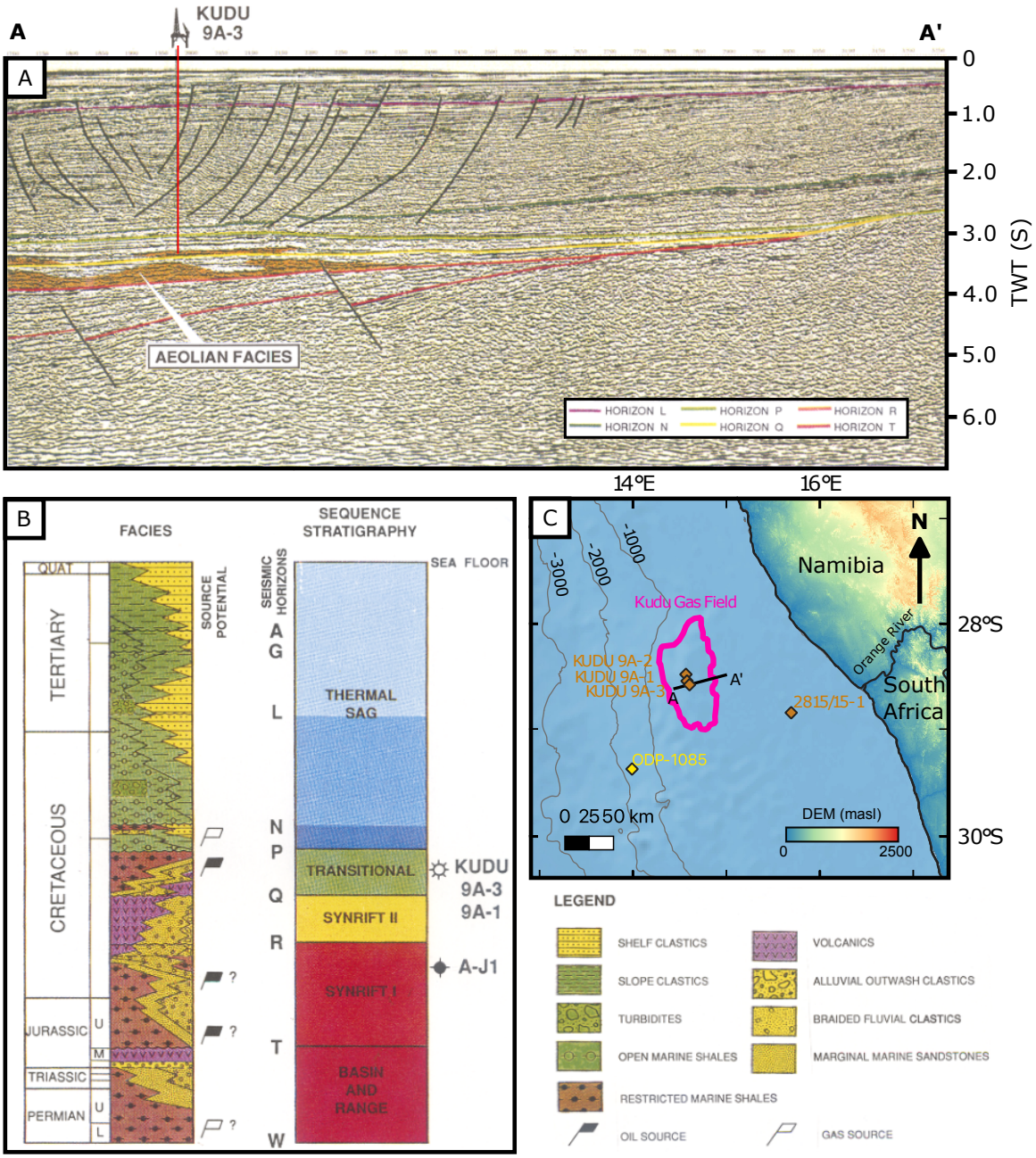

Figure 2.2: Seismic Stratigraphy and well-tie as proposed in Light et al. (1993) through the Kudu gas field. a) Seismic line ECL 89-011 with proposed seismic stratigraphy and the intersection with the Kudu 9A-3 well. b) Chronostratigraphy with seismic horizons based on the Kudu 9A-3 well. c) Location map showing location of seismic section along with the extent of the Kudu gas field.

The specific stations were compiled due to intersection with the seismic and well data, allowing the integration of the two distinct data types (Figure 2.1). The datasets compiled were: pore water CH_4 and SO_4 concentration; solid phase iron concentration; total organic carbon (TOC)/dissolved inorganic carbon (DIC) data; and physical rock properties such as porosity (Table A.3).

Each coring expedition used different acquisition methods leading to marine sediment cores with variable depths of penetration, between 0.25 and 600 m. The marine sediment cores analysed in the study were collected during (1) ODP Leg 175, a coring whilst drilling expedition 12th August - 9th October 1997 on R/V JOIDES Resolution, (2) a set of gravity cores collected during R/V Meteor expeditions M34/2 and M57/2 (3rd January - 15th April 1996 and 11th February to 12th March 2003, respectively), and (3) a set of multi-cores collected 6th - 12th May 2019, during 20°S and 23°S cruise transects on R/V Mirabilis as part of the Regional Graduate Network in Oceanography (RGNO) programme.

2.2.3 Methods

The interpretation of the multichannel seismic reflection data utilised computer-aided software, chiefly Petrel, provided from Schlumberger. Time, depth, and thickness maps, resulting from the interpretation of the 2D seismic grid, were generated using convergent interpolation algorithms found in Petrel. During these processes, conservative gridding was used, and a confined search window of 1 km was used to restrict the map extent, ensuring a more dependable extrapolation of the values of the picked horizons. Detailed litho- and chrono-stratigraphic descriptions of the seismic stratigraphy for the Namibian margin and the Lüderitz Basin is possible due to previous borehole calibrations of seismic data (Light et al., 1993; Wefer et al., 1997). In addition, previous published work focused in the study area, has also been utilised when interpreting the stratigraphic units present (Clemson et al., 1997; Moss, 2010). Therefore, a framework of major regionally correlatable seismic horizons was produced and has been used to define five major seismic packages in the study area. These packages are used to analyse the seismic facies of host units and the habitat of the DHIs. The qualitative interpretation of the seismic amplitude data and resulting mapped horizons was augmented by quantitative calculations to generate BSR thickness maps (Xu and Ruppel, 1999), geothermal gradients (Yamano et al., 1982; Dingle and Nelson, 1993) and biogenic gas production windows (Rice, 1993). This required assuming an average sediment velocity value of 1560 m/s, typical of

sediments located along the Namibian margin (Wefer et al., 1999). Finally, using the concentration gradient of core pore water SO_4 and CH_4 concentration data, the depth of the SMTZ has been approximated and, using a conservative spatial extent to reduce extrapolation error, can be interpolated across the study site (Dickens, 2001).

2.3 Geological Setting

2.3.1 Geodynamic Evolution of the Namibian Margin

The Lüderitz Basin, offshore Namibia in the South Atlantic Ocean, is one of the four major N-S bounded basins in the West African passive continental margin, developed by two major phases of tectonic extension that is attributed to the breakup of Gondwana (Figure 2.1; Daly et al. (1989); Delvaux (1991); Catuneanu et al. (2005); Guiraud et al. (2005); Jourdan et al. (2005); Eagles (2007); Renne et al. (1992); Seton et al. (2012); Moss and Cartwright (2010b); Lamotte et al. (2015)). Ever since rifting ended in the middle Cretaceous (120 - 90 Ma) the Namibian margin has been subject to tectonic drift, thermal subsidence and the progradational infilling of Mesozoic basins due to eustatic sea level change (Clemson et al., 1997; Moss and Cartwright, 2010a; Baby et al., 2018; Kirkpatrick et al., 2019a; Alves et al., 2020). This has led to well defined basins with a strong shelf, slope and basin structure in the present day (Maslanyj et al., 1992; Dingle, 1973; Pichel et al., 2023). The continental shelf is $\sim$40 km wide and relatively deep with the shelf-slope break occurring around 350 m water depth on average (Bauer et al., 2000; Kirkpatrick et al., 2019b; Pérez-Gussinyé et al., 2023). The West African passive continental margin is bounded to the North by Walvis Ridge, an aseismic hotspot-derived ocean ridge, $\sim$3000 km in length, and bounded to the south by the $\sim$1200 km long Agulhas Falkland Fracture Zone (AFFZ)(Rabinowitz and Labrecque, 1979; Cande et al., 2010; Chauvet et al., 2021; Sager et al., 2023). The West African passive continental margin is seismically and structurally analogous to the Santos-Pelotas basins offshore Brazil, an extremely productive and hydrocarbon-rich system (Mello et al., 2013; Polus et al., 2015; Strozyk et al., 2017).

2.3.2 Seismic Stratigraphy

The seismic stratigraphy of the Mesozoic basins can be subdivided into megasequences or 'tectono-stratigraphic units' related to regional tectonic events. The post-African basement phases are commonly referred to as the Karoo Rift with Post-Rift phases

Tectono-stratigraphic Unit		Horizon Name	Horizon Colour	Age (Ma)
Megasequence E	Drift Phase 3	HRZ560	Pink	66
	Drift Phase 2	HRZ530	Purple	93.9
	Drift Phase 1	HRZ500	Light Blue	119
Megasequence D	Transitional Phase	HRZ400	Dark Blue	127
Megasequence C	Atlantic Rift Phase 3	HRZ360	Light Green	131
	Atlantic Rift Phase 2	HRZ330	Dark Green	136
	Atlantic Rift Phase 1	HRZ300	Yellow	163
Megasequence B	Karoo Post-Rift Phase	HRZ200	Orange	237
Megasequence A	Karoo Rift Phase	HRZ100	Red	298
Pan-African Basement		N/A	N/A	

Table 2.1: Sequence stratigraphy of the Lüderitz Basin

referred as the 'Atlantic' Rift Phase (Clemson et al., 1997). The stratigraphy of sediments since the Permian until the modern can be separated into five major tectono-stratigraphic units (Table 2.1).

The sequence boundaries delineating these tectono-stratigraphic units are displayed on an interpreted regional 2D line, ECL-89-032 (Corner et al., 2002), that passes close to the ODP-1084 well (Figure 2.3a,c). The following seismic horizons (HRZXXX, named here) that are discussed in the below regional stratigraphy study are located within this figure. Corresponding seismic data along with the seismic character of the proposed tectono-stratigraphic units are shown in Figure 2.4 (Corner et al., 2002). Light et al. (1993) previously completed a well-tie further south on seismic data that intersects the Kudu 9A-3 well and can be viewed in Figure 2.2a-b.

The Pan-African megasequence is easily identifiable, thick but seismically opaque package that is observed on seismic data along the entire margin but is most evident on the Lüderitz arch. Unconformable surfaces mark the top of the megasequence with transitional and drift sediments. The base, when observed on seismic data, is characterised by an abrupt increase in amplitude where reflections have brighter amplitudes and are discontinuous (Figure 2.4; Clemson et al. (1997)). It has been proposed this contact be a shear-zone contact separating the lower Namaqua-Natal with the Pan-African basement domains (Light et al., 1993).

Megasequence A & B represent sediments accumulated in the Karoo rift phase that are pre-rift and early syn-rift sediments deposited in the Permian to the Middle Jurassic. The relationship between the two Megasequences, along with their relative

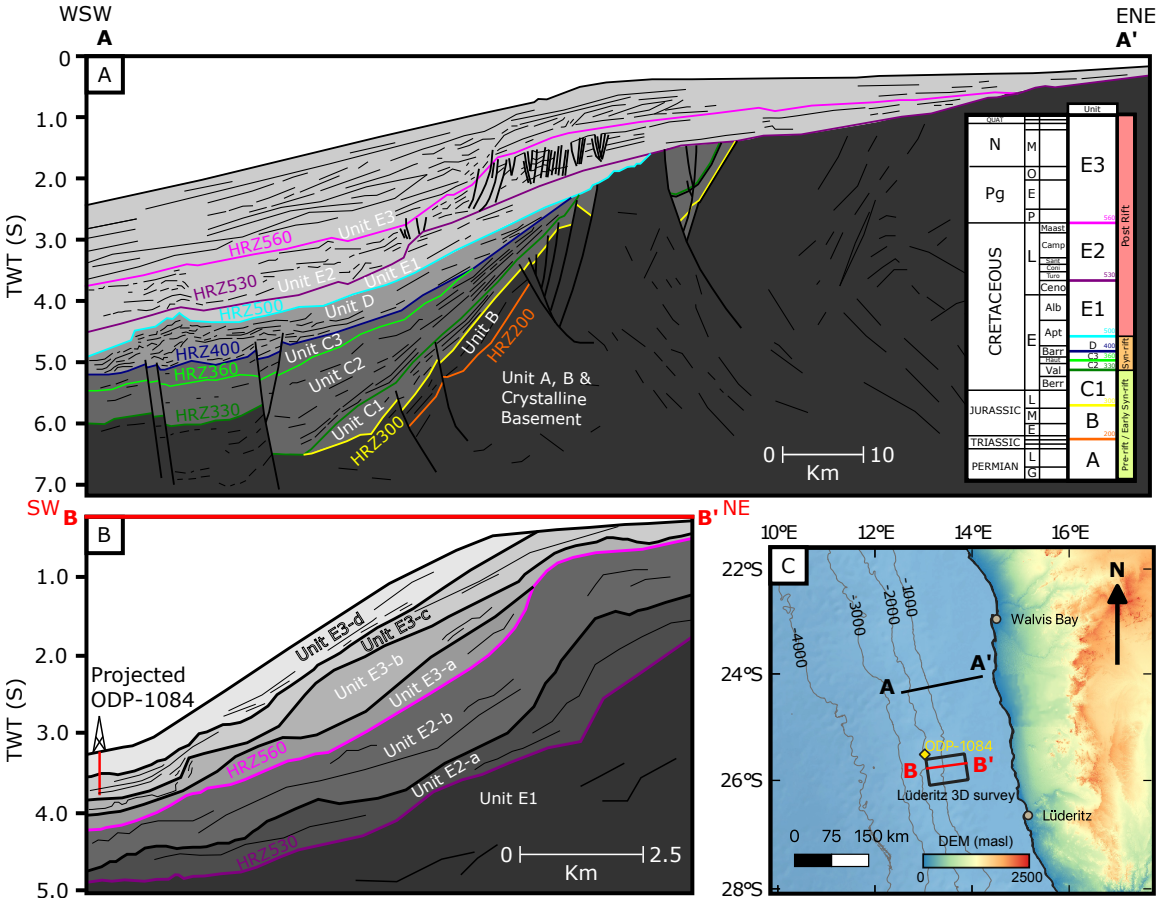

Figure 2.3: Interpreted line drawing of WSE-ENE orientated 2D seismic line ECL-89-032 (Clemson, 1997). a) All megasequences from the Namibian platform to the central graben-high are delineated as units and the bottom of each sequence is marked by a horizon (Stratigraphic column key & Table 2.1). b) Zoom-in of the final megasequence, Megasequence E, using the 3D seismic data block showing further subdivision of the unit. c) The location of both seismic lines are shown.

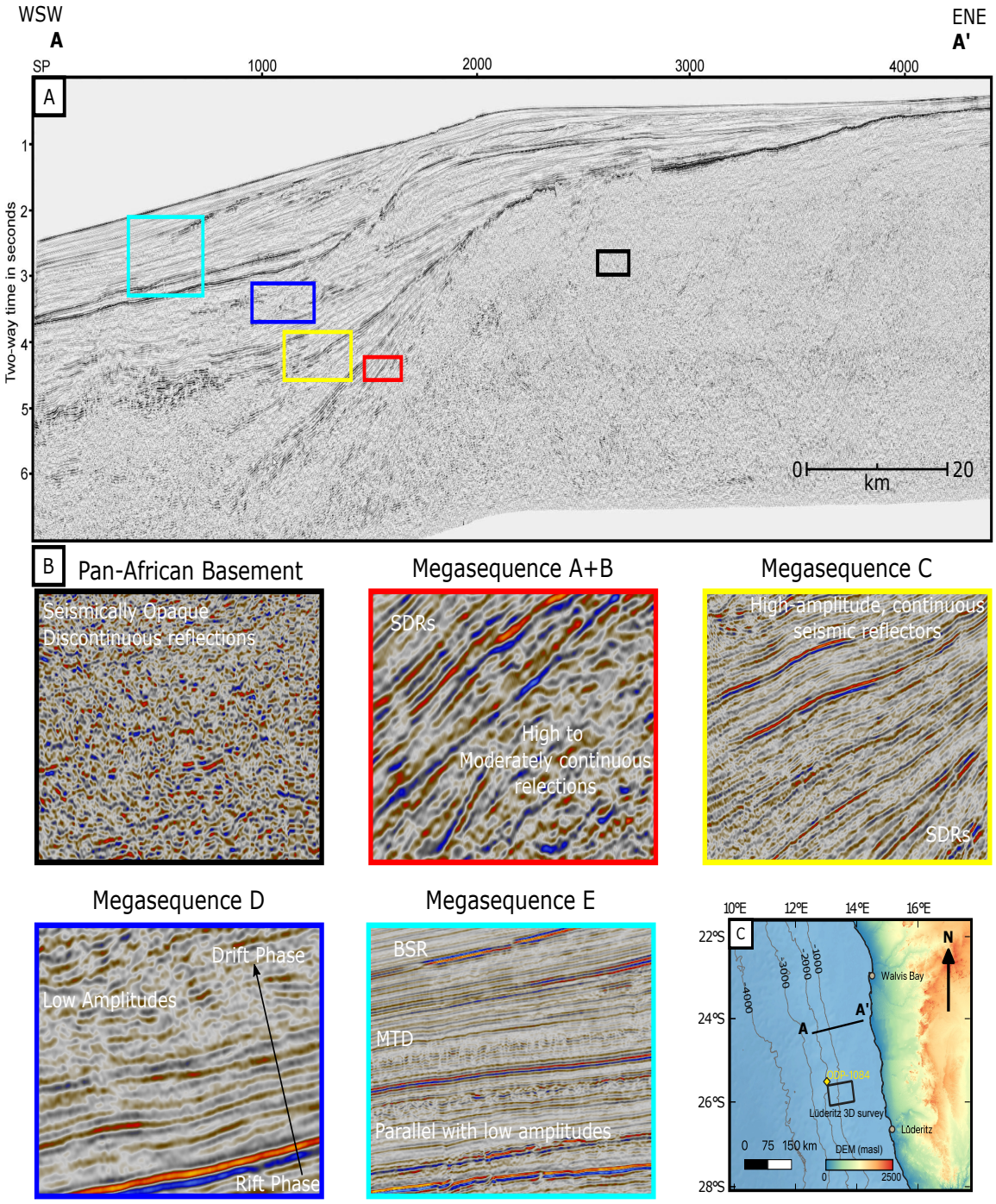

Figure 2.4: Seismic character of the different megasequences along the Namibian margin. a) 2D seismic cross-section of the Namibian margin showing locations of the sub-plots. The 2D line, ECL-89-32, has been adapted from seismic data displayed in Corner et al. (2002). b) Sub-plots of the 2D ECL-89-32 line showing the seismic character of the different megasequences along the Namibian margin. c) The location map of the seismic profile. The line shown is A-A' in the map.

position in the sediment stack between crystalline basement and the 'Atlantic' Rift phase sediments, suggest that Megasequence A & B can be correlated to onshore units that denote the Lower and Upper Karoo respectively (Horsthemke et al., 1990). The top of the Pan-African basement is truncated by an angular unconformity that defines the base of Megasequence A. Megasequence B sits above the Lower Karoo sediments and is separated by an angular unconformity (HRZ200; Figure 2.3a). A phase of inversion resulted in the uplifting and subsequent erosion of Megasequence A, attributed to the Mid-Triassic hiatus onshore (Clemson et al., 1997). Therefore, Megasequence B sediments onlap onto the flanks in areas where Megasequence A has been uplifted and faulted. On seismic data the two megasequences are expressed by moderately continuous, moderately high frequency amplitude reflections (Figure 2.4). Megasequence A is analogous to the lower Karoo lacustrine and fluvial cratonic sediments in the Huab area and Megasequence B is composed of the upper Karoo Plateau Formation sandstones (Horsthemke et al., 1990).

The Atlantic Rift phase, Megasequence C, defines the period of extension preceding the opening of the South Atlantic and is commonly split into three separate phases of rifting. Each rifting phase has been identified by their distinct reflection characteristics and intra-rift unconformities and have developed differently within the Lüderitz and Walvis basin (Clemson et al., 1997; Clemson, 1997). Sediments deposited during the first rift phase (Unit C1 - Rift phase 1) are only observed along a narrow strip west of the marginal hinge line because of increasingly steep dips (HRZ300; Figure 2.3a). On seismic data, the rift phase is expressed by continuous reflections of low to moderate amplitudes and frequencies thinning to the east (Figure 2.4). Reflections are stronger at the top of the sequence and could possibly be syn-rift volcanics (Adekola and Akinlua, 2013). A second phase of rifting (Unit C2 - Rift Phase 2) sits unconformably above the initial rift phase (HRZ330). Rift phase 2 is typically expressed as high-amplitude, continuous seismic reflectors that terminate abruptly (Figure 2.3a), suggesting volcanic content. Clemson et al. (1997) have tentatively correlated this with the short-lived Paraná-Etendeka flood basalts that ended in the late Valanginian (Renne et al., 1996). The final rift phase (Unit C3 - Rift Phase 3) is characterised by lower amplitude reflectors than the previous rift phases and is dominated by sedimentary fill (HRZ360; Figure 2.4). Rift phase 3 is thicker in the Walvis Basin than in the Lüderitz Basin due to differences in the timing of rifting (Light et al., 1993). The top of the unit is correlated with the transition to a Drift regime (HRZ400). Chronozone dating has

placed this unconformity at the earliest Barremian (Rabinowitz and Labrecque, 1979).

The transitional phase, Megasequence D, marks the end of rifting and contains the initial effects of the thermal sag phase (Light et al., 1993). Seismic reflections of the megasequence are continuous, high in frequency with low amplitudes and is the first megasequence to contain signs of a developing shelf edge (Figure 2.4). This is supported by the presence of continuous reflectors onlapping onto HRZ400 indicating active sedimentation of progradational sequences (Figure 2.3a; Maslanyj et al. (1992); Clemson (1997)). The package is thickest between the Hinge Line and the Outer High, thinning to the west and pinching out to the east. Thus, the unit is expressed differently in the offshore Mesozoic Basins. Drilling of the Kudu wells, west of the Hinge Line have intersected the Transitional Megasequence and samples range from continental beds at base to shallow marine sandstone at the top (Figure 2.2; Light et al. (1993); de Vera et al. (2010)).

The drift phase, Megasequence E, developed during continued subsidence in the Aptian to Turonian leading to stacked sedimentary wedges and progradational sequences that downlap onto HRZ500 (Figure 2.3a). Correlation to biostratigraphic data obtained in the Kudu wells indicate the entire unit consists of basinal shales all marine in origin (Mcmillan et al., 1997). The unit can be separated into three major sequences based on the stratigraphy (Figure 2.3b). The first unit (Unit E1) includes the first major progradational sequences deposited on the passive margin. Like the transitional phase, Unit E1 pinches out to the East onto the Namibian Platform and thickens seaward to the Hinge Line. The thickest sections are observed in the Lüderitz Basin and have high amplitude chaotic reflections that are likely indicative of volcanics (Figure 2.3b). Distinct flooding surfaces are observed at the base of Unit E1 and have been correlated with sediments of early- to mid-Aptian in age in the Kudu wells (Light et al., 1993). The top of the unit (HRZ530) represents a major transgression of abyssal marine sediments that correlates with the Turonian highstand (Haq et al., 1987). It is the first post-rift sequence to extend beyond the Hinge Line and deposit across the entire Namibian margin.

The second major sequence of the Drift Phase, Unit E2, is characterised by Late Cretaceous prograding sequences that deposit across the Turonian flooding surface (Figure 2.3b). Seismic reflections are indicative of a deltaic environment with reflections going from parallel with low amplitudes to discontinuous (Figure

2.4). Large canyons incise the delta slope so that channels cut through the Late Cretaceous sediments (Bagguley and Prosser, 1999). Within Unit E2, large listric faults are observed close to the shelf break. Late Cretaceous, Paleogene, and Neogene sand and mud dominated sediments represent the final sequence of the Drift phase (Unit E3) and marked by reduced sedimentation along the Late Cretaceous shelf break. This caused the majority of sediments to deposit inland (HRZ560). Over time a Paleogene-Neogene shelf break was established with listric faulting, contourites and well-defined channels being commonly observed (Clemson, 1997; Bagguley and Prosser, 1999). Due to the availability of core samples and a 3D seismic dataset the study site is focused on the lower continental shelf and upper continental slope of the Lüderitz Basin. The high-resolution 3D seismic data allows for a more detailed analysis of seismic stratigraphy for the post rift sediments and is discussed in detail in Appendix A.

2.4 Results

2.4.1 Seismic interpretation of direct hydrocarbon indicators and associated fluid flow features

The below section outlines the typical DHIs present in the Lüderitz Basin and aims to evaluate their relative importance in the HPS by analysing their spatial distribution.

2.4.1.1 Pockmarks

The resulting 2D and 3D seismic data feature a prominent positive seafloor reflection. Common along the continental shelf, this reflection is often punctuated by a discontinuity, expressed as a crater-like structure with varying diameters on the metre scale (Figure A.1). The downward deflected velocity push-down only extends vertically for $\sim$0.1 $TWTs$, below which seismic reflectors typically return to continuous again. In map view, the seismic anomalies are small (< 1 km diameter) circular, seabed depressions. In some cases, the crater can be asymmetrical. The identification of these seismic anomalies is dependent on the spatial and vertical resolution of the seismic survey and on the size of the crater. As such, the seismic anomalies are easily identifiable on the 3D seismic cube and cluster together above both drape deposits of the antiformal high (Figure A.1). Regionally, on 2D seismic data, the anomalies are distributed along the continental shelf, with some extending to the continental slope.

Based on the above observations these seismic anomalies are interpreted to be seafloor pockmarks, consistent with previous literature constraints (Gay et al., 2003; Moss, 2010; Moss et al., 2012; Pau et al., 2014; Foschi and Cartwright, 2016). Seabed pockmarks observed in the study area indicate that migrating fluid is being brought to the surface and expelled via a rapid blow out mechanism (Gay et al., 2007; Foschi and Cartwright, 2016; Løseth et al., 2011). Pockmarks are typically observed at the upper termini of pipes, indicating recent gas and fluid migration, that suggests an active HPS within the recent past (Eruteya et al., 2018).

2.4.1.2 Fluid Escape Pipes

Within the seismic data, multiple circular high amplitude soft anomalies causing sporadic vertical to sub-vertical breaks in reflectivity continuity are observed (Figure 2.5). The dimension of these anomalies range between 100 - 400 m in cross sectional width and $\sim$ 280 - 4000 m in height and the breaks associated with the background reflective continuity is abrupt. As such, the anomalies are crudely cylindrical, and narrowing is frequently observed throughout. The anomalies are not vertically continuous but the majority that terminate at the seafloor end in a pockmark. All the anomalies are located within Unit E3.

Based on these observations, the amplitude anomalies are interpreted to be fluid escape pipes, consistent with previous interpretations (Cartwright et al., 2007; Hustoft et al., 2007; Moss, 2010; Moss and Cartwright, 2010a; Andresen, 2012; Foschi and Cartwright, 2016). Three distinct types of pipes are observed within the Lüderitz Basin. All type 1 pipes are located within Unit E3-d and can be identified as a vertical zone of distorted and concave upward reflections with vertical extents of $\sim$ 2000 - 3750 m in height. Each pipe has variable cross-sectional width with depth, $\sim$ 100 - 300 m, giving 5 distinct zones implying multi-episodic fluid transfer into near surface environments (e.g., P1, P2, & P3; Figure 2.5c). Type 2 pipes are located within Unit E3-c and Unit E3-d and are narrower than type 1 pipes with variable cross-sectional widths of $\sim$ 50 - 150 m (e.g., P4, P4, & P5; Figure 2.5d). This again indicates episodic flow but with a reduced volume of gas source present. Type 3 pipes are located in Unit E3-d and are smaller in the vertical extent compared to type 1 and 2 pipes ($\sim$ 800 - 1200 m) and have more consistent cross-sectional width of $\sim$ 50 - 100 m (e.g., P7, P8, P9, & P10; Figure 2.5e).

The pipes are distributed across the entire basin; however, highly dense clusters, which align linearly with trails of fluid escape pipes, are observed along the shelf break within the continental drape deposits associated with the antiformal stratigraphic structure (Figure 2.5a & Figure 2.6c). Type 1 pipes are observed to cluster north of the antiformal stratigraphic structure where the highest density of pipes is observed. Across the upper continental slope pipe density is seen to reduce and pipes are mostly type 2. Pipe density increases again further south in the study area where pipes are type 3.

A coherency extraction show that across the entire 3D survey, pipes terminate at different depths, with less than 5% at seafloor, again implying multiple fluid expulsions (Figure 2.5a,b). Pipe outlets result in seabed pockmarks (e.g., Type 1 - P2). Less than 20% of total pipes transect the BSR, with most terminating within 200 m of BSR (e.g., Type 1 (P1 and P3) and Type 2 (P4)). The root zone depth and source of fluids/overpressure lie within Unit E3-c and beneath the BSR, coinciding with the head-scarp of a mass transport deposit (MTD), but the exact depth is uncertain due to acoustic blanking and reduced ER intensity; pipes are distributed above this feature (e.g., Type 2- P6; Figure 2.5c-e). This indicates a potential source and migration pathway for gas before entering pipes. A minority of pipes (e.g., Type 3) root into larger gas-filled layers, observed as amplitude anomalies in the high TOC intervals of Unit E3-d from the Late Pliocene. These pipes provide vertical bypasses between storage layers and can penetrate the entire hydrate stability zone.

The pipes identified in Unit E3 share similar geometry and acoustic features with those detailed by Foschi and Cartwright (2016) in the South Malvinas/Falkland Basin. In which, a mix of thermogenic and biogenic gases and oil were focused and migrated from subsurface to seabed via fluid escape pipes. A similar scenario is expected here in concordance with: the Namibian continental margin (Moss and Cartwright, 2010a); the Lower Congo Basin (Gay et al., 2007); NW offshore Svalbard (Hustoft et al., 2009); and offshore Nigeria (Løseth et al., 2011). The presence of an extensive pipe network strongly indicates fluid migration and expulsion that has implications for how the HPS is connected.

2.4.1.3 Bottom Simulating Reflector (BSR)

A discontinuous, negative polarity reflection was mapped across most of the Namibian margin within Unit E3-d, the topmost section of Unit E3. It is proposed

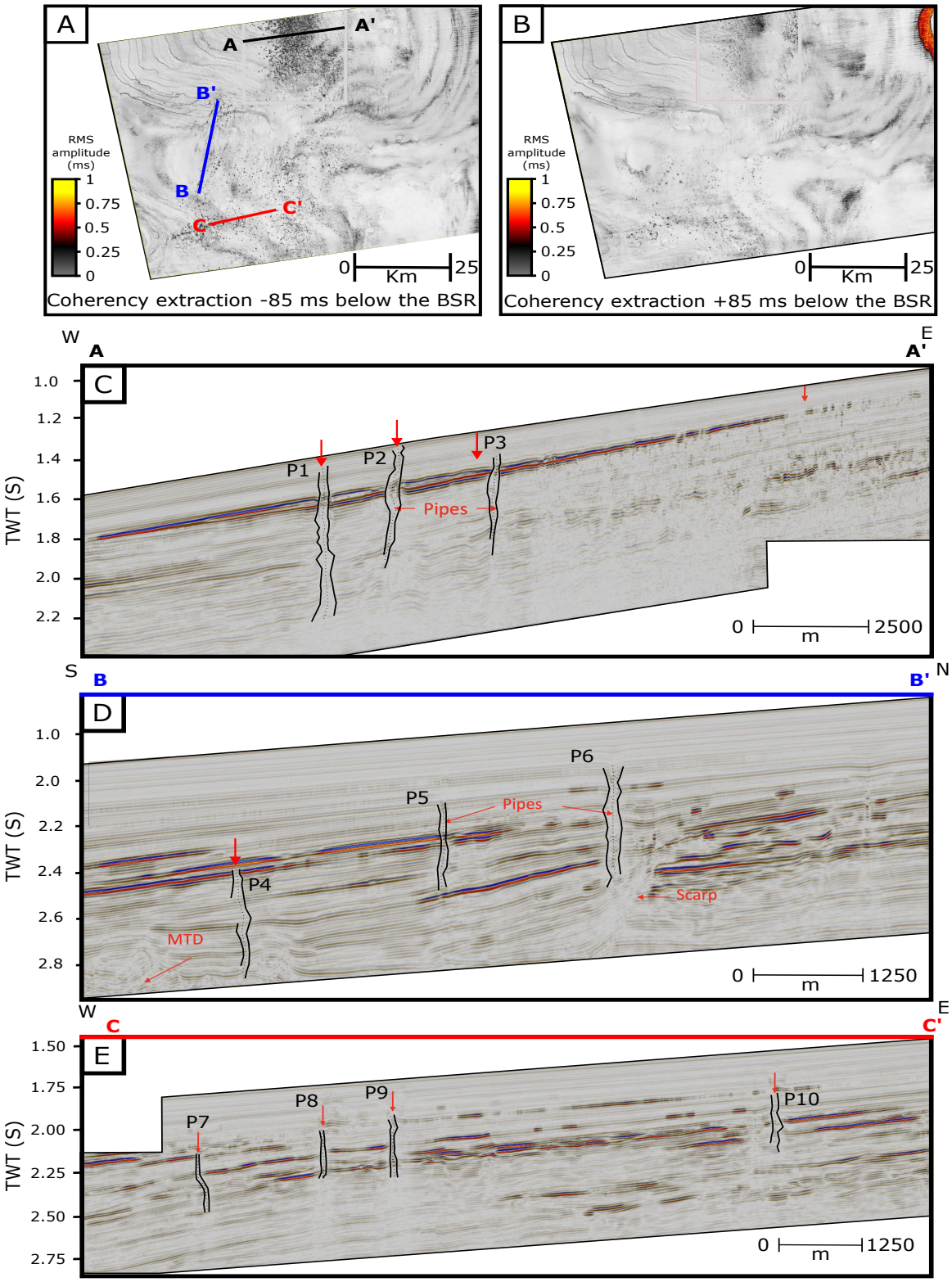

Figure 2.5: Expression of fluid escape pipes on 3D seismic data. a) A coherency extraction -85 *ms* below the BSR shows thousands of fluid escape pipes. b) However, only less than 20% of total pipes transect the BSR. c-e) Geometry and acoustic features of Pipes 1-10. Pipes root in Unit E3 with variable cross-sectional width with depth indicating episodic flow. Seismic is located in panel A.

that the reflection always has a negative polarity because of decreasing acoustic impedance with depth, caused by gas hydrate bearing sediments positioned above sediments charged with water or gas. Four representative traces have been extracted from a 2D seismic section in the Lüderitz Basin to analyse the polarity of the anomalous reflection (Figure 2.6c). In all traces the anomalous reflection exhibits an isolated, strong, negative amplitude response followed by multiple enhanced reflectors, with amplification approximately 1.5 - 2 times higher than the seabed. Secondly, the reflector has a cross-cutting nature in which it does not follow the surrounding, continuous reflectors but instead intersects or truncates them causing acoustic blanking (Figure 2.6c). Finally, in addition to the polarity reversal relative to the seafloor reflector, the anomalous reflector is seabed simulating, mimicking the seafloor topography at a constant depth of 150 - 200 metres below seafloor ($mbsf$)(Figure 2.6b).

Due to the characteristics of reversed polarity, seabed simulating, and cross-cutting acoustic blanking, the anomalous reflector is interpreted to be a BSR, consistent with previous assessments (Xu and Ruppel, 1999; Ben-Avraham et al., 2002; Lopez et al., 2005; Boswell et al., 2012; Wenau et al., 2015; Foschi and Cartwright, 2016; Flemings et al., 2020). BSRs are a common feature of continental slope settings, and in areas with known upward diffusing CH_4 flux are commonly interpreted as the base of the gas hydrate stability zone (BGHSZ)(Boswell et al., 2012; Flemings et al., 2020). In the Lüderitz Basin, the depth of the BSR horizon ($\sim$ 150 - 200 $mbsf$) throughout the sub-unit E3-d is compatible with the necessary pressure-temperature conditions required of the gas hydrate stability zone to facilitate hydrate formation (Figure A.2). Based on the above criteria, the BSR, and thus BGHSZ, was mapped across the extent of the study area using 2D and 3D seismic data (Figure 2.6a). The interpreted BGHSZ shows a patchy character. The interpreted BSR is relatively discontinuous and is expressed as seven independent areas along the Namibian continental shelf break. The individual areas where a BSR was present with confidence ranged in area from 184 km^2 to 7177 km^2 and in total they were 170803 km^2. Due to the lack of continuous seismic data, conservative interpolation was necessary rendering the discrete sections of BSRs; it is expected that a continuous BSR exists across the entire continental shelf break. For this study further analysis into the BSR was solely carried out in the Lüderitz Basin, the study site.

Within the Lüderitz Basin, the largest of the observed BSR areas, the interpreted BSR is practically continuous at the northern and southern bounds, in contrast to the central zone where it is more sporadic and discontinuous. This distribution of interpreted BSR is controlled by an antiform structure of draped fine grained deposits that is located above a structural high (Figure A.3). By comparing depth maps of the BSR and the seafloor, that are converted from TWT, the relationship between the two surfaces can be assessed for the study area and shows seabed simulation (Figure 2.6b; Calvès et al. (2008); Foschi and Cartwright (2016)). This relationship particularly holds true in the Lüderitz Basin when compared to other basins offshore Namibia, where continuous seafloor depth contours connect between the independent BSR areas at similar depths. The interpreted BSR map is seen to dip westward from 100 to 250 $mbsf$, in concordance with the shelf break so could be an important and large storage structure of CH_4. As the interpreted BSR indicates approximately the BGHSZ it provides valuable insight into how CH_4 flows through the sediment and is either trapped in hydrate stores or as free gas just beneath. The identification of CH_4 storage structures can help construct an HPS.

No physical gas hydrate samples have been successfully recovered within 600 $mbsf$ in the Lüderitz Basin during ODP Leg 175 along the Namibian margin (Berger et al., 2002a). However, ODP Leg 175 (Site 1084) reported an increase in sonic log velocity from 1475 to 1575 ms^{-1} through a unit that possesses a BSR in the seismic data (Wefer et al., 1999). Gas hydrate deposits were expected, and poor recovery is attributed to operational challenges in coring gas hydrate deposits due to stability conditions (Figure A.2). A single hydrate sample has been recovered within the Namibe basin, north of Walvis Ridge, by a 5 m drop core at approximately 1500 m water depth (Swart, 2009). The recovered hydrate has a muddy matrix, and the corresponding seismic data displayed a BSR at this locality. The interpreted BSR in the Lüderitz Basin likely represents the BGHSZ, with hydrate being a major CH_4 store in the study area.

2.4.1.4 Enhanced reflections (ERs)

Within the Lüderitz Basin, multiple amplified reflections are identified on the seismic data, where the degree of amplitude monotonically reduces with depth. The acoustic response of the amplitude anomalies typically follow the geometry of the background reflections, have a negative amplitude response and amplitude intensity increases updip, terminating sharply just beneath the BSR. On seismic the anomalies are low

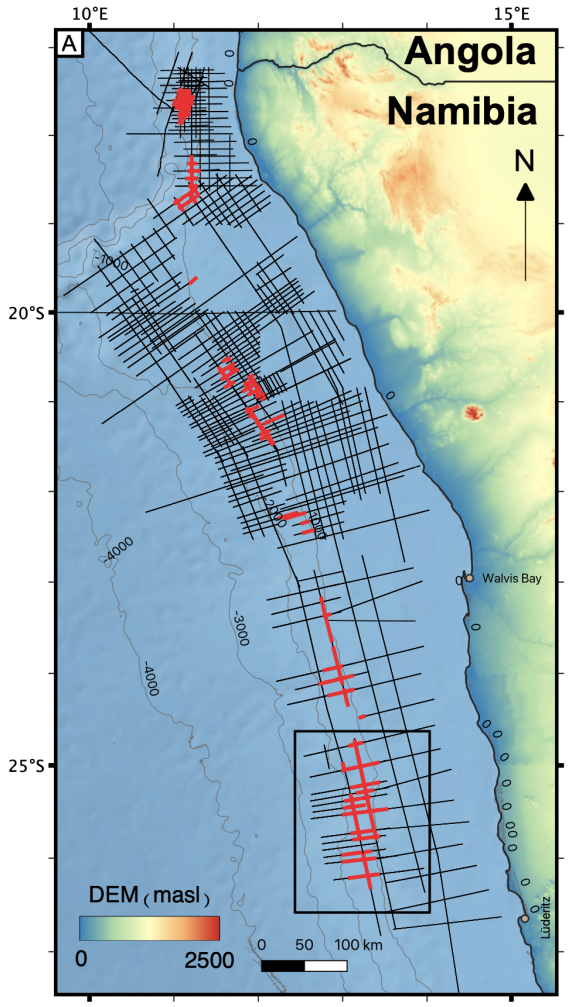

(a) Map of the interpreted, discontinuous BSR amplitude anomalies.

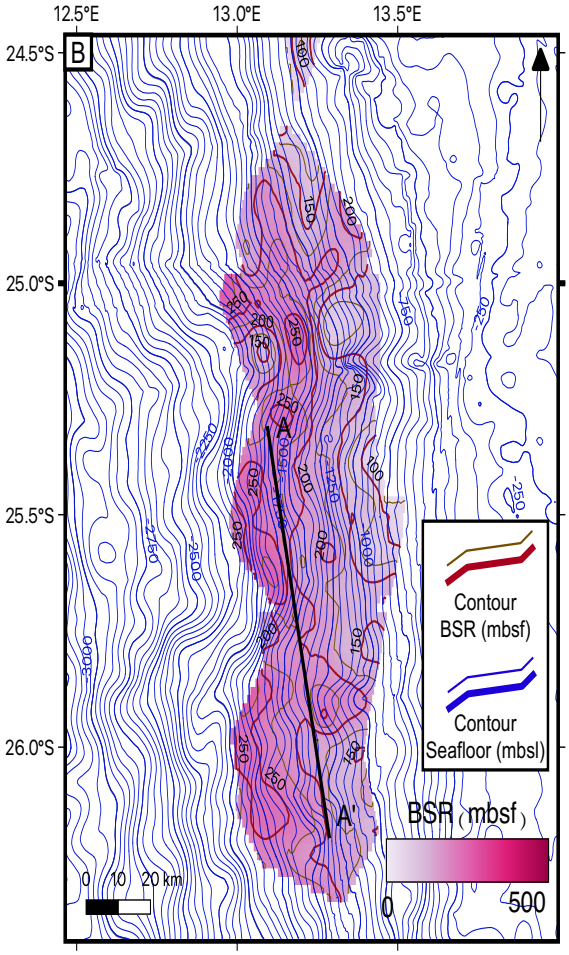

(b) Distribution and morphology of the interpreted BSR with the seafloor contour.

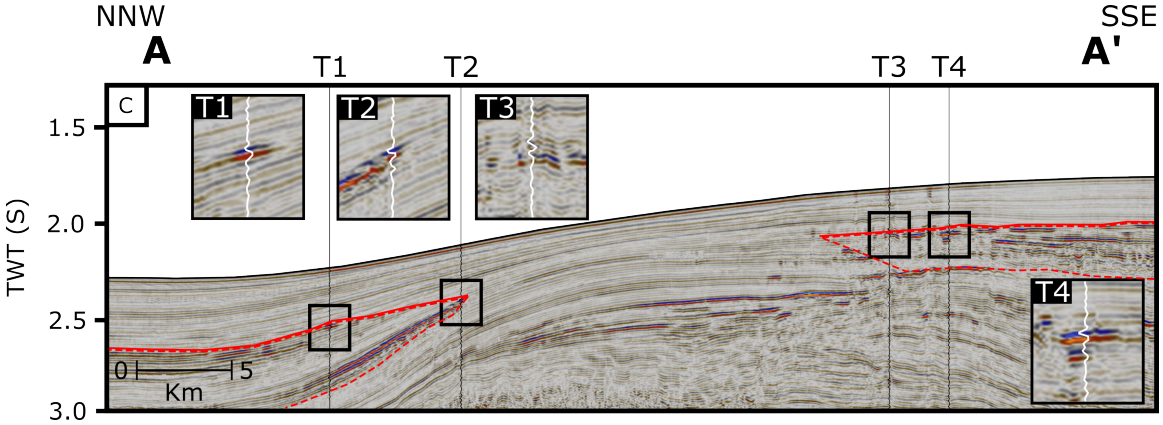

(c) 2D cross section depicting the BSR (red solid line) and FGZ (within red dashed area). Representative traces have been extracted in wiggle display. The BSR exhibits systematic negative amplitude response.

Figure 2.6: Map of the interpreted BSR and FGZ along with their expression in 2D seismic data. See Figure 2.6a for the location of Figure 2.6b.

in vertical extent, ranging from centimetre to metre thickness, and are more common in the sedimentary basins. Some of those located at the BSR have a 'serrated' or 'roof-tile' effect but the top is still parallel to the seafloor.

Based on these characteristics these amplitude anomalies are defined as ERs and are the most common form of DHI in the study area (Xu and Ruppel, 1999; Calvès et al., 2008; Fohrmann and Pecher, 2012). ERs are frequently interpreted as free gas charged layers just beneath the BGHSZ. The downdip extent of the ERs, where amplitude values return to background levels, is interpreted as the base of the free gas zone (FGZ). Variable attenuation below the BSR, seismic blanking from fluid escape pipes, and the complex geometry of the ERs complicate this interpretation in the Lüderitz Basin. However, the vertical separation between the BSR and the base of the FGZ can still be estimated in two-way travel time. Since the ERs appear confined within the basin, this vertical estimate can provide a rough maximum volume of gas stored in the Lüderitz Basin.

The resulting 'time-thickness' map of the interpreted FGZ shows most free gas being contained within the basin with a total area of 187.5 km^2, being bound to the north and south by stratigraphic anticlinal highs, 75 - 100 km (Figure 2.6c). The base of the FGZ is interpreted to be due to the presence of continental drape deposits and base of the antiformal stratigraphic structure. The volume of free gas in the FGZ can be roughly estimated using the time-thickness map and sediment properties from nearby ODP 1084 well data. Over 90% of the post-rift succession is silt with a grain size of $0.002 - 0.05$ mm (Baby et al., 2020). Using a typical sediment mixture porosity of 0.242 (Koltermann and Gorelick, 1995; Foschi and Cartwright, 2016), an average sediment velocity of 1500 m/s (Dullien, 1992; Wefer et al., 1999), and assuming loose, random packing and maximum gas fill, the free gas volume in the Lüderitz Basin could range from 199 km^3 (5% gas saturation) to 1991 km^3 (50% gas saturation). This free gas migrates through the stratigraphy and accumulates in various structures, causing the ERs to be prominently expressed across the basin within Unit E3. The spatial distribution of ERs directly indicates gas movement and storage within the HPS.

2.4.2 Geochemical indicators - indirect observation on fluid flow

The depth of the SMTZ of compiled published marine sediment core pore water SO_4 concentration data, ranges from 3.63 ± 1.58 $mbsf$ (±2SE, n = 5) on the innermost shelf, 20.1 ± 4.76 $mbsf$ (±2SE, n = 20) on the shelf, and, if detected 1915 ± 192 $mbsf$ (±2SE, n = 2) along Walvis Ridge (Figure 2.7). This is typical of previously recorded SMTZ depths in other similar oceanographic settings (Snyder et al., 2007b; Peketi et al., 2012; Hong et al., 2014b; Cho et al., 2017). No downward depletion of pore water SO_4 concentration is observed in the majority of cores below the shelf break along Walvis Ridge and values are at ambient seawater dissolved SO_4 concentration levels, 28 mM. Along the shelf break, ∼ 1500 metres below sea level ($mbsl$), the depth of the SMTZ is significantly shallower in areas where a BSR has been identified on seismic data (t(6.0659) = -2.7616, p = 0.03242). Within the mapped BSR the depth of the SMTZ ranges from 3 to 26 $mbsf$, with shallower depths recorded updip.

Compiled published CH_4 concentration data begin to sharply rise from ∼0.01 to 3.72 - 110 $mmol/L$ beneath the SMTZ in each marine sediment core due to AOM (Figure A.4). The upward diffusive CH_4 flux has been calculated (Equation 4; Boudreau (1997); Hong et al. (2013)).

$$\mathrm{J} = -\mathrm{D} \cdot \frac{\Delta(\varphi \cdot \mathrm{C})}{\Delta \mathrm{z}} \qquad \{4\}$$

Where J, D, C, and z denote the diffusive flux, tortuosity-corrected diffusion coefficient for CH_4 (183 cm/yr, assuming a constant temperature in the sediments of 4°C; Boudreau (1997)), pore water concentration of CH_4, and depth in the sediment, respectively. ϕ represents the depth-dependant porosity of the marine sediment core ($\phi = \phi_f + (\phi_0 - \phi_f) * exp^{\gamma * z}$, where ϕ_f and ϕ_0 are porosity at great depth and at the sediment-water interface (SWI), respectively. γ is an empirical constant, which can be obtained from data fitting). The concentration gradients are calculated for each marine sediment core where a first order linear regression is used to calculate each gradient as profiles are linear. Across the Namibian margin, the upward diffusive flux of CH_4 for marine sediment cores for where a BSR has been detected (42.1 ± 4.05 $mmol.m^{-2}.yr^{-1}$ (±2SE, n = 5)) is not significantly different to cores at the same water depth where no BSR has been identified (51.7 ± 3.25 $mmol.m^{-2}.yr^{-1}$ (±2SE, n = 2); t(4.0616) = -1.8527, p = 0.1365; Table A.3). Within the identified

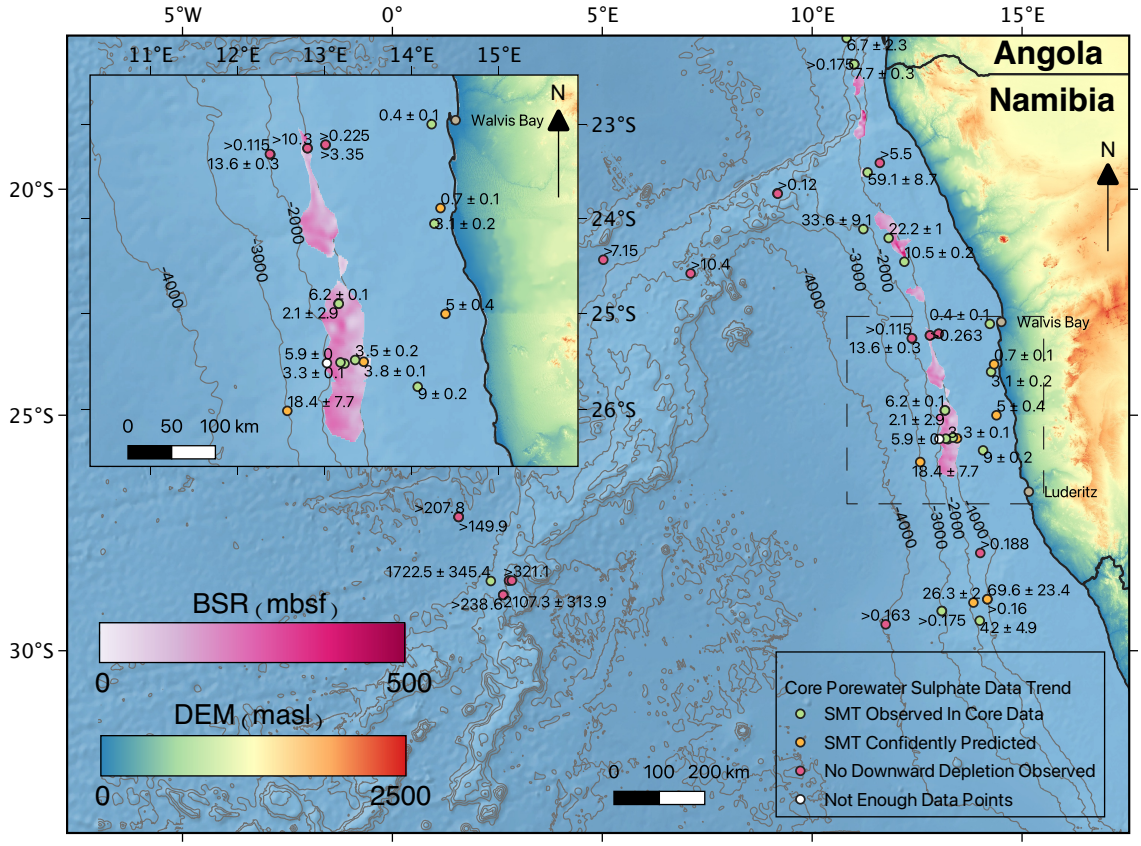

Figure 2.7: The predicted depth of the SMTZ is plotted for sites along the Namibian margin using marine sediment core pore water SO_4 concentration data from literature (Table A.3). The depth of the mapped BSR is plotted in purple. An inset shows a zoom-in section of the Lüderitz Basin.

BSR patch in the Lüderitz Basin the upward diffusive flux of CH_4 inversely scales with the depth of the SMTZ and increases for samples that are further updip (40.3 to 43.3 $mmol.m^{-2}.yr^{-1}$).

The TOC concentration in surface sediments along the Namibian margin vary heterogeneously, with typical background values of ∼2 wt% (Figure 2.8; Inthorn et al. (2006)). The highest surface sediment TOC concentration values (9 - 12 wt%) are in a mudbelt (∼ 25,000 km^2) on the inner shelf of the Lüderitz and Walvis Basins (20.6°S - 25.5°S). Slope surface sediments show no surface sediment TOC enrichment. However, a distinct 5,000 km^2 depocentre in the Lüderitz Basin (24°S - 26.5°S at 400 to 1500 $mbsl$) has surface TOC values up to 9 wt% (Figure 2.8a-b), aligning with the present-day mapped BSR location. Downcore TOC concentration data are seen to decrease downcore from 8.21 wt% in Unit E3-d to 2.87 wt% in Unit E3-c (Figure 2.8c; Wefer et al. (1999)). TOC enrichments in marine sediment are a potential source of organic matter for biogenic or thermogenic gas production and should be considered when constructing an HPS.

2.5 Discussion

2.5.1 Proposed Lüderitz Basin HPS model

To gain a comprehensive understanding of fluid flow within the Lüderitz Basin, it is essential to ascertain whether identified DHIs represent a connected HPS. Based on the presence and spatial distribution of DHIs the following HPS is proposed for the Lüderitz Basin:

1. Hydrocarbons and CH_4 are generated by the decomposition of organic matter from Barremian to Early Aptian source rock distributed within the transitional phase - Unit D. The presence of thermogenic hydrocarbon and CH_4 was previously identified during the discovery of the Kudu gas field.

2. Based on ERs, the majority of the gas is trapped within Unit D but some gas enters the crests of the overlying stacked sedimentary wedges and progradational sequence in Unit E due to gas buoyancy where an overlying continuous sedimentary body further inhibits cross-stratal gas flow.

3. TOC rich sediments within Unit E3-b and Unit E3-c align with the optimal conditions of mesophilic bacteria activity causing large scale production of biogenic gas.

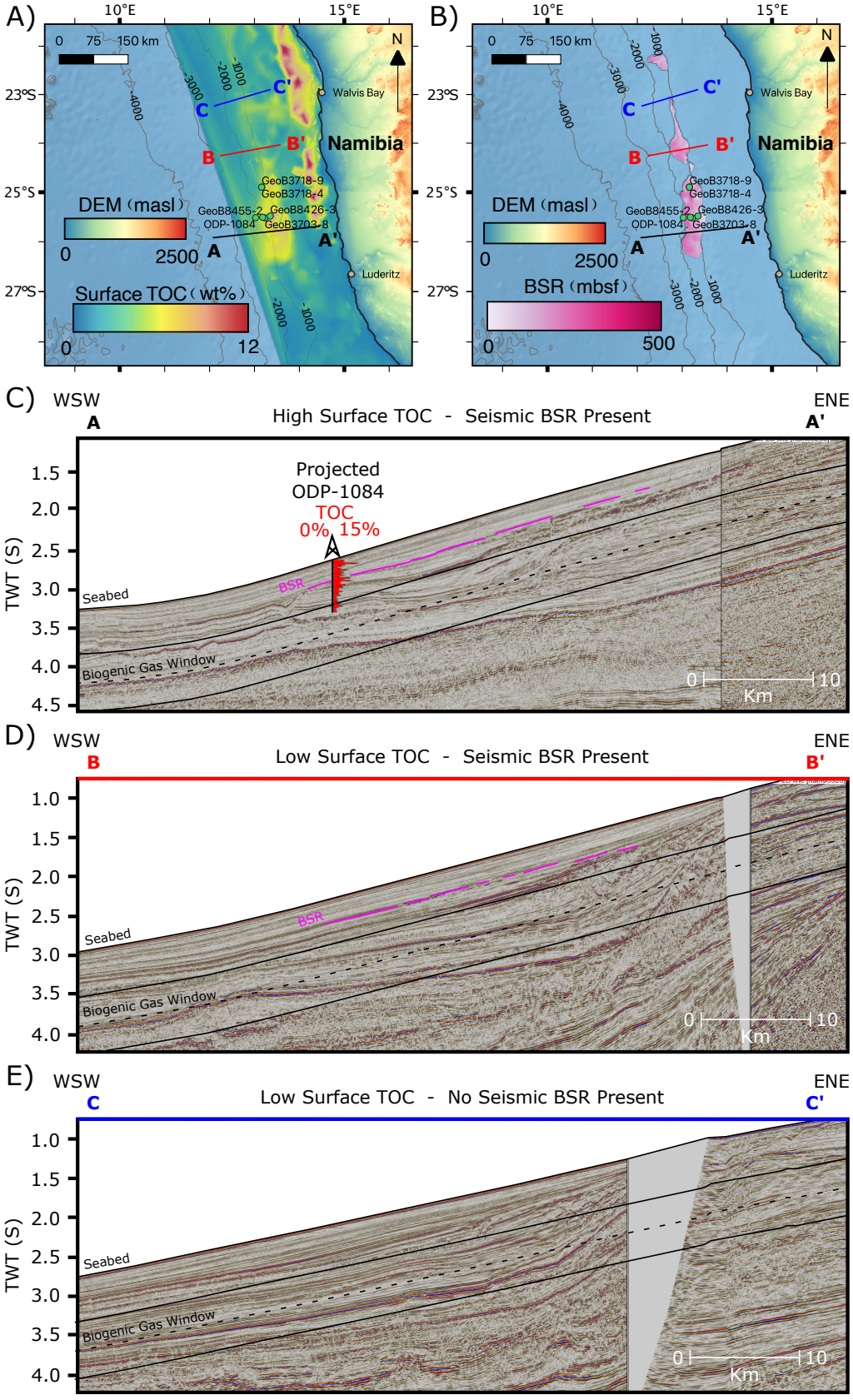

Figure 2.8: 2D seismic cross-sections displaying the spatial variation of high surface TOC along the Namibia margin, Lüderitz Basin. a) map showing changes in surface TOC with seismic line locations. b) map containing depth of BSR. c-e) Seismic showing changes in BSR with surface TOC. Where appropriate downcore TOC has been plotted from ODP-1084 data.

4. Biogenic gas then diffuses out of the peak generation window directly into the flanks of the antiformal structure in Unit E3-c or laterally via a sealing clay at the crest of the structure.

5. Gas then migrates via fluid escape pipes where the depth of the pipe root zone appears to coincide along strike of the head-scarp of a MTD located at the base of Unit E3-c, with a high density pipe network distributed above this throughout the rest of the sediment along the flanks of the antiformal structure.

6. The migrating gas then enters the required conditions for gas hydrate formation and eventually the resulting hydrate body becomes a seal for free gas to accumulate beneath and a BSR to be expressed on seismic data.

7. Some pipes puncture through the hydrate body and CH_4 gas diffusing to the seabed is utilised during AOM at the SMTZ. As the diffusive flux is variable, due to subsurface focused fluid flow, the depth of the SMTZ and further geochemical cycling is varied in sediment cores across the Lüderitz Basin.

8. In areas where the diffusive flux of CH_4 is so great, the SMTZ is overpowered and shoals in the top few cm and CH_4 is expelled via a rapid blow out mechanism resulting in the formation of a pockmark at the seabed surface.

The timing for the emplacement of the observed DHIs and resulting HPS is challenging due to lack of physical samples along with direct information on hydrate formation and dissociation, and the timing of migration processes (Moss and Cartwright, 2010b). However, an approximate timing model can be established based on the abundance and location of different DHIs. The presence of pockmarks at the seabed provides strong evidence that the migration of gas and fluid is active within the recent past (Gay et al., 2007). Pipes, with similar dimensions to those in adjacent basins, indicate that fluid expulsion via pipes is episodic and has persisted since the Late Cretaceous (Moss and Cartwright, 2010b; Foschi and Cartwright, 2016). The termination of pipes (e.g., Type 2, P5 & P6) at a depth of 740 $mbsf$ indicates that gas production and migration in this area terminated within the Cenozoic or the hydrate body developed into more of a seal with the increased CH_4 supply. The presence of a BSR denoting the BGHSZ suggests relatively stable conditions since the Late Pleistocene resulting in free gas accumulation under the hydrate body (Xu and Ruppel, 1999). Enhanced primary productivity in the surface oceans persisted throughout the Cenozoic, and could contribute to increases in

downcore TOC measurements (Wefer et al., 1999; Inthorn et al., 2006), providing the source of organic matter for mesophilic bacteria once sediments enter the biogenic gas production window.

Therefore, it is proposed that a fully-connected HPS is present in the Lüderitz Basin with active fluid movement. For frontier basins it is beneficial to discern whether the source of the hydrocarbons is biogenic, thermogenic, or of mixed origin (Andresen, 2012; Foschi and Cartwright, 2016). This will guide whether variable fluid flow impacts geochemical measurements in marine sediment cores.

2.5.2 Evidence for a Biogenic HPS

2.5.2.1 Production of Biogenic Methane

Biogenically derived CH_4, generated by methanogenic archaea bacteria, is the most likely explanation for the variable upward diffusive CH_4 flux and DHIs observed in the Lüderitz Basin. Methanogenesis (Equation 5), the breakdown of highly organic rich sediments, is attributed to the production of biogenic CH_4 occurring in wide depth ranges from near surface to as much as 4600 $mbsf$ (Rice, 1993; Hong et al., 2014a). Secondary methanogenesis (Equation 6), commonly known as CO_2 reduction, utilises the by-product of methanogenesis to produce additional biogenic CH_4 and is associated in similar depth ranges (Hong et al., 2013). The depth of biogenic gas production depends on the geothermal gradient and a ceiling value of 70°C is typically used (Rice, 1993). The factors that favour significant generation of biogenic gas are: abundant total organic carbon deposits, typically greater than 0.5% (Claypool and Kaplan, 1974); anoxic conditions (Claypool and Threlkeld, 1983); low temperature and low SO_4 environment (Rice, 1993); high sedimentation rate (50-200 m/My; Hong et al. (2014b); Clayton (1992)); and sufficient pore space for microbes to develop (Rice, 1993).

$$\mathrm{CH_2O} \longrightarrow \frac{1}{2}\,\mathrm{CH_4} + \frac{1}{2}\,\mathrm{CO_2} \qquad \{5\}$$

$$\mathrm{CO_2} + 4\,\mathrm{H_2} \longrightarrow \mathrm{CH_4} + 2\,\mathrm{H_2O} \qquad \{6\}$$

Using methodology detailed in Dickens and Quinby-Hunt (1994) and Yamano et al. (1982) the depth of biogenic gas production in the Lüderitz Basin was determined by calculation of the geothermal gradient (Figure A.2). The geothermal gradient was calculated using the depth of the picked seafloor horizon and BSR

horizon in TWT from 2D and 3D seismic data via a series of intermediate grids of depth to pressure to temperature. Predicted seafloor temperature was consistent with data previously reported for the Namibian margin (Dingle and Nelson, 1993). Calculated data was clipped at 70 °C (Rice, 1993) and rendered an average geothermal gradient of 32.8 $°C/km$ for the Lüderitz Basin. By utilising the peak production window of mesophilic bacteria and the calculated geothermal gradient, the depth of the biogenic gas window can be determined and modelled onto seismic data, corresponding to ∼550 - 1500 $mbsf$ (Figure 2.9a; Rice (1993); Stolper et al. (2014)).

Given the above parameters, identified seismic structures, and the predicted biogenic gas window, Unit E3-b and Unit E3-c are the probable source for significant biogenic CH_4 production. Firstly, the units are abundant in organic-rich carbon by the deposition of hemipelgic sediments since the Cenozoic expressed as an antiformal stratigraphic structure or afterwards as continental drape deposits at the flanks of the structure (Figure A.3 & Figure 2.8). Secondly, the combination of hydrology with variable currents dissolved oxygen concentration, strong perennial upwelling, and high surface ocean primary productivity contribute to the presence of an extended oxygen minimum zone (OMZ) overlying the continental shelf by $\sim$ 50 m, causing sediments to be deposited in anoxic conditions (Brüchert et al., 2003; Borchers et al., 2005). Finally, the predicted peak of biogenic gas generation is calculated within Unit E3-b and Unit E3-c, producing the optimal temperature window for methanogenesis to occur within the highly organic rich sediments of the antiformal structure (Figure 2.9). It is expected the resulting biogenic gas will be dry as the depth of the identified BSR matches the depth of the peak CH_4 production window.

2.5.2.2 Migration pathways of biogenic methane

Once accumulated, the biogenic CH_4 can diffuse out of the peak generation window directly into the flanks of the antiformal structure or via a sealing clay at the crest of the structure (Figure 2.9b). It is proposed that the CH_4 then migrates towards shallower parts of the basin via identified fluid escape pipes that have a root zone coinciding along strike of the head-scarp of a MTD located at the base of Unit E3-c. As a result, a high density pipe network is distributed above this along the flanks of the antiformal structure that will transport the large volume of CH_4 to shallower parts of the basin.

The migrating CH_4 then enters the required pressure-temperature conditions for gas hydrate formation and eventually the resulting hydrate body becomes a seal for free gas to accumulate beneath as identified by the BSR. Biogenic CH_4 is commonly considered the primary component of methane hydrates that form within the hydrate stability zone in numerous global continental margin settings (Ben-Avraham et al., 2002; Boswell et al., 2012; Hu et al., 2018). As an extensive and well-defined BSR is observed over significant areas of the Lüderitz Basin, and the seismic characteristics of this mapped BSR correspond to those typically associated with the BGHSZ, suggests that the laterally extensive hydrate body present likely originated from biogenic rather than thermogenic sources (Sun et al., 2012). Finally, <5% of fluid escape pipes are seen to punctuate through the BSR and continue CH_4 migration to the seafloor, terminating at a small pockmark. This results in a fully-connected biogenic gas production HPS (Figure 2.9).

However, caution must be exercised in this assessment as DHIs are observed in sediments in Unit E3-a and deeper. As these units are largely buried beneath the accepted temperature ceiling for active CH_4 generation, if the observed DHIs infer biogenic free-gas then a gas generation in the Cretaceous must have occurred when sediments were more shallowly buried. This is difficult to reconcile as it implies gas retention for tens of millions of years, which is unlikely based on gas diffusion (Boudreau, 1997). However, the lack of sedimentation rate data across the basin inhibits the determination of how long different ages of sediment spent in the biogenic gas production window. Secondly, in some areas of the basin, especially in deeper stratigraphic units, ERs are observed outside of the proposed biogenic HPS associated with amplitudes too great if they were only caused by free-gas derived from methanogenesis. Therefore, the irregular distribution of the ERs and mapped BSR cannot be fully explained by a biogenic HPS and suggests a small thermogenic component present.

2.5.3 Evidence for a Thermogenic HPS

Thermogenically derived CH_4, produced by the thermal maturation of organic matter, could be an alternative explanation for the variable upward diffusive CH_4 flux and DHIs observed in the Lüderitz Basin. The production depends on a combination of temperature and burial history and a series of migration structures would be required to justify a thermogenic HPS (Azambuja et al., 2010). The Kudu gas field discovered in the Orange Basin is a fully developed petroleum system and,

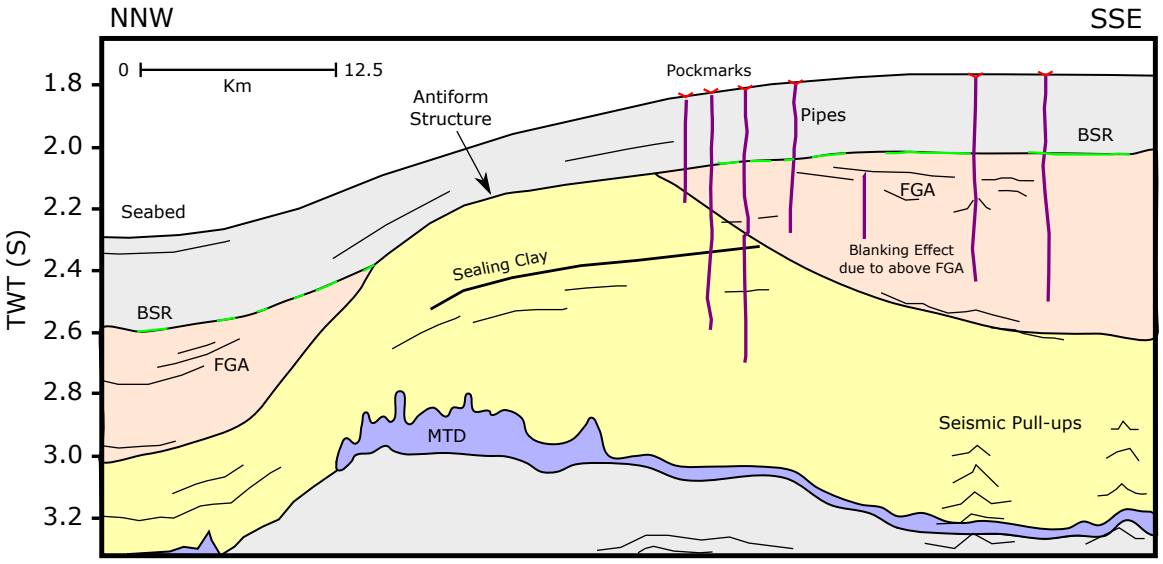

(a)

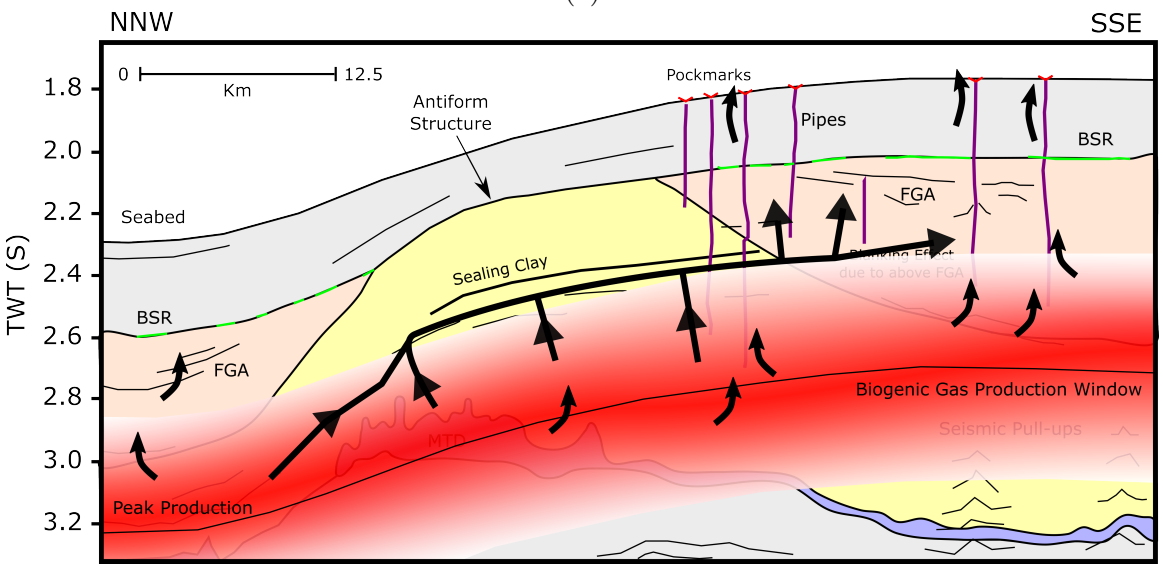

(b)

Figure 2.9: Predicted biogenic gas production window. a) Interpreted 3D seismic section, xline2969, with major sedimentary packages and structures displayed. Two sedimentary depocentres are observed on either side of a topographic high. Within these depocentres prevalent free gas anamolies are present accompanied with seismic blanking throughout the section. Note that the BSR is observed at the top of the units. The vertical exaggeration is set to 20. b) Biogenic window plotted on with movement of gas shown as black arrows.

along with recent extensive oil and gas discoveries such as the Mopane discovery, suggests a thermogenic gas source is possible for other basins in the Namibian margin. The sediment sequences overlying basaltic basement rock, maturing at a depth of 4500 $mbsf$, are Early Barremian in age ($\sim$129 Ma) and are younger than the Etendeka volcanics onshore Namibia that evolved during the Paraná-Etendeka traps. However, it is unknown whether this deep system could account for the basin-wide hydrocarbon accumulations in the shallower parts of the Lüderitz Basin, due to a required migration link.

2.5.3.1 Source Rock distribution

The source rock interval of Barremian age encountered in the Kudu gas field is majority located within Unit D, corresponding to the transitional phase, and is known to be laterally extensive throughout the Namibian margin (Figure 2.2 & Figure 2.3; Clemson et al. (1997)). Using a series of profiles close to the Kudu 9A-3 discovery well, a depth conversion was performed on sediments of Barremian age in the Orange Basin assuming typical sediment velocity of 2.4 km/s (Dullien, 1992; Wefer et al., 1999). The resulting contour was mapped throughout the basin fill to the Lüderitz Basin, assuming a uniformally distributed Unit D interval, providing an upper limit of source maturation for the Lüderitz Basin. Based on this, the potential generative kitchen is an E-W elongate zone, pinching out to the East onto the Namibian Platform, with the northern limit of Walvis Ridge, associated with sediments of Barremian to Early-Aptian age. Some laterally extensive, discontinuous ERs are observed within the unit which could indicate the production of thermogenic gas, but they are restricted to the unit (Figure A.5). In the Orange Basin the BSR and ERs are located directly above the mature source rock with a clear fault network, conducive for the migration of gas. However, in the Lüderitz Basin the other DHIs previously identified lie outside the area of thermogenic gas production, with distances of several thousands of metres. Therefore, some combination of stratal and cross-stratal migration is required if all the DHIs in the Lüderitz Basin are thermogenic in origin.

2.5.3.2 Stratal Migration

Based on the interpretation of observed seismic facies, Units D and E are composed of progradational sequences deposited on the passive margin to the maximum flooding surface consisting of sand or silt prone intervals. This is corroborated by biostratigraphic data obtained in the Kudu wells indicating the entire unit consists of basinal shales all marine in origin (Mcmillan et al., 1997). The coarser sediments

within these sediment packages offer multiple potential stratal migration routes for thermogenically derived gas as they are laterally extensive within each stratigraphic sub-unit. On seismic data they are acoustically characterised by alternating low-high reflection amplitudes. Observed stacked sedimentary wedges and progradational sequences in Unit E also provide a focused stratal migration pathway to the crests of the wedges due to gas buoyancy (Figure A.5).

2.5.3.3 Cross-stratal Migration

Faults are the most common form of cross-stratal, or vertical migration, for hydrocarbons to ascend to shallower parts of a basin. Faults are one of the three main groups of bypass systems and can act as fluid conduits or, in some cases, can prevent the migration of hydrocarbons and fluid to the surface (Cartwright et al., 2007). Within seismic they are typically associated with stacked amplitude anomalies and ERs clustered against the fault (Løseth et al., 2009). The limited number of faults identified within the Lüderitz Basin makes basinal-scale cross-stratal migration of hydrocarbons unlikely due to a lack of connectivity to the source rocks. Within Unit E2, Late Cretaceous, listric faults and fault-induced slumped masses are observed close to the shelf break and polygonal faulting is identified within the seismic data. However, these are seen to not cut through any of the other stratigraphic units making cross-stratal migration an unlikely mechanism to transport fluids into the previously identified shallow DHI network. Fluid escape pipes are seen to root within Unit E3-d, corresponding to the Late Pliocene, above the faults in Unit E2 indicating the faults are not focussing fluid into the pipe root zone. All other DHIs identified in the study are observed within Unit E3, with units below expressed by continuous reflections of low to moderate amplitudes with frequencies thinning to the east, further indicating limited cross-stratal migration in the Lüderitz Basin. In the Orange Basin large-scale high angle listric faulting caused the rotation of downfaulted blocks of sediment, imparting high angle reverse dip faults. This provides a robust fault network that allows the migration of the gas discovered in the Kudu wells (Light et al., 1993).

Due to the lack of migration pathways between Unit D, the Barremian source rock, and the overlying DHI network observed in Unit E3, a HPS based on solely thermogenic components is unlikely. Thermogenically derived CH_4 is likely to be produced within the correct depth-temperature window as indicated by ERs in Unit D, however the majority of the gas is likely to be trapped within this stratigraphic

unit as no major outward migration pathways exist. This would lead to an unconnected thermogenic HPS if the entire system was thermogenic. Therefore, the evidence for the origin of CH_4 in the study area strongly suggests a shallow biogenic source, however a small contribution from thermogenic CH_4 and the breakdown of hydrocarbons within Unit D cannot be excluded. Hence, a mixed but prominently biogenic HPS is present in the Lüderitz Basin. This is opposite of the HPS previously proposed for the adjacent Orange Basin, where a thermogenic source is more certain, and for the Brazilian conjugate passive margin in the Pelotas basin (Light et al., 1993; Paton et al., 2007; Conti et al., 2017). This could possibly be due to reduced deposition in the Lüderitz Basin during the Barremian and early Aptian resulting in a thinner Late Cretaceous section compared to the Orange Basin along with lack of migration pathways (Intawong et al., 2015).

2.5.4 Impacts on measured marine sediment core geochemical data

The construction of the HPS in the Lüderitz Basin can provide context for the interpretation of shallow marine sediment core geochemical data. Here the discontinuous BSR and irregular distribution of ERs in the Lüderitz Basin are due to focused fluid flow and sedimentary structures promoting lateral migration of produced gas into the drape deposits via diffusion, with pipes assisting vertical migration. As a result, the upward diffusive flux of CH_4 measured across the Lüderitz Basin can be explained by subsurface focused fluid flow (Figure 2.9). This is concordant with the highest upward diffusive CH_4 fluxes in the Lüderitz Basin were calculated in samples overlying the up-dip regions of the present-day mapped BSR, where focused fluid flow occurred.

The variable upward diffusive CH_4 fluxes causes the calculated variation in the depth of the SMTZ, and further geochemical species cycling such as the diagenetic remobilisation of barite phases in marine sediment due to changes in redox altering barite solubility in the Lüderitz Basin (Figure 2.7). Assuming no organoclastic SO_4 reduction was present within the sediment surface, Niewöhner et al. (1998) used marine sediment cores offshore Namibia to suggest that all the SO_4 depletion in this region can be fully explained by AOM. Therefore, the depth of the SMTZ can provide further context for the upward diffusing CH_4 flux. Within the mapped BSR in the Lüderitz Basin the depth of the SMTZ shallows updip, indicating a

higher upward diffusive flux of CH_4 further updip, which is likely due to gas buoyancy.

The major cause of variable upward CH_4 fluxes in the Lüderitz Basin are by either variations in TOC sources across the basin or by focused fluid flow. The continental drape deposits at the flanks of the antiformal structure provide a depocentre where the accumulation of organic sediment rich in TOC can accumulate since the Cenozoic (Figure 2.10). The depocentre coincides with the biogenic gas production window and is associated with ERs and seismic blanking across the continuous, moderate amplitude reflectors indicating the presence of free-gas. This structure is seen to thin down slope and would result in less organic-rich material being present and thus reduce the potential for the production in biogenic gas. Conversely, the accumulated CH_4, focused by the presence of a hydrate body, is observed to travel updip to the crest of the depocentre and subsequently diffuses out of the depocentre up to seabed via fluid escape pipes (Figure 2.10). This suggests that in the Lüderitz Basin the variable upward CH_4 flux is being predominately driven by migration pathways rather than a variable extent of source, a feature unknown if no geophysical assessment was undertaken. This is supported in that the depth of the SMTZ is shallower updip in crest of the depocentre and deeper overlying the thinned depocentre (Figure 2.10).

Therefore, caution must be exercised when interpreting geochemical data of shallow marine sediment cores in areas of known upward CH_4 flux when no subsurface geophysical data are available for context. Without initial, prior subsurface interpretation, it is rendered unknown the reason of variable upward CH_4 flux measured in marine sediment cores throughout the basin. This lack of spatial context could potential bias conclusions drawn from future marine sediment core samples due to varied redox conditions in surficial sediments.

2.6 Conclusion

The Lüderitz Basin exhibits a host of seismically recognisable amplitude anomalies that represent DHIs and their interpretation is consistent with previous studies. The combination of DHIs indicates a fully connected, active HPS is present. The evidence for the origin of CH_4 based on DHIs in the study area strongly suggests a shallow biogenic source, however a small contribution from thermogenic CH_4 and the breakdown of hydrocarbons within Unit D cannot be excluded. As such, this research

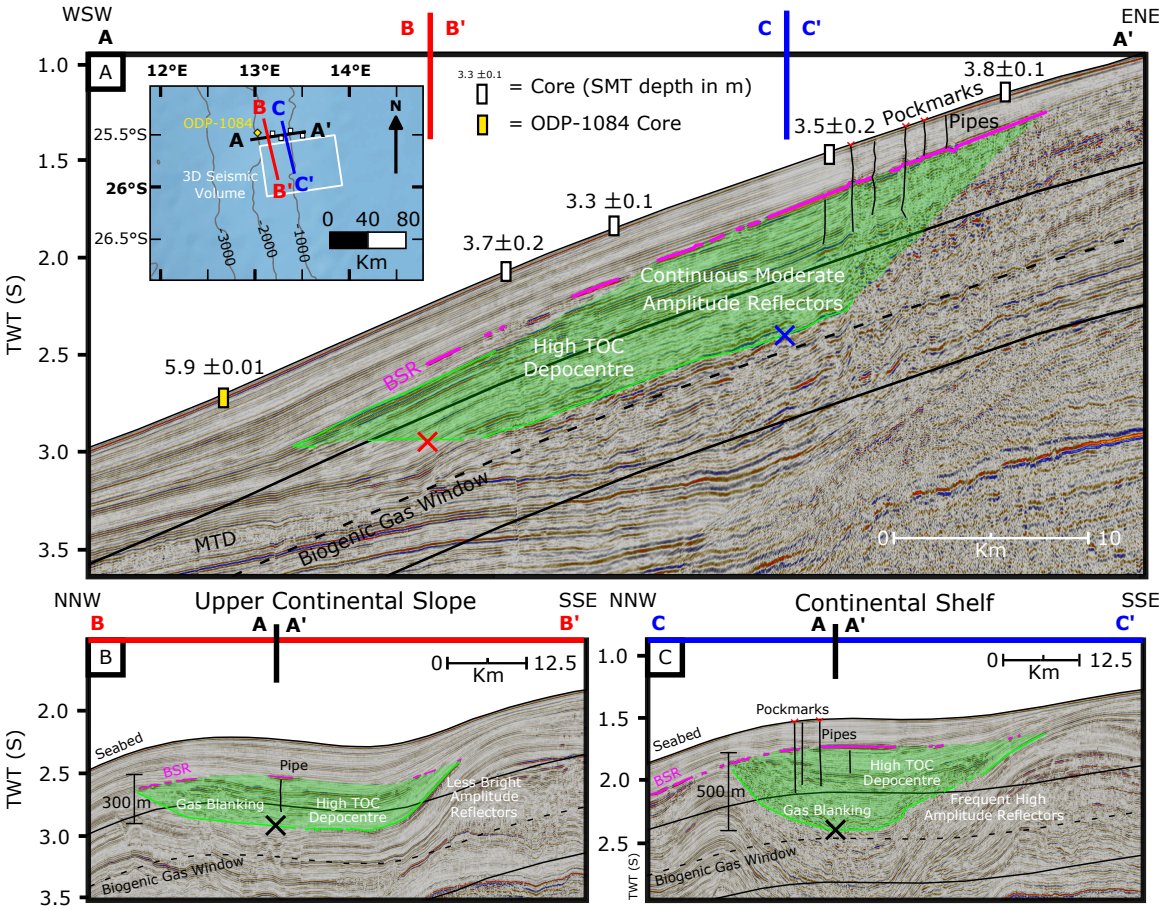

Figure 2.10: 2D Seismic cross-sections displaying the spatial variation of the structure of high TOC along the Namibia margin, Lüderitz Basin. High TOC depocentres are highlighted in green and are seen to thin down slope. This thinning would result in less organic-rich material and thus reduced production in biogenic gas. This could account for the variability in the overlying marine sediment core SMTZ depths (white and yellow rectangles). Seismic locations are shown in map inset.

suggests that the Lüderitz Basin has the potential to be developed for exploration as conditions favourable for hydrocarbon and gas production and trapping are present. Future work should investigate further into the migration pathways of the proposed HPS by utilising more 3D seismic datasets. In addition, developing models for the proposed gas flow and dynamics of the hydrate body would bolster this work and show how systematically similar the Lüdertiz basin is to the adjacent Kudu gas field, reducing the risk in frontier basins.

The upward diffusive flux of CH_4 is variable across the Lüderitz Basin attributed to subsurface focused fluid flow via migration pathways opposed to variable CH_4 sources. This drives the observed variable depths in the SMTZ across the Lüderitz Basin and subsequent biogeochemical cycling of other trace metal species such as Ba due to changes in surficial sediment redox conditions. Therefore, caution must be exercised when interpreting geochemical data from shallow marine sediment cores in regions of known upward CH_4 flux when no subsurface geophysical data are available for context, as erroneous conclusions on the causes of regional geochemical cycling can be drawn. For when an integrative study is not possible, future work should model shallow marine core CH_4 data to determine if any statistically significant spatial variation in upward diffusive CH_4 flux is present and if this links to any potential oceanographic structural features.

Chapter 3

Constraints on the Ba isotope composition of benthic inputs from reduced margin sediments

Barium (Ba) isotopes have the potential to form the basis of novel marine paleo-proxy applications, but to achieve this requires comprehensive constraints on the marine Ba isotope mass balance. Recent studies identify large Ba fluxes (17 Gmol/yr; Rahman et al. (2022); Whitmore et al. (2022)) from continental margin sediments. However, uncertainty in the mechanism and Ba isotope composition of this flux means its role within the global marine Ba isotope mass balance is still unknown. This study aims to (1) determine the mechanism controlling the observed Ba fluxes from anoxic continental margin settings, (2) constrain their associated Ba isotopic compositions, and (3) investigate what are the wider implications for the marine Ba isotope mass balance. To achieve this, Ba concentration ($[Ba]$) and Ba isotope ($\delta^{138/134}Ba$) data are presented for marine sediments and co-existing pore waters along with overlying seawater and suspended particulate samples along the Namibian continental shelf and slope. Pore water $[Ba]$ data are observed only to correlate with changes in pore water sulphate concentration (r^2 = 0.9704). This coincides with calculated barite ($BaSO_4$) solubility where cores with pore water sulphate depletion become increasingly undersaturated with respect to $BaSO_4$ despite the fact that pore water $[Ba]$ are increasing. This suggests that the main mechanism for the remobilisation of sedimentary Ba, is $BaSO_4$ solubility. The $[Ba]$ of upwelling seawater increases by 10.6% (40.6 to 44.9 nmol/kg) as it circulates over the Namibian shelf attributed to benthic inputs. The isotopic data for these samples can be feasibly explained by the input of Ba with $\delta^{138/134}Ba \approx +0.31‰$, consistent with measured pore water values from underlying anoxic sediments. Consequently, the remobilised benthic

Ba input becomes enriched in heavier Ba isotopes relative to the initial input from sinking particles, leading to the buried Ba reservoir evolving towards a lighter isotopic composition. The results of this study imply that large benthic Ba fluxes from continental shelves may constitute a recycling of authigenic Ba phases (e.g. $BaSO_4$), rather than an input of 'new' Ba. This has implications for how this component of the Ba cycle is considered in marine Ba mass balance and helps to bring the current constraints on the marine input and output fluxes into balance.

3.1 Introduction

Barium (Ba) isotopes are a novel tracer with potential for marine geochemical proxies such as productivity (Cao et al., 2016; Bridgestock et al., 2019; Carter et al., 2020; Horner and Crockford, 2021). Confidence in Ba isotope proxy applications requires a comprehensive understanding of the marine Ba isotope mass balance. However, certain components of the marine Ba cycle and their associated isotope compositions remain poorly constrained.

Large fluxes of Ba are entering the ocean from continental shelves, up to $\sim$17 $Gmol/yr$, with unknown isotopic composition (Mayfield et al., 2021; Rahman et al., 2022). This input of Ba to the ocean could constitute up to 50% of the total dissolved Ba (DBa) input flux to the ocean, so should be considered a major vector in the marine Ba cycle (Whitmore et al., 2022; Mete et al., 2023). Anoxic conditions along continental margins promote Ba remobilisation into the overlying water column (McManus et al., 1999; Eagle et al., 2003; Martinez-Ruiz et al., 2018; Gäng et al., 2023; Griffith et al., 2021). The processes driving this input of Ba are unknown but could reflect release of authigenic or detrital Ba phases during early diagenesis. Barite ($BaSO_4$) precipitation is the dominant sink of DBa from the ocean (Paytan and Griffith, 2007; Griffith and Paytan, 2012; Horner et al., 2015; Bates et al., 2017; Carter et al., 2020; Horner and Crockford, 2021). Sedimentary environments featuring substantial sulphate (SO_4) reduction promote dissolution of this authigenic phase (Borowski et al., 1996; Niewöhner et al., 1998; Dickens, 2001; Riedinger et al., 2006; Henkel et al., 2012; Lin et al., 2012). Diffusion of this DBa across the sediment-water interface (SWI) constitutes a 'recycling' of DBa back into the water column. Dissolution of eroded continental minerals could alternatively provide a detrital source of Ba to the ocean, constituting a 'new' Ba input, (Rahman et al., 2022; Whitmore et al., 2022). Distinguishing between these potential

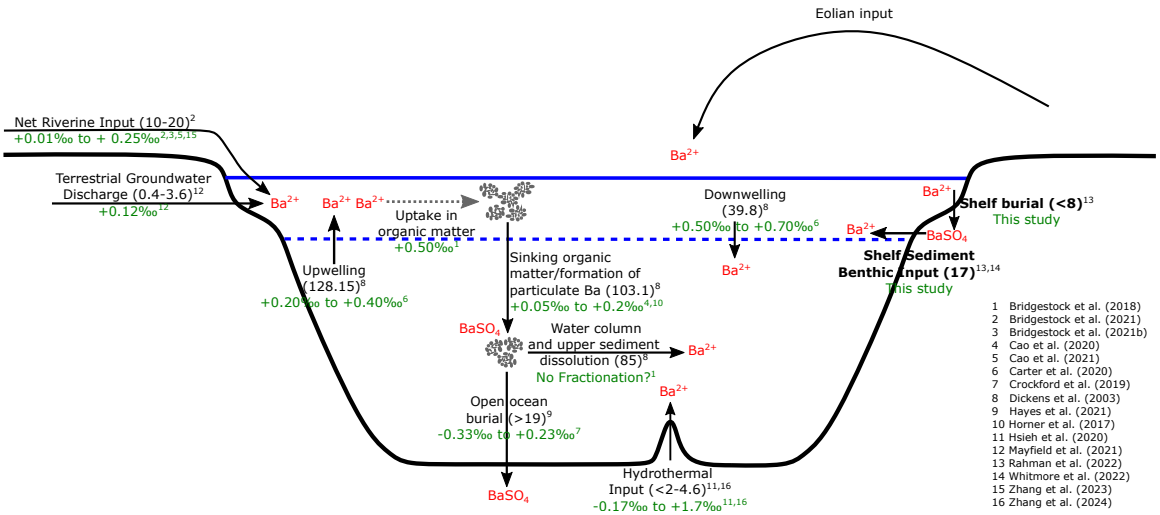

Figure 3.1: A simplified diagram of the marine Ba cycle. Direction of fluxes are shown with black arrows, with the value of the flux in parentheses (in $Gmol.yr^{-1}$). The associated phase of barium (Ba) is shown in red, with Ba^{2+} as the dissolved phase and $BaSO4$ as the solid phase. Currently the isotopic composition of the shelf sediment burial and the shelf sediment benthic input are the two remaining components to be constrained.

'recycling' vs 'new' Ba sources has implications for whether continental shelf benthic Ba fluxes should be viewed as internal or external components of the marine Ba cycle.

Recent studies have provided updated constraints on the input and output fluxes (Figure 3.1; Carter et al. (2020); Bridgestock et al. (2021b); Hayes et al. (2021); Hsieh et al. (2021); Mayfield et al. (2021); Rahman et al. (2022); Whitmore et al. (2022)). Including the shelf sediment benthic input in the marine Ba mass balance as an input causes a two-thirds imbalance between inputs and outputs (Rahman et al., 2022; Horner et al., 2021). A possible explanation of this flux imbalance is that shelf benthic inputs could be an internal ('recycling') rather than external ('new') component of the Ba cycle. The likely source of this imbalance is the uncertain nature of shelf sediment inputs (Zhang et al., 2023). By considering them as part of the internal 'recycling' Ba budget nearly balances the mass balance.

Recent studies have constrained the Ba isotope composition of important external components of the marine Ba cycle, including inputs from rivers (Bridgestock et al., 2021a,b; Cao et al., 2021; Zhang et al., 2023), groundwater (Mayfield et al., 2021; Rahman et al., 2022) and hydrothermal vents (Hsieh et al., 2021; Zhang et al., 2024), and output via burial in open ocean sediments (Crockford et al., 2019).

With current constraints, inputs appear systematically offset to heavy Ba isotope compositions relative to the main output (Horner and Crockford, 2021). Two key isotopic constraints are missing from this budget: the continental shelf benthic input and burial of authigenic Ba on margins.

This study aims to (1) determine the mechanism of continental shelf benthic inputs of DBa, (2) provide first insights into the isotopic composition of this input, and (3) constrain how this diagenetic remobilisation alters the isotopic composition of authigenic Ba buried in continental shelf sediments. These added constraints will help advance the debate on whether the global marine Ba mass balance is at steady state (Table 3.1) and provide insights into the impact of ocean redox changes on the global seawater Ba isotope inventory.

3.2 Study Area & Samples

3.2.1 Scientific Background of Study Area

The study area focuses on the Benguela Upwelling System (BUS), an example of an Eastern Boundary Upwelling System (EBUS), located along the Namibian coastal margin (Figure 3.2a; García-Reyes and Largier (2010); Santos et al. (2012); Varela et al. (2015); Wang et al. (2015); Brady et al. (2019); Seabra et al. (2019); Abrahams et al. (2021); Bograd et al. (2022)). The BUS is defined as an upwelling centre that has high biological primary productivity, with an annual average rate between 580 and 1470 $gCm^{-2}a^{-1}$ (Small and Menzies, 1981; Demarcq, 2009; Barlow et al., 2009; Monteiro, 2010; Verheye et al., 2016; Emeis et al., 2018; Jacobs et al., 2020; Paparazzo et al., 2021), and large gradients in shelf sediment redox conditions/diagenesis (Brüchert et al., 2003; Borchers et al., 2005; Brüchert et al., 2006; Abshire et al., 2020; Wyatt et al., 2021; Hunt et al., 2022; Liu et al., 2022; Gäng et al., 2023; Kossack et al., 2023; Chen et al., 2024b). Upwelling strength varies seasonally in response to changes in the wind field (Mohrholz et al., 2008; Bordbar et al., 2021; Polonsky and Serebrennikov, 2022; Bordbar et al., 2023). The high rates of productivity, driven by upwelling, in turn drive water column anoxia and an oxygen minimum zone (OMZ), <50 $\mu mol/kg$, can be present overlying the continental shelf by $\sim 50\ m$ (Chapman and Shannon, 1987; Tyson and Pearson, 1991; Berger et al., 2002b; Brüchert et al., 2003; Pitcher et al., 2014; Schmidt and Eggert, 2016; Rixen et al., 2021; Lovecchio et al., 2022; Said et al., 2023). This creates distinct redox zones along the Namibian margin sediments where the inner shelf

Input				
Process	Flux (Gmol/yr)	Flux Error (Gmol/yr)	$\mu_\delta^{138/134}Ba$ (‰)	±2SE
Effective Riverine Input	15[b]	10 - 20[b]	0.13[b,c,e,o]	0.05
Terrestrial Groundwater Discharge	1.57[l]	0.4 - 3.6[l]	0.18[l]	0.05
Hydrothermal Vents	3.5[k,p]	0 - 4.6[k,p]	0.31[k,p]	0.56
Total	20.1	15.3	0.16	0.98

Process	Flux (Gmol/yr)	Flux Error (Gmol/yr)	$\delta^{138/134}Ba$ (‰)	±2SE
Shelf Sediment Benthic Input	17[m,n]	Unconstrained	**This Study**	

Internal Cycling				
Process	Flux (Gmol/yr)	Flux Error (Gmol/yr)	$\mu_\delta^{138/134}Ba$ (‰)	±2SE
Upwelling	128.15[h]	Unconstrained	0.47[f]	0.02
Sinking Organic Matter / Formation of Particulate Barite	103.1[h]	Unconstrained	0.02[d,j]	0.04
Water Column and Upper Sediment Dissolution	85[h]	Unconstrained	No fractionation?[a]	n/a
Downwelling	39.8[h]	Unconstrained	0.51[f]	0.03
Total	148.32		0.23	0.03

Output				
Process	Flux (Gmol/yr)	Flux Error (Gmol/yr)	$\delta^{138/134}Ba$ (‰)	±2SE
Shelf Burial	8[m]	15[m]	**This Study**	
Open Ocean Burial	19[i]	10[i]	0.05[g]	0.01
Total	27	18	**This Study**	

Table 3.1: Fluxes and isotopic compositions of marine Ba mass balance, categorised into inputs, internal recycling, and outputs. Currently there is a lack of existing constraints on the isotope composition of benthic shelf sediment benthic inputs and burial fluxes. In addition, the role of shelf sediment benthic input as either an input or part of the internal cycling is not known. References: [a] Bridgestock et al. (2018), [b] Bridgestock et al. (2021b), [c] Bridgestock et al. (2021a), [d] Cao et al. (2020), [e] Cao et al. (2021), [f] Carter et al. (2020), [g] Crockford et al. (2019), [h] Dickens et al. (2003), [i] Hayes et al. (2021), [j] Horner et al. (2017), [k] Hsieh et al. (2021), [l] Mayfield et al. (2021), [m] Rahman et al. (2022), [n] Whitmore et al. (2022), [o] Zhang et al. (2023), [p] Zhang et al. (2024).

has the lowest oxygen penetration depth (<0.01 metres below seafloor ($mbsf$)) and highest degree of core pore water SO_4 depletion, with total depletion at 0.32 $mbsf$ (Figure 3.2a). Therefore, the seasonal upwelling causes distinct spatial and temporal fluctuations in pore water chemistry, ranging from highly reducing to slightly less reducing conditions across the continental shelf and slope (Wyatt et al., 2021; Hunt et al., 2022; Liu et al., 2022; Gäng et al., 2023; Kossack et al., 2023; Chen et al., 2024b).

The principal water mass located in the BUS is the South Atlantic Central Water (SACW) that is transported by two major currents: the northward flowing Benguela Current (BC) and the southward flowing, recirculated Angola Current (AC), that meet at the Angola Benguela Front (ABF)(Nelson, 1992; Dowsett et al., 1996; Schneider et al., 1996; Wefer et al., 1999; Berger et al., 2002b; Hutchings et al., 2009; Blamey et al., 2012; Koseki et al., 2019). Waters located in the Benguela Coastal Current (BCC) are typically cooler, less saline and more oxygen rich (8 - 19 °C, 34.35 - 35.5 PSU, 249 - 300 $\mu mol/L$; Mohrholz et al. (2008); Werner et al. (2012); Huenerlage and Buchholz (2013)) than Angolan Coastal Current (ACC) waters (8 - 28 °C, 34.4 - 35.8 PSU, 22.4 - 68.5 $\mu mol/L$; Poole and Tomczak (1999); Kopte et al. (2017); Tchipalanga et al. (2018); Körner et al. (2024)). The ABF is a diffuse frontal zone between these two water masses that sets the initial oxygen levels in the system, based on its position, due to the fractional contribution of either water mass, contributing to the redox conditions present (Summerhayes et al., 1995; Tim et al., 2015; Schmidt and Eggert, 2016; Nardini et al., 2019; Awo et al., 2022; Brandt et al., 2024). Therefore, at the time of sampling it is expected that inner shelf sediments further south will be subjected to more reducing conditions.

3.2.2 Types of Samples Used in the Study

Cores of marine sediment and pore water, along with overlying seawater and suspended particulate samples, were collected during two expeditions (Figure 3.2 & Table B.4). Continental shelf samples were collected 6th - 12th May 2019 during cruise transects on R/V Mirabilis as part of the Regional Graduate Network in Oceanography (RGNO) programme (referred to as the RGNO expedition herein). Sampling occurred at nine stations along two transects across the continental shelf at 20°S and 23°S (Figure 3.2 & Table B.4). To achieve regional context samples along Walvis Ridge were collected, during EXP 391 (6th December 2021 to 5th February 2022) as part of the International Ocean Discovery Program (IODP), on board the R/V JOIDES Resolution (referred to as IODP EXP 391 herein). Sampling occurred at

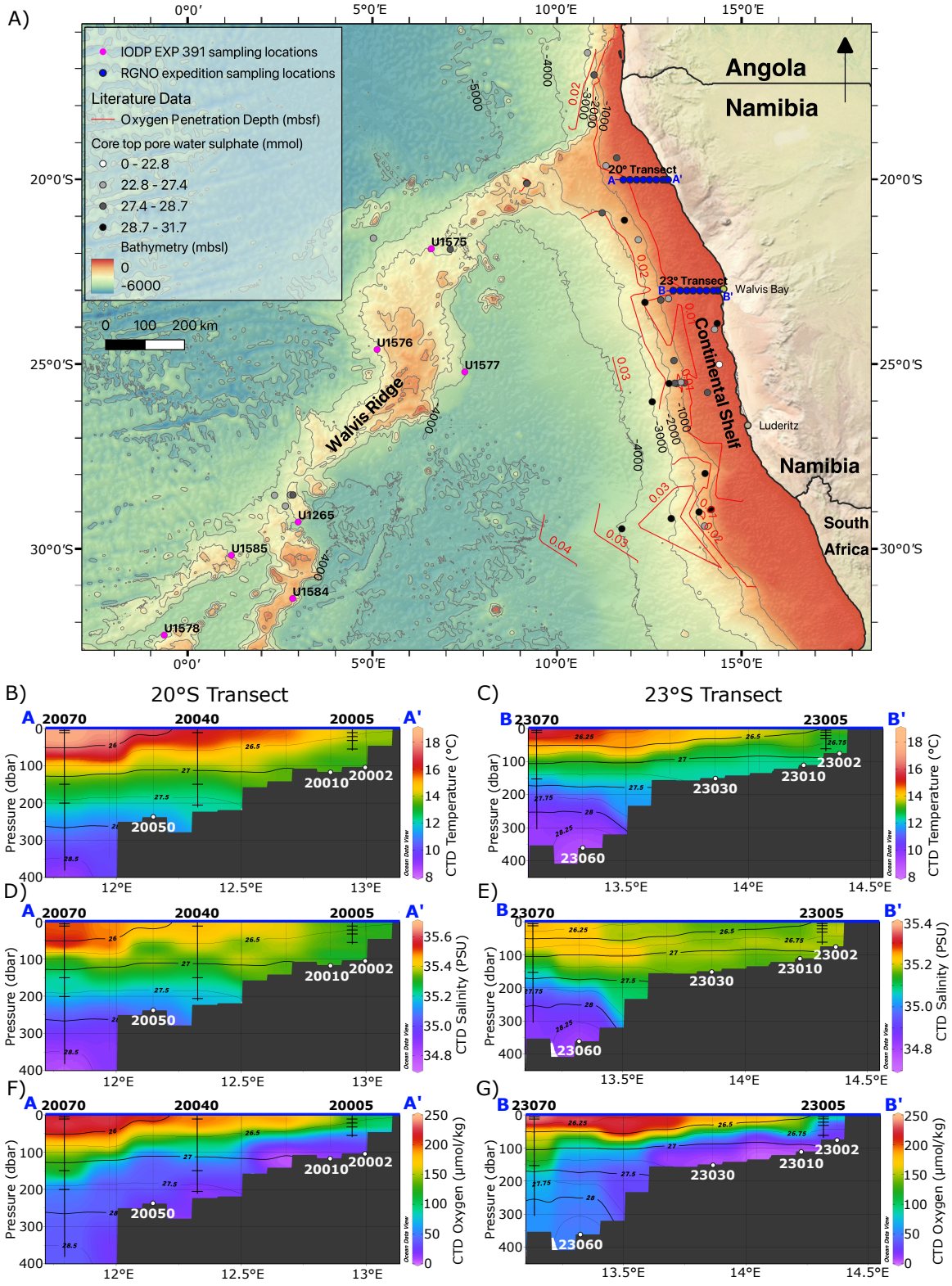

Figure 3.2: Map and hydrography of sampling site. a) Map of the Benguela Upwelling System offshore Namibia showing the sampling locations for the RGNO (blue circles) and IODP EXP 391 expeditions (pink circles). Literature data of pore water oxygen penetration depth and core top pore water SO_4 [*continued on the following page*]

Figure 3.2: [*caption continued*] concentrations for samples spanning the BUS and Walvis Ridge have been compiled from literature sources to provide a more regional context of pore water redox conditions, relevant for understanding benthic Ba fluxes in this region (Tables B.1 and B.2; Glud et al. (1994); Hensen (1996); Wefer et al. (1997); Niewöhner et al. (1998); Wefer et al. (1998); Zachos et al. (2004); Riedinger et al. (2006); Goldhammer et al. (2011); Emeis et al. (2018)). b-g) Seawater CTD profiles for temperature, salinity, and dissolved oxygen for the 20°S and 23°S transect. The profiles show the location of sediment cores with station numbers (white circles) and location of seawater depth profiles, with horizontal black lines showing depths of water samples, and labels denoting station numbers (black lines). The black contours represent the *in situ* density anomaly (kg/m^3).

a total of six drilling locations along the Walvis Ridge and further seawater sampling was executed during transits (Figure 3.2 & Table B.4).

3.2.3 Sample collection methods

3.2.3.1 Seawater samples

The RGNO expedition collected seawater samples at three stations (20005, 20040, and 20070) along transect 20°S, and at two stations (23005 and 23070) along transect 23°S off the Namibian margin (Figure 3.2 & Table B.4).

Approximately 60 *ml* of seawater were collected at depth from Niskin bottles mounted on a CTD Sea-Bird SBE 9 rosette. Seawater was filtered directly from the Niskin bottles using acid cleaned 0.2 μm Acropak™ 500 polyethersulfone membrane filter capsules and collected into acid cleaned 60 *ml* high-density polyethylene (HDPE) bottles, before being acidified to pH $\approx$ 1 to 2 by addition of distilled HCl. Filters and bottles were both rinsed with the sampled seawater prior to sub sample collection. These conventional sampling techniques should be suitable for DBa but are known to contaminate other trace metals (Cutter et al., 2017; Middag et al., 2023). To confirm that the Niskin sampling did not significantly contaminate for Ba, surface waters (10 metres below sea level (*mbsl*)) were also collected using protocols designed to minimise trace metal contamination. To achieve this, Masterflex tubing was lowered to 10 *mbsl* on a nylon rope, weighted with plastic coated steel. Water was pumped through the tubing using a peristaltic pump (Cole-Parmer) and was filtered through acid cleaned 0.2 μm Acropak™ 500 polyethersulfone membrane filter capsules directly into an acid cleaned HDPE bottle. Samples were subsequently acidified to pH $\approx$ 1 to 2 by addition of distilled HCl. Prior to sample collection, the

tubing and filter were rinsed with at least 3 times the tubing volume with seawater. Both the tubing and the filters were acid cleaned and rinsed with Milli-Q water prior to the cruise.

In addition to seawater samples the CTD Sea-Bird SBE 9 rosette measured dissolved oxygen concentration, pressure, temperature, and salinity at constant depth intervals.

Seawater samples acquired during IODP EXP 391 were collected and processed using similar methodology as RGNO expedition seawater samples and were recovered from seven stations (U1265, U1575, U1576, U1577, U1578, U1584, and U1585) situated along the Walvis Ridge (Figure 3.2 & Table B.4). Surface seawater ($\sim$ 1 - 3 *mbsl*) were collected by lowering a 10 L HDPE bottle on a nylon rope, weighted with plastic coated steel. For seawater collected at depth, a Niskin bottle was lowered whilst mounted on a stainless-steel frame and was fired at desired depth. After collection, seawater was filtered using 0.2 μm Isopore membrane filters and decanted on board into acid-cleaned 1 L volume HDPE bottles and was subsequently acidified to pH $\approx$ 1 to 2 by addition of distilled HCl. Both the collection bottle for the surface waters and the filters were acid cleaned and rinsed with Milli-Q water prior to use.

Seawater samples collected on both expeditions were stored at 4°C on board the research vessel until they were transferred back to Department of Earth Sciences, University of Oxford and stored at 4°C for further processing.

3.2.3.2 Suspended Particulate samples

Suspended particulate samples were only collected during the RGNO expedition at the same stations as seawater was collected i.e. at three stations (20005, 20040, and 20070) along transect 20°S, and at two stations (23005 and 23070) along transect 23°S (Figure 3.2 & Table B.4).

For these samples: between 40 - 60 L of seawater were collected into cubic containers using the peristaltic pump from 10 *mbsl* as described above. This water was subsequently filtered using 47 *mm* Supor® polyethersulfone (PES) filters, 0.8 μm, and an enclosed vacuum filtration unit made of Nalgene. The filters were acid-cleaned before the cruise, and the filter holder/unit was rinsed with Milli-Q between sample collections. After filtration, the PES filters, hosting the suspended

particulate material were detached and stored frozen (-20 °C) in acid rinsed zip-lock bags prior to further processing for geochemical measurements.

3.2.3.3 Marine sediment cores

Marine sediment cores were collected during the RGNO expedition at seven stations distributed across two transects: three stations (20002, 20010, and 20050) along the 20°S transect and four stations (23002, 23010, 23030, and 23060) along the 23°S transect (Figure 3.2 & Table B.4). Marine sediment cores were recovered utilising a MC-400 Multi-corer equipped with four polycarbonate sample tubes (10 cm diameter by 58 cm height), that preserved the SWI in all cores retrieving surface sediments from seafloor to ~ 0.3 $mbsf$. Holes were pre-drilled into all sample tubes at 2 - 3 cm resolution for pore water extraction using pre-cleaned Rhizons (0.6 μm pore size) at 2 - 3 cm intervals. Pore waters were extracted via the Rhizon samples using syringes and were transferred to acid-cleaned, $\sim$ 60 ml, HDPE bottles prior to storage at 4°C. Samples were then acidified to pH < 2 by addition of distilled HCl.

After pore water extraction, sediment cores were sub-sampled at 1 cm intervals. The samples were then sealed in acid-cleaned plastic bags and stored at -20 °C.

Marine sediment cores from IODP Expedition 391 were recovered from four stations (U1575, U1576, U1577, and U1578) situated along the Walvis Ridge (Figure 3.2 & Table B.4). Sediment cores were collected using a rotary core barrel (RCB) coring system and were completed using standard IODP conventions resulting in sediment from seafloor to basement (Sager et al., 2023). Typical surface sediment recovery was 70% and the SWI was only captured in core U1577. Biostratigraphy was used in cores that did not capture the SWI and show surface sediments (0.02 $mbsf$) younger than 0.22 Ma (Gaudio et al., 2024). Pore water was extracted for the top 10 cm of each station using the same methodology as the RGNO cores detailed above. The marine sediment core was processed following standard IODP procedure, as detailed in Sager et al. (2023), resulting in sediment slices for the top 10 cm at 1 cm resolution.

All sediment core slices were stored frozen (-20 °C), until sub sampling. Sub-samples ($\sim$ 10 g) were freeze dried prior to further processing for geochemical measurements.

3.3 Analytical Techniques

All chemical procedures during sample preparation were conducted in a Class 100 laminar flow hood within Class 10000 metal-free clean laboratories. The acids utilised in this study (HCl, HNO3, and HF) underwent purification via an in-house sub-boiling distillation system. Additionally, all water (H_2O) employed was of 18.2 $M\Omega$-grade quality sourced from a Merck Millipore water purification system. Acetone and ethanol used were from reagent grade solution. Finally, hydrogen peroxide (H_2O_2) used in this study were commercial Merck suprapur® reagents.

3.3.1 Sample Preparation

For the sediment samples, $\sim$0.1 g of freeze-dried sediment powder was accurately weighed into Teflon beakers. Total digestion was achieved by the sequential addition, reflux and evaporation of 4 ml HF/HNO_3 in a 1:3 volumetric mixture at 85°C overnight, followed by 4 ml 6M HCl at 120°C for 24 hours. Beakers were ultrasonicated for 30 minutes immediately after each respective acid addition. Once cooled, 6 ml 16M HNO_3 were added to the aliquots to form reverse aqua regia, ultrasonicated for 30 minutes and refluxed overnight at 120°C. The solutions were dried at 120°C and 3 ml H_2O_2 was then added at room temperature in 0.5 ml increments and left to react at room temperature overnight to break down organic material further. The aliquots were dried down at 85°C to avoid strong effervescence and finally, 1 ml 16M HNO_3 + 1 ml Milli-Q was added to the residue, refluxed at 120°C. If total digestion had not occurred, samples were subjected to repeat H_2O_2 and 1 ml 16M HNO_3 + 1 ml Milli-Q cycles until the residues were fully dissolved. Finally, the aliquots were dried down and re-dissolved in 5 ml 2M HNO_3 for storage. Finally, a sample aliquot of 1.5 ml was diluted to 10 ml with Milli-Q (total dilution 333.5) and taken forward for measurement.

For suspended particulate samples, the total digestion method was adapted from that provided in the GEOTRACES cookbook (Cutter et al., 2017). The PES filters containing the suspended particulate fraction were halved using a ceramic scissor (KYOCERA, Japan). The halved filters were placed in a PFA vial positioned against the vial wall, near the top edge, to prevent submersion in the digestion medium and facilitate refluxing. To ensure tight adherence to the wall and to prevent refluxing acid from passing underneath, the other sides of the filters without samples were moistened with residual seawater or added acid. Refluxing was performed with 1

ml of 50% HNO_3 / 10% HF at 130°C for 4 hours. Although the filter material remained intact, the potential of increasing the organic matter matrix of digested solution has been raised for the hot immersion of filters (Cutter et al., 2017). After cooling, droplets were collected from the cap and inside the vials by tapping or rolling the solution. The aliquots for each sample were combined and dried at 85°C, then 0.2 ml of 16M HNO_3 was added to switch the matrix to nitric acid for analysis, followed by another drying at 130°C. The residues were dissolved in 3 ml 2% HNO_3 for storage. A sample aliquot of 0.1 ml was diluted to 6 ml with Milli-Q water and taken forward for measurement.

For sediment digestions, the USGS organic rich shale standard SGR-1b, and for suspended particulate sample digestions, the phytoplankton standard BCR-414, were digested alongside samples, respectively. In addition, to quantify the contribution of Ba from sample digestion, a blank was digested alongside each batch of samples. For the particulate sample blank, a blank filter was refluxed and rinsed.

3.3.2 Measurement of elemental concentrations

All concentrations of major and trace elements reported in this study were measured using a PerkinElmer NexION 350D quadrupole inductively coupled plasma mass spectrometer (ICP-MS). The PerkinElmer NexION 350D quadrupole ICP-MS utilised in this study is connected to an Elemental Scientific Inc. (ESI, USA) Prep-FAST M5 Auto-sampler system. This setup enables the dilution and injection of micro-volume aliquots of blanks, standards, and samples directly into the mass spectrometer using the flow injection automation system (FIAS) facility. Injections are monitored by the fast-scanning quadrupole of the ICP-MS, and the average data are derived from three injections per replicate.

Marine sediment and suspended particulate samples were measured using the PrepFAST system and direct injection for all major and trace element concentrations. Barium concentration ($[Ba]$) for seawater and pore water samples were measured without dilution utilising the FIAS on the NexION using kinetic energy discrimination (KED) mode on the collision/reaction cell. Pore water iron (Fe) and manganese (Mn) concentration ($[Fe]$ and $[Mn]$, respectively) were determined using the SeaFAST coupled to the NexION using KED mode on the collision/reaction cell.

Pore water sulphate concentration ($[SO_4]$) was determined using ion chromatography (IC) by taking an un-acidified aliquot and diluting 200-fold using Milli-Q. Pore water samples for three marine sediment cores (20050, 23030, and 23060) located on the continental shelf were subsequently combined in order to increase sample concentration so a Ba isotopic composition for each core site core pore water would be viable.

3.3.3 Measurement of Ba isotope compositions

The $[Ba]$ and isotope compositions of samples were determined using thermal ionisation mass spectrometry (TIMS; TRITON instrument, Thermo Scientific), utilising a previously described double spike technique of a ^{137}Ba–^{135}Ba spike solution to correct for instrumental mass bias (Hsieh and Henderson, 2017).

Prior to Ba isotope measurements, Ba was purified from sample matrices following previously described protocols (Bridgestock et al., 2018; Hsieh et al., 2021). For sediment and suspended particulate samples, aliquots of the digested solutions containing $\sim$ 500 - 1000 ng and $\sim$250 ng of Ba, respectively, along with pore water and seawater samples containing $\sim$ 50 - 150 ng and $\sim$250 ng of Ba, respectively, were mixed with appropriate and known amounts of ^{137}Ba–^{135}Ba double spike solution. All samples were left to equilibrate for at least twenty-four hours. Once the samples had equilibrated, only the pore water and seawater samples were subjected to the addition of 3 ml of a 0.9M Na_2CO_3 solution to co-precipitate the Ba with $CaCO_3$. The supernatant was separated from the precipitate by centrifuging, and the precipitate was rinsed with $\sim$ 5 - 15 ml Milli-Q, prior to dissolution in 1 ml 3M HCl. All samples (including sediment and suspended particulate samples) were then purified via cation exchange chromatography (Bridgestock et al., 2021b). Organics leached from the cation exchange resin were oxidised by the sequential addition and evaporation of small amounts of 7.5M HNO_3 and 9.8M H_2O_2 (Bridgestock et al., 2018).

A double Re filament assembly was used for sample measurement. The double filaments were outgassed before sample loading. The purified Ba was loaded onto the evaporation filament in 2M HCl without an activator gel and were then loaded into the TIMS instrument on the sample wheel. Once samples were loaded and positioned, and near instrumental vacuum conditions achieved, each sample was run consecutively. The samples were heated until Ba ionisation was achieved, and typical

beam size of ∼10 V for ^{138}Ba was recorded. This corresponded to applying currents of ∼ 2200 - 2500 mA to the ionisation filament and ∼ 50 - 300 mA to the evaporation filament. Once a stable beam at the desired beam size was achieved, the sample underwent 54 blocks of analysis, with 10 measurements in each block. Before starting the analysis, peak centring and baseline monitoring were performed. Throughout the run, the resulting ion beams were monitored using Faraday cups that are equipped with 10^{11} ohm resistors. The raw isotopic ratios were processed offline to correct for instrumental mass bias and finally, data are reported in the δ-notation (‰) ($\delta^{138/134}Ba$) relative to the National Institute of Standards and Technology (NIST) 3104a standard (Equation 7).

$$\delta^{138/134}\mathrm{Ba} = \left(\frac{^{138}\mathrm{Ba}/^{134}\mathrm{Ba}_{\mathrm{sample}}}{^{138}\mathrm{Ba}/^{134}\mathrm{Ba}_{\mathrm{NIST3104a}}} - 1\right) \cdot 1000 \qquad \{7\}$$

The internal precision for each run was monitored through the 2SE of repeat integrations in a single TIMS analysis. Standards were utilised in each sample batch run to track and correct for any drift in the double spike calibration: NIST 3104a measurements were included in each sample batch run and used to correct for instrumental drift which spanned a range of -0.12 to 0.06‰ (Table B.3). The National Bureau of Standards (NBS) NBS-127 standard was also measured to validate this drift correction and its long-term reproducibility is used as a measure of external reproducibility.

The accuracy of this data is confirmed by replicate measurements of select samples using a multiple collector Inductively coupled plasma mass spectrometry (MC-ICP-MS) at a separate laboratory, National Taiwan University (NTU). Detailed methodology can be found in Appendix Section B.1.

3.4 Results

All data generated in this study is reported in Table B.4.

3.4.1 Data Quality

Barium concentrations and $\delta^{138/134}Ba$ values measured on co-located samples collected using Niskin bottles and the peristaltic pump agree within analytical uncertainty, except in sample 23005 (Figure B.1). Barium concentrations measured by ICP-MS and TIMS isotope dilution agree within 14.5% for seawater samples

(Figure B.2A), 71.5% for particulate samples, where TIMS reported consistently higher $[Ba]$ (Figure B.2B), 7.42% for marine sediment samples, except for samples from core 23010, where ICP-MS records consistently higher $[Ba]$ values by on average 27% (Figure B.2C), and 18.8% for pore water samples (Figure B.2D). Finally, measurements of CRM SGR-1b produced $[Ba]$ results within 91.8% of the certified values (Table B.5). Aluminium, Mn, and Fe concentration agree within 92.1, 91.2, and 84.3%, respectively of certified values. Measurements of CRM BCR-414 report lower percentage yields, 56.8 to 78%, compared to published certified values (Table B.5). Manganese concentration reported agreement within 56.8% of certified values. Barium is not reported as one of the certified values so a yield of 56.8 to 78% is assumed.

Standards and samples typically yielded an internal precision of $\delta^{138/134}Ba$ between +0.01 and +0.02‰ (±2SE, n = 540) during each isotope analysis. The $\delta^{138/134}Ba$ value for the secondary Ba standard, NBS-127, after drift correction measured $\delta^{138/134}Ba \approx$ -0.29 ± 0.04‰ (±2SD, n = 30)(Table B.3), which agrees with published values from previous studies (Horner et al., 2017; Crockford et al., 2019; Tian et al., 2019; Tieman et al., 2020; Hsieh et al., 2021). The external reproducibility is assumed to represent the level of uncertainty for Ba isotope analyses for the majority of the samples. Eight samples featured lower ion beam intensities, usually relating to low sample concentration and availability, and as such the internal reproducibility is instead reported for these individual samples (between 0.03‰ - 0.08‰, 2SE).

Replicate samples measured at the University of Oxford are within 3.81% agreement in $[Ba]$ and within ±0.01‰ agreement in $\delta^{138/134}Ba$ values (Table B.6). The $\delta^{138/134}Ba$ and $[Ba]$ of samples measured on the MC-ICP-MS at NTU are within ±0.02‰ and 9.86% agreement, respectively, with data generated via TIMS (Table B.6). Procedural blanks range between 0.02 and 13.51 ng Ba representing less than 5.4% of the Ba processed in the seawater, sediment and particulate samples. Pore water blank contributions are up to 6.6%, due to the lower quantity of sample Ba processed (Table B.7). The MC-ICP-MS instrument has the highest blank contribution and is attributed to either (1) Ba blank introduced in the $NaCO_3$ solution during the co-precipitation step, or (2) samples not being maintained in a clean environment during processing due to laboratory failures.

3.4.2 Hydrography at the time of sampling

CTD profiles were conducted along two transects at 20° and 23° south during the RGNO expedition and reveal the water masses in the BUS at the time of sampling (Figure 3.2b-g). The 400 m profiles have a temperature (8 - 19 °C) and salinity (34.7 - 35.6 PSU), typical of SACW, consistent with previous studies (Figure 3.3; Schneider et al. (1996); Berger et al. (2002a); Schlitzer and Wegener (2000); Hutchings et al. (2009); Locarnini et al. (2010); Schlitzer et al. (2018)). Two distinct varieties of SACW are present at the time of sampling: a warmer, oxygen poor variety (10 - 19 °C, 40 to 225 $\mu mol/L$) more prominent in the north and a cooler, oxygen rich variety (8 - 15 °C, 75 - 250 $\mu mol/L$) more prominent in the south (Figure 3.2b-g & Figure 3.3). The measured dissolved oxygen concentration is consistent with previously reported values taken at the time of sampling (50 - 200 $\mu m/kg$; He et al. (2021); Rixen et al. (2021)). The *in situ* density anomaly for the BUS, calculated from temperature and salinity profiles, enables tracking of current water masses laterally. Both CTD transects reveal a distinct water package with a density of 27 to 27.5 kg/m^3 and a temperature around 13°C circulating over the continental shelf (Figure 3.2b-g). This phenomenon connects outer shelf waters with surface waters at the coast, indicating the presence of the upwelling of colder, nutrient-rich waters into the photic zone of the water column at the time of sampling. Finally, in both transects shelf bottom waters have a dissolved oxygen concentration of 0 - 40 $\mu mol/L$, referred to here as an OMZ. The OMZ in both transects extends into the water column over the continental shelf by $\sim$ 50 m and is more laterally extensive in the 23°S transect (Figure 3.2f,g).

3.4.3 Pore water Fe, Mn and SO_4 results

Measured pore water Fe (57.1 $nmol/kg$ - 14.3 $\mu mol/kg$, declining with increasing depth) and Mn (0.364 - 32.2 $nmol/kg$) concentrations (Figure 3.4b,c) are low relative to other continental margin settings (Fe: 20 - 200 $\mu mol/kg$, Mn: 8 - 80 $\mu mol/kg$; Schenau et al. (2002); Burdige and Komada (2020); Vollebregt et al. (2023)). However, values are similar to previous observations in the BUS (Fe: 0.5 - 60 $\mu mol/kg$; Böning et al. (2020)).

The changes in pore water $[SO_4]$ across the stations are more pronounced. On the outer shelf, marine sediment cores (20050, 23030, and 23060) show constant pore water $[SO_4]$ values of 28 $mmol/kg$, consistent with seawater values (Figure 3.4d). At the inner shelf station 20010, pore water $[SO_4]$ is depleted relative to seawater at 25

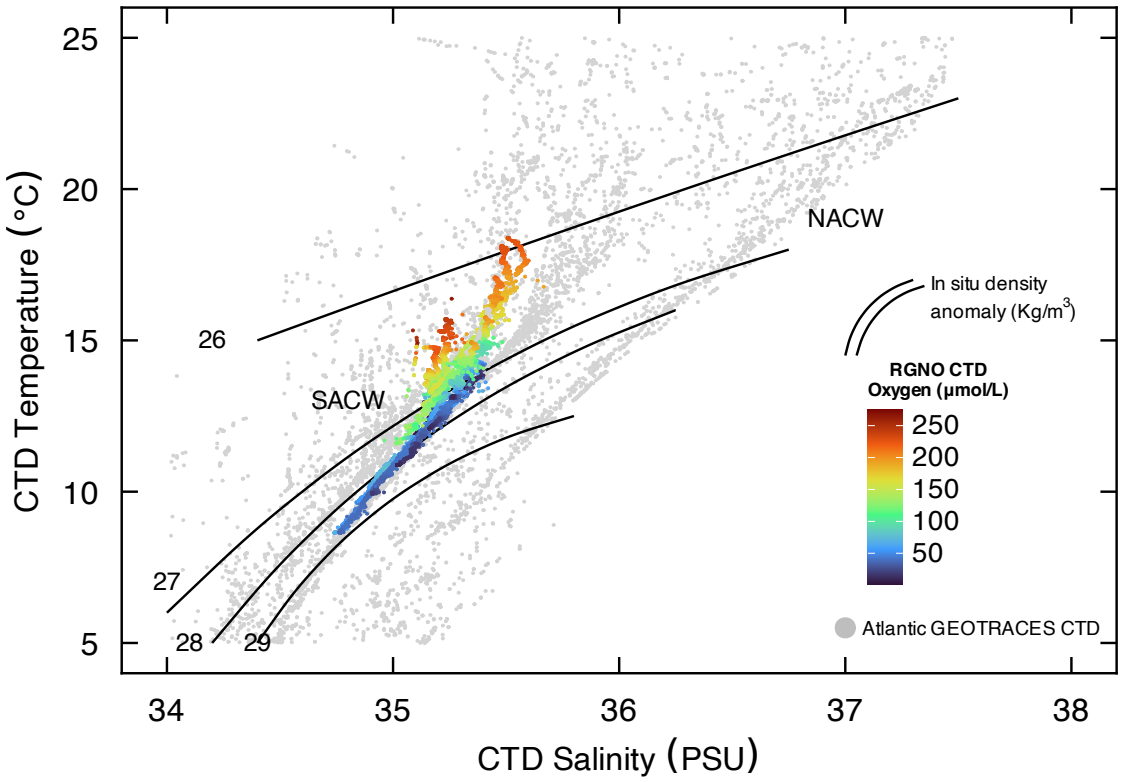

Figure 3.3: Hydrology of RGNO CTD data. The hydrology of sampled water masses have a temperature-salinity profile characteristic of SACW, consistent with previously measured Atlantic waters (Schlitzer and Wegener, 2000; Schlitzer et al., 2018). Two varieties of SACW have been sampled: a warmer, oxygen poor variety (10 - 19 °C, 40 to 225 $\mu mol/L$) more prominent in the 20°S transect and a cooler, oxygen rich variety (8 - 15 °C, 75 - 250 $\mu mol/L$) more prominent in the 23° transect.

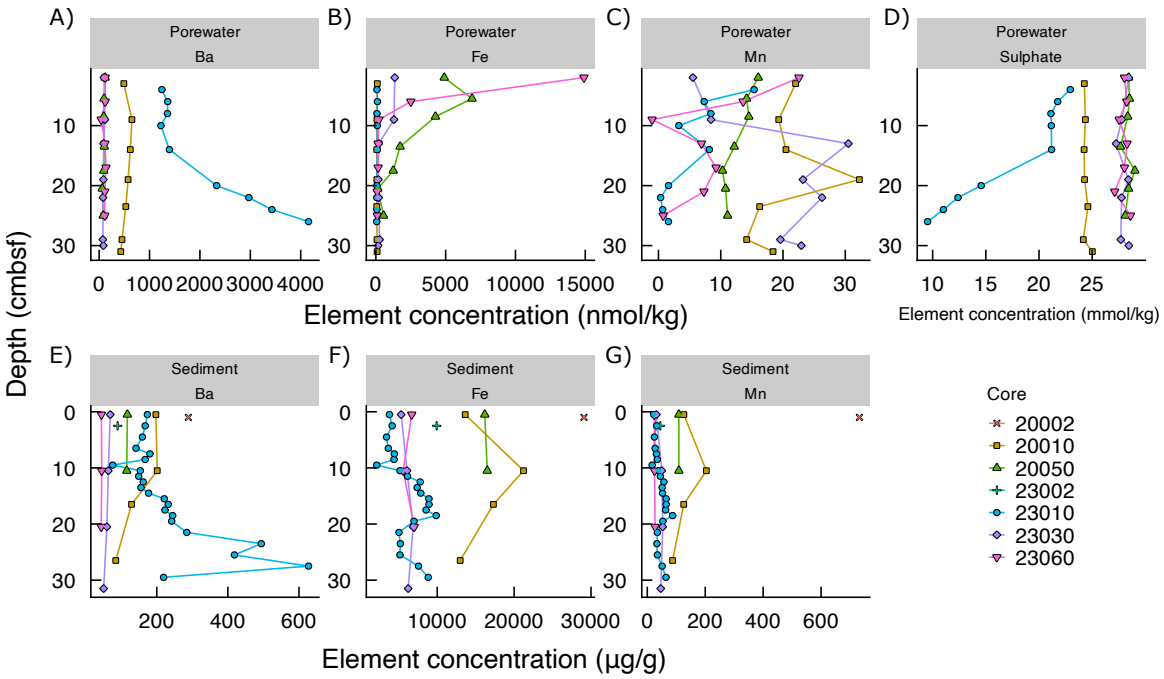

Figure 3.4: Sediment and pore water Ba, Fe, Mn, and SO_4 concentration data. Changes in pore water fraction a) $[Ba]$ do not coincide with changes in b) $[Fe]$, or c) $[Mn]$, but do coincide with d) $[SO_4]$. This pattern is consistent in the sediment fraction: e) $[Ba]$, f) $[Fe]$, and g) $[Mn]$. Depth scale is cm below seafloor (cmbsf). Barium, Fe, and Mn data presented here were measured on the ICP-MS.

$mmol/kg$. At station 23010, where dissolved oxygen in overlying seawater is near zero, pore water $[SO_4]$ decreases with depth from 24 to 8 $mmol/kg$. No depletion in pore water $[SO_4]$ relative to seawater in samples along the Walvis Ridge is observed in the upper 10's of metres (Sager et al., 2023).

3.4.4 Seawater distribution of dissolved Ba concentrations and isotope compositions

DBa concentrations of seawater overlying the inner shelf (42.6 ± 2.0 $nmol/kg$ (±2SE, n = 9)) are higher than both outer shelf stations (40.6 ± 1.4 $nmol/kg$ (±2SE, n = 19)) and those overlying Walvis Ridge (39.5 ± 1.3 $nmol/kg$ (±2SE, n = 7); Figure 3.5a). In addition, no significant difference in vertical changes with depth in DBa concentration is measured (t(8.1413) = -0.58885, p = 0.5719). Inner shelf seawater (station 20005) in the 20°S transect are not enriched in DBa concentration compared to outer shelf stations (20070 & 20040; Figure 3.6a,c). The DBa concentration of upwelling seawater (specifically 27 to 27.5 kg/m^3 dense water corresponding to the 13°C isotherm) in the 23°S transect (station 23005) significantly increases by 10.6%

(40.6 to 44.9 $nmol/kg$; t(4.003) = 8.3402, p = 0.001126) as it circulates over the Namibian shelf prior to upwelling (station 23070; Figure 3.6b,c). Barium enrichment at 23°S coincides with a more intense OMZ/pore water SO_4 depletion in inner shelf sediment. Measured dissolved seawater $\delta^{138/134}Ba$ values are within uncertainty of each other at all shelf and Walvis Ridge stations and depths, +0.61 ± 0.01‰ (±2SE, n = 26; Figure 3.5b). No significant difference in dissolved seawater $\delta^{138/134}Ba$ values are observed as upwelling water (specifically 27 to 27.5 kg/m^3 dense water) circulates over the Namibian shelf (t(1.24) = -0.16249, p = 0.8933; Figure 3.6b,d).

Suspended particulate Ba (pBa_{bulk}) concentrations average 222 ± 38.9 $pmol/kg$ (±2SE, n = 5; Figure 3.5e), which is consistent with previously published values at a similar depth range, < 20 $mbsl$ (250.48 ± 99.9 $pmol/kg$ (±2SE, n = 5); Horner et al. (2017); Cao et al. (2020)). The pBa_{bulk} concentration decreases towards open ocean from 260 and 80 $pmol/kg$ and is two orders of magnitude lower than corresponding DBa values. In contrast, the $\delta^{138/134}Ba$ of pBa_{bulk} samples (+0.21 ± 0.04‰ (±2SE, n = 5) increase systematically towards the open ocean (Figure 3.5f). Measured values are slightly heavier to published literature data for the upper water column, < 178 $mbsl$ (+0.02 ± 0.04‰ (±2SE, n = 42); Horner et al. (2017); Cao et al. (2020)). The $\delta^{138/134}Ba$ of pBa_{bulk} is systematically offset from surface waters by $\Delta^{138/134}Ba_{pBa_{bulk}-DBa}$ = -0.40 ± 0.03‰ (±2SE, n = 17), where $\Delta^{138/134}Ba_{pBa_{bulk}-DBa}$ = $\delta^{138/134}Ba_{pBa_{bulk}}$ - $\delta^{138/134}Ba_{DBa}$, consistent with previously reported values (-0.41 ± 0.09‰ (±2SE, n = 20) & -0.53 ± 0.04‰ (±2SE, n = 6); Horner et al. (2017); Cao et al. (2020); Horner and Crockford (2021)).

3.4.5 Sediment distributions of Ba concentrations and isotope compositions

The $[Ba]$ in marine sediments from cores on the shelf are constant at 130 ± 11 $\mu g/g$ (±2SE, n = 29), except for the inner shelf station 23010 where $[Ba]$ increases to ∼ 400 $\mu g/g$ in the lower section of the core (Figure 3.5g & Figure 3.4e). Sediment cores from Walvis Ridge have higher $[Ba]$ values compared to the shelf (359 ± 33.4 $\mu g/g$ (±2SE, n = 17)). The Ba/Al ratios of marine sediment cores at Walvis Ridge (0.106 ± 0.0108 (±2SE, n = 16)) are higher than those on the continental shelf (0.018 ± 0.006 (±2SE, n = 30); Figure 3.7a).

Sediment $\delta^{138/134}Ba$ values generally increase with distance from shore, from +0.06 ± 0.01‰ (±2SE, n = 30) at inner shelf stations (20002, 20010, 23002, &

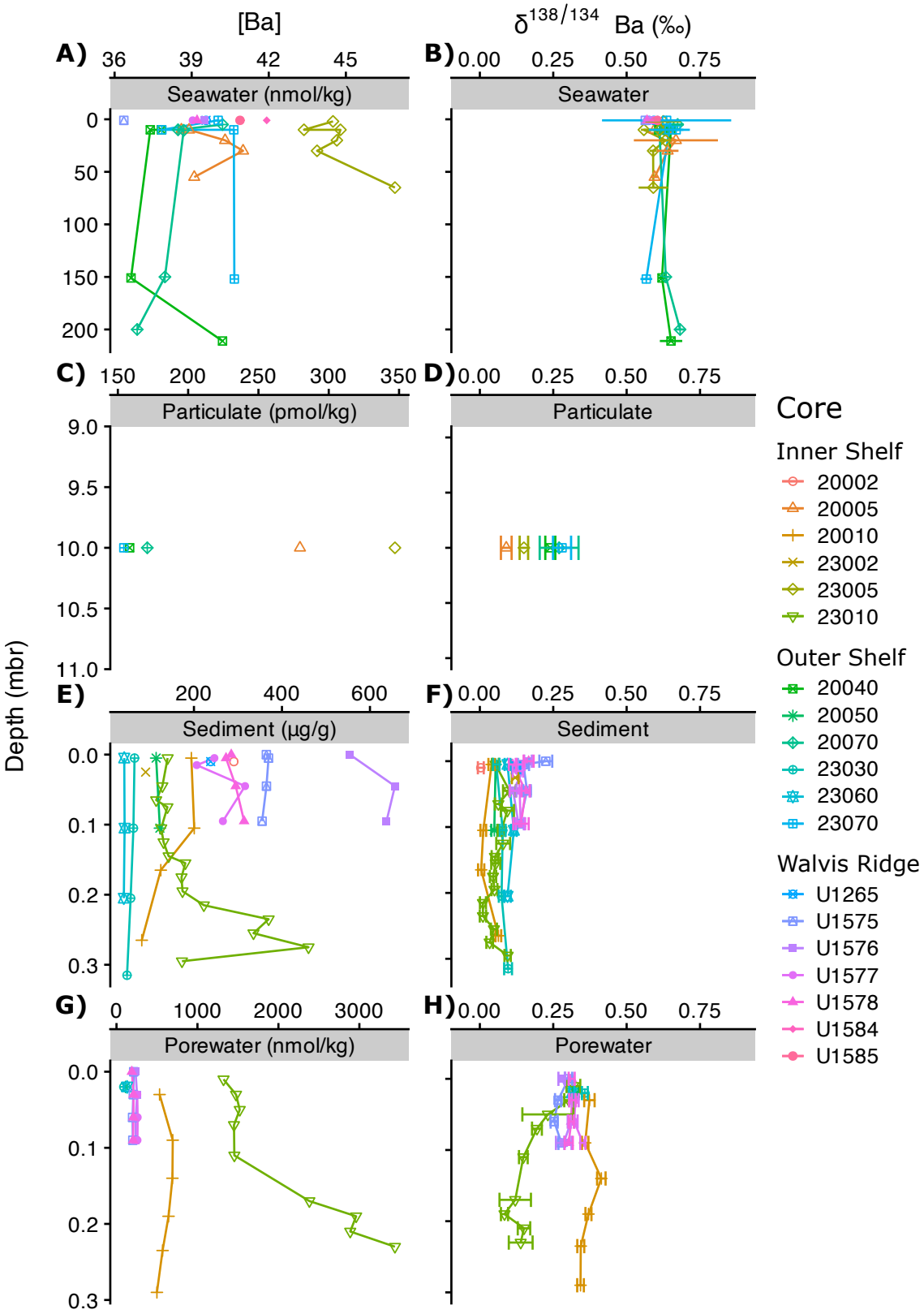

Figure 3.5: Ba concentration and $\delta^{138/134}Ba$ data vs depth faceted by each data type. Depth scale is metres below reference (mbr): for seawater and particulate samples this is below sea level whilst for sediment and pore water samples it is below seafloor. Axes units for each $[Ba]$ subplot are listed in the respective title grey box.

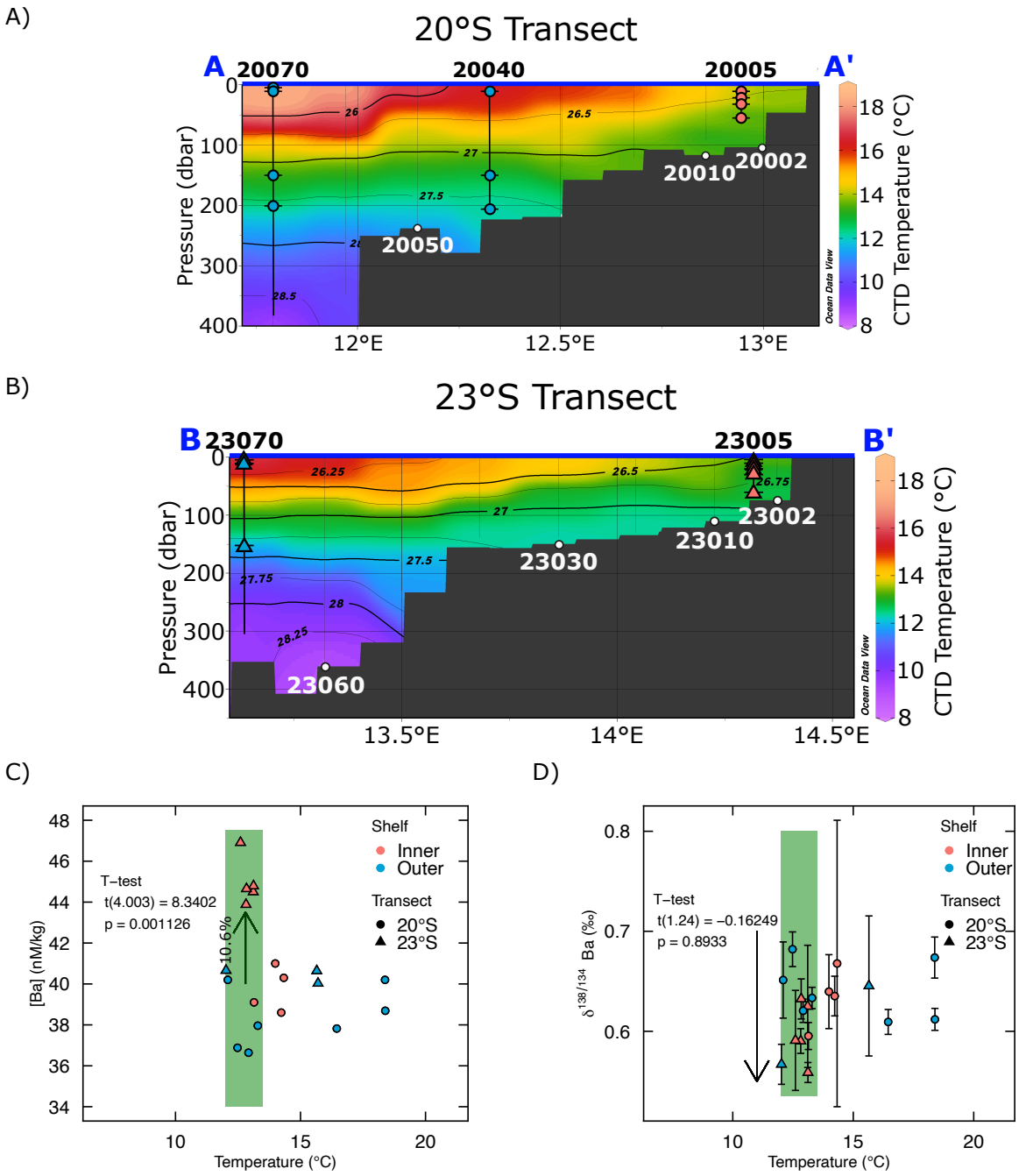

Figure 3.6: Ba concentration and $\delta^{138/134}Ba$ data in upwelling water. Seawater CTD profiles for temperature for the a) 20°S and b) 23°S transect. The profiles show the location of sediment cores with station numbers (white circles) and location of seawater depth profiles, showing depths of water samples and location on the continental shelf, and labels denoting station numbers (blue or red circles or triangles). The black contours represent the *in situ* density anomaly (kg/m^3). The location of transects can be see on Figure 3.2. c) The $[Ba]$ of upwelling seawater (27 to 27.5 kg/m^3 density horizon corresponding to the 13°C isotherm) for both transects. The increase in DBa concentration is only observed in the 23°S transect and the 20°S inner shelf seawaters show no Ba enrichment. d) The $\delta^{138/134}Ba$ values of upwelling seawater (27 to 27.5 kg/m^3 density horizon corresponding to the 13°C isotherm) for both transects.

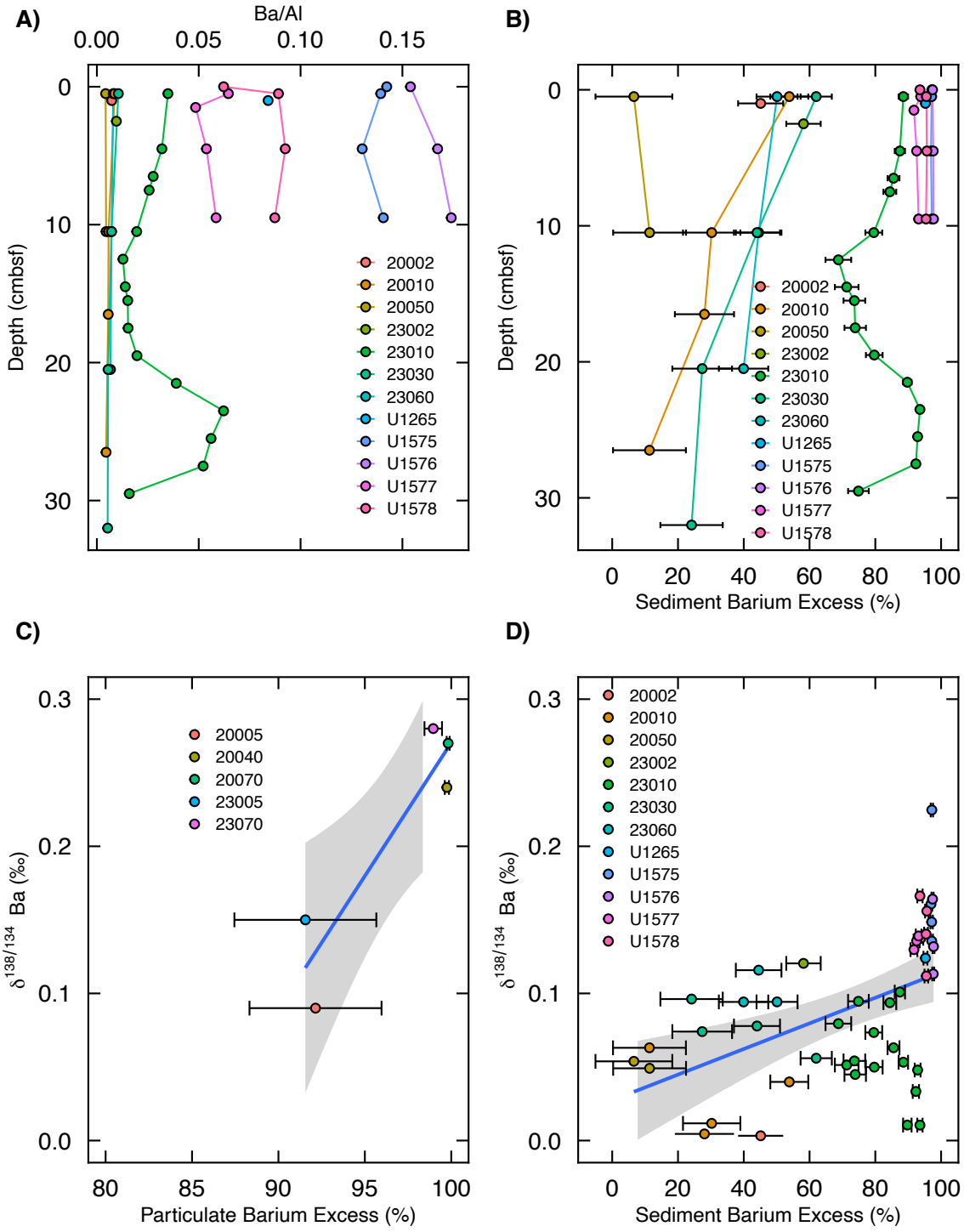

Figure 3.7: Distributions and relationships between Ba/Al, Ba_{excess} and $\delta^{138/134}Ba$ values in the marine sediment cores. a) Ba/Al as a function of depth below seafloor for the RGNO and IODP EXP 391 cores. b) Sediment and c) particulate Ba_{excess} as a function of depth below seafloor for the RGNO and IODP EXP 391 cores. d) Sediment Ba_{excess} against $\delta^{138/134}Ba$ values for marine sediment cores. The Ba_{excess} is calculated Equation 8 using a Ba/Al detrital reference ratio of 0.004 ± 0.0005 (Reitz et al., 2004). Blue lines are linear regressions with grey shade regions denoting 95% confidence intervals.

23010), to +0.15 ± 0.01‰ (±2SE, n = 16) at Walvis Ridge (Figure 3.5h). As such, samples located at Walvis Ridge show similar $\delta^{138/134}Ba$ values to measured suspended particulate values (+0.09‰ to +0.28‰). Surface marine sediments are offset from surface waters by $\Delta^{138/134}Ba_{sediment-DBa}$ = -0.49 ± 0.03‰ (±2SE, n = 24), where $\Delta^{138/134}Ba_{sediment-DBa} = \delta^{138/134}Ba_{sediment}$ - $\delta^{138/134}Ba_{DBa}$. This value is consistent with the degree of fractionation noted previously between sediment and DBa in marine settings (-0.51 ± 0.03‰ (±2SE, n = 32); Bridgestock et al. (2018); Horner et al. (2021); Middleton et al. (2023a)).

The fractional contribution of Ba from both detrital and non-detrital sources can be determined for the marine sediment samples, and suspended particulate samples, through the calculation of Ba_{excess} (Equation 8).

$$Ba_{excess}(\%) = 1 - (Ba/Al_{detrital} * Al_{total})/Ba_{total} * 100 \quad \{8\}$$

where Ba_{excess} denotes Ba from non-detrital sources, Ba_{total} and Al_{total} are $[Ba]$ and aluminium concentration ($[Al]$) from marine sediment core respectively, and $Ba/Al_{detrital}$ denotes the reference ratio of the detrital material. The precision of the calculation relies on selecting an appropriate reference ratio for the detrital component, which varies regionally (Reitz et al., 2004). As no direct measurements exist for the Namibian margin, a reference ratio of 0.004 ± 0.0005 is used, encompassing data from the Congo Fan and the Angolan basin (Table B.8; Rutsch et al. (1995); Pfeifer et al. (2001); Reitz et al. (2004)). For suspended particulate data Fe is selected instead of aluminium (Al) and as such the Ba/Al ratio has been converted to Ba/Fe using the Al/Fe ratio of detrital phases on marine particles (0.275; Ohnemus and Lam (2015)).

The Ba_{excess}, and thus non-detrital Ba contributions, of both marine sediment and suspended particulate is lower in the inner shelf stations (5 - 94.4 % & 92%, respectively) compared to the outer shelf stations (90 - 98% & 99%, respectively; Figure 3.7b & Figure 3.7c). The calculated Ba_{excess} at all inner shelf stations systematically decrease by $\sim$ 10 - 45 % downcore, expect the inner most station at 23010 where Ba_{excess} values vary between 70 - 90 % throughout the extent of the core (Figure 3.7b). A relatively weak relationship exists between measured $\delta^{138/134}Ba$ and calculated Ba_{excess} ($r^2 = 0.23$, $p = 0.000713$; Figure 3.7d).

The $[Ba]$ of marine sediment pore waters is relatively constant for most cores (206 ± 8.17 $nmol/kg$ (±2SE, n = 37)), except for the two most inner shelf stations (station 20010 & 23010) where $[Ba]$ is higher (Figure 3.5c & Figure 3.4a). At station 20010 $[Ba]$ is elevated at 605 ± 31.4 $nmol/kg$ (±2SE, n = 7) with the highest values in the centre of the core, whilst the pore water fraction at station 23010 increases from 1322 to 3439 $nmol/kg$ over the extent of the core. Measured pore water $[Ba]$, except for the two inner shelf stations, is lower than previously reported average values for similar core depths (< 0.3 $mbsf$, 385 ± 25.4 $nmol/kg$ (±2SE, n = 288); Paytan and Kastner (1996); Cao et al. (2023); Middleton et al. (2023a); Scholz et al. (2023)). At all sites pore water $[Ba]$ is greater than the bottom seawater samples. Pore water $[Ba]$ is negatively correlated to pore water $[SO_4]$ (r^2 = 0.9704) and has no correlation with pore water $[Fe]$ or $[Mn]$ (Figure 3.4a-d).

The average $\delta^{138/134}Ba$ of marine sediment pore waters located on both the continental shelf and Walvis Ridge is +0.30 ± 0.04‰ (±2SE, n = 25; Figure 3.5d), except for one inner shelf station, 23010, where $\delta^{138/134}Ba$ decrease from +0.34‰ to +0.07‰ with depth. Results are consistent with previously published pore water $\delta^{138/134}Ba$ values at a similar depth range, < 20 $mbsf$ (+0.28 ± 0.01‰ (±2SE, n = 101); Cao et al. (2023); Middleton et al. (2023a); Scholz et al. (2023)). On average, pore waters are offset from co-located sediment by $\Delta^{138/134}Ba_{sediment-pore\ water}$ = -0.18 ± 0.03‰ (±2SE, n = 17), where $\Delta^{138/134}Ba_{sediment-pore\ water} = \delta^{138/134}Ba_{sediment}$ - $\delta^{138/134}Ba_{pore\ water}$, consistent with previously reported fractionation (-0.16 ± 0.04‰ (±2SE, n = 11; Middleton et al. (2023a)) & -0.09 ± 0.08‰ (van Zuilen et al., 2023)).

3.5 Discussion

3.5.1 Pore water redox conditions at time of sampling

Using the bottom seawater oxygen concentrations and pore water $[Fe]$, $[Mn]$ and $[SO_4]$ the following redox zones in the sediment can be defined: Oxic (contains oxygen), Sub-oxic (no oxygen, but features peaks in Fe and Mn due to reductive dissolution of these phases), anoxic/sulphidic (features hydrogen sulphide, and depleted SO_4 concentrations), and methanic (contains methane and no SO_4).

No peaks in pore water Fe and Mn are observed in any of the inner shelf sediment cores (20002, 20010, 23002, & 23010; Figure 3.4b,c). In addition, pore water $[SO_4]$ is less than seawater values inferring SO_4 reduction is present at the time of sampling

(Figure 3.4d; Dickens (2001); Lin et al. (2012); Hong et al. (2013, 2014b)). Literature data of pore water oxygen penetration depth and core top pore water $[SO_4]$ for samples spanning the BUS and Walvis Ridge have been compiled from literature sources to provide a more regional context of pore water redox conditions, relevant for understanding benthic Ba fluxes in this region (Table B.1 & B.2; Glud et al. (1994); Hensen (1996); Wefer et al. (1997); Niewöhner et al. (1998); Wefer et al. (1998); Zachos et al. (2004); Riedinger et al. (2006); Goldhammer et al. (2011); Emeis et al. (2018)). At a regional scale, using literature data surface pore water SO_4 values are observed to be the most depleted at inner shelf locations (0 - 27.4 $mmol/kg$; Figure 3.2a). An OMZ is identified overlying inner shelf sediment cores (20002, 20010, 23002, & 23010) with a more laterally extensive OMZ and reduced overlying seawater oxygen concentration observed in the 23°S transect compared to the 20°S transect (Figure 3.2f,g). The general trends in pore water redox observed in this study are consistent with previous studies finding the lowest oxygen penetration ($<$0.01 $mbsf$) at the inner shelf that increases with distance from shore (Figure 3.2a; Wefer et al. (1997); Glud et al. (1994); Emeis et al. (2009)). Details on how core pore water oxygen penetration depth data were contoured can be found in Appendix Section B.2. Therefore, based on the distribution of these redox indicators it is inferred that at the time of sampling the inner shelf sediment cores (20002, 20010, 23002, & 23010) are subject to anoxic/sulphidic conditions, with the most reducing conditions present in the 23°S transect.

Distinct peaks in pore water Fe and Mn are observed in some of the outer shelf sediment cores (20050, 23030, & 23060; Figure 3.4b,c). In addition, pore water $[SO_4]$ is the same as ambient seawater values inferring that no SO_4 reduction is occurring at the time of sampling (Figure 3.4d; Dickens (2001); Lin et al. (2012); Hong et al. (2013, 2014b)). This is supported by regional core top pore water $[SO_4]$ data that show outer shelf values of 27.4 - 31.7 $mmol/kg$ (Figure 3.2a). For the outer shelf stations an OMZ is identified only overlying sediment core 23030, with those from the 20°S transect having higher dissolved oxygen concentrations ($\sim$40 $\mu mol/kg$; Figure 3.2f,g). Based on the above pore water data, it is proposed that redox conditions get less reducing with distance from shore with outer shelf sediment cores (20050, 23030, & 23060) being subject to sub-oxic conditions.

For Walvis Ridge samples multiple pore water Fe and Mn peaks are identified within the core extent (Sager et al., 2023). In addition, no SO_4 depletion is observed

in the core extent (Sager et al., 2023) with literature core top pore water $[SO_4]$ values of 28.7 - 31.7 $mmol/kg$ being reported (Figure 3.2a). Finally, no OMZ is identified overlying the samples (Figure 3.2f,g). Therefore, it is inferred that Walvis Ridge samples are subject to oxic conditions.

3.5.2 Evidence for the benthic input of barium from the continental shelf

The observed increase in $[Ba]$ between stations 23005 and 23070 in waters featuring 27 to 27.5 kg/m^3 is interpreted to be caused by a benthic input of DBa as this water transits across the shelf prior to coastal upwelling (Figure 3.6). Other factors influencing $[Ba]$ variance between inner and outer stations in upwelled water should also be considered. An external Ba flux from continental sources such as rivers or aeolian input may also elevate $[Ba]$ levels at inner shelf stations. However, the Namibian margin is unique among EBUS locations due to its arid conditions with only two major perennial rivers (Kunene and Orange) providing limited detrital input to coastal waters (Bremner and Willis, 1993; Vermeesch et al., 2010; Garzanti et al., 2012; Vermeesch et al., 2017). In addition, delivery of Ba to the ocean by aerosol deposition is negligible and the soluble fraction is only expected to impact, if at all, the surface waters (Desboeufs et al., 2024). As such, the contribution of $[Ba]$ from river and aeolian sources to seawater overlying the continental shelf is unlikely to cause the observed changes in $[Ba]$ between outer shelf and inner shelf stations.

Temporal and/or spatial variability in the Ba concentration of regional water masses supplying the upwelling centre could be an alternative explanation to the observed Ba increase. However, literature data suggests that waters from this depth range are homogeneous at a basin scale, ruling out this interpretation (Delvaux, 1991; Summerhayes et al., 1995; Hutchings et al., 2009; Blamey et al., 2012; Horner et al., 2015; Bates et al., 2017; Hsieh and Henderson, 2017; Koseki et al., 2019).

Therefore, based on the above discussion it seems most probable that benthic inputs of Ba from continental margins are the cause of significant enrichment of seawater $[Ba]$ at inner shelf stations within the recirculated water mass. This is supported in that, at the BUS, benthic inputs of other trace metal species have been identified and confirmed e.g. Fe (Noble et al., 2012; Böning et al., 2020; Hunt et al., 2022; Liu et al., 2022), Mn (Noble et al., 2012; Liu et al., 2022; Chen et al., 2024b), Al (Chen et al., 2024b), nickel (Liu et al., 2022; Chen et al., 2024a), cobalt (Noble

et al., 2012; Chen et al., 2024b), uranium (Abshire et al., 2020; He et al., 2021), molybdenum (He et al., 2021), copper (Chen et al., 2024a), cadmium (Chen et al., 2024a), and zinc (He et al., 2023; Chen et al., 2024a) and that Ba benthic inputs are common in other continental margin settings (Paytan and Kastner, 1996; Rahman et al., 2022; Whitmore et al., 2022).

3.5.3 The drivers of the identified benthic flux

At all sites measured pore water $[Ba]$ is one order of magnitude greater than the measured $[Ba]$ of bottom seawater samples thus driving a diffusive flux from the sediments to bottom waters and the identified benthic input (Figure 3.5a,c). Within the measured sample set the biggest diffusional gradients, and thus largest benthic input, are observed in marine sediment cores that are located on the inner continental shelf (20010 & 23010) where pore water $[Ba]$ is 3-6 times greater than other marine sediment cores (Figure 3.5c). These elevated pore water $[Ba]$ correspond to depletions in $[SO_4]$, with a negative correlation existing between pore water $[Ba]$ and $[SO_4]$ (Figure 3.4a,d). These observations are interpreted to reflect that Ba diffusive fluxes are principally controlled by $BaSO_4$ solubility that is driven by $[SO_4]$ reduction (Equation 9). The $BaSO_4$ saturation index for the marine sediment core is modelled by:

$$\mathrm{SI} = \frac{\mathrm{Q}}{\mathrm{K_{sp}}} \qquad \{9\}$$

Where SI, Q and K_{sp} denote the saturation index of $BaSO_4$, the Ba-SO_4 ionic product ($m_{Ba^{2+}(aq)} * m_{SO_4^{2-}(aq)} * \gamma^2_{BaSO_4(aq)}$; being the respective total (measured) molalities of the ions and the $BaSO_4$ activity coefficient, 0.144, at 1°C and 50 MPa (Monnin, 1999; Monnin et al., 1999), respectively), and the $BaSO_4$ solubility product at equilibrium constant ($10^{-9.957}$; Monnin (1999)). The molarity of ions is converted to molalitiy using $m = M/density$ where: M is the molarity in moles/L and density is the density of the solution in kg/L (here: average seawater density of 1.027 kg/L; Schlitzer et al. (2018)). Barite is undersaturated in the cores that feature seawater $[SO_4]$, which is consistent with observations for other seawater and pore water settings (Church and Wolgemuth (1972); Monnin et al. (1999); Figure 3.8). Pore waters are generally oversaturated compared to seawater, with lower $[SO_4]$ and higher $[Ba]$ (Figure 3.8). This is interpreted to reflect that SO_4 depletion promotes Ba release via $BaSO_4$ dissolution to shift towards $BaSO_4$ saturation, as previously identified by Monnin et al. (2001). This suggests in anoxic sediments where SO_4

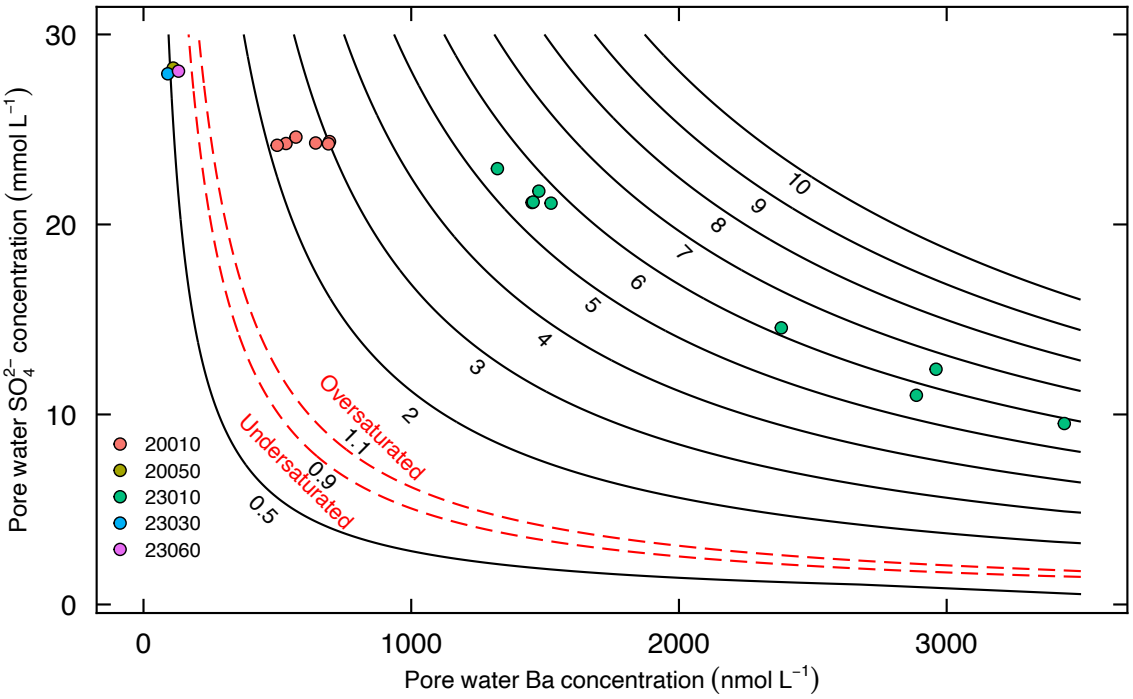

Figure 3.8: Relationship between pore water Ba and SO_4 concentrations. Contours show $BaSO_4$ saturation indices calculated using Equation 9 using the values of $10^{-9.957}$ and 0.144 for the $BaSO_4$ solubility product and activity coefficient of $BaSO_4$ at 1°C and 50 MPa, respectively (Monnin, 1999). The red lines of saturation index values equal to 0.9 and 1.1 mark the zones of undersaturation and oversaturation (Monnin et al., 1999).

becomes depleted by SO_4 reduction the dissolution of $BaSO_4$ is promoted, releasing large amounts of Ba from the solid phase back into the pore water. Marine sediment cores with the greatest pore water SO_4 depletion relative to seawater are located on the inner continental shelf (20010 & 23010), where the highest DBa concentration is measured in both the pore water and overlying water column, coinciding with the area of greatest benthic input. Therefore, it is proposed that Ba diffusive fluxes are controlled by $BaSO_4$ solubility driven by SO_4 reduction, which is linked to the distribution of the OMZ. Finally, the oversaturation of these cores is hypothesised to be due to complicated time-dependent redox conditions and the cores not having achieved steady-state (Figure 3.4).

The remobilised pool of Ba, derived from the diagenetic alteration of authigenic $BaSO_4$, indicates that Ba benthic inputs are part of the internal cycling of the global marine Ba mass balance and not a source of new Ba. This is opposite to previous categorisation and would account for the large, unknown fluxes of Ba that are entering the ocean from continental shelves (Rahman et al., 2022; Whitmore et al., 2022). It has been previously identified that the likely source of the imbalance to the marine Ba mass balance is the uncertain nature of shelf sediment inputs (Zhang et al., 2023). By defining Ba benthic inputs as part of the internal 'recycling' Ba budget would reduce the observed two-thirds imbalance between inputs and outputs and bring the marine Ba mass balance further into alignment (Horner and Crockford, 2021).

3.5.4 Constraining the Ba isotopic composition of the observed benthic fluxes

The isotopic composition of benthic inputs can be further constrained by comparing to overlying measured seawater $\delta^{138/134}Ba$ values. The impact of shelf sediment Ba benthic input on seawater $[Ba]$ and $\delta^{138/134}Ba$ values, and extent required to explain the observed variance, can be quantified using an isotopic mass balance (Equation 10 & 11).

$$[Ba]_{shelf\ seawater} = [Ba]_{pre} + [Ba]_{benthic\ input} \quad \{10\}$$

$$\delta^{138/134}Ba_{shelf\ seawater} = \delta^{138/134}Ba_{pre} * f_{pre} + \delta^{138/134}Ba_{benthic\ input} * f_{benthic\ input} \quad \{11\}$$

Where the subscripts 'shelf seawater', 'pre', and 'benthic input' denote the $[Ba]$ and $\delta^{138/134}Ba$ of the seawater after circulating over the continental shelf and the components of its dissolved Ba budget derived from initial seawater ('pre') and benthic inputs respectively. In equation 11 f_{pre} and $f_{benthic\ input}$ represent the fraction of the Ba from the 'preformed' and 'benthic input' reservoirs respectively (e.g. $f_{pre} = [Ba]_{pre}/[Ba]_{shelf\ seawater}$, where $f_{pre} + f_{benthic\ input} = 1$).

Based on the regeneration mass balance (Equations 10 & 11), the isotopic data for samples measured in waters featuring 27 to 27.5 kg/m^3 can be feasibly explained by the benthic input of Ba with $\delta^{138/134}Ba \approx +0.30‰$ (Figure 3.9a). Although there is a noticeable difference in dissolved seawater $[Ba]$ due to benthic input, the relative fractional increases (i.e. changes in $f_{benthic\ input}$) are minimal at 0.06 to 0.13, which reduces the sensitivity of this mass balance for constraining $\delta^{138/134}Ba_{benthic\ input}$ (Figure 3.9b). Core top pore water $\delta^{138/134}Ba$ values offer an alternative constraint on $\delta^{138/134}Ba_{benthic\ input}$ assuming there is no isotope fractionation associated with the flux of this Ba across the SWI. Notably, average core top pore water from cores 20010 and 23010 are consistent with the $\delta^{138/134}Ba_{benthic\ input}$ value constrained by the seawater mass balance ($\delta^{138/134}Ba \approx +0.31 \pm 0.02‰$ (±2SE, n = 13)) justifying the proposed benthic input isotopic composition.

The constrained value of $\delta^{138/134}Ba_{benthic\ input}$ is offset to higher values relative to the marine sediments ($\delta^{138/134}Ba \approx +0.09 \pm 0.01‰$ (±2SE, n = 46)), indicating a preferential remobilisation of the heavier Ba isotopes back to the overlying water column. This reflects an isotope fractionation between co-located pore water and sediment samples of $\Delta^{138/134}Ba_{sediment-pore\ water}$ = -0.18 ± 0.03‰ (±2SE, n = 17) which is consistent with literature observations from other settings (Middleton et al., 2023a; van Zuilen et al., 2023). Recent studies have shown that this isotope fractionation is related to ion exchange processes between Ba in pore waters and $BaSO_4$ in marine sediments (Middleton et al., 2023a; van Zuilen et al., 2023).

3.5.5 Mass balance considerations on the loss of isotopically heavy Ba from reducing sediments

The preferential remobilisation of heavier Ba isotopes to the water column implies a preferential burial of lighter Ba isotopes along anoxic continental shelves. Inner shelf sediment $\delta^{138/134}Ba$ are offset to lower values (+0.06 ± 0.01‰ (±2SE, n = 30)) and are significantly different compared to those on the outer shelf and Walvis

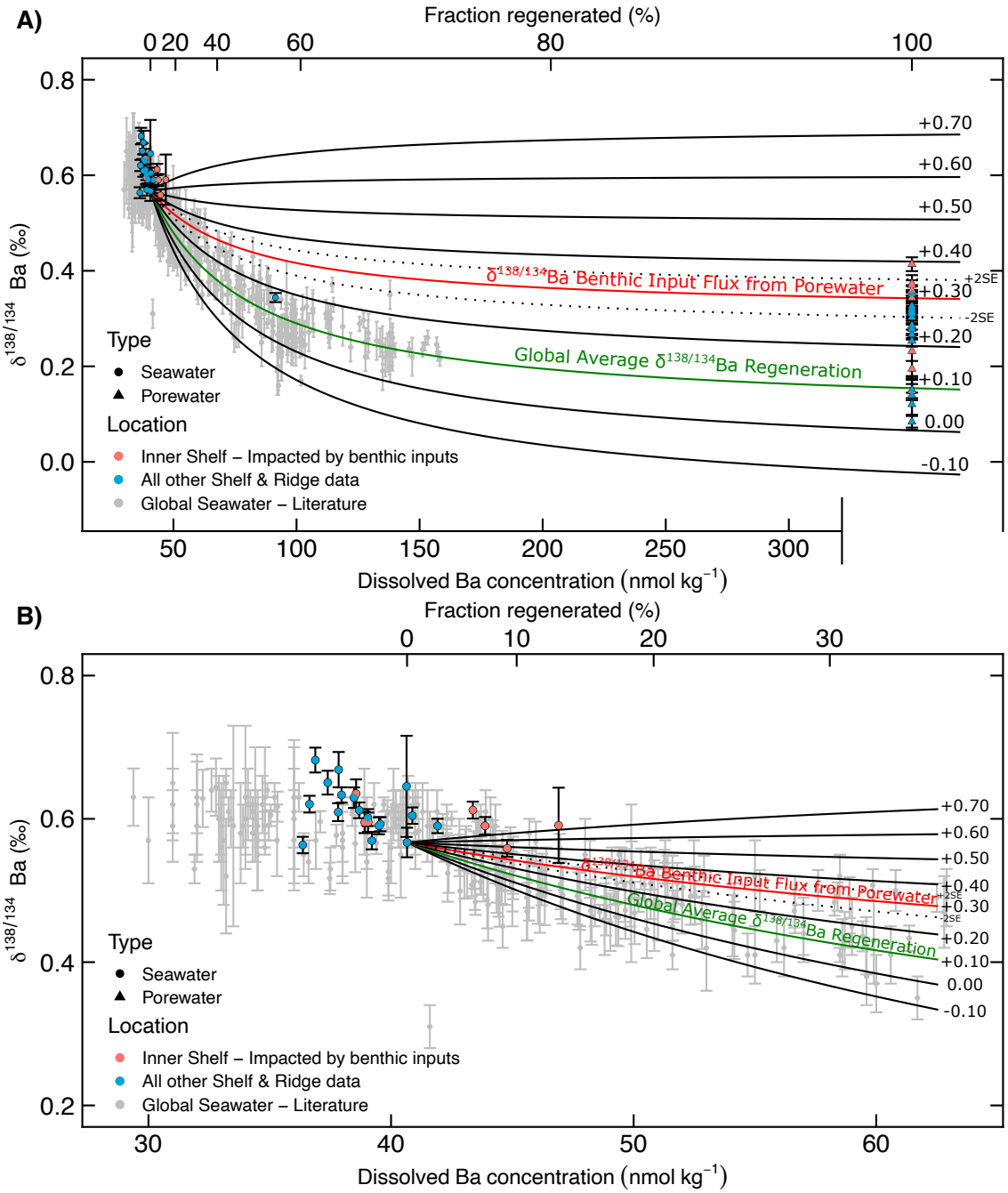

Figure 3.9: The relationship between $[Ba]$ and $\delta^{138/134}Ba$ values for seawater samples. Black curves represent the array of benthic input $\delta^{138/134}Ba$ values used to predicted the regenerated seawater fraction, calculated using a mass balance framework (Equation 10 & 11). a) Seawater samples overlying the inner shelf do not fall on the global average seawater regeneration line but fall along a regeneration curve of $\sim +0.30‰$, consistent with inner shelf $\delta^{138/134}Ba$ pore water values. b) A zoom-in of panel of the dissolved seawater data presented in subplot a. Changes in DBa concentration between those impacted by benthic input and those not are minimal. Global seawater dataset was compiled from Horner et al. (2015); Bates et al. (2017); Hsieh and Henderson (2017); Bridgestock et al. (2018); Hemsing et al. (2018); Geyman et al. (2019); Cao et al. (2020); Yu et al. (2022); Middleton et al. (2023a); Zhang et al. (2023).

Ridge (+0.15 ± 0.01‰ (±2SE, n = 16); t(8.6272) = -4.5999, p = 0.001442), despite there being no significant difference between the overlying surface waters (t(5.2269) = 1.5338, p = 0.1832; Figure 3.10). This difference could be interpreted to reflect the consequences of preferential remobilisation of heavier Ba isotopes from the anoxic inner shelf. However, this observed spatial gradient in sediment $\delta^{138/134}Ba$ is best explained by mixing between authigenic and detrital Ba end-members given the relationship between sediment $\delta^{138/134}Ba$ and Ba_{excess} (Figure 3.7d). Direct observational evidence of changes in $\delta^{138/134}Ba$ of authigenic Ba in the inner shelf cores due to diagenetic Ba remobilisation is unfortunately obscured by the high detrital Ba (∼5.6 - 95%) to these sediments.

Given the lack of direct observational evidence of authigenic $\delta^{138/134}Ba$ values in inner shelf sediments, the likely compositions of this burial flux are estimated using mass balance constraints. The fraction of Ba that is remobilised and the fraction that is buried can be quantified using a secondary isotopic mass balance (Equation 12 & 13).

$$[Ba]_{system\ input} = [Ba]_{residual} + [Ba]_{remobilisation} \quad \{12\}$$

$$\delta^{138/134}Ba_{residual} = \frac{\delta^{138/134}Ba_{system\ input} - (\delta^{138/134}Ba_{remobilised} * f_{remobilised})}{1 - f_{remobilised}} \quad \{13\}$$

Where the subscripts 'residual', 'system input', and 'remobilised' denote the buried sediment that remains unaltered, input to the system ergo the suspended particulate isotopic composition ($\delta^{138/134}Ba \approx +0.21 \pm 0.07$‰ (±2SE, n = 5)), and the remobilised sediment, respectively. In equation 13, $f_{remobilised}$ represents the fraction of the Ba from the 'remobilised' reservoir (e.g. $f_{remobilised} = [Ba]_{remobilised}/[Ba]_{system\ input}$). It is acknowledged that the data for the suspended particulate samples is of questionable quality based on the relatively low yield to certified values (56.8% - 76%; CRM BCR-414) and a discrepancy within data derived from TIMS vs ICP-MS instruments (71.5% agreement). Using the $\delta^{138/134}Ba$ from the measured pore waters impacted by diagenesis and resulting regeneration curve from previous seawater regeneration mass balance can provide an independent constraint of +0.31‰ for the isotope composition of the remobilised flux. Within these constraints, the isotopic composition of the buried sediment (i.e. $\delta^{138/134}Ba_{residual}$) is predicted as a function of changes in $f_{remobilised}$ (Figure 3.11a,b). The $\delta^{138/134}Ba_{residual}$ is predicted

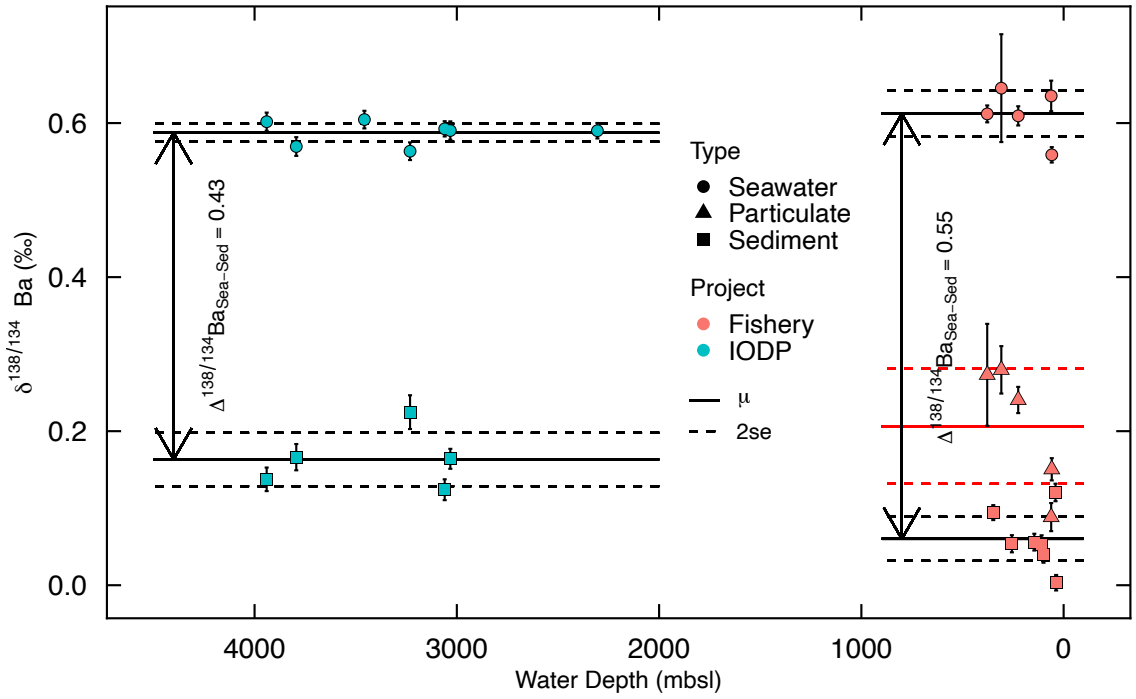

Figure 3.10: Surface sediment, pore water and suspended particulate $\delta^{138/134}Ba$ data across the Namibian continental shelf (red points) and slope (blue points). Black solid and dashed lines represent the average and 2SE for seawater and sediment samples. The difference between average surface sediment ('Sed') and seawater ('Sea') $\delta^{138/134}Ba$ values is greater in the inner shelf dataset compared to continental slope (black arrows). Average suspended particulate $\delta^{138/134}Ba$ data (red mean and 2SE lines) are not significantly different to continental slope surface sediment and are isotopically heavier than underlying shelf surface sediments (offset by +0.15‰).

to decrease by ∼0.11‰ with a remobilisation fraction of 50% and by up to 10.55‰ as 100% remobilisation is approached. The exact fraction of remobilisation is unknown in this dataset due to high detrital contribution and would also likely vary from location to location. Rahman et al. (2022) proposed average burial efficiencies of Ba to be ∼ 37% from a similar EBUS in the Pacific, which would result in a $\delta^{138/134}Ba$ composition of +0.02‰ for the buried sediment using the proposed mass balance (Equations 12 & 13). The exact isotopic composition of the buried sediment is thus a function of how much is remobilised and this is linked to the extent of SO_4 reduction (Figure 3.8). Therefore, it is hypothesised that increased anoxia on the continental shelves, will cause a higher percentage of authigenic Ba to remobilise, in turn decreasing the $\delta^{138/134}Ba$ value of authigenic Ba burial on continental shelves (i.e. following the green curve down, Figure 3.11a,b).

3.5.6 Implications for the global Ba mass balance

The role of shelf sediment benthic input in the global marine Ba mass balance is still unknown and currently is considered as a new, major vector in the marine Ba cycle (Rahman et al., 2022; Whitmore et al., 2022; Mete et al., 2023). However, data from this study indicate that at this location the benthic input of shelf sediments originates from the diagenetic remobilisation of Ba recently removed from the marine DBa pool, although results are limited by significant detrital mixing in the dataset. Therefore, this flux should arguably be included as an 'internal cycling' component of the global Ba mass balance rather than as an additional 'input'. By doing so the current two-thirds imbalance between flux estimates of inputs and outputs is reduced and the marine Ba mass balance is more in alignment (Table 3.1).

A key question is whether the inferred mechanism of benthic Ba flux observed by this study in the BUS, being $BaSO_4$ dissolution driven by depletion of SO_4 in core top pore waters, is also the driver behind large benthic Ba fluxes observed from other continental shelf regions (Moore and Shaw, 1998; Rahman et al., 2022; Whitmore et al., 2022). This study finds benthic Ba fluxes in the Namibian shelf are driven by $BaSO_4$ dissolution in response to SO_4 depletion in core top pore waters. This mechanism has been demonstrated in other EBUS settings where active upwelling drives anoxic pore water conditions facilitating the build-up of a remobilised pool of Ba (Vedamati et al., 2015; Burdige and Komada, 2020; García-Reyes et al., 2023). However, there is evidence that changes in $BaSO_4$ saturation, driven by SO_4 reduction cannot alone explain measured Ba fluxes (McManus et al., 1994, 1998,

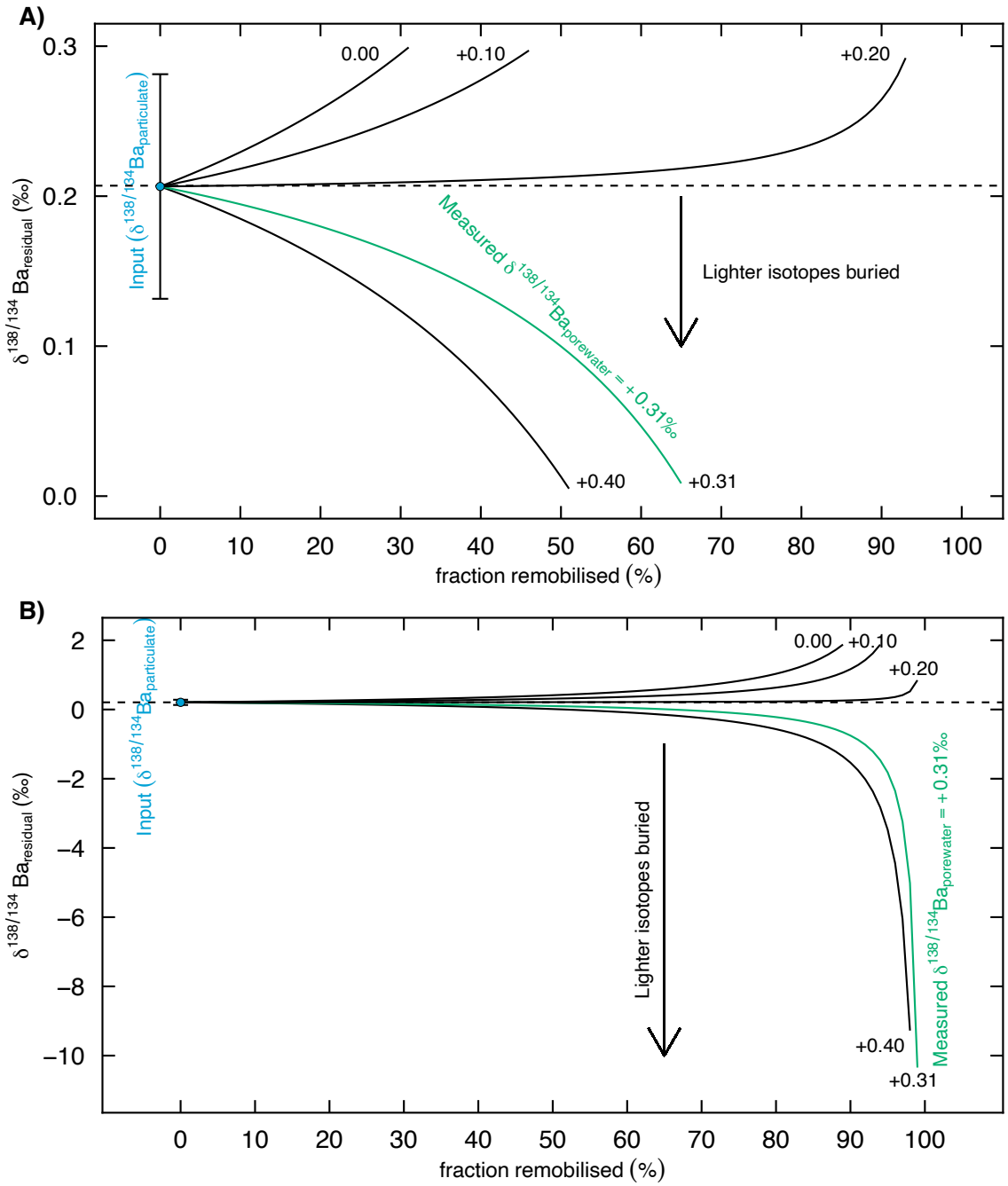

Figure 3.11: The relationship between $\delta^{138/134}Ba$ values and fraction buried vs remobilised in shelf sediment samples. Black curves represent the array of remobilised $\delta^{138/134}Ba$ values used to predicted the residual $\delta^{138/134}Ba$ composition, calculated using a mass balance framework (Equation 12 & 13). The $\delta^{138/134}Ba$ value for measured suspended particulate has been used as the input to the sediment system. The resulting $\delta^{138/134}Ba$ pore water value of +0.31‰ can be used as an approximation for the remobilised $\delta^{138/134}Ba$ composition and is coloured in green. a) Zoom-in with y-axis scaled so the smaller initial variation in $\delta^{138/134}Ba_{residual}$ can be observed. b) Larger y-axis showing the full extent of the mass balance framework and maximum potential isotopic impact due to fraction remobilised.

1999). In addition, SO_4 depletion in core top sediments in other regions is likely, either by upwelling driving anoxic pore water conditions or by a high upward diffusive or advective methane flux via biogenic/thermogenic sources or the dissociation of hydrate bodies, a common feature of continental margin settings (Rice, 1993; Xu and Ruppel, 1999; Boswell et al., 2012; Andresen, 2012; Foschi and Cartwright, 2016; Flemings et al., 2020). As such, by implication, the same conditions that lead to large benthic Ba fluxes are expected in not just other EBUS settings but at other continental margin settings globally. Large, periodic shelf sediment benthic inputs of Ba previously identified at other continental shelf and EBUS settings could be explained by anoxia driven SO_4 depletion (Moore, 1997; Shaw et al., 1998; Moore and Shaw, 2008; Rahman et al., 2022), but methane derived from melting permafrost could contribute to SO_4 reduction via AOM (Whitmore et al., 2022). Finally, the seasonal nature of upwelling is expected to drive temporal changes in the redox conditions in sediments at EBUS, resulting in a seasonal flux of shelf sediment benthic input (Chapman and Shannon, 1987; Díaz-Ochoa et al., 2011; Abshire et al., 2020; Rixen et al., 2021).

Previous studies have noted that the Ba inputs to the ocean appear to be systematically offset to higher $\delta^{138/134}Ba$ values compared to burial in open ocean sediments (Horner and Crockford (2021); Figure 3.12). The total isotope composition of the summed inputs can be determined based on both the isotope composition of each input, and their respective flux weighted fraction (Equation 14).

$$\delta^{138/134}\mathrm{Ba}_{\text{total input}} = \sum_{i=1}^{n} \delta^{138/134}\mathrm{Ba}_{\text{input(i)}} \cdot \mathrm{f}_{\text{input(i)}} \qquad \{14\}$$

Where $\delta^{138/134}Ba_{input(i)}$ is the $\delta^{138/134}Ba$ of each individual component, and $f_{input(i)}$ is the fraction of the total flux that this individual component represents. The individual data points for each component, and the mean and uncertainty for each, are presented in Table B.9 and Table 3.1, respectively. By categorising shelf sediment benthic input as an internal component of the marine mass balance, a total input flux of 20.1 ± 15.31 $Gmol.yr^{-1}$ is calculated associated with an isotopic composition of $\delta^{138/134}Ba_{total\ input} \approx +0.16 \pm 0.98‰$ ($\pm 2\sigma$; Appendix Section B.3)(Equation 14; Bridgestock et al. (2021a,b); Cao et al. (2021); Zhang et al. (2023); Mayfield et al. (2021); Hsieh et al. (2021); Zhang et al. (2024)). As such, Ba inputs to the ocean appear to be systematically offset to higher $\delta^{138/134}Ba$ values compared

to burial in open ocean sediments (Figure 3.12).

New constraints on the $\delta^{138/134}Ba$ values of continental shelf benthic inputs and burial of authigenic Ba on continental shelves presented in this study can be used to advance this debate. If the benthic input from shelf sediments does represent a new input of Ba, rather than a part of the internal Ba cycle as suggested here, then this would further re-enforce this offset ($\delta^{138/134}Ba \approx +0.30‰$, heavier than output in open ocean sediment burial; Figure 3.12). Therefore, this study proposes that benthic input from shelf sediments is likely an internal component but needs validation from other settings. In addition, the burial of Ba shelf sediments is poorly constrained in both the magnitude of its flux and its isotope composition. However, results from this study indicate it is likely to feature $\delta^{138/134}Ba$ values of less than $+0.21 \pm 0.07‰$ ($\pm$2SE, n = 5), due to preferential remobilisation of heavier Ba isotopes. Therefore, the burial of Ba on continental shelves is unlikely to be the missing flux required to reconcile the observed imbalance between the observed flux estimate inputs and outputs $\delta^{138/134}Ba$ values in the marine Ba mass balance, as it would need to feature higher $\delta^{138/134}Ba$ values to bring the observed flux estimate inputs and outputs into balance.

If the preferential remobilisation of heavier Ba isotopes and the burial of lighter Ba isotopes were a global phenomenon, it would have significant implications for interpreting paleo records of Ba isotopes. Firstly, it would be expected that sediment $\delta^{138/134}Ba$ values would shift to lighter values during periods of ocean anoxia. This would have implication for previous interpretations of $\delta^{138/134}Ba$ records as indicators of productivity change during past warm intervals, such as the Paleocene-Eocene Thermal Maximum (PETM), where measured changes in $\delta^{138/134}Ba$ may not be productivity driven but have shifted due to anoxia-driven diagenetic remobilisation and yet to locally reset (Bridgestock et al., 2019). Therefore, caution must be held when choosing sample sites for paleo Ba studies and other redox proxies must be used in conjunction to ascertain the degree of redox and $BaSO_4$ saturation state of the ocean, such as Ba/Sr ratios (Bridgestock et al., 2019). Secondly, changes in the extent of seafloor anoxia could result in changes in the release of heavy Ba isotopes to the overlying ocean, causing complementary increases in light Ba isotopes to be buried on shelves. If this were to occur globally, the mechanism that increased release from shelves should be balanced by an increase burial in deep ocean to maintain $BaSO_4$ saturation in ocean (Dickens et al., 2003; Paytan et al., 2007; Frieling et al., 2019).

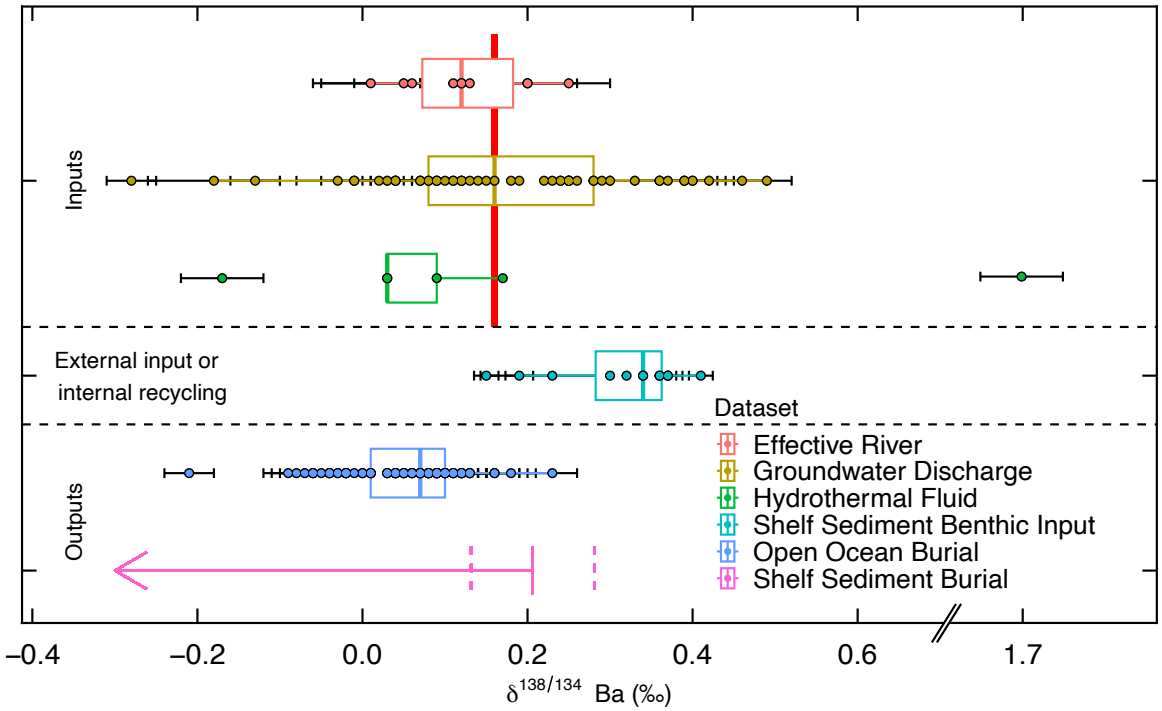

Figure 3.12: Marine Ba input-output $\delta^{138/134}Ba$ values using literature constraints (Crockford et al., 2019; Bridgestock et al., 2021a,b; Cao et al., 2021; Hsieh et al., 2021; Mayfield et al., 2021; Rahman et al., 2022; Zhang et al., 2023, 2024). Shelf sediment benthic input is placed in its own band due to undetermined role in the marine Ba mass balance. Results from this study indicate the burial of Ba on shelf sediments is likely to feature $\delta^{138/134}Ba$ values of less than +0.21 ± 0.04‰ (±2SE, n = 5; pink lines). The isotopic composition of the total input fluxes, +0.16 ± 0.98‰ (±2σ)) is calculated using Equation 14 and is displayed as a red line. The associated error is not shown due to axis extent. Data used to generate this plot are provided in Table B.9.

This would result in burying a reduced amount of lighter Ba isotopes in continental shelf settings, and switch to burying more Ba in the deep ocean with a preference for heavier isotopes (Paytan et al., 2007). This would cause further complication to balance the marine Ba mass balance and create uncertainty in interpreting paleo records of Ba for use as a paleo proxy.

3.6 Conclusion

This study presents an initial assessment of the Ba isotopic composition of the final two remaining components of the marine Ba mass balance: heavier Ba isotopes preferentially released from continental shelves ($\delta^{138/134}Ba \approx +0.31$‰) drive the burial of a residual pool of Ba enriched in lighter isotopes. The study proposes

that the mechanism causing these identified shelf sediment benthic input, is the diagenetic remobilisation of $BaSO_4$ in marine sediments caused by changes in the $BaSO_4$ solubility, which in turn is related to bottom water anoxia. These results provide insights into how the global seawater Ba isotope inventory could be impacted by global changes in ocean redox, which should be considered when interpreting Ba isotope records in sediments. Future studies should prioritise sampling in continental shelf settings with minimal detrital contributions to marine sediments. In addition, studies are needed in a variety of other continental shelf settings to determine the global importance of the proposed mechanism for driving shelf benthic fluxes.

Re-categorising shelf sediment benthic inputs as part of the internal marine Ba cycle and providing an initial assessment for the isotopic composition of shelf sediment burial reveal that the marine Ba mass balance remains imbalanced. However large uncertainty is associated with previously recorded flux estimates and as such require refinement to reduce the imbalance. This has further implications for interpreting historic sedimentary deposits of $BaSO_4$, particularly during past climatic warming periods. Widespread suboxic conditions during these periods could lead to substantial Ba release into the water column, increasing seawater saturation with respect to $BaSO_4$ and contribute to the enhanced $BaSO_4$ burial observed during these warming periods (Paytan et al., 2007; Frieling et al., 2019; Griffith et al., 2021; Miyazaki et al., 2023).

Chapter 4

Examining the utility of barium isotopes as a tracer of large-scale seafloor methane venting

Increased sedimentary barium (Ba) burial rates have been used to determine that climate driven sedimentary methane (CH_4) release can cause large-scale global warming. Interpretations of these records are however ambiguous and as such Ba isotopes could be developed to provide added constraints. Therefore, this study aims to (1) gain first constraints on the isotopic composition of benthic Ba fluxes associated with CH_4 cold seeps to assess the utility of Ba isotopes as a tracer for the associated CH_4 release, and (2) make an initial assessment of Ba isotopes partitioning in authigenic carbonates for recording past changes in Ba cycling in cold seep settings. To achieve this, Ba concentration ($[Ba]$) and isotope data are presented for seawater samples at different altitudes above the seafloor (1 m to 60 m) and seafloor authigenic carbonate samples collected across the Regab pockmark, a methane cold seep offshore Congo Margin. The measured seawater Ba isotope values from all sites possess $\delta^{138/134}Ba$ values between +0.23‰ to +0.42‰ and dissolved $[Ba]$ values between 80.0 to 90.6 nmol/kg, which are typical of ambient seawater from this depth range. Furthermore, no difference in dissolved Ba isotopes or $[Ba]$ with altitude at each location is observed. Measured dissolved $[Ba]$ and $\delta^{138/134}Ba$ provide limited evidence of benthic Ba release associated with CH_4 venting occurring at Regab pockmark, with the new seawater data presented in this study tentatively suggesting cold seep relative benthic inputs feature $\delta^{138/134}Ba \approx$ -0.14‰, but are subjected to uncertainty. This may reflect the quantitative removal of pore water Ba by barite precipitation within the upper sediments, preventing significant Ba release to the water column. This finding consequently does not support use of sedimentary $[Ba]$ and isotope records as

a tracer of past CH_4 release events. The measured authigenic carbonate Ba isotope values possess $\delta^{138/134}Ba$ values -0.30‰ to +0.20‰, lower than measured seawater and pore water measurements. This suggests a fractionation of lighter Ba isotopes during authigenic carbonate precipitation from CH_4-rich fluids. As such, authigenic carbonate nodules record [Ba] and Ba isotope composition related to past venting activity, which could be developed to constrain the timing of past vent activity.

4.1 Introduction

Global warming has the potential to release large quantities of methane (CH_4) stored as methane hydrate from marine sediments, representing a positive carbon cycle-climate feedback (James et al., 2016). Unambiguous evidence of this feedback in the geological record will improve understanding of the potential risk it poses for exacerbating anthropogenic global warming. For example, climate driven sedimentary CH_4 release is one of the hypothesised mechanisms for the onset of the Paleocene-Eocene Thermal Maximum (PETM)(Dickens et al., 2003; Frieling et al., 2016; Haynes and Hönisch, 2020; Inglis et al., 2021; Berndt et al., 2023). Increased sedimentary barium (Ba) burial rates have been interpreted as evidence of this mechanism (Dickens et al., 2003; Frieling et al., 2019), but these records are also sensitive to other processes, such as diagenetic remobilisation (Dickens, 2001; Schenau et al., 2001; Henkel et al., 2012; Martinez-Ruiz et al., 2015; Bridgestock et al., 2019; House and Norris, 2020; Scholz et al., 2023). Stable Ba isotope variations are a new geochemical tool that may improve interpretations of such records, potentially leading to clearer geological insights into the significance of this carbon cycle-climate feedback.

At cold seep environments sedimentary CH_4 release is accompanied by variable rates of Ba discharge (Torres et al., 1996a,b; Greinert et al., 2002; Aloisi et al., 2004; Castellini et al., 2006; McQuay et al., 2008; Hanor and Mercer, 2011; Feng and Roberts, 2011). This has largely been attributed to the consumption of pore water sulphate (SO_4) during the anaerobic oxidation of methane (AOM) at the sulphate-methane transition zone (SMTZ), which is an important biogeochemical sink of SO_4 in reducing environments (Dickens, 2001; Lin et al., 2012). Here SO_4 is microbially mediated to oxidise CH_4 in a 1:1 ratio to form bicarbonate (Equation 15; Borowski et al. (1996); Niewöhner et al. (1998)).

$$CH_4 + SO_4{}^{2-} \longrightarrow HCO_3{}^{-} + HS^{-} + H_2O \quad \{15\}$$

This process promotes the dissolution of barite ($BaSO_4$) in marine sediments at cold seep environments, due to $BaSO_4$ solubility, causing $BaSO_4$ in marine sediments to become undersaturated. As a result, large amounts of dissolved Ba accumulate in the pore waters below the SMTZ (Dickens, 2001; Riedinger et al., 2006; Henkel et al., 2012). Consequently, CH_4 cold seeps are associated with variable Ba efflux, up to four times greater than non-seep environments (Torres et al., 1996b). Therefore, CH_4 venting from cold seep environments could be an important Ba input to the ocean, and this mechanism would provide a source of the Ba for the enhanced Ba burial rate observed during the PETM (Dickens et al., 2003; Frieling et al., 2019).

The impact of benthic Ba fluxes associated with CH_4 cold seeps on the global seawater Ba inventory is, however, unknown. The magnitude of this benthic input can vary due to the extent of $BaSO_4$ re-precipitation, at, or close to, the sediment water interface (SWI), where Ba-rich pore waters encounter SO_4 rich seawater (Aloisi et al., 2004). In addition, variable fluid seepage rates measured at global cold seeps impact the measured $BaSO_4$ accretion rate, and drive variation in the deep and surface measured seawater Ba flux (Aquilina et al., 1992; Dia et al., 1993; Torres et al., 1996b; Aloisi et al., 2004; Castellini et al., 2006; Hein et al., 2007; Snyder et al., 2007a; Canet et al., 2013; Stevens et al., 2015; Núñez-Useche et al., 2018; Bei et al., 2020; Zhou et al., 2022). Therefore, the amount of Ba that enters the dissolved pool of the ocean depends on both the strength of the Ba efflux and how much Ba is re-precipitated at the seafloor. However, both these attributes are variable at different cold seep settings and difficult to constrain.

Stable Ba isotope variations could be developed as a new tool to test the fidelity of Ba as a tracer of large scale CH_4 release. Seafloor hydrothermal vents, analogous to cold seeps, are also associated with a fluid efflux that is Ba rich and SO_4 poor, though the mechanism producing this efflux is different (Eickmann et al., 2014; Jamieson et al., 2016; Hsieh et al., 2021; Zhang et al., 2024). The large initial dissolved Ba input is reduced by re-precipitation as $BaSO_4$ upon mixing with seawater, leading to significant Ba isotope fractionation: greater precipitation results in a larger isotopic difference (Hsieh et al., 2021). Though the extent of dissolved Ba removal and magnitude of fractionation may be dependent on hydrothermal vent setting (Zhang et al., 2024). It is hypothesised that Ba release from CH_4 cold seeps

should exhibit similar systematics, generating distinct isotopic signatures with the potential for tracing these inputs.

Authigenic carbonates forming at cold seeps can provide an additional method of tracing past CH_4 cycling as they record fluid geochemistry and its temporal variation, given the carbonates are not recrystallised (Ruban et al., 2020; Thiagarajan et al., 2020; Wei et al., 2020; Miyajima et al., 2023). The precipitation of authigenic carbonates is caused by an alkalinity increase promoted by AOM at the SMTZ (Equation 15; Torres et al. (2020); Kravchishina et al. (2021); Loyd and Smirnoff (2022); Akam et al. (2023); Lu et al. (2023); Miyajima et al. (2023)), which in turn is related to CH_4 cycling (Borowski et al., 1996; Niewöhner et al., 1998; Dickens, 2001; Lin et al., 2012). As Ba can be incorporated into carbonate during the abiotic precipitation at or above the SMTZ, records of Ba concentration ($[Ba]$) and Ba isotope composition could reflect the source fluid at the time of precipitation. In addition, authigenic carbonates can be dated accurately using U/Pb or U/Th geochronometers making it possible to constrain the timing of past vent activity (Zhang et al., 2021; Lan et al., 2022; Li et al., 2024). As such, the $[Ba]$ and isotope composition of authigenic carbonates could provide insights into past cold seep dynamics, but in the first instance requires fundamental understanding of Ba isotope partitioning into these phases.

This study aims to (1) gain first constraints on the isotopic composition of benthic Ba fluxes associated with CH_4 cold seeps to assess the utility of Ba isotopes as a tracer for the associated CH_4 release, and (2) make an initial assessment of Ba isotopic partitioning in authigenic carbonates for recording past changes in Ba cycling in cold seep settings. To this end, dissolved $[Ba]$ and Ba isotope data are presented for seawater samples at different altitudes and for seafloor authigenic carbonate samples collected across the Regab pockmark, a CH_4 cold seep offshore Congo, in areas with varying CH_4 concentration ($[CH_4]$). Samples were collected with a remotely operated vehicle, providing a high resolution of seawater sample collection within 60 m of the seafloor.

4.2 Study area and samples

4.2.1 Scientific Background

This study focuses on the Regab, or Giant, Pockmark, an extensive pockmark about 800 m wide, located at 3150 m water-depth near the Congo submarine canyon, north side of the present-day Zaire channel (Gay et al., 2006; Lemaitre et al., 2014). The Regab pockmark was initially investigated during the ZAIANGO project (1998 – 2000), utilising bathymetric–reflectivity maps and 2D high-resolution seismic profiles to further understand the Quaternary history of the Zaire fan (Savoye et al., 2000). Subsequent expeditions further examined this site, and the entire extent of the pockmark has been mapped along with multiple gas, fluid, and rock sampling expeditions (Ondréas et al., 2005; Ristova et al., 2012; Lemaitre et al., 2014).

Since the Quaternary period, the Congo submarine canyon has served as a direct conduit for sediment transport from the continent to the deep-sea basin via the Congo River producing a direct source-to-sink route (Babonneau et al., 2002). It contributes significant quantities of organic-rich sediments to the entire Congo submarine system (Baudin et al., 2010). Other deposition in this region primarily consists of fine sediments not confined to the Zaire channel, likely originating from riverine plumes and contour currents. These sediments are mixed with hemipelagic sediments, derived from active upwelling driving high rates of surface primary productivity, and subsequently deposited on the continental slope through processes such as sedimentation by aggregates and faecal pellets (Rogers and Bremner, 1991; Berger et al., 2002a; Awo et al., 2022; Martins and Stammer, 2022; Hunt et al., 2022). As such, high accumulation rates of organic material, and authigenic $BaSO_4$, are delivered to the seafloor (Dehairs et al., 1980; Baudin et al., 2010; Schnyder et al., 2017; Baudin et al., 2020; Hussain and Al-Ramadan, 2022; Hage et al., 2024). The progressive accumulation of organic rich sediments overtime promotes methanogenesis and the subsequent migration of CH_4-rich fluids via stratal and cross-stratal structures is observed along the Congo Margin (Rice, 1993; Gay et al., 2006, 2007; Hong et al., 2013; Foschi and Cartwright, 2016).

Active seafloor venting of CH_4-rich gases and fluids is commonly observed along the Congo Margin, Gulf of Guinea, and similar continental margin settings, identified through seismic acoustic backscatter data (Orange et al., 2002; Pierre and Fouquet, 2007; Ho et al., 2012; Wenau et al., 2015). This phenomenon is often associated with

the formation of pockmarks at the seabed surface, indicating the rapid expulsion of migrating fluids (Foschi and Cartwright, 2016; Løseth et al., 2011). Pockmarks are found typically at the upper termini of pipes and can serve as indicators of recent active venting (Eruteya et al., 2018). Along the Congo Margin, especially within the Lower Congo Basin where the Regab pockmark is located, pockmarks are not randomly distributed, but are always associated with fault zones, salt diapirs or a bottom-simulating reflector (BSR), suggesting the presence of gas hydrates (Gay et al., 2003).

The origin of CH_4-rich fluids at Regab pockmark is attributed to the buried palaeo-channel of the Congo River. Previous seismic surveys show the Regab pockmark appears to take root via a pipe at the northern flank of the channel–levee interface of the shallow buried paleochannel (Gay et al., 2003). A paleo-pockmark is observed on the adjacent southern flank but is sealed at depth (Gay et al., 2006). Active CH_4 venting is sustained by a relict of biogenic fluid entrapped within the channel that continuously supplies CH_4 (Gay et al., 2003; Charlou et al., 2004). As a result, the Regab pockmark exhibits intense CH_4 seepage and features gas hydrates, substantial authigenic carbonate deposits, and abundant living or dead chemosynthetic communities within the small coalescent depressions across the pockmark (Ondréas et al., 2005; Charlou et al., 2004; Pierre and Fouquet, 2007; Gay et al., 2006; Roy et al., 2007; Olu et al., 2009; Marcon et al., 2014; Duperron et al., 2014; Wenau and Spiess, 2018).

Seawater measurements reveal variable dissolved $[CH_4]$ across the extent of the pockmark, which could suggest that the source of venting moves around laterally or that the fluid leakage is episodic (Gay et al., 2006). During all previous sampling campaigns, the highest $[CH_4]$ in water overlying the seafloor at Regab pockmark (up to 130 $\mu l/L$) is observed at the centre of the pockmark indicating a central CH_4 leakage point (Charlou et al., 2004; Gay et al., 2007; Lemaitre et al., 2014). Methane hydrate deposits have also been identified outcropping at the seafloor, overpowering sulphate-reduction and shoaling the SMTZ at the seafloor, at the centre of the pockmark further supporting the current central leakage point (Emeis et al., 2004; Castellini et al., 2006; Gay et al., 2006). The variable measured $[CH_4]$ dynamics present at Regab pockmark are consistent with other active venting sites located along the northern Congo Margin (Sahling et al., 2008; Pierre et al., 2012).

Finally, the generation of diagenetic $BaSO_4$ fronts has been observed in the sediments of cold seep environments along the Congo Margin, including at Regab pockmark (Nöthen and Kasten, 2011; Kasten et al., 2012; Pierre and Fouquet, 2007). This feature is also common in continental slope settings along the Congo Margin where deep water anoxia is present indicating that the diagenetic remobilisation of $BaSO_4$ must be occurring (McManus et al., 1994; Dickens, 2001; Riedinger et al., 2006; Castellini et al., 2006; Henkel et al., 2012).

4.2.2 Types of Samples Used in the Study

Seawater and authigenic carbonate rock samples analysed in this study were collected in January 2011 during cruise transects on R/V *Pourquoi Pas?* as part of the West Africa Cold Seeps (WACS) cruise programme (Olu, 2011; Lemaitre et al., 2014; Guillon et al., 2017; Rabouille et al., 2017). A total of eighteen seawater samples were measured for dissolved $[Ba]$ and isotope compositions in this study, taken from three vertical water-column profiles, that cover the entire extent of the Regab pockmark to capture a variety of oceanographic regimes with different, qualitative CH_4 release (Figure 4.1). This ranged from (1) a highly active site of gas venting in the centre of the pockmark (hereafter referred to as the 'Bubble' site); (2) an active venting area of less intensity in the eastern part of the pockmark (East Pockmark Site); and (3) a reference site 0.6 km outside of the pockmark, where no CH_4 venting was observed. The selection of samples sites was derived from a previous ROV survey, during which bottom water samples were collected and analysed for $[CH_4]$, with $[CH_4]$ of approximately 130 $\mu l/L$, 17 $\mu l/L$, and 0.05 $\mu l/L$, at the proposed sites respectively (Charlou et al., 2004). Despite the bottom water sample at the reference site possessing significantly lower CH_4 content, this value is greater than typical deep-water CH_4 background levels in the Atlantic Ocean (6–8 nl/L; Lamontagne et al. (1973)), implying the influence of methane plumes from Regab at this location. Seawater was additionally collected across the pockmark in areas overlying different macrofaunal assemblages: vesicomyid clams, mussels (two sites) and microbial mats. Finally, two surface seawater samples were measured for comparison and are located on the Congo Margin and Gabon margin. For context, global seawater $[Ba]$ and isotope compositions previously reported in various studies have been incorporated into analyses (Horner et al., 2015; Bates et al., 2017; Hsieh and Henderson, 2017; Bridgestock et al., 2018; Hemsing et al., 2018; Geyman et al., 2019; Cao et al., 2020; Yu et al., 2022; Middleton et al., 2023a; Zhang et al., 2023). In addition, four seafloor authigenic carbonate nodules were collected within the pockmark extent:

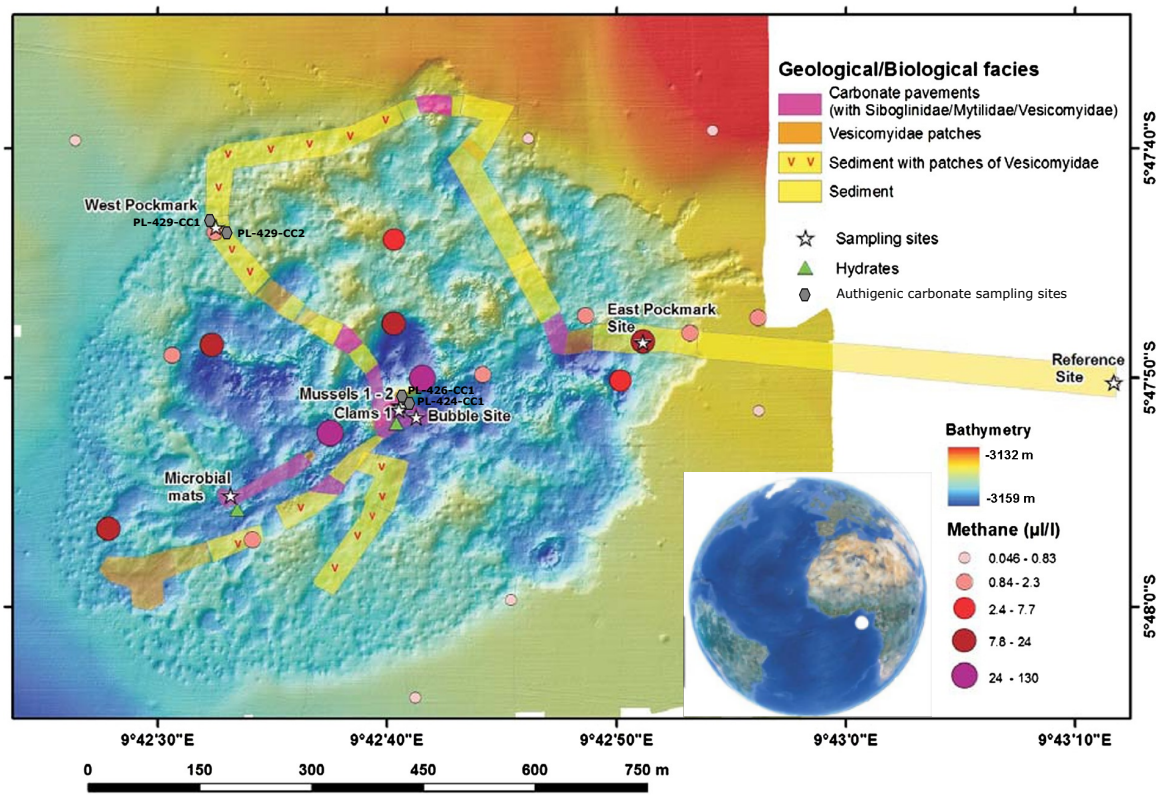

Figure 4.1: Location map adapted from those published in Lemaitre et al. (2014). Microbathymetric map of the Regab pockmark showing the location of sampled water sites and the distribution of seafloor habitats and carbonate-paved areas, as inferred from ROV observations during the WACS cruise (2011). The distribution of $[CH_4]$ in water overlying the seafloor by +1 to +2 metres are also displayed, determined during the ZAI-ROV project (2000)(Charlou et al., 2004). Permission has been granted by Elsevier to reprint this figure for use in this thesis. This figure was originally published in 'Trace element behaviour at cold seeps and the potential export of dissolved iron to the ocean', Earth and Planetary Science Letters, Volume 404, 2014, Pages 376-388, Lemaitre et al., Figure 2, copyright Elsevier.

two located at the Bubble Site, where the greatest degree of CH_4 venting is observed (130 $\mu l/L$), and two located at West Pockmark Site, where a lesser degree of CH_4 venting occurred (0.84 - 2.3 $\mu l/L$). Authigenic carbonate samples were requested from the Marine Geological Samples Repository of Brest (IFREMER). All collected samples were taken forward for both major and minor concentration and Ba isotopic composition determination. A detailed list of samples and localities is presented in Table C.1.

4.2.3 Sample collection methods

Seawater samples were collected with a remotely operated vehicle (ROV), providing a high resolution of sample collection within 60 m of the seafloor, spanning areas of varying CH_4 venting fluxes (Olu (2011); Lemaitre et al. (2014); WACS cruise dive and sample logs available at DOI 10.17600/11030010). The ROV was attached with an automated PEP system (Prélèvement d'Eau par Pompage - a system pumping water from the ROV), which allowed sampling of twelve individual acid-cleaned 2 L plastic bottles during each ROV dive. The two surface seawater samples were taken directly using acid-cleaned Nalgene high-density polyethylene (HDPE) bottles. Aliquots of all samples were then filtered on board onto <0.45 μm cellulose filters. Filtered samples were then directly transferred into acid-cleaned HDPE Nalgene bottles, and further acidified on board with twice subboiled nitric acid to pH $\sim$ 2.

Authigenic carbonate samples were collected using ROV techniques, where direct sampling of the carbonate crust was performed using the ROV arm attachment. The samples were then stored in clean, sealed bags upon retrieval. Samples were then split along the primary axis for fresh surface and three representative zones in each sample were drilled using a high precision micro-drill to generate powdered carbonate sample.

4.3 Analytical Techniques

Initial dissolved $[Ba]$ for the seawater samples were determined with a quadrupole X-Series II ICP-MS after sample dilution (30-fold) with 2% Ultrex II nitric acid at the University of Brest by Dr Nolween Lemaitre. Elemental concentrations were calculated by external calibration. The concentrations for other trace elements, i.e. iron and manganese (Fe and Mn, respectively), were determined by sector field ICP-MS (Element2) and methodology is further described in Lemaitre et al. (2014).

To isolate the Ba and other trace metals within the carbonate phase of the collected authigenic carbonate samples, the samples were first split, polished and drilled at National Taiwan University (NTU), Taipei, Taiwan, to obtain fresh, unaltered powdered sample. After which, a sequential leaching technique with dilute acid was applied to the powdered samples (Miyajima et al., 2023). Three sub-samples were taken from each carbonate sample for coherency (Figure C.1). To determine the bulk fraction of each sample, 0.1 g of powdered sample was dissolved

in 2 ml 6 M ultrapure HCl overnight at room temperature after 15 minutes of ultrasonic agitation. For carbonate leaching, another 0.1 g of powdered sample was first ultrasonically washed with Milli-Q water for 15 minutes in ultrasonic agitation and stored overnight at room temperature. After centrifugation and removal of the supernatant, the washed sample was sequentially leached four times with the addition of 5 ml of 0.1 M ultrapure HCl, ultrasonically for 15 minutes, and then supernatant discarded after 15 minutes of centrifugation. The second to fourth leachates (dissolving $\sim$ 40 – 80 wt% $CaCO_3$ in the sample; Miyajima et al. (2023)) were combined to obtain the carbonate fraction. Element concentration determination was performed on a quadrupole X-Series II ICP-MS at Academica Sinica, Taipei and included Ba, Fe, Mn and calcium (Ca).

Prior to Ba isotope measurements, Ba was purified from sample matrices following previously described protocols (Bridgestock et al., 2018; Hsieh et al., 2021). Following concentration determination, aliquots of the digested carbonate solutions containing $\sim$250 ng of Ba were taken and mixed with appropriate and known amounts of the ^{137}Ba–^{135}Ba double spike solution to correct for instrumental mass bias (Hsieh and Henderson, 2017). Seawater samples (50 ml, $\sim$250 ng Ba) were also spiked with a known quantity of Ba double spike solution. All samples were left to equilibrate for at least a day.

Once samples had equilibrated, 3 ml of a 0.9 M Na_2CO_3 solution were added to the seawater samples to co-precipitate the Ba with $CaCO_3$. The samples were centrifuged, and the resulting precipitate was taken forward for further analysis. All samples were then purified via cation exchange chromatography (Foster et al., 2004; Nan et al., 2015). Organics leached from the cation exchange resin were oxidised by the sequential addition and evaporation of small amounts of 7.5M HNO_3 and 9.8M H_2O_2 (Bridgestock et al., 2018). Finally, samples were dissolved in 1 ml of 2% HNO_3 solution.

The $[Ba]$ and isotope compositions of samples were determined using a multiple-collector inductively coupled plasma-mass spectrometry (MC-ICP-MS; Nu Plasma HR, Nu Instruments) at NTU with a DSN-100 desolvation system (Nu Instruments) and a C-Flow (50 $\mu L/min$) nebuliser (Savillex). The Ba isotopes ^{136}Ba, ^{135}Ba, ^{137}Ba, and ^{138}Ba were collected on the L1, C, H1, and H2 Faraday cups, respectively. Simultaneously, ^{139}La and ^{140}Ce were collected on an H3 and

L2 Faraday cup to correct for the isobaric interferences on ^{138}Ba and ^{136}Ba. Each analysis block comprised 40 cycles of data, with a 10-second integration time per cycle. Prior to and after each sample analysis, a National Institute of Standards and Technology (NIST) 3104a standard was measured, and each analysis was repeated three times for the same sample solution. To prevent potential cross-contamination, the sample introduction system was cleaned with 10% then 2% HNO_3 (m/m) for two minutes between measurements until the ^{138}Ba signal decreased to less than 10 mV. The raw isotopic ratios were processed offline to correct for instrumental mass bias and finally, data are reported in the δ-notation (‰) ($\delta^{138/134}Ba$) relative to the NIST 3104a standard (Equation 16).

$$\delta^{138/134}\mathrm{Ba} = \left(\frac{^{138}\mathrm{Ba}/^{134}\mathrm{Ba}_{\mathrm{sample}}}{^{138}\mathrm{Ba}/^{134}\mathrm{Ba}_{\mathrm{NIST3104a}}} - 1\right) \cdot 1000 \qquad \{16\}$$

The resulting dataset was further tested for validity where one select sample was measured for comparison using a Thermo Scientific TRITON Thermal Ionising Mass Spectrometer (TIMS) instrument at a separate laboratory, University of Oxford (Appendix C).

4.4 Results

All data generated in this study is reported in Table C.1.

4.4.1 Data Quality

Standards and samples typically yielded an internal precision of $\delta^{138/134}Ba$ between +0.05 and +0.19‰ (±2SE, n = 40) during each isotope analysis. Over the course of the study, SRM NIST 3104a values ranged between -0.54‰ to +0.1‰ reflecting instrumental drift. Bracketing SRM NIST 3104a measurements of each sample were used to correct for this drift. The external reproducibility and accuracy was determined by repeat measurements of a secondary Ba standard, National Bureau of Standards (NBS) NBS-127, measured throughout the sample runs. The average $\delta^{138/134}Ba$ value measured was -0.26 ± 0.09‰ (±2SD, n = 13), which agrees with published values from previous studies ($\delta^{138/134}Ba \approx$ -0.29‰; Horner et al. (2017); Crockford et al. (2019); Tian et al. (2019); Tieman et al. (2020); Hsieh et al. (2021)).

The analytical uncertainty for the samples is assigned to this level of reproducibility (± 0.09‰; 2SD) or that of the internal precision if higher than this value. The $\delta^{138/134}Ba$ of seawater samples measured on the TIMS are concordant with data generated via MC-ICP-MS further supporting the reproducibility of data generated in this study (For Bubble Site samples, TIMS derived: $\delta^{138/134}Ba \approx +0.25 \pm 0.02$‰ (±2SE, n = 1) and MC-ICP-MS derived: $\delta^{138/134}Ba \approx +0.27 \pm 0.05$‰ (±2SE, n = 2)).

The reproducibility of measured $[Ba]$ and $\delta^{138/134}Ba$ data can be tested using the three sub-samples of each authigenic carbonate. For both $[Ba]$ and $\delta^{138/134}Ba$ the maximum standard deviation obtained from all the samples was $\pm 1.96\ \mu mol/g$ and ±0.18‰, respectively (Table C.1). Therefore, it is assumed that the sub-samples are largely representative replicates of each other, and the data are reproducible. Some variance is observed in sample PL-424-CC1 with the $\delta^{138/134}Ba$ being heavier for one of the sub-samples but as the $[Ba]$ for these three sub-samples agree within 7.9% of each other it is assumed the measured $\delta^{138/134}Ba$ variance is real and could represent a non-carbonate phase being sampled and measured. In addition, the $[Ba]$ of all sub-samples was measured at two separate laboratories on different instruments: the quadrupole X-Series II ICP-MS at Academica Sinica, Taipei and on the MC-ICP-MS at NTU. The $[Ba]$ of sample PL-424-CC1 measured by both methods are within 0.67% of each other. However, all other sub-samples have $[Ba]$ that are 45% higher when measured at NTU compared to the values obtained at Academia Sinica (Figure C.2). As this variance in $[Ba]$ is consistent between all sub-samples it is attributed to Academica Sinica instrumental error in internal standard calibrations, with the $[Ba]$ data produced using MC-ICP-MS considered reliable due to the double-spiking method.

To quantify the contribution of Ba contamination incurred during both sample digestion and ion exchange chromatography, a procedural blank was included alongside each batch of samples. The procedural blank ranges between 3.5 - 13.51 ng of Ba for seawater samples and 0.58 ng of Ba for authigenic carbonate samples (Table C.3). Based on typical $[Ba]$ values measured for each sample type, the procedural blank contribution for each sample type is maximum: 5.4% for seawater samples and 0.23% for authigenic carbonate. This observed difference is attributed to either (1) the additional co-precipitation step required when processing the seawater samples, with Ba blank introduced in the $NaCO_3$ solution, or (2) seawater samples not being

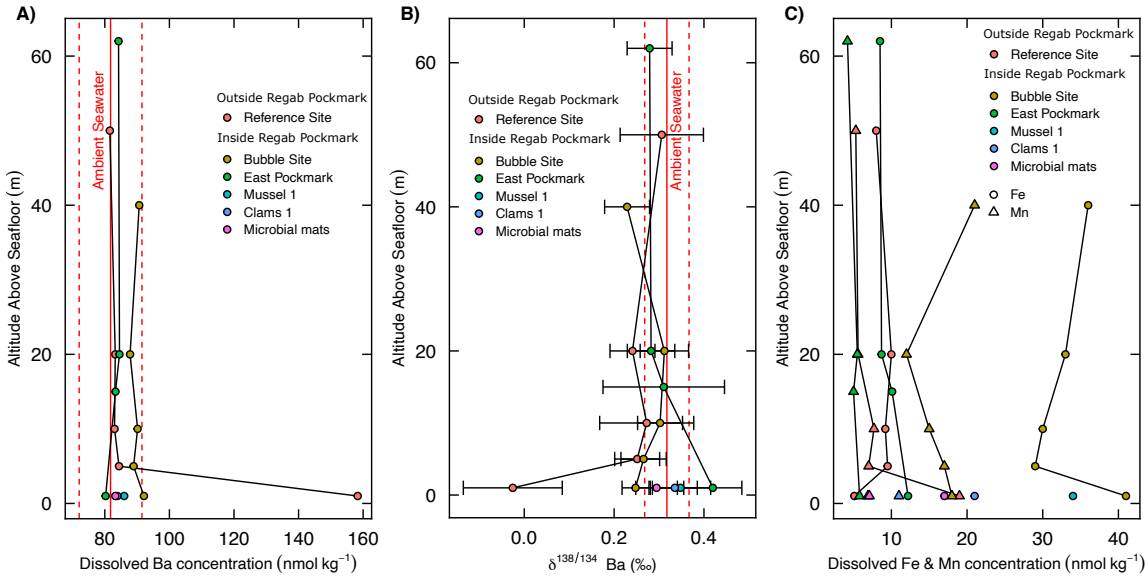

Figure 4.2: $[Ba]$ and $\delta^{138/134}Ba$ values generated in this study. a) Dissolved seawater $[Ba]$ against depth above seafloor and b) measured $\delta^{138/134}Ba$ against depth above seafloor. Red solid and dashed lines represent the ambient seawater values and associated error (South Atlantic water samples with a similar water mass *in situ* density anomaly - 42.0 kg/m^3). c) Dissolved $[Mn]$ and $[Fe]$ against depth above seafloor. Both dissolved $[Fe]$ and $[Mn]$ measured here are 2 - 33 times greater than ambient seawater values (1.23 $nmol/kg$ & 0.415 $nmol/kg$, respectively; Lin et al. (2022)). Dissolved $[Fe]$ and $[Mn]$ are published in Lemaitre et al. (2014).

maintained in a clean environment during processing due to laboratory failures. As such, blank contributions were determined to be negligible.

4.4.2 Seawater distribution of dissolved Ba concentrations and isotope compositions

All seawater samples measured within 60 m of the seafloor, except the reference site sample at 1 m altitude, have similar dissolved $[Ba]$ values ranging from 80.2 to 92.1 $nmol/kg$ (Figure 4.2a) and possess $\delta^{138/134}Ba$ values between +0.20‰ to +0.40‰ (Figure 4.2b). These values are consistent to those previously reported for South Atlantic water samples with a similar water mass *in situ* density anomaly (42.0 kg/m^3), 80.59 ± 7.04 $nmol/kg$ (±2SE, n = 11) and $\delta^{138/134}Ba \approx +0.33‰ \pm 0.04$ (±2SE, n = 9; Horner et al. (2015); Hsieh and Henderson (2017); Bridgestock et al. (2018); Zhang et al. (2023), with water profile data from Schlitzer and Wegener (2000) & Schlitzer et al. (2018)). The reference site sample at 1 m altitude has a higher dissolved $[Ba]$ value of 158 $nmol/kg$ and lower $\delta^{138/134}Ba$ signal of ≈ -0.03‰

± 0.11, but both parameters are seen to return to ambient levels in all other reference site samples (Figure 4.2a,b). Samples from the Bubble Site, where the highest $[CH_4]$ is recorded, have a significantly higher average dissolved $[Ba]$ value compared to other sites (t(7.33) = 7.48, p = 0.00011; Figure 4.2a), but are not significantly different in associated $\delta^{138/134}Ba$ signal compared to other sites (t(13.9) = -2.10, p = 0.0547; Figure 4.2b). However, the samples are still within the typical dissolved $[Ba]$ range for South Atlantic seawater at the same density horizon. In addition, no significant difference in vertical changes in dissolved $[Ba]$ is measured between samples directly overlying the seafloor and ambient seawater (t(4.14) = -0.11742, p = 0.912; Figure 4.2a) or in $\delta^{138/134}Ba$ values (t(6.00) = 1.10, p = 0.315; Figure 4.2b). Samples collected overlying different macrofaunal assemblages are consistent with overlying ambient seawater in both dissolved $[Ba]$ and $\delta^{138/134}Ba$ value (Figure 4.2a,b). Finally, average dissolved $[Ba]$ values measured in the surface water samples, 54.7 ± 13.9 $nmol/kg$ (±2SE, n = 2), and $\delta^{138/134}Ba$ values, +0.51‰ ± 0.17 (±2SE, n = 2), align with those previously reported for global surface waters (dissolved $[Ba]$ average 46.2 ± 2.53 $nmol/kg$ (±2SE, n = 169) and $\delta^{138/134}Ba \approx +0.53‰ \pm 0.02$ (±2SE, n = 167; Horner et al. (2015); Bates et al. (2017); Hsieh and Henderson (2017); Bridgestock et al. (2018); Hemsing et al. (2018); Geyman et al. (2019); Cao et al. (2020); Yu et al. (2022); Middleton et al. (2023a); Zhang et al. (2023)).

The measured dissolved Mn concentration ($[Mn]$) varies between the sites and increases with depth at the individual sites (Bubble Site: 16.6 ± 3.01 $nmol/kg$ (±2SE, n = 5), East Pockmark: 5.13 ± 0.699 $nmol/kg$ (±2SE, n = 4), Reference site: 8.92 ± 5.12 $nmol/kg$ (±2SE, n = 5)), with the greatest increase observed in the reference site sample at 1 m altitude where dissolved $[Mn]$ increases three-fold, to 19 $nmol/kg$ (Figure 4.2c; Lemaitre et al. (2014)). This is consistent with dissolved Fe concentration ($[Fe]$), where the greatest variation with depth is recorded by the reference site sample at 1 m altitude, but here dissolved $[Fe]$ decreases by 44.4% to 5.1 $nmol/kg$ (Bubble Site: 33.8 ± 4.35 $nmol/kg$ (±2SE, n = 5), East Pockmark: 9.88 ± 1.71 $nmol/kg$ (±2SE, n = 4), Reference site: 8.36 ± 1.76 $nmol/kg$ (±2SE, n = 5); Figure 4.2c; Lemaitre et al. (2014)). The decrease in dissolved $[Fe]$ and increase in dissolved $[Mn]$ occurs at the same depth horizon as the large dissolved $[Ba]$ increase measured in the reference site 1 m altitude sample (Figure 4.2a). Both dissolved $[Fe]$ and $[Mn]$ measured here are 2 - 33 times greater than ambient seawater values, South Atlantic water samples with a similar water mass *in situ* density

anomaly (42.0 kg/m^3), 1.23 $nmol/kg$ & 0.415 $nmol/kg$, respectively (Lin et al., 2022).

The relationship between dissolved $[Ba]$ and $\delta^{138/134}Ba$ values for measured seawater samples are consistent with previously measured global seawater and are indiscernible from the global relationship between these two variables, except the reference site sample at 1 m altitude (Figure 4.3; Horner et al. (2015); Bates et al. (2017); Hsieh and Henderson (2017); Bridgestock et al. (2018); Hemsing et al. (2018); Geyman et al. (2019); Cao et al. (2020); Yu et al. (2022); Middleton et al. (2023a); Zhang et al. (2023)). The reference site sample at 1 m altitude is observed to have lighter $\delta^{138/134}Ba$ than previously measured samples that possess a similar $[Ba]$. However, all other measured reference site seawater samples plot along the global array. Samples from the Bubble Site have a significantly higher average dissolved $[Ba]$ value compared to other measured sites and plot further down the global array, but are not significantly different in measured $\delta^{138/134}Ba$ values (t(13.9) = -2.10, p = 0.0547; Figure 4.3). Finally, the $\delta^{138/134}Ba$ values measured in the surface water samples align with those previously reported for surface waters and fall along the global array (Figure 4.3).

4.4.3 Carbonate phase concentrations and Ba isotopic composition

The $[Ba]$ of the authigenic carbonate phase is consistent between the measured samples at an average of 4.34 ± 0.38 $\mu mol/g$ (±2SD, n = 9), except sample PL-429-CC2 where $[Ba]$ is 445.87% higher, 23.7 $\mu mol/g$ (Table C.1 & Figure C.2). The lowest $[Ba]$ is measured in authigenic carbonates collected at vent sites with the highest CH_4 release, PL-424-CC1 and PL-426-CC1, and is significantly different from vent sites with lower CH_4 release (t(5.8784) = -3.411, p = 0.01476). Conversely, the measured Ca concentration ($[Ca]$) of the authigenic carbonate samples is consistent for all samples regardless of vent site activity, averaging 0.04 ± 0.01 mol/g (±2SD, n = 12; Table C.1). The variation in the Ba/Ca ratio of the samples is thus due to changes in the measured $[Ba]$. Samples from high CH_4 release vent sites, PL-424-CC1, average Ba/Ca ratios of 9.76 ± 2.85 $\mu mol/mol$ (±2SD, n = 3), while those from low CH_4 release sites average 622 ± 102 $\mu mol/mol$ (±2SD, n = 3)(Figure 4.4). Only Ba/Ca ratios of samples from PL-424-CC1 are consistent to those previously reported for shallow and deep water coral skeletons, 9.82 ± 1.04 $\mu mol/mol$ (±2SE, n = 132; Pretet et al. (2015); Hemsing et al. (2018); Geyman et al. (2019); Liu et al. (2019); Hsieh et al. (2022); Lin et al. (2022)) and bulk carbonate

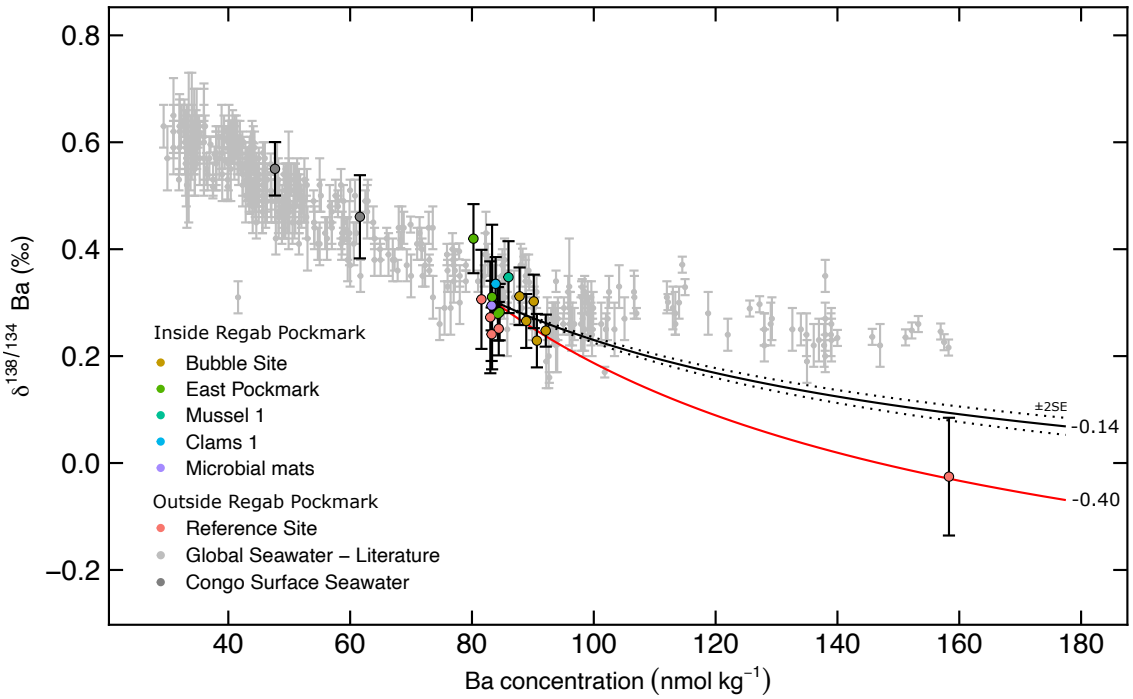

Figure 4.3: $[Ba]$ vs $\delta^{138/134}Ba$ values for seawater measured at Regab Pockmark. All seawater samples, except the reference site sample at 1 m altitude, plot along the global array. The $[Ba]$ values at the Bubble Site are significantly higher than other sites and can be explained with a benthic input $\delta^{138/134}Ba$ of -0.14‰, however is subject to uncertainty due to limited variation in $[Ba]$ at the site due to benthic input (black line - calculated using Equation 17 & 18). The reference site 1 m altitude sample can be explained with a $\delta^{138/134}Ba$ value of -0.40‰ (red line - calculated using Equation 17 & 18). Global seawater dataset was compiled from Horner et al. (2015); Bates et al. (2017); Hsieh and Henderson (2017); Bridgestock et al. (2018); Hemsing et al. (2018); Geyman et al. (2019); Cao et al. (2020); Yu et al. (2022); Middleton et al. (2023a); Zhang et al. (2023).

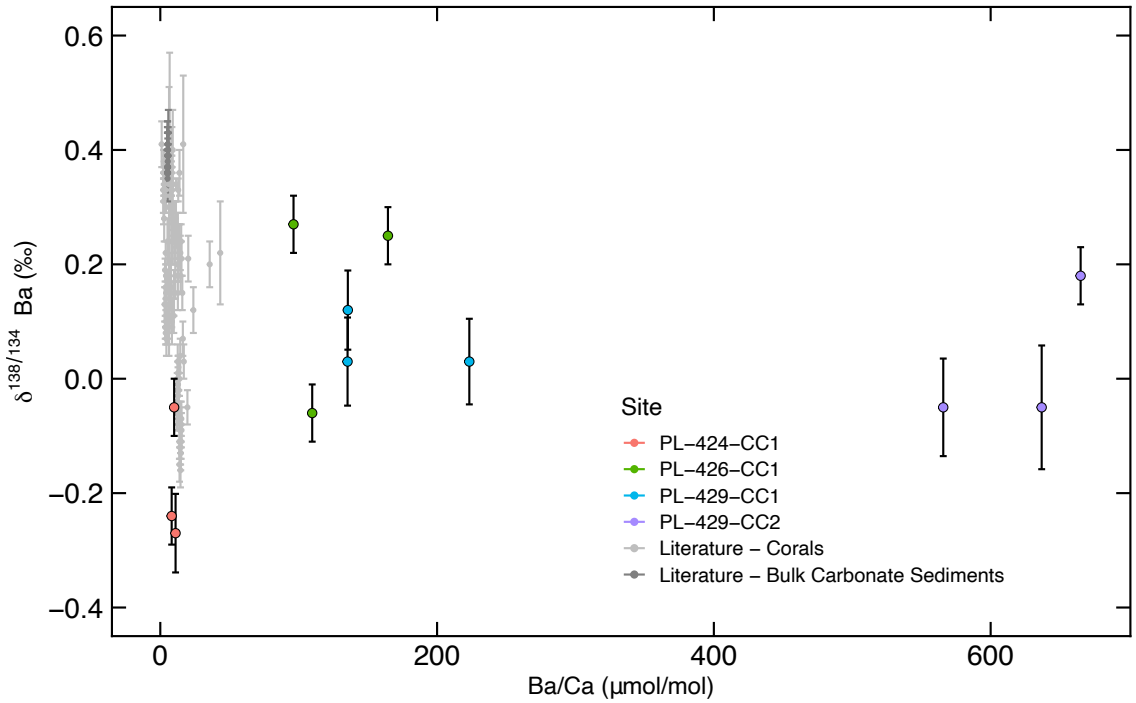

Figure 4.4: Authigenic carbonate phase Ba/Ca vs $\delta^{138/134}Ba$ values. No relationship is observed between dissolved Ba/Ca ratio and $\delta^{138/134}Ba$ values for the measured authigenic carbonate samples. Only Ba/Ca ratios of samples from PL-424-CC1 are consistent to those previously reported for shallow and deep water coral skeletons (Pretet et al., 2015; Hemsing et al., 2018; Geyman et al., 2019; Liu et al., 2019; Hsieh et al., 2022; Lin et al., 2022).

sediments, 5.35 ± 0.52 $\mu mol/mol$ (±2SD, n = 30; Lin et al. (2022); Figure 4.4).

The $\delta^{138/134}Ba$ values of the measured authigenic carbonate, $\delta^{138/134}Ba = +0.06‰$ ± 0.08 (±2SE, n = 10) are broadly similar to previously reported for shallow and deep water coral skeletons, $\delta^{138/134}Ba \approx +0.17‰$ ± 0.03 (±2SE, n = 132; Pretet et al. (2015); Hemsing et al. (2018); Geyman et al. (2019); Liu et al. (2019); Hsieh et al. (2022); Lin et al. (2022)), except in two sub-samples of PL-424-CC1 that recorded lighter $\delta^{138/134}Ba$ values of ≈ -0.26‰ (Figure 4.4). Authigenic carbonate $\delta^{138/134}Ba$ are offset to lower values compared to the literature ranges exhibited by core top pore waters ($\delta^{138/134}Ba \approx +0.28 \pm 0.01‰$; ±2SE, n = 101; Cao et al. (2023); Middleton et al. (2023a); Scholz et al. (2023)), and the overlying seawater (+0.23‰ - +0.42‰; Figure 4.2b). No relationship is observed between dissolved Ba/Ca ratio and $\delta^{138/134}Ba$ values for the measured authigenic carbonate samples (Figure 4.4).

4.5 Discussion

4.5.1 Impact of CH_4 venting on the marine Ba inventory

The impact of Ba benthic inputs linked to CH_4 venting at the cold seep on seawater dissolved $[Ba]$ and $\delta^{138/134}Ba$ values can be quantified using an isotopic mass balance (Equation 17 & 18).

$$[Ba]_{benthic\ seawater} = [Ba]_{pre} + [Ba]_{benthic\ input} \quad \{17\}$$

$$\delta^{138/134}Ba_{benthic\ seawater} = \delta^{138/134}Ba_{pre} * f_{pre} + \delta^{138/134}Ba_{benthic\ input} * f_{benthic\ input} \quad \{18\}$$

Where the subscripts 'benthic seawater', 'pre', and 'benthic input' denote the $[Ba]$ and $\delta^{138/134}Ba$ of the seawater impacted by benthic input, the ambient seawater, and benthic input, respectively. In equation 18 f_{pre} and $f_{benthic\ input}$ represent the fraction of the Ba from the 'preformed' and 'benthic input' reservoirs respectively (e.g. $f_{pre} = [Ba]_{pre}/[Ba]_{benthic\ seawater}$, where $f_{pre} + f_{benthic\ input} = 1$).

Based on the regeneration mass balance (Equation 17 & 18), the isotopic data for all seawater samples, except the reference site sample at 1 m altitude, can be explained within error along the global array (Figure 4.3). These results reflect that there is no resolvable difference in the $[Ba]$ vs. $\delta^{138/134}Ba$ relationship over the pockmark, attributed to negligible benthic Ba fluxes associated with CH_4 venting at this cold seep. The seawater samples at the Bubble Site show a significant increase in $[Ba]$ compared to other sites, but with no change in Ba isotope composition indicating that there is no resolvable difference in the $[Ba]$ vs. $\delta^{138/134}Ba$ relationship across the extent of the pockmark (Figure 4.3). This could indicate a minor detection of a benthic input signal which would suggest a $\delta^{138/134}Ba$ of the input of -0.14‰ (Equation 17 & 18). However, this input is subject to uncertainty due to limited changes in dissolved $[Ba]$ caused by cold seep benthic inputs at this site and given the uncertainty of measured seawater samples $\delta^{138/134}Ba$ data (±0.03‰ - ±0.10‰).

The high gradient between surface pore water (385 ± 25.4 $nmol/kg$ (±2SE, n = 288); Paytan and Kastner (1996); Cao et al. (2023); Middleton et al. (2023a); Scholz et al. (2023)) and dissolved seawater $[Ba]$ (80.2 to 92.1 $nmol/kg$; Table C.1) must drive a diffusive flux of Ba across the SWI. This is interpreted to be

controlled by $BaSO_4$ solubility causing the diagenetic remobilisation of $BaSO_4$ in marine sediments beneath the SWI (Gingele and Dahmke, 1994; Kasten et al., 2012; Zhang et al., 2023). However, seawater dissolved $[Ba]$ at each site are not enriched compared to overlying ambient conditions and show no increase towards the seafloor (Figure 4.2a). This likely reflects the quantitative removal of pore water Ba by rapid $BaSO_4$ precipitation within the upper sediments, where SO_4 becomes readily available again, preventing significant Ba release to the water column. However, the Ba/CH_4 flux ratio can inform on the end member amount of Ba benthic input addition to the seawater. Using the difference of Bubble Site $[Ba]$ to background divided by the difference of $[CH_4]$ Bubble Site to background gives a Ba/CH_4 flux ratio of 0.06 $nmol$ of Ba per μl efflux as an end member amount of Ba addition.

Barite precipitation is known to fractionate Ba isotopes, with preferential incorporation of the lighter isotopes into $BaSO_4$ (von Allmen et al., 2010; Böttcher et al., 2018; Wang et al., 2021). As such, residual dissolved Ba inputs to the overlying water column would be expected to shift to higher $\delta^{138/134}Ba$ values if $BaSO_4$ precipitation were to occur at cold seep environments prior to fluid entry into the seawater overlying the seafloor. Analogous Ba isotope systematics have been observed in hydrothermal vent systems, where the residual dissolved Ba inputs to the ocean are inferred to feature high $\delta^{138/134}Ba$ values (+1.7‰ ± 0.7; Hsieh et al. (2021)). Although, Zhang et al. (2024) reported the concentrations and isotopic compositions of dissolved and labile particulate Ba in the non-buoyant hydrothermal plume can be explained by conservative mixing between a Ba-enriched hydrothermal component and ambient water. In either instance, it would be expected that $\delta^{138/134}Ba$ values of seawater samples overlying the seafloor would show significantly different values to overlying ambient water $\delta^{138/134}Ba$ values and align with the potential benthic input signal of -0.14‰, but this is not supported by the measured seawater data in this study (Figure 4.2b).

In summary, the new seawater data presented in this study tentatively suggest cold seep relative benthic inputs feature $\delta^{138/134}Ba \approx$ -0.14‰. This composition is not particularly distinctive relative to other marine Ba sources and hence suggest only limited utility of Ba isotopes to trace past episodes of large-scale seafloor CH_4 release. However, these insights are hampered by uncertainty due to limited changes in dissolved $[Ba]$ attributable to cold seep benthic inputs at this site. Due to the spatial and temporal variability of cold seep dynamics (Li et al., 2016; Feng et al.,

2018; de Groot et al., 2024), this initial finding does not preclude distinctive $\delta^{138/134}Ba$ values being associated with other cold seep settings, warranting further research into this topic.

4.5.2 Ba response during release from Fe-Mn phases

The reference site sample at 1 m altitude has a higher dissolved $[Ba]$ (158 $nmol/kg$) compared to South Atlantic seawater with a similar water mass *in situ* density anomaly, 42.0 kg/m^3 (80.59 ± 7.04 $nmol/kg$ (±2SE, n = 11); Horner et al. (2015); Hsieh and Henderson (2017); Bridgestock et al. (2018); Figure 4.3). The additional Ba to the reference site sample is interpreted to be due to the benthic input addition of dissolved Ba from the sediment to the seawater due to diffusion gradients, unrelated to CH_4-SO_4-Ba dynamics typical of cold seeps. As this Ba enrichment at the reference site sample at 1 m altitude is associated with an increase in dissolved $[Mn]$ and a decrease in dissolved $[Fe]$ it is assumed to be from more oxidised sediments (Figure 4.2c; Lemaitre et al. (2014)). Reductive dissolution of Fe and Mn oxyhyrodroxide phases close to the SWI can drive the diffusive input of dissolved Fe and Mn into the overlying water column. The dissolution of these phases are only found at the reference site because there is not enough oxygen at the pockmark sites. Therefore, the high recorded signal of Ba recorded in the 1 m altitude reference sample could be attributed to Ba being released from Mn-phases that are cycling at the SWI (Bayon et al., 2011; He et al., 2021; Gäng et al., 2023).

The reference site sample at 1 m altitude is the only sample that clearly lies off the global relationship between seawater $[Ba]$ and isotope compositions with a measured $\delta^{138/134}Ba$ of -0.03‰ ± 0.11 (Figure 4.3). It has a lower $\delta^{138/134}Ba$ value compared to both, all other reference site samples (+0.25‰ - +0.31‰) and overlying ambient waters (+0.33‰ ± 0.04 (±2SE, n = 9; Horner et al. (2015); Hsieh and Henderson (2017); Bridgestock et al. (2018); Zhang et al. (2023)). The shift to a lower $\delta^{138/134}Ba$ value is opposite to observations by Bates et al. (2017) where bottom seawater samples featured a shift to higher $\delta^{138/134}Ba$ relative to the global seawater relationship between $[Ba]$ and $\delta^{138/134}Ba$. This was tentatively attributed to benthic input (Bates et al., 2017). Iron oxyhydroxides preferentially adsorb lighter Ba isotopes relative to the co-existing dissolved pool (Knight et al., 2024). This is consistent with the proposed mass balance model that predicts a $\delta^{138/134}Ba$ value of -0.40‰ for this Ba release, which is lighter than measured seawater and literature measurements of pore waters (Figure 4.3). In addition, Gong et al. (2020) measured $\delta^{138/134}Ba \approx$

-0.43‰ to -0.21‰ in Fe-Mn phases in a weathering profile, corroborating the value predicted by the mass balance model. Therefore, it is proposed that the measured $\delta^{138/134}Ba$ value of the reference site sample at 1 m altitude is caused by the release of Ba from Fe-Mn phases.

4.5.3 Incorporation of Ba isotopes into authigenic carbonates

The $\delta^{138/134}Ba$ of all the authigenic carbonate samples measured in this study ($\delta^{138/134}Ba \approx +0.06‰ \pm 0.08$ ($\pm$2SE, n = 10)) are lower than both core top pore water from marine sediment core at a similar depth range beneath the SWI ($\delta^{138/134}Ba \approx +0.28 \pm 0.01‰$, $\pm$2SE, n = 101; Cao et al. (2023); Middleton et al. (2023a); Scholz et al. (2023)) and overlying bottom seawater ($\delta^{138/134}Ba$ values +0.23‰ to +0.42‰; Figure 4.2 & Figure 4.4). This tentatively suggests a fractionation of lighter $\delta^{138/134}Ba$ during authigenic carbonate precipitation, similar to that observed in literature for precipitation in natural corals ($\Delta^{138/134}Ba_{coral-seawater} \approx$ -0.21 to -0.28 $\pm$ 0.06‰; Hemsing et al. (2018); Hsieh et al. (2022)) and cultured corals ($\Delta^{138/134}Ba_{coral-seawater} \approx$ –0.01‰ to –0.35‰; Pretet et al. (2015); Wang et al. (2021)). It is also consistent with results from carbonate precipitation experiments ($\Delta^{138/134}Ba_{carbonate-pore\ water} \approx$ -0.03‰ to -0.43‰; von Allmen et al. (2010); Böttcher et al. (2018); Wang et al. (2021)). The comparison to pore water is tentative given that measurements of the specific pore waters these carbonates formed from are not available and pore water values in general are used for comparison, but these data nonetheless provide important initial insights into Ba isotope partitioning into authigenic carbonates. This suggests that authigenic carbonate precipitation incorporate light Ba and cause the potential input to dissolved seawater to be heavier. However this is not justified by the proposed benthic input signal ($\delta^{138/134}Ba$ of -0.14‰) but would corroborate those measured at hydrothermal seep settings ($\delta^{138/134}Ba \approx +1.7‰$; Hsieh et al. (2021)).

Only Ba/Ca ratios of samples from PL-424-CC1 are consistent to those previously reported for shallow and deep water coral skeletons, 9.82 $\pm$ 1.04 $\mu mol/mol$ ($\pm$2SE, n = 132; Pretet et al. (2015); Hemsing et al. (2018); Geyman et al. (2019); Liu et al. (2019); Hsieh et al. (2022); Lin et al. (2022)) and bulk carbonate sediments, 5.35 $\pm$ 0.52 $\mu mol/mol$ ($\pm$2SD, n = 30; Lin et al. (2022); Figure 4.4) with all other samples being one to two orders of magnitude greater. This increase in Ba/Ca could be due to the authigenic carbonates formed in fluids with a higher $[Ba]$ under conditions which promote a different partition coefficient between Ba and Ca incorporation into the

carbonate mineral. Alternatively, this Ba enrichment could reflect the importance of non-carbonate phases, such as disseminated $BaSO_4$ for hosting Ba in these samples.

4.6 Conclusion

This study provides initial insights of Ba isotope cycling at cold seep settings. Measured dissolved $[Ba]$ and $\delta^{138/134}Ba$ values provide limited evidence of benthic Ba release associated with CH_4 venting is occurring at Regab pockmark, with $[Ba]$ differences at the Bubble Site being explained by a benthic input $\delta^{138/134}Ba$ of -0.14‰. These observations are interpreted to reflect the removal of dissolved Ba by $BaSO_4$ precipitation close to the SWI. This precludes gaining insights that validate predictions on the isotopic signature of such inputs, based on analogies with hydrothermal vent studies. Future work at other CH_4 vent sites along the Congo Margin and globally, specifically at the San Clemente Fault Scarp cold seep where Ba efflux into the water column was recorded (Torres et al., 2002), is required to determine if the observed dissolved $[Ba]$ and $\delta^{138/134}Ba$ dynamics are typical. In addition, investigation into other ways $\delta^{138/134}Ba$ could be impacted, such as mediation by seafloor macrofaunal assemblages, is required. This will offer perspectives into how CH_4 seep environments can have the potential to impact the global marine Ba mass balance like hydrothermal seep settings. And furthermore, if using sedimentary Ba burial rates to determine climate driven sedimentary CH_4 release is reliable.

The lower $\delta^{138/134}Ba$ value observed at the reference site sample at 1 m altitude compared to all seawater samples is attributed to Ba released by Fe-Mn oxyhydroxide sorbed Ba phases at the SWI. Using mass balance considerations constrains the Fe-Mn release of Ba to be equal to $\delta^{138/134}Ba \approx$ -0.4‰, consistent with literature constraints on the likely composition of these phases (Gong et al., 2020; Knight et al., 2024). Care should be taken in future studies in selecting an appropriate reference site that is not impacted by the seep site.

Finally, this study presents a first analysis of the isotopic composition of Ba from the authigenic carbonates. Lighter Ba isotopes are preferentially incorporated during precipitation from pore water, and the degree of fractionation could be influenced by the amount of CH_4 release. Therefore, the authigenic carbonate phase could serve as an archive for recording past Ba cycling in cold seep settings, providing

insights into past CH_4 cycling. A more comprehensive and widespread study on the isotopic composition of authigenic carbonates at cold seeps is necessary to conclusively determine whether these phases record the initial fluid composition and if the measured associated Ba fractionation is consistent.

4.7 Sample origin and data contribution statement

Seawater and authigenic carbonate samples were requested from the Marine Geological Samples Repository of Brest (IFREMER) which were originally collected on the WACS cruise programme, January 2011, on R/V *Pourquoi Pas?* (Olu, 2011). Initial Ba and other trace metal concentrations were measured by Nolween Lemaitre at the University of Brest (Lemaitre et al., 2014) and were used to select seawater samples appropriate to measure $[Ba]$ and $\delta^{138/134}Ba$ values at NTU, Taipei, Taiwan. Powdered authigenic carbonate samples were obtained by using a high precision micro-drill at NTU and subsequently leached to isolate the carbonate fraction. Trace metal concentrations of the carbonate fraction were measured at Academica Sinica by Professor Kuo-Fang (Denner) Huang and data were used to select appropriate samples to measure $[Ba]$ and $\delta^{138/134}Ba$ values at NTU.

Chapter 5

Conclusion

This study provides initial insights into the utility of barium concentration ($[Ba]$) and barium isotopes ($\delta^{138/134}Ba$) as a tracer of methane cycling in continental margin settings. To achieve this required examining the marine barium (Ba) mass balance, in particular the two remaining unknown constraints and the current dispute of the role of continental shelf sediment benthic inputs, which has implication for the use of Ba as a marine paleoproxy. In addition, the migration of methane (CH_4) through sedimentary basins along the Namibian continental margin has been investigated using 2D and 3D multichannel seismic reflection data. Therefore, an integrative study can aid in tracing CH_4 cycling and its further potential impact on the Ba marine mass balance in frontier basins along continental shelves where limited data are available, which have implication for both the energy industry and climate.

This study presents an initial assessment of the Ba isotopic composition of the final two remaining components of the marine Ba mass balance: heavier Ba isotopes preferentially released from continental shelves ($\delta^{138/134}Ba \approx +0.31‰$) drive the burial of a residual pool of Ba enriched in lighter isotopes. The study proposes that the mechanism causing these identified shelf sediment benthic inputs is the diagenetic remobilisation of $BaSO_4$ in marine sediments caused by changes in the $BaSO_4$ solubility, driven by sulphate depletion, which in turn can be linked to CH_4 cycling. This is corroborated by the combination of direct hydrocarbon indicators (DHI) identified on 2D and 3D seismic data that indicate a predominantly shallow biogenic source of CH_4, driven by methanogenesis, and subsequent upward migration of CH_4, via diffusion and advection through stratal and cross-stratal structures along the Namibian continental margin. As such, a fully connected, active hydrocarbon plumbing system (HPS) is present along the Namibian continental margin with the potential to continually supply CH_4 to shallower parts of the basin, promoting

changes in $BaSO_4$ saturation. The diagenetic remobilisation of $BaSO_4$ in marine sediments caused by changes in $BaSO_4$ solubility is expected at other continental margin settings and these results provide insights into how the global seawater Ba isotope inventory could be impacted by global changes in ocean redox, which should be considered when interpreting Ba isotope records in sediments. Future studies should prioritise sampling in continental shelf settings with minimal detrital contributions to marine sediments. In addition, studies are needed in a variety of other continental shelf settings to determine the global importance of the proposed mechanism for driving shelf benthic fluxes.

Re-categorising shelf sediment benthic inputs as part of the internal marine Ba cycle and providing an initial assessment for the isotopic composition of shelf sediment burial reveal that the marine Ba mass balance remains imbalanced. However, the current two-thirds imbalance between flux estimates of inputs and outputs is reduced and the marine Ba mass balance is more in alignment than if shelf sediment benthic input is considered as a input component. Large uncertainty is associated with previously recorded flux estimates and as such require refinement to reduce the imbalance. This has further implications for interpreting historic marine sedimentary records of $BaSO_4$, particularly during past climatic warming periods. Widespread suboxic conditions during these periods could lead to substantial Ba release into the water column, increasing seawater saturation with respect to $BaSO_4$ and contribute to the enhanced $BaSO_4$ burial observed during these warming periods (Paytan et al., 2007; Frieling et al., 2019; Griffith et al., 2021; Miyazaki et al., 2023).

Along continental shelves where the upward diffusive and advective flux of CH_4 is large, where active CH_4 venting is observed, the measured dissolved $[Ba]$ and $\delta^{138/134}Ba$ provide limited evidence of benthic Ba release associated with CH_4 venting. At Regab pockmark, Congo Margin, $[Ba]$ differences across the vent site with variable rates of CH_4 efflux can being explained by a benthic input $\delta^{138/134}Ba$ of -0.14‰. These observations are interpreted to reflect the removal of dissolved Ba by $BaSO_4$ precipitation close to the sediment-water interface. This precludes gaining insights that validate predictions on the isotopic signature of such inputs, based on analogies with hydrothermal vent studies. However, initial insights into the $[Ba]$ and $\delta^{138/134}Ba$ of authigenic carbonate phases present at cold seeps could serve as an archive for recording past Ba cycling in cold seep settings, providing insights into past CH_4 cycling. Future work at other CH_4 vent sites along the Congo Margin

and globally, specifically at the San Clemente Fault Scarp cold seep where Ba efflux into the water column was recorded (Torres et al., 2002), is required to determine if the observed dissolved $[Ba]$ and $\delta^{138/134}Ba$ dynamics are typical. This will offer perspectives into how CH_4 seep environments can have the potential to impact the global marine Ba mass balance like hydrothermal seep settings. And furthermore, if using sedimentary Ba burial rates to determine climate driven sedimentary CH_4 release is reliable.

The overarching aim of this thesis is to investigate CH_4 outgassing from a range of scales and perspectives and explore the benefits and challenges of integrating geophysical and geochemical studies. This study demonstrates that integrating these two fields is not only feasible but also mutually beneficial, enhancing the reliability and robustness of the results. Geophysical studies that primarily rely on seismic data can be significantly enhanced by incorporating petrophysical data to align borehole data with physical samples and use pore water and seawater chemistry to indirectly track fluid flow and CH_4 efflux, thereby corroborating conclusions drawn from seismic observations. Geochemical studies can be enriched by a broader understanding of regional subsurface fluid flow and CH_4 efflux, enabling researchers to determine whether geochemical changes observed in shallow marine sediment cores are driven by local processes or by larger-scale regional structures and fluid dynamics. However, challenges related to differences in scale between the two disciplines, as well as the tendency for cruise expeditions to focus on collecting only one type of data, must be addressed to facilitate the seamless and routine integration of these fields.

As outlined in the thesis aims, an integrative approach has addressed key questions at the interface of the two fields: how frontier basins with limited understanding of subsurface CH_4 flow affect Ba cycling and how comprehensive constraints on the marine Ba isotope mass balance inform on Ba burial rates and global scale CH_4 release. Future work should aim to quantitatively constrain the effect of mass-dependent processes and ion-exchange on Ba isotopic fractionation. Additionally, integrating Ba with other trace metal isotopic systems, such as nickel and uranium, and performing clumped isotope analysis on sulphur within the same $BaSO_4$ crystals would enhance understanding of Ba cycling in anoxic settings. This would ultimately improve $BaSO_4$ as a paleoceanographic proxy, particularly for reconstructing export production, and as a tracer of large-scale seafloor CH_4 venting.

Appendix A

Appendix For Chapter 2

Property	Value
3D Volume	Luderitz3DPSTM
Area	4206.59 km^2
In-line xline-spacing	12.5 m
Ns	934
Dt	4 ms
Polarity	American RC+ Peak (red)
Phase	0 degree
State	Data cut at 1s TWT below seafloor

Table A.1: Volume properties of the 3D seismic block provided by the Sereco Group. Note that the data are cut 1s TWT below the seafloor.

A.1 3D study site stratigraphy

As discussed in Section 2.3.2, the four major sedimentary basins are predominately filled by two major syn-rift megasequences and a post-rift thermal sag phase (Clemson et al., 1997). Due to the availability of core samples and a 3D seismic dataset the study site is focused on the lower shelf and upper slope of the Lüderitz Basin. The high-resolution 3D seismic data allows for a more detailed analysis of seismic stratigraphy for the post rift sediments (Megasequence E). The sequence boundaries delineating these tectono-stratigraphic sub-units are displayed on an interpreted 3D dip-line from the 3D seismic volume that passes close to the ODP-1084 well (Figure 2.3B). The ODP well terminates within the topmost sediments of Unit E3 and is discussed further below. The top 3500 ms of the sedimentary column represent Unit E3 Cenozoic sediments that thicken from 250 ms to 1400 ms down-dip above Unit E2 Late Cretaceous sediments that are seen to thin down-dip from 1500 ms to 700

Line	Location	Page
ecl-89-04	Clemson (1997)	126
ecl-89-06	Clemson (1997)	123
ecl-89-11	Light et al. (1993)	166
ecl-89-14	Clemson (1997)	105
ecl-89-22	Clemson (1997)	69
ecl-89-27	Clemson (1997)	96
ecl-89-29	Clemson (1997)	85
ecl-89-32	Corner et al. (2002)	211
ecl-89-41	Hopkins and Cartwright (2021)	3-23
ecl-89-43	Clemson (1997)	117
ecl-89-44	Hopkins and Cartwright (2021)	4-23
ecl-89-50g	Hopkins and Cartwright (2021)	4-19
ecl-91-405	Corner et al. (2002)	212
ecl-91-412	Clemson (1997)	125
ecl-91-478	Clemson (1997)	75
n2-93-401	Hopkins and Cartwright (2021)	4-25
n2-93-405	Hopkins and Cartwright (2021)	4-28
n2r-93-208	Hopkins and Cartwright (2021)	4-19
n2r-93-229	Hopkins and Cartwright (2021)	1-17
n2r-93-237	Hopkins and Cartwright (2021)	3-30
n2r-93-252	Hopkins and Cartwright (2021)	4-27
nh-9206-205	Hopkins and Cartwright (2021)	4-38
nh-9206-230	Hopkins and Cartwright (2021)	4-35 & 5-11
nh-9206-234	Hopkins and Cartwright (2021)	5-21
nh-9206-238	Hopkins and Cartwright (2021)	5-21
nh-9206-241	Hopkins and Cartwright (2021)	5-21
nh-9206-249	Hopkins and Cartwright (2021)	4-45
nh-9206-420	Hopkins and Cartwright (2021)	4-38
nh-9206-426	Hopkins and Cartwright (2021)	5-19
nh-9206-434	Hopkins and Cartwright (2021)	5-12
nh-9206-435	Hopkins and Cartwright (2021)	5-6
nwg-98-406	Hopkins and Cartwright (2021)	3-30
nwg-98-407	Hopkins and Cartwright (2021)	4-25
nwg-98-411	Hopkins and Cartwright (2021)	4-45
nwg-98-413	Hopkins and Cartwright (2021)	3-25
nwg-98-415	Hopkins and Cartwright (2021)	3-28

Line	Location	Page
san-014	Hopkins and Cartwright (2021)	2-8
san-015	Hopkins and Cartwright (2021)	4-30
rol93-2213-120	Clemson (1997)	169
rol93-2213-112	Clemson (1997)	171
rol93-2213-127	Clemson (1997)	174
rol93-2213-213	Clemson (1997)	176
rol93-2213-118	Clemson (1997)	177
rol93-2213-108	Clemson (1997)	182
rol93-2213-122	Clemson (1997)	191
rol93-2213-119	Clemson (1997)	199
rol93-2213-125	Clemson (1997)	207
ecl-91-358	Clemson (1997)	256
ecl-91-355	Clemson (1997)	259
ecl-89-50h	Clemson (1997)	277
ecl-89-50L	Clemson (1997)	279
ecl-89-50z	Bagguley and Prosser (1999)	39
ecl-89-11	Bagguley and Prosser (1999)	40
ecl-89-32	Bagguley and Prosser (1999)	59
AM-54	Wefer et al. (1997)	45
AWI 96-001	Wefer et al. (1997)	46
AWI 96-003	Wefer et al. (1997)	48
AWI 96-009	Wefer et al. (1997)	59
AWI 96-011	Wefer et al. (1997)	60
AWI 96-012	Wefer et al. (1997)	65
AWI 96-014	Wefer et al. (1997)	66
AWI 96-022	Wefer et al. (1997)	74
AWI 96-021	Wefer et al. (1997)	75
AWI 96-015	Wefer et al. (1997)	77+78
AWI 96-024	Wefer et al. (1997)	80
GeoB/AWI 96 024	ODP 1081 Initial Report	230/233
GeoB/AWI 96-015	ODP 1081 Initial Report	231/235
GeoB/AWI 96-017	ODP 1081 Initial Report	232/237
GeoB/AWI 96-014	ODP 1084 Initial Report	345/346
GeoB/AWI 96-009	ODP 1085 Initial Report	387
GeoB/AWI 93-030	ODP 1080 Initial Report	206/207

Table A.2: References for collated 2D seismic line database

Sample	Latitude	Longitude	Cruise	SO_4	SMTZ depth (mbsf)	DIC/TOC	CH_4	Diffusive CH_4 flux ($mmol\ m^{-2}\ yr^{-1}$)	Porosity	Fe & Mn
20010	-20.0	12.9	RGNO 2019 Cruise	This Study	>0.3	This Study				This Study
20050	-20.0	12.2	RGNO 2019 Cruise	This Study	>0.3	This Study				This Study
23030	-23.0	13.9	RGNO 2019 Cruise	This Study	>0.3	This Study				This Study
23060	-23.0	13.3	RGNO 2019 Cruise	This Study	>0.3	This Study				This Study
23010	-23.0	14.2	RGNO 2019 Cruise	This Study	0.4	This Study				This Study
GeoB1023-4	-17.2	11.0	M6/6	Hensen (1996)	7.7	Gingele (1992)			Müller (2004)	Haese et al. (1998)
GeoB1028-2	-20.1	9.2	M6/6	Hensen (1996)		Müller (2003)			Müller (2004)	
GeoB1028-4	-20.1	9.2	M6/6	Hensen (1996)	>0.12	Müller (2003)			Müller (2004)	
GeoB1031-3	-21.9	7.1	M6/6	Hensen (1996)	>10.4				Müller (2003)	
GeoB1035-5	-21.6	5.0	M6/6	Hensen (1996)	>7.15	Gingele (1992)			Müller (2003)	Haese et al. (1998)
GeoB12802-3	-25.5	13.5	M76/1	Goldhammer et al. (2011)	3.8	Lin et al. (2012)	Lin et al. (2012)	37.1	Goldhammer et al. (2011)	Lin et al. (2012)
GeoB12803-1	-25.8	14.1	M76/1	Goldhammer et al. (2011)	9	Lin et al. (2012)	Lin et al. (2012)		Goldhammer et al. (2011)	Lin et al. (2012)
GeoB12806-1	-25.0	14.4	M76/1	Goldhammer et al. (2011)	5	Goldhammer et al. (2011)	Böning et al. (2020)		Goldhammer et al. (2011)	Goldhammer et al. (2011)
GeoB12810-2	-24.1	14.3	M76/1	Goldhammer et al. (2011)	3.1	Goldhammer et al. (2011)			Goldhammer et al. (2011)	Goldhammer et al. (2011)
GeoB12811-3	-26.0	12.6	M76/1	Goldhammer et al. (2011)	18.4	Lin et al. (2012)	Lin et al. (2012)		Goldhammer et al. (2011)	Lin et al. (2012)
GeoB1704-3	-19.4	11.6	M20	Hensen (1996)	>5.5				Müller (2003)	Haese et al. (1998)
GeoB1711-3	-23.3	12.4	M20	Hensen et al. (1997)	13.6				Müller (2003)	Haese et al. (1998)
GeoB1711-6	-23.3	12.4	M20	Hensen et al. (1997)	>0.115				Hensen (1996)	Haese et al. (1998)
GeoB1712-1	-23.3	12.8	M20	Hensen (1996)	>0.263				Müller (2004)	Haese et al. (1998)
GeoB1712-3	-23.3	12.8	M20	Hensen et al. (2003)	>10.3				Müller (2004)	Haese et al. (1998)
GeoB1713-3	-23.2	13.0	M20	Hensen et al. (2003)	>3.35				Müller (2003)	Haese et al. (1998)
GeoB1713-5	-23.2	13.0	M20	Hensen (1996)	>0.225				Müller (2004)	Haese et al. (1998)
GeoB1716-1	-28.0	14.0	M20	Hensen (1996)	>0.188				Müller (2004)	Haese et al. (1998)
GeoB1719-4	-28.9	14.2	M20	Hensen (1996)	>0.16				Müller (2004)	Haese et al. (1998)
GeoB1719-6	-28.9	14.2	M20	Hensen (1996)	69.6				Müller (2004)	Haese et al. (1998)
GeoB1720-1	-29.0	13.8	M20	Hensen (1996)	26.3				Müller (2003)	Haese et al. (1998)
GeoB1721-5	-29.2	13.1	M20	Hensen (1996)	>0.175				Müller (2004)	Haese et al. (1998)
GeoB1721-6	-29.2	13.1	M20	Hensen (1996)	58				Müller (2003)	Haese et al. (1998)
GeoB1722-2	-29.5	11.8	M20	Hensen (1996)	>0.163				Müller (2004)	Haese et al. (1998)
GeoB3607-1	-23.9	14.3	M34/2	Hensen (1996)	0.67				Müller (2004)	
GeoB3703-8	-25.5	13.2	M34/2	Niewöhner et al. (1998)	3.3	Niewöhner et al. (1998)	Niewöhner et al. (1998)	35.5	Müller (2004)	Haese et al. (1998)
GeoB3707-8	-21.6	12.2	M34/2	Niewöhner et al. (1998)	10.5		Niewöhner et al. (1998)	48.5	Müller (2004)	Haese et al. (1998)
GeoB3714-3	-17.2	11.0	M34/2	Hensen (1996)	>0.175				Müller (2004)	Haese et al. (1998)
GeoB3714-9	-17.2	11.0	M34/2	Niewöhner et al. (1998)	5.6	Niewöhner et al. (1998)	Niewöhner et al. (1998)	55.0	Müller (2004)	Haese et al. (1998)
GeoB3718-4	-24.9	13.2	M34/2	Hensen (1996)	2.1	Zabel et al. (2003)			Müller (2004)	Haese et al. (1998)
GeoB3718-9	-24.9	13.2	M34/2	Riedinger et al. (2006)	6.2	Heuer (2002)	Niewöhner et al. (1998)	37.1	Müller (2004)	Haese et al. (1998)
GeoB8426-3	-25.5	13.4	M57/2	Riedinger et al. (2006)	3.5	Ashe (2018)	Riedinger et al. (2006)	57.3	Riedinger et al. (2006)	Ashe (2018)
GeoB8455-2	-25.5	13.2	M57/2	Riedinger et al. (2006)	3.7	Ashe (2018)	Riedinger et al. (2006)	43.6	Zabel et al. (2003)	Ashe (2018)
ODP-1080	-16.6	10.8	ODP Leg 175	Wefer et al. (1997)	6.7	ODP 1080 Initial Report	ODP 1080 Initial Report		ODP 1080 Initial Report	
ODP-1081	-19.6	11.3	ODP Leg 175	Wefer et al. (1997)	59.1	ODP 1081 Initial Report	ODP 1081 Initial Report		ODP 1081 Initial Report	
ODP-1082	-21.1	11.8	ODP Leg 175	Wefer et al. (1997)	22.2	ODP 1082 Initial Report	ODP 1082 Initial Report		ODP 1082 Initial Report	
ODP-1083	-20.9	11.2	ODP Leg 175	Wefer et al. (1997)	33.6	ODP 1083 Initial Report	ODP 1083 Initial Report		ODP 1083 Initial Report	
ODP-1084	-25.5	13.0	ODP Leg 175	Wefer et al. (1997)	5.9	ODP 1084 Initial Report	ODP 1084 Initial Report		ODP 1084 Initial Report	
ODP-1085	-29.4	14.0	ODP Leg 175	Wefer et al. (1997)	42	ODP 1085 Initial Report	ODP 1085 Initial Report		ODP 1085 Initial Report	
ODP-208-1262A	-27.2	1.6	ODP Leg 208	Zachos et al. (2004)	>149.9	ODP 1262A Initial Report	ODP 1262A Initial Report		ODP 1262A Initial Report	
ODP-208-1262B	-27.2	1.6	ODP Leg 208	Zachos et al. (2004)	>207.8	ODP 1262B Initial Report	ODP 1262B Initial Report		ODP 1262B Initial Report	
ODP-208-1262C	-27.2	1.6	ODP Leg 208	Zachos et al. (2004)		ODP 1262C Initial Report	ODP 1262C Initial Report		ODP 1262C Initial Report	
ODP-208-1263A	-28.5	2.8	ODP Leg 208	Zachos et al. (2004)	>321.1	ODP 1263A Initial Report	ODP 1263A Initial Report		ODP 1263A Initial Report	
ODP-208-1263B	-28.5	2.8	ODP Leg 208	Zachos et al. (2004)	>269.3	ODP 1263B Initial Report	ODP 1263B Initial Report		ODP 1263B Initial Report	
ODP-208-1264A	-28.5	2.8	ODP Leg 208	Zachos et al. (2004)	>269.1	ODP 1264A Initial Report	ODP 1264A Initial Report		ODP 1264A Initial Report	
ODP-208-1265A	-28.8	2.6	ODP Leg 208	Zachos et al. (2004)	2107.3	ODP 1265A Initial Report	ODP 1265A Initial Report		ODP 1265A Initial Report	
ODP-208-1265B	-28.8	2.6	ODP Leg 208	Zachos et al. (2004)	>238.6	ODP 1265B Initial Report	ODP 1265B Initial Report		ODP 1265B Initial Report	
ODP-208-1266A	-28.5	2.3	ODP Leg 208	Zachos et al. (2004)	1722.5	ODP 1266A Initial Report	ODP 1266A Initial Report		ODP 1266A Initial Report	

Table A.3: Literature sources of geochemical data used in this study, Chapter 2.

ms. Figure A.3 shows the major structures observed in post rift sediments and is displayed on a 3D dip-line.

The base of the 3D seismic data terminates within Unit E1 sediments expressed as discontinuous reflectors with medium to high amplitudes (Figure A.3). The lithology is unknown due to lack of deep wells in the Lüderitz Basin but is commonly interpreted as a volcanic unit or as a carbonate platform based on internal geometries and seismic attributes (Rochelle-Bates et al., 2017). Microbialite could also be present in this unit due to its proximity and tectostratigraphic similarity to the pre-salt basins of Brazil and Angola.

Sediments of the second major sequence of the Drift Phase deposited in the Late Cretaceous (Unit E2) can be subdivided into two sub-units: Sub-unit E2-a and Sub-unit E2-b. Sub-unit E2-a is characterised by prograding sequences that deposit across the postulated volcanics or carbonate platform of Unit E3, typical of a deltaic depositional environment (Figure A.3). Both sub-units contain parallel to low amplitude reflectors with low resolution and appear non-continuous. This pattern is caused by a degradation in the signal accompanied by a rise in noise. Some anomalously high amplitude packages are observed but have limited extent and are more frequent in Sub-unit E2-b. Polygonal faulting is seen to separate the two sub-units and is continuous throughout the entire 3D seismic volume (Figure A.3).

Unit E3 is the final sequence of the Cenozoic Drift phase sediments and can be subdivided based on their seismic characteristics. Sub-unit E3-a onlaps on the top of Unit E2 and has continuous low amplitude reflectors throughout that are seen to be truncated at the base of the above unit. Sub-unit E3-a pinches out to the east onto the Late Cretaceous shelf break, thinning considerably (Figure A.3). Polygonal faults are common at the base of the sub-unit identified by breaks in reflection continuity due to displacement along a fault plane.

Sub-unit E3-b sits above the truncated Sub-unit E3-a package and has mostly clinoform geometry with high amplitude reflectors at the crest. The package is seen to thicken down-dip to where it abruptly thins on the upper slope. This extension up dip has been interpreted as a head scarp. Below which, amplitudes are chaotic and faulted, with some remnant reflections that could represent intact blocks. Further down dip, the sub-unit is structurally dominated by thrusts. All of these observations

suggest a mass transport deposit within sub-unit E3-b possibly triggered by a failure on the Early Cenozoic shelf break (de Vera et al., 2010). The base of the sub-unit is associated with wave-like features that can be interpreted as sediment waves.

Sitting unconformably above the Sub-unit E3-b is Sub-unit E3-c, a laterally continuous package with clinoform geometry and low amplitude reflectors (Figure A.3). The sub-unit truncates at the seafloor and thins down-dip depositing over the mass transport section of the below unit (Figure 2.3B). Discontinuous, anomalous, high amplitude reflectors are observed throughout the sub-unit that are not bound to a certain horizon. The anomalies have a 'soft' acoustic response due to a sudden decrease in acoustic impedance downward, have a significantly higher amplitude than the background reflectivity and the margins of the anomalies are abrupt in their amplitude cut off. Given the above, and the depth in the sediment stack these reflectors are commonly interpreted as gas accumulations. Sporadic vertical to sub-vertical breaks in reflectivity continuity that have a columnar geometry in 3D are observed within the sub-unit and are interpreted as fluid escape pipes (Moss and Cartwright, 2010b; Cartwright and Santamarina, 2015). The pipes are typically 1 - 10 m diameter width and $\sim$ 280 - 500 m height and the breaks associated with the background reflective continuity is abrupt. The pipes are crudely cylindrical, and narrowing is frequently observed throughout. The majority of pipes terminate within the sediment however some pipes extend through the topmost sedimentary unit and terminate at the seafloor, usually with a pockmark, as observed in Figure A.6 (Gay et al., 2007; Moss and Cartwright, 2010a; Foschi and Cartwright, 2016).

The topmost sequence of the sedimentary column is Sub-unit E3-d and contains continuous low amplitude reflectors that are prevalent throughout the lower section. The unit truncates at the seafloor with sub-parallel reflectors and contains a discontinuous, negative polarity reflector throughout the majority of this sub-unit (Figure A.3 & Figure A.6).

A.2 ODP site 1084 well data

Limited well data are available for the Namibian margin and the wells are relatively shallow, terminating in Sub-unit E3-c sediments. ODP site 1084 is located in the Lüderitz Basin and due to its proximity, can be tied to the 3D seismic data (Figure A.6). The well is tied to the continuous low amplitude reflectors of Sub-units E3-c

and E3-d and terminates just above the mass transport deposit present in Sub-unit E3-b. From core data obtained at ODP-1084, the lithology of the Sub-unit E3-d is split into three packages ranging from a nannofossil clay to a diatom-bearing clay to a diatomaceous ooze (Unit IA, IB & IC described in Wefer et al. (1999)). Lithology obtained from coring in the ODP-1084 well for Sub-unit E3-c sediments show a gradual change from a diatomaceous ooze to a nannofossil ooze (Units II, III and IV in Wefer et al. (1999)).

TOC concentration data was determined for selected samples in each of the subunits and show large variations within the different lithological units (Wefer et al., 1999). TOC concentration data are seen to decrease downcore from Sub-unit E3-d (averaging 8.21 wt% in ODP Unit IA, 7.00 wt% in Unit IB, 4.92 wt% in Unit IC) to Sub-Unit E3-c (averaging 3.36 wt% in ODP Unit II, 4.55 wt% in Unit III, and 2.87 wt% in Unit IV)(Wefer et al., 1999). The high TOC concentrations in Sub-unit E3-d can be attributed to both elevated paleoproductivity of the Benguela Current upwelling system, that delivered abundant organic matter to the sediments and an enhanced preservation of the organic matter due to a high accumulation rate of sediments (Wefer et al., 1999).

No direct hydrate deposits were encountered during sampling at ODP site 1084, however, evidence from the wireline log data suggest the presence of a GHSZ (Wefer et al., 1999). The porosity (porosity log) over Sub-unit E3-d decreases from 90% at top to 74% at 395 $mbsf$. This is accompanied by an increase in the average velocity of 1475 to 1575 ms^{-1} (Sonic VP2 log) of the sediments and a slight elevation of 0.1 - 0.2 $ohm.m$ resistivity (Res-dit log) in this interval compared to background values. These marked changes in sediment conditions are typical characteristics of hydrate-filled sediments and suggest the presence of hydrate deposits, with an average velocity of 1540 ms^{-1} throughout the GHSZ.

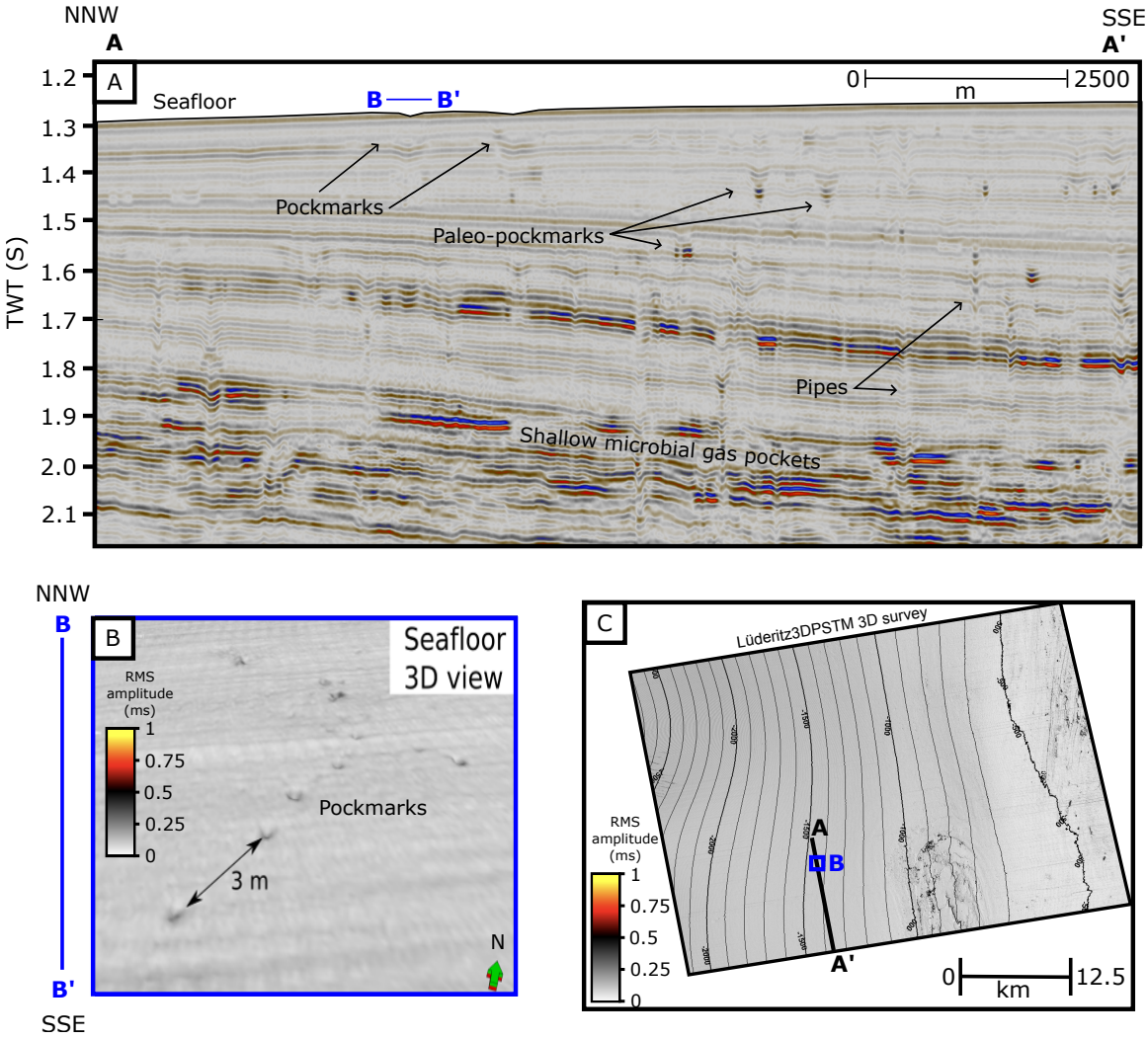

Figure A.1: Pockmark expression on seismic data. a) xline4500 shows seafloor punctured with crater-like structures with downward deflected velocity push-down observed in underlying seismic data. b) Seafloor 3D view shows crater-like structures with varying diameter. c) Seabed dip attribute map of 3D seismic volume (ms TWT) showing the extent of Panel A (xline4500) and the location of Panel B (seafloor 3D map). The location of the 3D seismic volume is displayed in Figure 2.3c.

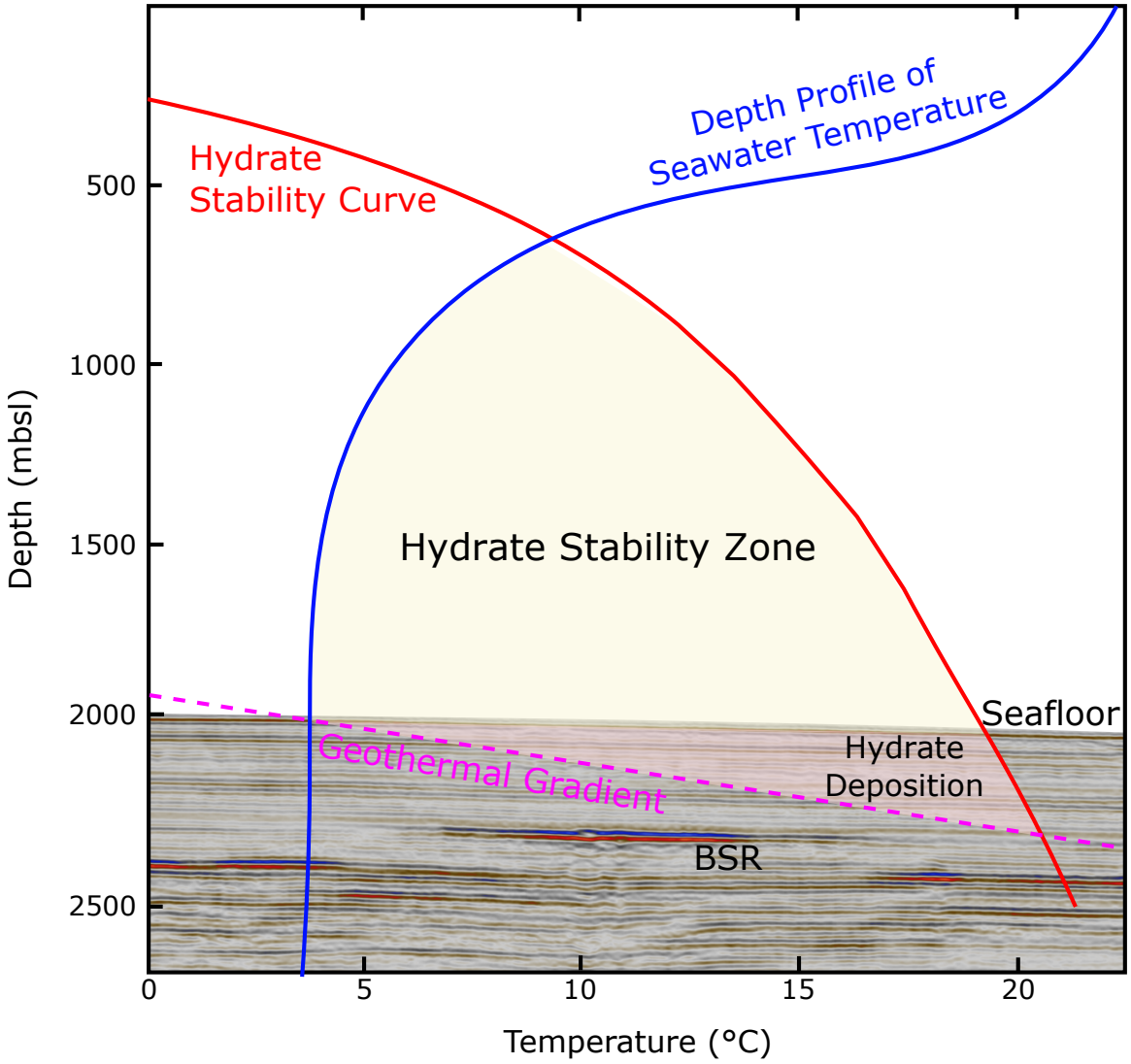

Figure A.2: The calculated gas hydrate stability zone (shaded yellow area). An average geothermal gradient of $32.8°C/km$ (as calculated using Dickens and Quinby-Hunt (1994) methods; pink dashed line) was selected and intersects the hydrate stability curve (red line; Flemings et al. (2020)) and depth profile of seawater temperature (blue line; Flemings et al. (2020)) to show the required pressure-temperature conditions for hydrate stability. The zone of shaded pink shows the specific temperature and pressure conditions where for gas hydrate formation can occur in the marine sediments.

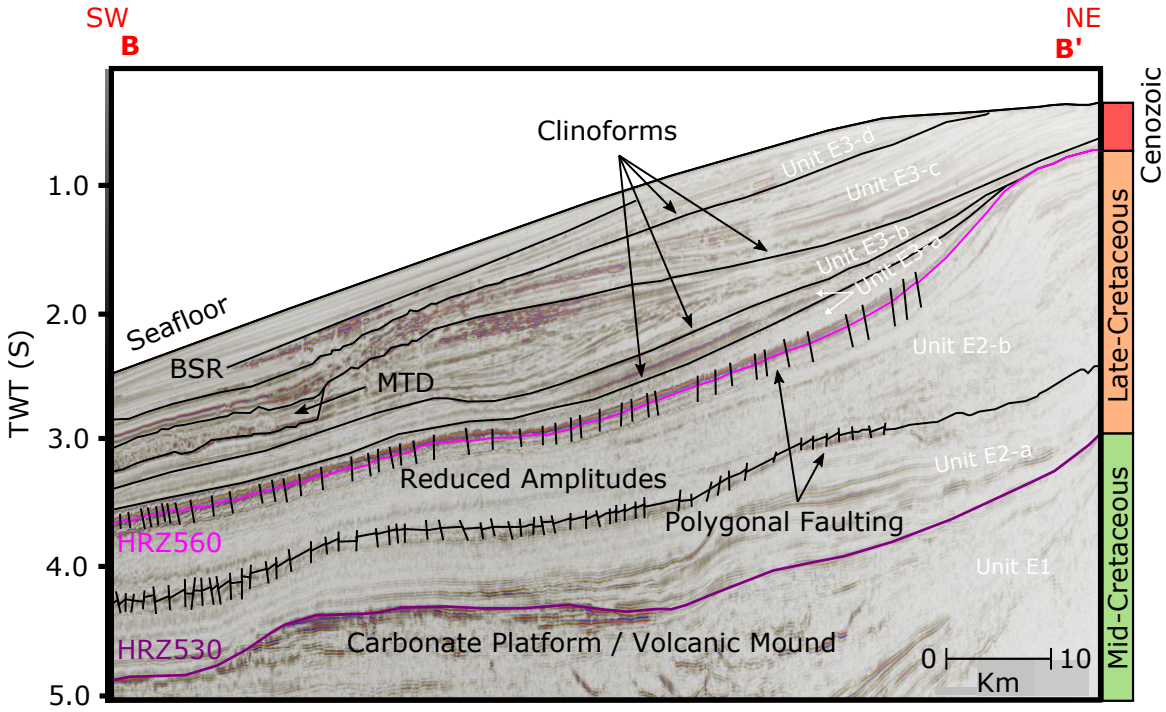

Figure A.3: 3D Seismic cross-section displaying the seismic structures along the Namibia margin, Lüderitz Basin. The figure highlights the BSR, prograding clinoforms and polygonal faulting as well as position of Cenozoic, Late Cretaceous Mid-Cretaceous sediment. The location of the seismic profile is B-B' as displayed in Figure 2.3c. Figure and seismic data has been adapted from those shown in Campbell (2017).

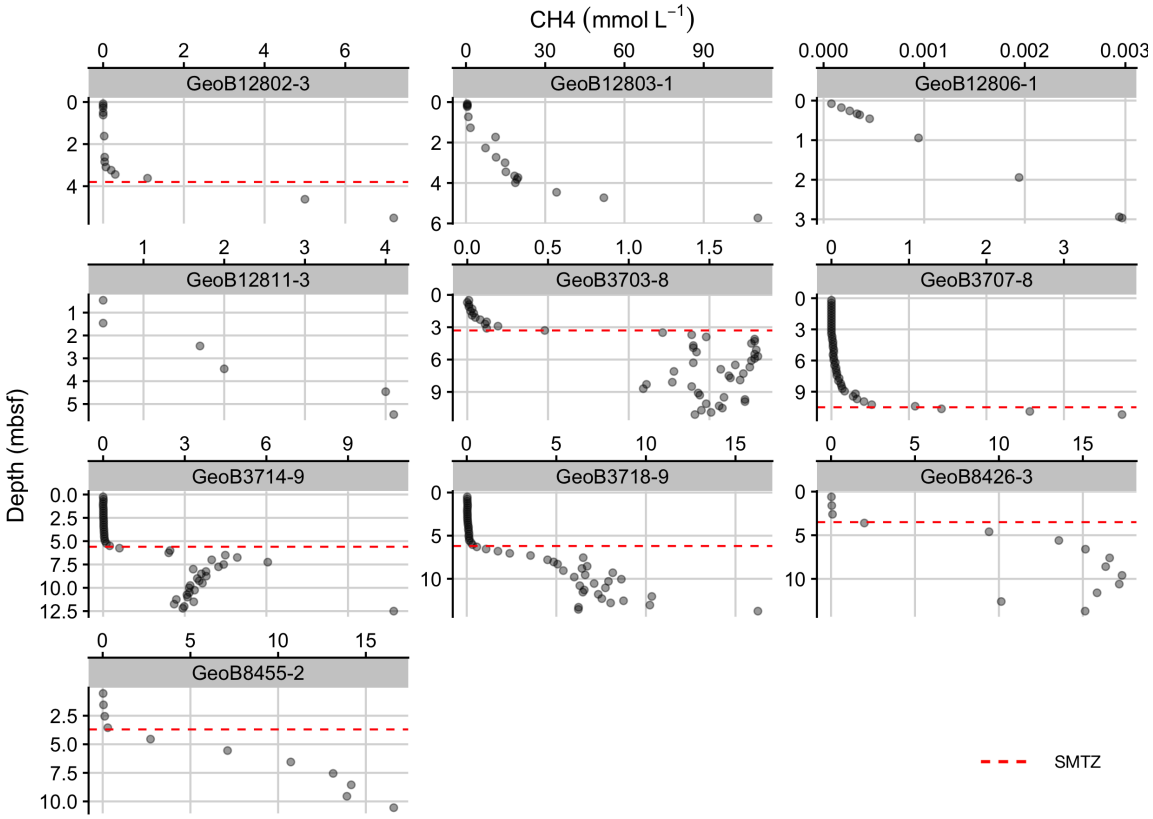

Figure A.4: Compiled published CH_4 concentration data. Literature sources are shown in Table A.3. Red dashed line marks the SMTZ.

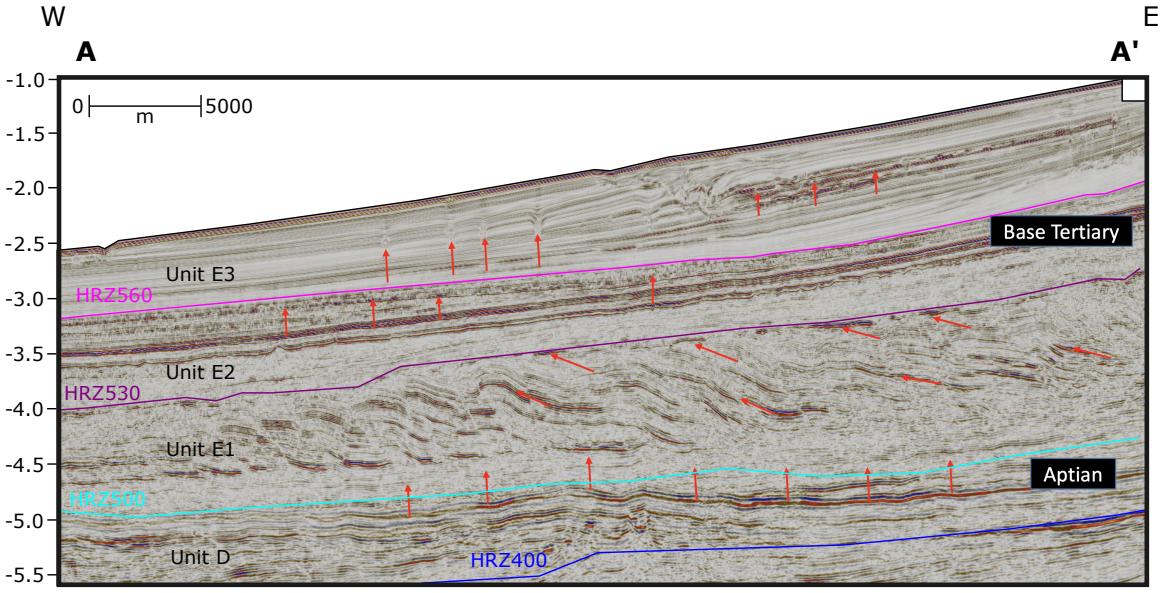

Figure A.5: Proposed thermogenic HPS with direction of gas flow marked by red arrows. Methane is produced within sediments of Unit D with the majority being trapped within the unit or at the crests of stacked sedimentary wedges above. Seismic line is located on Figure 2.3, half of map line extent.

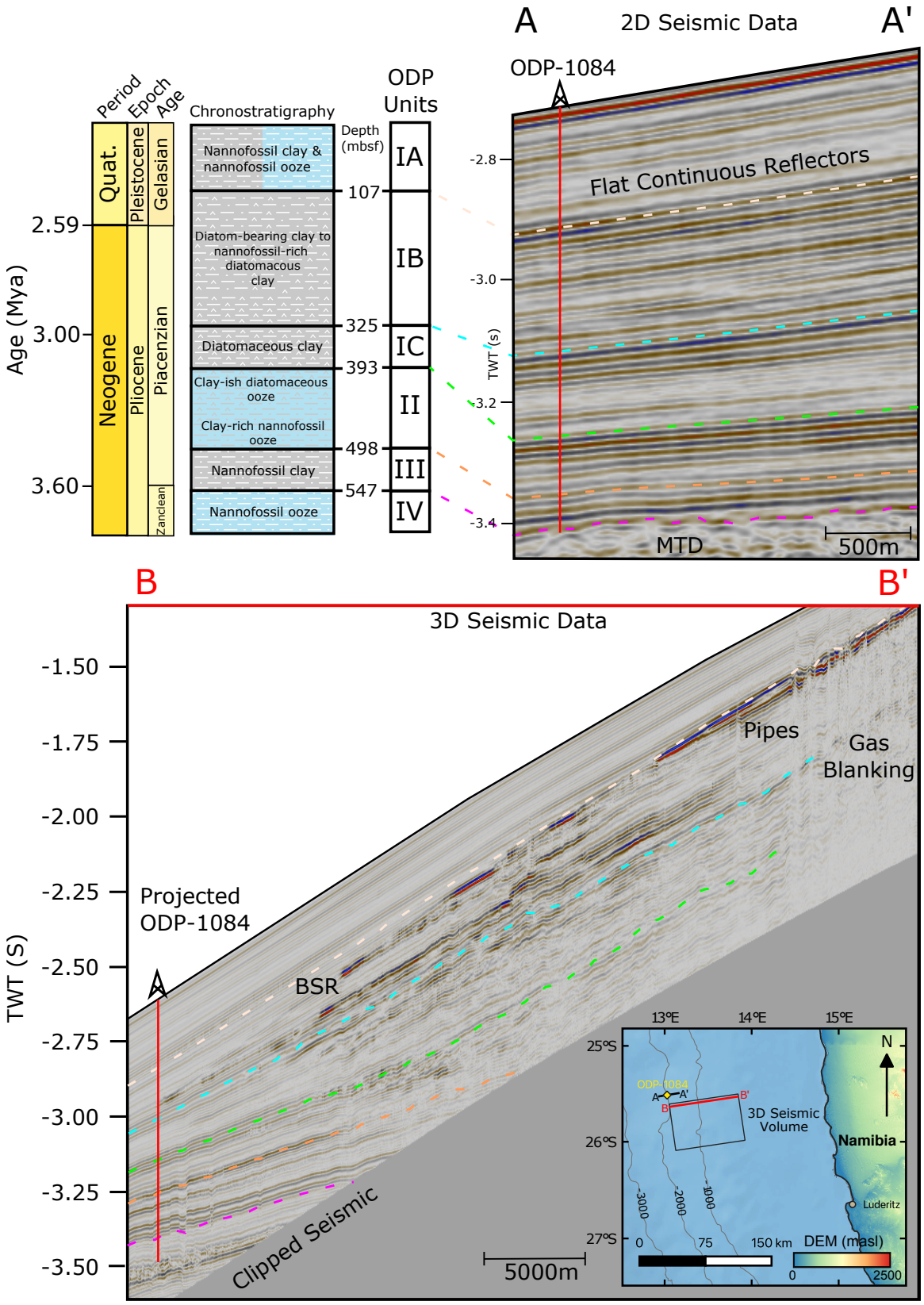

Figure A.6: Well-tie of the ODP-1084 well with 2D seismic data found within ODP literature (Wefer et al., 1999). The data are projected onto the closest corresponding 3D seismic data. Map displays location of seismic lines.

Appendix B

Appendix For Chapter 3

B.1 MC-ICP-MS methodology

The accuracy of data collected in this study is confirmed by replicate measurements of select samples using a different measuring technique at a different laboratory, National Taiwan University (NTU), Taipei, Taiwan. The same methodology in sample processing and Ba purification as those measured at the University of Oxford occurred.

The $[Ba]$ and isotope compositions of samples were determined using a multiple-collector Inductively coupled plasma-mass spectrometry (MC-ICP-MS; Nu Plasma HR, Nu Instruments) at NTU with a DSN-100 desolvation system (Nu Instruments) and a C-Flow (50 $\mu L/min$) nebuliser (Savillex). The Ba isotopes ^{136}Ba, ^{135}Ba, ^{137}Ba, and ^{138}Ba were collected on the L1, C, H1, and H2 Faraday cups, respectively. Simultaneously, ^{139}La and ^{140}Ce were collected on an H3 and L2 Faraday cup to correct for the isobaric interferences on ^{138}Ba and ^{136}Ba. Each analysis block comprised 40 cycles of data, with a 10-second integration time per cycle. Prior to and after each sample analysis, a National Institute of Standards and Technology (NIST) 3104a standard was measured, and the analyses were repeated three times for the same sample solution. To prevent potential cross-contamination, the sample introduction system was cleaned with 10% then 2% HNO_3 (m/m) for two minutes between measurements until the ^{138}Ba signal decreased to less than 10 mV. The raw isotopic ratios were processed offline to correct for instrumental mass bias and finally, data are reported in the δ-notation (‰) ($\delta^{138/134}Ba$) relative to the NIST 3104a standard (Equation 16).

Sample	Latitude	Longitude	Oxygen Bottom water conc. (μmol/l)	Oxygen Penetration Depth (m)	Oxygen Penetration Depth Error (±SD)	Cruise	Reference
GeoB2002	-31.486667	15.48	190.1	0.022		M34	Wefer et al. (1997)
GeoB3701	-27.95167	14.00333	199.35	0.026		M34	Wefer et al. (1997)
GeoB3702	-26.79167	13.455	191.39	0.0105		M34	Wefer et al. (1997)
GeoB3703	-25.51667	13.23167	194	0.00825		M34	Wefer et al. (1997)
GeoB3704	-25.46667	13.08333	209	0.0185		M34	Wefer et al. (1997)
GeoB3705	-24.30333	12.99667	194	0.00825		M34	Wefer et al. (1997)
GeoB3706	-22.71667	12.60167	198	0.01375		M34	Wefer et al. (1997)
GeoB3707	-21.625	12.19333	198	0.01725		M34	Wefer et al. (1997)
GeoB3708	-21.09	11.825	102	0.01425		M34	Wefer et al. (1997)
GeoB3709	-21.48333	11.255	263.27	0.0245		M34	Wefer et al. (1997)
GeoB3710	-20.66167	11.4	175	0.0175		M34	Wefer et al. (1997)
GeoB3711	-19.835	10.77167	187.354	0.013027		M34	Wefer et al. (1997)
GeoB3712	-17.18667	11.125	114.566	0.005987		M34	Wefer et al. (1997)
GeoB3713	-15.62833	11.58	129.612	0.012478		M34	Wefer et al. (1997)
GeoB3715	-15.62667	11.58167	165.288	0.009224		M34	Wefer et al. (1997)
GeoB3717	-24.83333	13.36333	69	0.01425		M34	Wefer et al. (1997)
GeoB3718	-24.895	13.16	199.41	0.0135		M34	Wefer et al. (1997)
GeoB3719	-24.995	12.87167	132	0.01575		M34	Wefer et al. (1997)
GeoB3721	-25.15167	12.4	222.51	0.02675		M34	Wefer et al. (1997)
GeoB1724-3	-29.9717	8.0417	228	0.05	4	M20/2	Glud et al. (1994)
GeoB1722-2	-29.45	11.75	233	0.025	3	M20/2	Glud et al. (1994)
GeoB1721-5	-29.1733	13.09	237	0.041	2	M20/2	Glud et al. (1994)
GeoB1720-3	-28.9983	13.8367	225	0.0085	0.4	M20/2	Glud et al. (1994)
GeoB1719-4	-28.9267	14.1733	180	0.0115	0.5	M20/2	Glud et al. (1994)
GeoB1711-6	-23.3167	12.3733	215	0.009	1	M20/2	Glud et al. (1994)
GeoB1712-1	-23.2533	12.805	160	0.0069	0.2	M20/2	Glud et al. (1994)
GeoB1713-5	-23.2167	13.0117	96	0.0059	0.8	M20/2	Glud et al. (1994)
GeoB1708-1	-20.0967	8.9667	214	0.009	1	M20/2	Glud et al. (1994)
GeoB1704-2	-19.405	11.6117	64	0.0058	0	M20/2	Glud et al. (1994)
GeoB1703-3	-17.4533	11.0167	210	0.009	1	M20/2	Glud et al. (1994)
MSM17/3_233-8	-26.667	14.76	2.8	0.0011		MSM17/3	Emeis et al. (2018)
MSM17/3_235-9	-26.667	14	149.6	0.0011		MSM17/3	Emeis et al. (2018)
MSM17/3_236-11	-26.667	13.5	163.7	0.014		MSM17/3	Emeis et al. (2018)
MSM17/3_237-4	-26	13.55	147.1	0.011		MSM17/3	Emeis et al. (2018)
MSM17/3_238-7	-25	13.333	163.9	0.011		MSM17/3	Emeis et al. (2018)
MSM17/3_240-6	-24	13.11	124.3	0.009		MSM17/3	Emeis et al. (2018)
MSM17/3_241-9	-23	11.75	221.2	0.027		MSM17/3	Emeis et al. (2018)
MSM17/3_242-11	-23	12.5	199.6	0.022		MSM17/3	Emeis et al. (2018)
MSM17/3_243-10	-23	12.8	131.7	0.014		MSM17/3	Emeis et al. (2018)
MSM17/3_246-7	-23	13.05	93.1	0.016		MSM17/3	Emeis et al. (2018)
MSM17/3_250-13	-23	13.334	99.7	0.01		MSM17/3	Emeis et al. (2018)
MSM17/3_266-8	-22.765	13.468	48.5	0.006		MSM17/3	Emeis et al. (2018)
MSM17/3_267-4	-22.019	13.18	13.2	0.004		MSM17/3	Emeis et al. (2018)
MSM17/3_268-10	-21.029	13.486	92.5	0.004		MSM17/3	Emeis et al. (2018)
MSM17/3_272-7	-21	12.5	59.2	0.008		MSM17/3	Emeis et al. (2018)
MSM17/3_274-6	-20	11.833	38.3	0.011		MSM17/3	Emeis et al. (2018)
MSM17/3_276-5	-20	12.5	1.9	0.004		MSM17/3	Emeis et al. (2018)
MSM17/3_278-4	-20	13	12.4	0.007		MSM17/3	Emeis et al. (2018)
MSM17/3_292-8	-19	11.433	58.5	0.007		MSM17/3	Emeis et al. (2018)
MSM17/3_295-9	-19	11	185.1	0.01		MSM17/3	Emeis et al. (2018)
MSM17/3_298-10	-19	10.5	228.6	0.018		MSM17/3	Emeis et al. (2018)
MSM17/3_299-7	-18.5	11.417	54.6	0.006		MSM17/3	Emeis et al. (2018)
MSM17/3_300-3	-18	11.5	25.6	0.004		MSM17/3	Emeis et al. (2018)
MSM17/3_304-10	-17.25	11.717	66.3	0.005		MSM17/3	Emeis et al. (2018)
MSM17/3_305-9	-17.254	11.507	65.3	0.005		MSM17/3	Emeis et al. (2018)
MSM17/3_306-11	-17.25	11.288	42.6	0.005		MSM17/3	Emeis et al. (2018)
MSM17/3_308-8	-17.25	11	236.8	0.015		MSM17/3	Emeis et al. (2018)
MSM17/3_309-10	-17.25	10.783	238.1	0.022		MSM17/3	Emeis et al. (2018)
MSM17/3_310-6	-17.25	10.5	229.2	0.03		MSM17/3	Emeis et al. (2018)
MSM17/3_311-2	-17.25	11.183	145.5	0.015		MSM17/3	Emeis et al. (2018)
MSM17/3_316-3	-17.25	10	224.7	0.027		MSM17/3	Emeis et al. (2018)

Table B.1: Oxygen penetration depth and bottom water oxygen concentration across the Namibian margin compiled from literature sources (Wefer et al., 1997; Glud et al., 1994; Emeis et al., 2018).

Sample	Latitude	Longitude	Core top Sulphate Concentration (mM)	Predicted SMTZ Depth (mbsf)	Cruise	Reference
20010	-20	12.86	24.26		RGNO	This Study
20050	-20	12.15	28.42		RGNO	This Study
23030	-23	13.86	28.44		RGNO	This Study
23060	-23	13.33	28.04		RGNO	This Study
23010	-23	14.23	22.94	0.32	RGNO	This Study
GeoB1023-4	-17.160133	10.9986	28.54	7.73	M6/6	Hensen (1996)
GeoB1028-2	-20.09	9.17	27.81		M6/6	Hensen (1996)
GeoB1028-4	-20.099333	9.177667	27.81	2.75	M6/6	Hensen (1996)
GeoB1031-3	-21.883333	7.103333	27.6		M6/6	Hensen (1996)
GeoB1035-5	-21.578333	5.023333	26.98		M6/6	Hensen (1996)
GeoB12802-3	-25.499833	13.450167	28.085	3.77	M76/1	Goldhammer et al. (2011)
GeoB12803-1	-25.76	14.07	28.548	8.9	M76/1	Goldhammer et al. (2011)
GeoB12806-1	-25	14.389	17.316	5	M76/1	Goldhammer et al. (2011)
GeoB12810-2	-24.053167	14.2615	23.042	3.1216	M76/1	Goldhammer et al. (2011)
GeoB12811-3	-26.010333	12.573167	31.7	18.42181	M76/1	Goldhammer et al. (2011)
GeoB1704-3	-19.405	11.61	28.48	43.87	M20	Hensen (1996)
GeoB1711-3	-23.321667	12.378333	28.79	13.6	M20	Hensen (1996)
GeoB1711-6	-23.316667	12.373333	29.26		M20	Hensen (1996)
GeoB1712-1	-23.253333	12.805	29.26	0.94	M20	Hensen (1996)
GeoB1712-3	-23.255	12.805	28.36		M20	Hensen (1996)
GeoB1713-3	-23.22	13.013333	29.23	34.3	M20	Hensen (1996)
GeoB1713-5	-23.216667	13.011667	26.46	1.13	M20	Hensen (1996)
GeoB1716-1	-27.951667	14.003333	28.77		M20	Hensen (1996)
GeoB1719-4	-28.926667	14.173333	30		M20	Hensen (1996)
GeoB1719-6	-28.925	14.171667	29.8	66.6	M20	Hensen (1996)
GeoB1720-1	-28.995	13.84	29.56	32.35	M20	Hensen (1996)
GeoB1721-5	-29.173333	13.09	29.6		M20	Hensen (1996)
GeoB1721-6	-29.171667	13.085	29.06	57.59	M20	Hensen (1996)
GeoB1722-2	-29.45	11.75	29.16		M20	Hensen (1996)
GeoB3607-1	-23.888333	14.331667	28.79	0.658	M34/2	Hensen (1996)
GeoB3703-8	-25.518333	13.23	27.8	3.25	M34/2	Niewöhner et al. (1998)
GeoB3707-8	-21.62333333	12.195	27.036	10.3	M34/2	Niewöhner et al. (1998)
GeoB3714-3	-17.16	10.998333	29.06	6.23	M34/2	Hensen (1996)
GeoB3714-9	-17.16	10.998333	27.81	5.63	M34/2	Niewöhner et al. (1998)
GeoB3718-4	-24.895	13.16	28.04	2.14	M34/2	Hensen (1996)
GeoB3718-9	-24.89333333	13.16333333	28.041	6.2	M34/2	Niewöhner et al. (1998)
GeoB8426-3	-25.481667	13.351667	27.06	3.45	M57/2	Riedinger et al. (2006)
GeoB8455-2	-25.506667	13.183333	27.695	4	M57/2	Riedinger et al. (2006)
ODP-1080	-16.559672	10.820048	26.17	6.7	Leg 175	Wefer et al. (1998)
ODP-1081	-19.619697	11.31933	26.54	59.1	Leg 175	Wefer et al. (1998)
ODP-1082	-21.093955	11.820602	29	22.18	Leg 175	Wefer et al. (1998)
ODP-1083	-20.894735	11.217867	27.93	33.6	Leg 175	Wefer et al. (1998)
ODP-1084	-25.513908	13.02778	29.27	5.9	Leg 175	Wefer et al. (1998)
ODP-1085	-29.374442	13.990107	27.18	41.9	Leg 175	Wefer et al. (1998)
ODP-208-1262A	-27.186	1.577	23.21	828.69	Leg 208	Zachos et al. (2004)
ODP-208-1262B	-27.18583	1.577	22.48		Leg 208	Zachos et al. (2004)
ODP-208-1262C	-27.18565	1.57698	22.76		Leg 208	Zachos et al. (2004)
ODP-208-1263A	-28.53283	2.77948	23.32		Leg 208	Zachos et al. (2004)
ODP-208-1263B	-28.53266	2.77941	25.54		Leg 208	Zachos et al. (2004)
ODP-208-1264A	-28.53268	2.84551	28.5		Leg 208	Zachos et al. (2004)
ODP-208-1265A	-28.83501	2.63933	26.8	2107.3	Leg 208	Zachos et al. (2004)
ODP-208-1265B	-28.83501	2.63911	24.2		Leg 208	Zachos et al. (2004)
ODP-208-1266A	-28.54268	2.3435	26.17	1659	Leg 208	Zachos et al. (2004)

Table B.2: Pore water $[SO_4]$ data compiled from literature sources (Hensen, 1996; Niewöhner et al., 1998; Wefer et al., 1998; Zachos et al., 2004; Riedinger et al., 2006; Goldhammer et al., 2011). The predicted depth of the sulphate-methane transition zone (SMTZ) is displayed and where blank no downward depletion was observed in the core extent.

Table B.3: SRM NIST 3104a and NBS-127 data generated in this study, Chapter 3.

Count	Standard	Date Measured	$\delta^{138/134}Ba$	$\delta^{138/134}Ba$ error	Average	2SE
1	NIST 17.1	01/06/2021	0.00	0.01		
2	NIST 17.2	01/06/2021	-0.03	0.01	-0.01	0.0165
3	NIST 17.3	01/06/2021	-0.01	0.01		
4	NIST 18.1	01/08/2021	-0.02	0.01		
5	NIST 18.2	01/08/2021	-0.03	0.01	-0.02	0.0067
6	NIST 18.3	01/08/2021	-0.03	0.01		
7	NIST 18.4	01/08/2021	-0.02	0.01		
8	NIST 19.1	01/05/2022	-0.06	0.01		
9	NIST 19.2	01/05/2022	-0.03	0.01		
10	NIST 19.3	01/05/2022	-0.07	0.01		
11	NIST 19.4	01/05/2022	-0.03	0.01	-0.04	0.0192
12	NIST 20.1	01/06/2022	-0.04	0.01		
13	NIST 20.2	01/06/2022	-0.02	0.01		
14	NIST 20.3	01/06/2022	0.01	0.01		
15	NIST 21.1	12/01/2023	-0.10	0.01		
16	NIST 21.2	12/01/2023	-0.04	0.01		
17	NIST 21.3	12/01/2023	-0.07	0.01		
18	NIST 21.4	12/01/2023	-0.07	0.01		
19	NIST 21.5	12/01/2023	-0.08	0.01		
20	NIST 22.1	10/02/2023	-0.12	0.01		
21	NIST 22.2	10/02/2023	-0.10	0.01		
22	NIST 22.3	10/02/2023	-0.06	0.01		
23	NIST 22.4	10/02/2023	-0.05	0.01		
24	NIST 22.5	10/02/2023	-0.01	0.01		
25	NIST 22.6	10/02/2023	0.00	0.01		
26	NIST 22.7	10/02/2023	-0.02	0.01		
27	NIST 22.8	10/02/2023	-0.01	0.01		
28	NIST 22.9	10/02/2023	0.00	0.01	-0.02	0.0177
29	NIST 23.1	30/04/2023	-0.03	0.01		
30	NIST 23.2	30/04/2023	-0.04	0.01		
31	NIST 23.3	30/04/2023	-0.04	0.01		
32	NIST 23.4	30/04/2023	0.00	0.01		
33	NIST 23.5	30/04/2023	0.00	0.01		
34	NIST 23.6	30/04/2023	-0.01	0.01		
35	NIST 23.7	30/04/2023	0.04	0.02		
36	NIST 24.1	20/05/2023	-0.01	0.01		
37	NIST 24.2	20/05/2023	0.02	0.01		
38	NIST 24.3	20/05/2023	0.02	0.01		
39	NIST 24.4	20/05/2023	0.01	0.01		
40	NIST 24.5	20/05/2023	0.05	0.01		
41	NIST 24.6	20/05/2023	0.06	0.01		

Table B.3: SRM NIST 3104a and NBS-127 data generated in this study, Chapter 3.

Count	Standard	Date Measured	$\delta^{138/134}Ba$	$\delta^{138/134}Ba$ error	Average	2SE
1	NBS 9.1	01/06/2021	-0.31	0.01	-0.30	0.0178
2	NBS 9.2	01/06/2021	-0.29	0.01		
3	NBS 10.1	01/08/2021	-0.30	0.01		
4	NBS 10.2	01/08/2021	-0.35	0.01	-0.31	0.0373
5	NBS 10.3	01/08/2021	-0.29	0.01		
6	NBS 11.1	01/05/2022	-0.34	0.01		
7	NBS 11.2	01/05/2022	-0.25	0.01		
8	NBS 11.3	01/05/2022	-0.31	0.01	-0.29	0.0267
9	NBS 11.4	01/05/2022	-0.28	0.01		
10	NBS 12.1	01/06/2022	-0.27	0.01		
11	NBS 12.2	01/06/2022	-0.26	0.01		
12	NBS 13.1	12/01/2023	-0.32	0.01		
13	NBS 13.2	12/01/2023	-0.32	0.01		
14	NBS 13.3	12/01/2023	-0.29	0.01		
15	NBS 13.4	12/01/2023	-0.34	0.01		
16	NBS 14.1	10/02/2023	-0.28	0.02		
17	NBS 14.2	10/02/2023	-0.25	0.01		
18	NBS 14.3	10/02/2023	-0.31	0.01		
19	NBS 14.4	10/02/2023	-0.30	0.01		
20	NBS 14.5	10/02/2023	-0.29	0.01		
21	NBS 14.6	10/02/2023	-0.29	0.01	-0.27	0.0188
22	NBS 15.1	30/04/2023	-0.26	0.01		
23	NBS 15.2	30/04/2023	-0.27	0.01		
24	NBS 15.3	30/04/2023	-0.23	0.01		
25	NBS 15.4	30/04/2023	-0.28	0.01		
26	NBS 16.1	20/05/2023	-0.27	0.01		
27	NBS 16.2	20/05/2023	-0.19	0.01		
28	NBS 16.3	20/05/2023	-0.24	0.01		
29	NBS 16.4	20/05/2023	-0.23	0.02		
30	NBS 16.5	20/05/2023	-0.20	0.01		

Table B.4: Total regional concentration and $\delta^{138/134}Ba$ data generated in this study, Chapter 3.

Depth (mbsl)	Type	Core	Latitude	Longitude	[Ba] TIMS	[Ba] ICP	[Mn]	[Fe]	Unit	$\delta^{138/134}Ba$ (‰)	$\delta^{138/134}Ba$ error (±2SE)
10	Particulate	20005	-20.000000	12.940000	279.5	206.9		21358.3	pmol/kg	0.09	0.02
10	Particulate	20040	-20.000000	12.150000	158.4	79.5		389.6	pmol/kg	0.24	0.02
10	Particulate	20070	-20.000000	11.790000	170.9	80.9		298.6	pmol/kg	0.27	0.07
10	Particulate	23005	-23.000000	14.370000	347.1	263.4		28502.5	pmol/kg	0.15	0.01
10	Particulate	23070	-23.000000	13.330000	154.3	90.6		1564.2	pmol/kg	0.28	0.03

Depth (mbsf)	Type	Core	Latitude	Longitude	[Ba] TIMS	[Ba] ICP	[Mn]	[Fe]	Unit	$\delta^{138/134}Ba$ (‰)	$\delta^{138/134}Ba$ error (±2SE)
0.03	Porewater	20010	-20.000000	12.860000	532.3	490.3	22.02	104.2	nmol/kg	0.37	0.02
0.09	Porewater	20010	-20.000000	12.860000	694.7	650.3	19.31	73.5	nmol/kg	0.36	0.01
0.14	Porewater	20010	-20.000000	12.860000	690.8	618.5	20.47	65.7	nmol/kg	0.41	0.01
0.19	Porewater	20010	-20.000000	12.860000	643.0	574.8	32.27	71.7	nmol/kg	0.37	0.01
0.235	Porewater	20010	-20.000000	12.860000	569.3	529.3	16.25	63.0	nmol/kg	0.34	0.01
0.29	Porewater	20010	-20.000000	12.860000	499.2	453.4	14.16	82.9	nmol/kg	0.34	0.01
0.31	Porewater	20010	-20.000000	12.860000		429.9	18.40	89.6	nmol/kg		
0.02	Porewater	20050	-20.000000	12.150000	111.1	121.1	16.02	4896.3	nmol/kg	0.33	0.01
0.055	Porewater	20050	-20.000000	12.150000		97.4	14.16	6891.9	nmol/kg		
0.085	Porewater	20050	-20.000000	12.150000		91.5	14.51	4268.5	nmol/kg		
0.135	Porewater	20050	-20.000000	12.150000		102.3	12.18	1737.5	nmol/kg		
0.175	Porewater	20050	-20.000000	12.150000		92.1	10.28	1243.1	nmol/kg		
0.205	Porewater	20050	-20.000000	12.150000		60.4	10.77	137.9	nmol/kg		
0.25	Porewater	20050	-20.000000	12.150000		82.2	11.10	549.5	nmol/kg		
0.01	Porewater	23010	-23.000000	14.230000	1322.0	1244.1	15.35	73.4	nmol/kg	0.32	0.02
0.03	Porewater	23010	-23.000000	14.230000	1476.5	1359.5	7.33	110.4	nmol/kg	0.30	0.02
0.05	Porewater	23010	-23.000000	14.230000	1522.2	1356.0	8.41	74.3	nmol/kg	0.23	0.09
0.07	Porewater	23010	-23.000000	14.230000	1451.3	1225.3	3.26	93.6	nmol/kg	0.19	0.02
0.11	Porewater	23010	-23.000000	14.230000	1455.6	1394.4	8.16	108.7	nmol/kg	0.15	0.01
0.17	Porewater	23010	-23.000000	14.230000	2382.4	2331.9	1.61	66.7	nmol/kg	0.12	0.05
0.19	Porewater	23010	-23.000000	14.230000	2960.2	2969.4	0.34	64.0	nmol/kg	0.08	0.01
0.21	Porewater	23010	-23.000000	14.230000	2886.9	3427.4	0.67	70.4	nmol/kg	0.15	0.02
0.23	Porewater	23010	-23.000000	14.230000	3439.4	4154.4	1.60	57.1	nmol/kg	0.14	0.04
0.02	Porewater	23030	-23.000000	13.860000	90.6	95.4	5.53	1352.4	nmol/kg	0.36	0.01
0.09	Porewater	23030	-23.000000	13.860000		115.3	8.43	1294.3	nmol/kg		
0.13	Porewater	23030	-23.000000	13.860000		89.7	30.50	206.8	nmol/kg		
0.19	Porewater	23030	-23.000000	13.860000		84.9	23.21	174.1	nmol/kg		
0.22	Porewater	23030	-23.000000	13.860000		78.2	26.27	197.4	nmol/kg		
0.29	Porewater	23030	-23.000000	13.860000		74.6	19.58	264.5	nmol/kg		
0.3	Porewater	23030	-23.000000	13.860000		83.6	22.94	165.4	nmol/kg		
0.02	Porewater	23060	-23.000000	13.330000	130.7	121.7	22.56	14907.9	nmol/kg	0.31	0.01
0.06	Porewater	23060	-23.000000	13.330000		120.9	13.60	2505.0	nmol/kg		
0.09	Porewater	23060	-23.000000	13.330000		41.6	-1.02	217.1	nmol/kg		

Table B.4: Total regional concentration and $\delta^{138/134}Ba$ data generated in this study, Chapter 3.

Depth (mbsf)	Type	Core	Latitude	Longitude	[Ba] TIMS	[Ba] ICP	[Mn]	[Fe]	Unit	$\delta^{138/134}Ba$ (‰)	$\delta^{138/134}Ba$ error (±2SE)
0.13	Porewater	23060	-23.000000	13.330000		116.4	6.90	163.5	nmol/kg		
0.17	Porewater	23060	-23.000000	13.330000		136.8	9.25	160.8	nmol/kg		
0.21	Porewater	23060	-23.000000	13.330000		111.7	7.30	93.9	nmol/kg		
0.25	Porewater	23060	-23.000000	13.330000		113.2	0.76	100.9	nmol/kg		
0.0	Porewater	U1575	-21.866097	6.590614	29.1	30.0	1181.90		nmol/kg	0.30	0.01
0.0	Porewater	U1575	-21.866097	6.590614	28.5	29.7	49.13		nmol/kg	0.27	0.01
0.1	Porewater	U1575	-21.866097	6.590614	27.2	29.1	41.48		nmol/kg	0.25	0.01
0.1	Porewater	U1575	-21.866097	6.590614	27.7	29.1	13.12		nmol/kg	0.28	0.01
0.0	Porewater	U1576	-24.595867	5.121939	32.3	32.6	1477.17		nmol/kg	0.28	0.01
0.0	Porewater	U1576	-24.595867	5.121939	34.9	36.3			nmol/kg	0.31	0.01
0.1	Porewater	U1576	-24.595867	5.121939	32.7	34.4			nmol/kg	0.31	0.01
0.1	Porewater	U1576	-24.595867	5.121939	32.7	34.4			nmol/kg	0.29	0.03
0.0	Porewater	U1577	-25.202397	7.496900	254.3	13.2	403.93		nmol/kg	-0.12	0.11
0.0	Porewater	U1577	-25.202397	7.496900	35.2	36.5	53.47		nmol/kg	0.33	0.01
0.1	Porewater	U1577	-25.202397	7.496900	35.9	37.3	217.30		nmol/kg	0.32	0.01
0.1	Porewater	U1577	-25.202397	7.496900	35.6	37.3			nmol/kg	0.35	0.01
0.0	Porewater	U1578	-32.328061	-0.643128	26.0	27.0	148.57		nmol/kg	0.31	0.01
0.0	Porewater	U1578	-32.328061	-0.643128	28.9	29.9	236.92		nmol/kg	0.32	0.01
0.1	Porewater	U1578	-32.328061	-0.643128	28.6	29.8			nmol/kg	0.31	0.01
0.1	Porewater	U1578	-32.328061	-0.643128	28.2	29.5	13.89		nmol/kg	0.30	0.01

Depth (mbsl)	Type	Core	Latitude	Longitude	[Ba] TIMS	[Ba] ICP	[Mn]	[Fe]	Unit	$\delta^{138/134}Ba$ (‰)	$\delta^{138/134}Ba$ error (±2SE)
10	Seawater	20005	-20.000000	12.940000	38.6	39.0			nmol/kg	0.64	0.02
10	Seawater	20005_pump	-20.000000	12.940000	38.9	35.1			nmol/kg	0.60	0.01
20.0	Seawater	20005	-20.000000	12.940000	40.3	40.3			nmol/kg	0.67	0.14
30.0	Seawater	20005	-20.000000	12.940000	41.0	41.0			nmol/kg	0.64	0.04
55	Seawater	20005	-20.000000	12.940000	39.1	36.6			nmol/kg	0.60	0.01
10	Seawater	20040	-20.000000	12.150000	37.8	34.6			nmol/kg	0.61	0.01
10	Seawater	20040_pump	-20.000000	12.150000	37.4	33.5			nmol/kg	0.65	0.02
151	Seawater	20040	-20.000000	12.150000	36.6	35.4			nmol/kg	0.62	0.01
211	Seawater	20040	-20.000000	12.150000	40.2	40.2			nmol/kg	0.65	0.04
5	Seawater	20070	-20.000000	11.790000	40.2	40.2			nmol/kg	0.67	0.02
10	Seawater	20070_pump	-20.000000	11.790000	38.5	38.1			nmol/kg	0.63	0.01
10.5	Seawater	20070	-20.000000	11.790000	38.7	34.9			nmol/kg	0.61	0.01
150	Seawater	20070	-20.000000	11.790000	38.0	35.7			nmol/kg	0.63	0.01
200	Seawater	20070	-20.000000	11.790000	36.9	34.2			nmol/kg	0.68	0.02
2	Seawater	23005	-23.000000	14.370000	44.5	44.5			nmol/kg	0.62	0.06
10	Seawater	23005_pump	-23.000000	14.370000	43.4	41.9			nmol/kg	0.61	0.01
10	Seawater	23005	-23.000000	14.370000	44.8	42.8			nmol/kg	0.56	0.01
20	Seawater	23005	-23.000000	14.370000	44.6	44.6			nmol/kg	0.63	0.02

Table B.4: Total regional concentration and $\delta^{138/134}Ba$ data generated in this study, Chapter 3.

Depth (mbsl)	Type	Core	Latitude	Longitude	[Ba] TIMS	[Ba] ICP	[Mn]	[Fe]	Unit	$\delta^{138/134}Ba$ (‰)	$\delta^{138/134}Ba$ error (±2SE)
30	Seawater	23005	-23.000000	14.370000	43.9	39.7			nmol/kg	0.59	0.01
65	Seawater	23005	-23.000000	14.370000	46.9	43.3			nmol/kg	0.59	0.05
1	Seawater	23070	-23.000000	13.330000	40.0	40.0			nmol/kg	0.64	0.22
10	Seawater	23070_pump	-23.000000	13.330000	37.8	34.2			nmol/kg	0.67	0.02
10	Seawater	23070	-23.000000	13.330000	40.6	35.1			nmol/kg	0.65	0.07
152	Seawater	23070	-23.000000	13.330000	40.7	35.2			nmol/kg	0.57	0.02
1.0	Seawater	U1265	-29.265500	2.983100	39.6	41.7			nmol/kg	0.59	0.01
1.0	Seawater	U1575	-21.866097	6.590614	36.4	39.6			nmol/kg	0.56	0.01
1.0	Seawater	U1576	-24.595867	5.121939	39.5	41.7			nmol/kg	0.59	0.01
1.0	Seawater	U1577	-25.202397	7.496900	39.0	40.4			nmol/kg	0.60	0.01
1.0	Seawater	U1578	-32.328061	-0.643128	39.2	41.1			nmol/kg	0.57	0.01
3847.2	Seawater	U1578	-32.328061	-0.643128	91.5	95.3			nmol/kg	0.34	0.01
1.0	Seawater	U1584	-31.338700	2.837017	41.9	42.9			nmol/kg	0.59	0.01
1.0	Seawater	U1585	-30.166933	1.177483	40.9	42.9			nmol/kg	0.60	0.01

Depth (mbsf)	Type	Core	Latitude	Longitude	[Ba] TIMS	[Ba] ICP	[Mn]	[Fe]	Unit	$\delta^{138/134}Ba$ (‰)	$\delta^{138/134}Ba$ error (±2SE)
0.0	Sediment	20002	-20.000000	13.000000	290.7	288.7	732.28	29081.97	μg/g	0.00	0.01
0.0	Sediment	20010	-20.000000	12.860000	194.1	197.4	126.23	13638.67	μg/g	0.04	0.01
0.1	Sediment	20010	-20.000000	12.860000	200.6	201.3	203.92	21221.72	μg/g	0.01	0.01
0.2	Sediment	20010	-20.000000	12.860000	124.7	129.0	125.79	17307.48	μg/g	0.00	0.01
0.3	Sediment	20010	-20.000000	12.860000	81.5	84.6	87.26	12984.65	μg/g	0.06	0.01
0.0	Sediment	20050	-20.000000	12.150000	114.1	117.3	109.05	16180.78	μg/g	0.05	0.01
0.1	Sediment	20050	-20.000000	12.150000	122.6	115.5	108.95	16503.95	μg/g	0.05	0.01
0.0	Sediment	23002	-23.000000	14.370000	90.2	89.9	44.97	9925.53	μg/g	0.12	0.01
0.005	Sediment	23010	-23.000000	14.230000	140.2	173.5	22.60	3780.20	μg/g	0.05	0.01
0.025	Sediment	23010	-23.000000	14.230000		167.4	32.60	4133.10	μg/g		
0.045	Sediment	23010	-23.000000	14.230000	128.2	159.4	24.40	3405.80	μg/g	0.10	0.02
0.065	Sediment	23010	-23.000000	14.230000	114.2	141.4	27.00	3634.80	μg/g	0.06	0.01
0.075	Sediment	23010	-23.000000	14.230000	139.7	180.6	31.60	4415.10	μg/g	0.09	0.02
0.085	Sediment	23010	-23.000000	14.230000		167.2	34.50	4379.10	μg/g		
0.095	Sediment	23010	-23.000000	14.230000		75.9	16.70	2123.90	μg/g		
0.105	Sediment	23010	-23.000000	14.230000	125.6	153.8	38.90	5155.80	μg/g	0.07	0.01
0.115	Sediment	23010	-23.000000	14.230000		149.0	45.00	6132.10	μg/g		
0.125	Sediment	23010	-23.000000	14.230000	131.0	161.9	57.10	7780.00	μg/g	0.08	0.02
0.135	Sediment	23010	-23.000000	14.230000		155.4	51.10	7379.50	μg/g		
0.145	Sediment	23010	-23.000000	14.230000	142.5	176.8	52.60	7853.80	μg/g	0.05	0.01
0.155	Sediment	23010	-23.000000	14.230000	180.4	221.0	64.90	8907.10	μg/g	0.05	0.02
0.165	Sediment	23010	-23.000000	14.230000		232.0	64.90	8916.70	μg/g		
0.175	Sediment	23010	-23.000000	14.230000	171.8	222.9	63.20	8543.30	μg/g	0.04	0.01
0.185	Sediment	23010	-23.000000	14.230000		244.5	87.50	9866.10	μg/g		

Table B.4: Total regional concentration and $\delta^{138/134}Ba$ data generated in this study, Chapter 3.

Depth (mbsf)	Type	Core	Latitude	Longitude	[Ba] TIMS	[Ba] ICP	[Mn]	[Fe]	Unit	$\delta^{138/134}Ba$ (‰)	$\delta^{138/134}Ba$ error (±2SE)
0.195	Sediment	23010	-23.000000	14.230000	174.0	241.8	53.60	6971.80	μg/g	0.05	0.01
0.215	Sediment	23010	-23.000000	14.230000	222.5	284.3	34.80	5015.90	μg/g	0.01	0.01
0.235	Sediment	23010	-23.000000	14.230000	369.8	494.0	33.20	5203.40	μg/g	0.01	0.01
0.255	Sediment	23010	-23.000000	14.230000	335.3	418.5	34.90	5145.00	μg/g	0.05	0.01
0.275	Sediment	23010	-23.000000	14.230000	460.4	626.8	51.10	7561.40	μg/g	0.03	0.01
0.295	Sediment	23010	-23.000000	14.230000	172.8	219.1	64.30	8829.90	μg/g	0.09	0.01
0.0	Sediment	23030	-23.000000	13.860000	65.0	69.1	31.40	5308.00	μg/g	0.06	0.01
0.1	Sediment	23030	-23.000000	13.860000	62.5	63.6	49.97	6075.76	μg/g	0.08	0.01
0.2	Sediment	23030	-23.000000	13.860000	56.1	59.6	53.32	6871.33	μg/g	0.07	0.01
0.3	Sediment	23030	-23.000000	13.860000	47.9	50.5	46.45	6219.47	μg/g	0.10	0.01
0.0	Sediment	23060	-23.000000	13.330000	41.6	44.3	23.59	6680.30	μg/g	0.09	0.01
0.1	Sediment	23060	-23.000000	13.330000	42.4	45.1	25.07	5576.64	μg/g	0.12	0.01
0.2	Sediment	23060	-23.000000	13.330000	40.7	43.7	26.76	7017.43	μg/g	0.09	0.01
0.01	Sediment	U1265	-29.265500	2.983100	238.0	236.9	243.27	1865.48	μg/g	0.12	0.01
0	Sediment	U1575	-21.866097	6.590614	364.6	363.5	236.32	1998.72	μg/g	0.22	0.02
0.005	Sediment	U1575	-21.866097	6.590614	369.5	382.0	263.01	1902.91	μg/g	0.15	0.02
0.045	Sediment	U1575	-21.866097	6.590614	364.8	377.5	235.24	2031.64	μg/g	0.16	0.01
0.095	Sediment	U1575	-21.866097	6.590614	354.9	362.2	264.61	1867.02	μg/g	0.14	0.02
0	Sediment	U1576	-24.595867	5.121939	554.3	576.3	298.31	2214.95	μg/g	0.16	0.01
0.005	Sediment	U1576	-24.595867	5.121939		454.7	287.09	1597.39	μg/g		
0.045	Sediment	U1576	-24.595867	5.121939	656.8	662.7	308.91	2444.47	μg/g	0.11	0.01
0.095	Sediment	U1576	-24.595867	5.121939	637.6	644.4	327.29	2320.34	μg/g	0.13	0.02
0.005	Sediment	U1577	-25.202397	7.496900	246.5	244.4	251.96	2628.01	μg/g	0.14	0.02
0.015	Sediment	U1577	-25.202397	7.496900	206.4	205.9	251.48	3356.70	μg/g	0.13	0.02
0.045	Sediment	U1577	-25.202397	7.496900	316.1	320.1	325.55	3735.41	μg/g	0.14	0.03
0.095	Sediment	U1577	-25.202397	7.496900	265.8	268.9	274.82	2837.10	μg/g	0.14	0.02
0	Sediment	U1578	-32.328061	-0.643128	284.8	285.6	459.33	3029.01	μg/g	0.17	0.02
0.005	Sediment	U1578	-32.328061	-0.643128	272.9	273.6	312.49	1984.35	μg/g	0.11	0.01
0.045	Sediment	U1578	-32.328061	-0.643128	294.9	293.1	328.19	2010.08	μg/g	0.16	0.01
0.095	Sediment	U1578	-32.328061	-0.643128	314.0	313.0	353.59	2316.82	μg/g	0.14	0.03

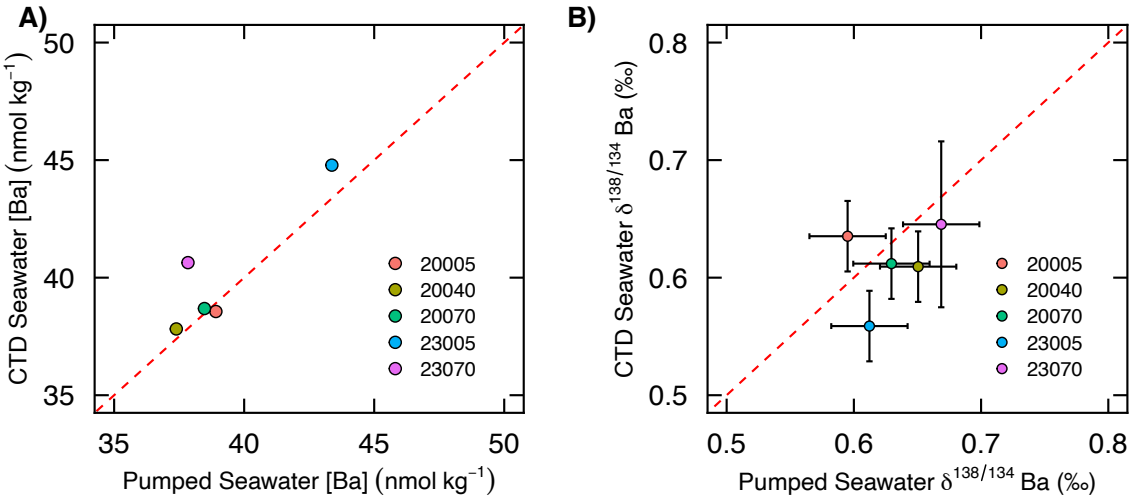

Figure B.1: DBa concentration and $\delta^{138/134}Ba$ of pumped vs CTD Niskin bottle collection methods. a) DBa concentration and b) $\delta^{138/134}Ba$ values measured on co-located samples collected using Niskin bottles mounted on a CTD Sea-Bird SBE 9 rosette and the peristaltic pump methods. The red dashed line is 1:1.

B.2 Contouring of oxygen penetration depth data

Literature data of pore water oxygen penetration depth for samples spanning the BUS and Walvis Ridge have been compiled from literature sources to provide a more regional context of pore water redox conditions, relevant for understanding benthic Ba fluxes in this region (Table B.1; Glud et al. (1994); Wefer et al. (1997); Emeis et al. (2018)). To identify spatial changes in redox zones the pore water oxygen penetration depth has been contoured using QGIS 3.34.2-Prizren mapping software using the contour plugin. In which, a contour layer was generated based on an attribute of a point vector layer in this case pore water oxygen penetration depth. Contours were generated using a fixed contour interval of 0.01 $cmbsf$ with a tolerance of 0.001 and were bound to the initial data extent (Figure 3.2a).

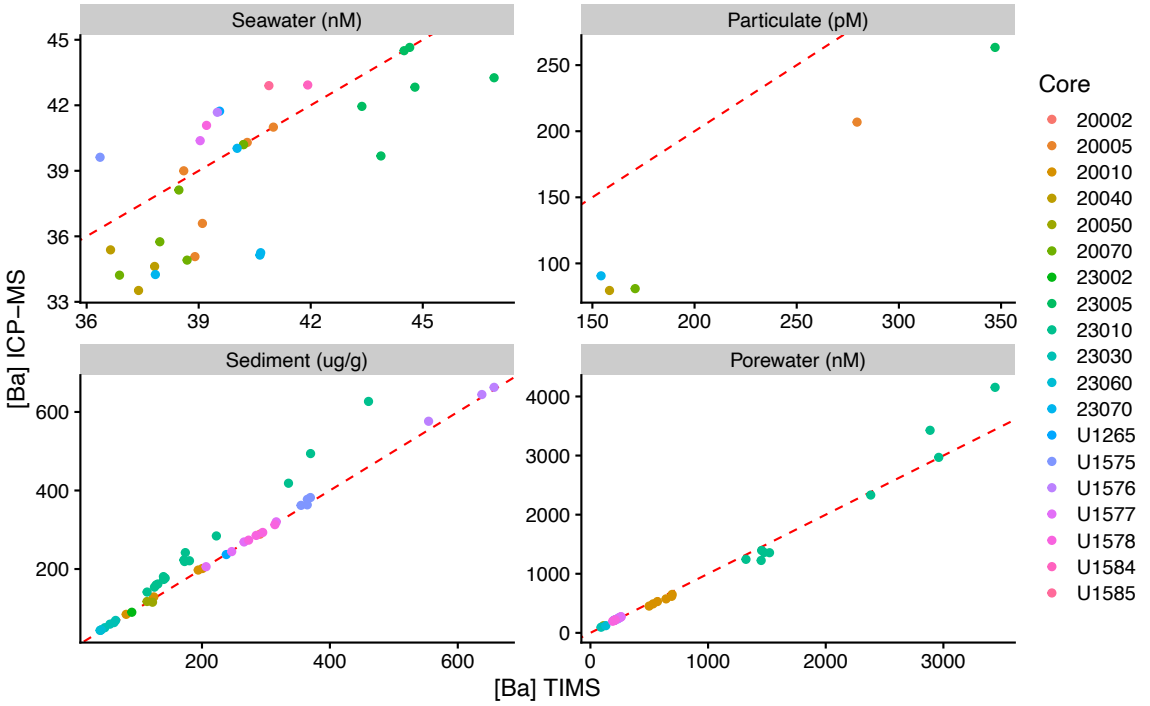

Figure B.2: TIMS vs ICP-MS derived Ba concentration. Data are presented for a) seawater samples, b) suspended particulate samples, c) marine sediment samples, and d) pore water samples. The red dashed line is 1:1. Axes units for each subplot are listed in the respective title grey box.

Element	SGR-1b (μg/g)	Certified (μg/g)	Recovery (%)	BCR-414 (μg/g)	Certified (μg/g)	Recovery (%)
Fe	19345	21200	91.2	1728		
P	1191	1430	83.3	11329		
Ti	1331	1520	87.5	102		
V	116	128	90.6	5.39	8.10	66.6
Cr	29.2	30.0	97.5	16.9	23.8	70.8
Mn	225	267	84.3	170	299.0	56.8
Co	11.2	12.0	93.2	1.08		
Ni	27.7	29.0	95.6	11.3	18.8	60.0
Cu	55.2	66.0	83.7	18.0	29.5	61.1
Zn	62.2	74.0	84.1	87.4	111.6	78.3
Ba	266	290	91.8	26.3		
Ca	51626	59900	86.2			
Mo	36.2	35.0	103	1.17		
Cd	1.04	0.900	116	-0.181	0.383	-47.3
Sr	368	420	87.7			
K	12564	13800	91.0			
Mg	24633	26800	91.9			
Al	31786	34500	92.1			

Table B.5: Sediment and particulate digestion efficiencies measured on the ICP-MS. The efficiency of the sediment and particulate digestion method was evaluated by comparing the measured to published CRM data for SGR-1b and BCR-414, respectively.

Depth (mbr)	Type	Core	Latitude	Longitude	Instrument	[Ba]	Unit	$\delta^{138/134}Ba$	$\delta^{138/134}Ba$ error
1	Seawater	U1265	-29.2655	2.9831	TIMS	39.6	nM	0.59	0.01
1	Seawater	U1265	-29.2655	2.9831	TIMS	39.6	nM	0.58	0.02
3847.2	Seawater	U1578	-32.328061	-0.643128	TIMS	91.5	nM	0.35	0.01
3847.2	Seawater	U1578	-32.328061	-0.643128	TIMS	91.5	nM	0.34	0.01
3847.2	Seawater	U1578	-32.328061	-0.643128	TIMS	91.5	nM	0.35	0.03
0.045	Sediment	U1577	-25.20239722	7.4969	MC-ICP-MS	346	ug/g	0.14	0.04
0.045	Sediment	U1577	-25.20239722	7.4969	TIMS	320	ug/g	0.14	0.03
10	Particulate	20005	-20	12.94	MC-ICP-MS	228	pM	0.10	0.01
10	Particulate	20005	-20	12.94	TIMS	207	pM	0.09	0.02
10	Particulate	23005	-23	14.37	MC-ICP-MS	241	pM	0.13	0.04
10	Particulate	23005	-23	14.37	TIMS	263	pM	0.15	0.01
0.01	Pore water	23010	-23	14.23	MC-ICP-MS	183	ug/L	0.34	0.04
0.01	Pore water	23010	-23	14.23	TIMS	182	ug/L	0.32	0.02

Table B.6: Ba concentration and $\delta^{138/134}Ba$ values for repeated selected samples of different sample type. Samples analysed on the MC-ICP-MS were measured at NTU whilst samples analysed on the TIMS were measured at the University of Oxford. Depth scale is metres below reference (mbr): for seawater and particulate samples this is below sea level whilst for sediment and pore water samples it is below seafloor.

ID	Date	Instrument	Sample Type	DS conc (ppb)	DS amount (ml)	Blank (ng)	Blank contribution (%)
1	17/03/2021	ICP-MS	Sediment	n/a	n/a	0.793	0.124
2	15/06/2021	TIMS	Sediment	10951	0.104	3.06	0.00156
3	07/09/2021	TIMS	Pore water	10438	0.0501	2.14	0.982
4	09/05/2022	ICP-MS	Sediment	n/a	n/a	0.237	0.0724
5	23/05/2022	TIMS	Pore water & Seawater	10765	0.0502	2.17	2.61
6	28/06/2022	TIMS	Sediment	10492	0.296	0.710	0.000670
7	07/10/2022	ICP-MS	Pore water & Seawater	n/a	n/a	0.021	0.0890
8	11/01/2023	TIMS	Pore Water	10912	0.0776	2.33	3.98
9	10/02/2023	TIMS	Pore water	10585	0.0500	2.05	6.60
10	29/03/2023	ICP-MS	Particulate	n/a	n/a	0.072	2.77
11	29/03/2023	ICP-MS	Sediment	n/a	n/a	0.199	0.0182
12	04/05/2023	TIMS	Sediment	10872	0.297	0.690	0.000193
13	13/06/2023	TIMS	Sediment & Particulate	10420	0.0500	1.23	0.000398
14	02/11/2023	MC-ICP-MS	Seawater	n/a	0.0516	13.51	5.4
15	20/11/2023	MC-ICP-MS	Seawater	n/a	0.0516	4.98	2
16	17/01/2024	MC-ICP-MS	Sediment	n/a	0.298	0.93	0.000202
17	17/01/2024	MC-ICP-MS	Particulate	n/a	0.05	11.43	1.4

Table B.7: Procedural blank data generated throughout the processing of seawater, suspended particulate matter, marine sediment, and pore water in Chapter 3. The instrument used to measure the procedural blank data is included, and, where appropriate, details of double-spike added.

Location	$Ba/Al_{detrital}$ reference ratio	Reference
Congo Fan	0.0045	Rutsch et al. (1995)
Angola Basin	0.0035	Pfeifer et al. (2001)
Atlantic Average	0.0031	Reitz et al. (2004)
Global Average	0.0037	Reitz et al. (2004)
Atlantic Transect	0.0055 ± 0.0005	Bridgestock et al. (2018)
Upper Continental Crust	0.0075	Reitz et al. (2004)

Table B.8: $Ba/Al_{detrital}$ reference ratios. Varied $Ba/Al_{detrital}$ reference ratios have been measured across the modern oceans that can be used during the calculation of Ba_{excess}. No direct measurements exist for the Namibian margin, ergo a reference ratio of 0.004 ± 0.0005 is selected for this study to encompass data from the Congo Fan and the Angolan basin

Table B.9: $[Ba]$ and $\delta^{138/134}Ba$ data for each input and output flux component of the marine Ba mass balance from literature.

Dataset	Origin (location or depth (mbsl))	$\delta^{138/134}Ba$	$\delta^{138/134}Ba$ error	[Ba]	error	Reference
River	Amazon	0.01	0.06	268	46	Bridgestock et al. (2021b)
River	Johor	0.11	0.06	512	74	Bridgestock et al. (2021b)
River	Fly	0.06	0.12	1039	318	Bridgestock et al. (2021b)
River	Eastward Lena River Plume	0.2	0.06	197	27	Bridgestock et al. (2021a)
River	Northward Lena River Plume	0.25	0.05	100	11	Bridgestock et al. (2021a)
River	Yangtze 2015	0.13	0.05	450	5	Cao et al. (2021)
River	Yangtze 2019	0.12	0.05	565	5	Cao et al. (2021)
River	Pearl 2015	0.2	0.05	235	5	Cao et al. (2021)
River	Pearl 2017	0.12	0.05	265	5	Cao et al. (2021)
River	Congo	0.05	0.06	203.6	2.9	Zhang et al. (2023)
Groundwater Discharge	KaBpiez1 - Extrusive Igneous	0.4	0.04	10		Mayfield et al. (2021)
Groundwater Discharge	KaBWell - Extrusive Igneous	0.16	0.03	2		Mayfield et al. (2021)
Groundwater Discharge	KONA_104 - Extrusive Igneous	0.08		16		Mayfield et al. (2021)
Groundwater Discharge	KONA_300 - Extrusive Igneous	0.02		8		Mayfield et al. (2021)
Groundwater Discharge	KONA_85 - Extrusive Igneous	0.11		12		Mayfield et al. (2021)
Groundwater Discharge	KONA_92 - Extrusive Igneous	-0.03		10		Mayfield et al. (2021)
Groundwater Discharge	KONA_93 - Extrusive Igneous	0.03		9		Mayfield et al. (2021)
Groundwater Discharge	M1 - Extrusive Igneous	-0.18	0.08	4		Mayfield et al. (2021)
Groundwater Discharge	M9 - Extrusive Igneous	0.42	0.03	6		Mayfield et al. (2021)
Groundwater Discharge	Th_12 - Extrusive Igneous	0.11		58		Mayfield et al. (2021)
Groundwater Discharge	Th_53 - Extrusive Igneous	0.19		6		Mayfield et al. (2021)
Groundwater Discharge	Th_60 - Extrusive Igneous	0.13		76		Mayfield et al. (2021)
Groundwater Discharge	LJL228 - Extrusive Igneous	0.36	0.03	15		Mayfield et al. (2021)
Groundwater Discharge	LJL229 - Extrusive Igneous	0.33	0.03	205		Mayfield et al. (2021)
Groundwater Discharge	V Artisian Well - Carbonate	0.04	0.03	313		Mayfield et al. (2021)
Groundwater Discharge	VP4 - Carbonate	0.1	0.03	68		Mayfield et al. (2021)
Groundwater Discharge	Rott4 - Carbonate	0.24	0.06	2		Mayfield et al. (2021)
Groundwater Discharge	Rott5 - Carbonate	0.09	0.04	30		Mayfield et al. (2021)
Groundwater Discharge	CAL 212 - Carbonate	-0.13	0.03	117		Mayfield et al. (2021)
Groundwater Discharge	CAL 213 - Carbonate	0.09	0.03	261		Mayfield et al. (2021)
Groundwater Discharge	GW 213 - Carbonate	0.46	0.03	14		Mayfield et al. (2021)
Groundwater Discharge	FIC_17 - Carbonate	0.24	0.04	51		Mayfield et al. (2021)

Table B.9: $[Ba]$ and $\delta^{138/134}Ba$ data for each input and output flux component of the marine Ba mass balance from literature.

Dataset	Origin (location or depth (mbsl))	$\delta^{138/134}Ba$	$\delta^{138/134}Ba$ error	[Ba]	error	Reference
Groundwater Discharge	SGD Eilat - Intrusive Igneous	0.49	0.03	16		Mayfield et al. (2021)
Groundwater Discharge	MB Hopkins 11 - Intrusive Igneous	0.23	0.03	37		Mayfield et al. (2021)
Groundwater Discharge	MB Hopkins 18 - Intrusive Igneous	0.39	0.03	39		Mayfield et al. (2021)
Groundwater Discharge	WP 3-S - Intrusive Igneous	0.25	0.05	11		Mayfield et al. (2021)
Groundwater Discharge	WP 5-5 - Intrusive Igneous	0.04	0.05	13		Mayfield et al. (2021)
Groundwater Discharge	WP 6-5 - Intrusive Igneous	0.07	0.06	9		Mayfield et al. (2021)
Groundwater Discharge	DT1 - Intrusive Igneous	0.04	0.04	1		Mayfield et al. (2021)
Groundwater Discharge	DT2 - Intrusive Igneous	-0.28	0.03	106		Mayfield et al. (2021)
Groundwater Discharge	GSB Ba peak - Intrusive Igneous	0.07	0.03	173		Mayfield et al. (2021)
Groundwater Discharge	GSB Fresh - Intrusive Igneous	-0.01	0.07	25		Mayfield et al. (2021)
Groundwater Discharge	AK_102 - Intrusive Igneous	0.28		15		Mayfield et al. (2021)
Groundwater Discharge	AK_115 - Intrusive Igneous	0.39		10		Mayfield et al. (2021)
Groundwater Discharge	AK_131 - Intrusive Igneous	0.4		9		Mayfield et al. (2021)
Groundwater Discharge	AK_15 - Intrusive Igneous	0.37		8		Mayfield et al. (2021)
Groundwater Discharge	AK_48 - Intrusive Igneous	0.3		9		Mayfield et al. (2021)
Groundwater Discharge	AK_49 - Intrusive Igneous	0.22		20		Mayfield et al. (2021)
Groundwater Discharge	AK_75 - Intrusive Igneous	0.25		8		Mayfield et al. (2021)
Groundwater Discharge	Aus 3 - Sedimentary	-0.01	0.04	775		Mayfield et al. (2021)
Groundwater Discharge	MB_31 - Sedimentary	0.26		27		Mayfield et al. (2021)
Groundwater Discharge	MB_34 - Sedimentary	0.28		14		Mayfield et al. (2021)
Groundwater Discharge	MB_38 - Sedimentary	0.36		12		Mayfield et al. (2021)
Groundwater Discharge	MB_56 - Sedimentary	0.25		13		Mayfield et al. (2021)
Groundwater Discharge	MB_78 - Sedimentary	0.29		8		Mayfield et al. (2021)
Groundwater Discharge	SA Fresh - Sedimentary	0.25	0.03	60		Mayfield et al. (2021)
Groundwater Discharge	SA SL-EM-#3 - Sedimentary	0.15	0.03	26		Mayfield et al. (2021)
Groundwater Discharge	SFB_2 - Sedimentary	0.09		30		Mayfield et al. (2021)
Groundwater Discharge	SFB_22 - Sedimentary	0.25		22		Mayfield et al. (2021)
Groundwater Discharge	SFB_27 - Sedimentary	0.14		36		Mayfield et al. (2021)
Groundwater Discharge	SFB_39 - Sedimentary	0.18		37		Mayfield et al. (2021)
Groundwater Discharge	SFB_72 - Sedimentary	0.08		39		Mayfield et al. (2021)
Hydrothermal fluid	MAR Rainbow (36°N)	0.17		92	7	Hsieh et al. (2021)
Hydrothermal fluid	EPR (9–10°N)	0.03		10	2	Hsieh et al. (2021)

Table B.9: $[Ba]$ and $\delta^{138/134}Ba$ data for each input and output flux component of the marine Ba mass balance from literature.

Dataset	Origin (location or depth (mbsl))	$\delta^{138/134}Ba$	$\delta^{138/134}Ba$ error	[Ba]	error	Reference
Hydrothermal fluid	EPR (13°N)	0.03		16	2	Hsieh et al. (2021)
Hydrothermal fluid	JdFR MEF	0.09		70	6	Hsieh et al. (2021)
Hydrothermal fluid	Effective Hydrothermal input	1.7	0.07			Hsieh et al. (2021)
Hydrothermal fluid	Extrapolated Rainbow Vent Fluid	-0.17	0.05	4.6	2.2	Zhang et al. (2024)
Barite Deposit	Pelagic	0.09	0.03			Crockford et al. (2019)
Barite Deposit	Pelagic	0.09	0.03			Crockford et al. (2019)
Barite Deposit	Pelagic	0.03	0.03			Crockford et al. (2019)
Barite Deposit	Pelagic	0.00	0.03			Crockford et al. (2019)
Barite Deposit	Pelagic	0.05	0.03			Crockford et al. (2019)
Barite Deposit	Pelagic	0.08	0.03			Crockford et al. (2019)
Barite Deposit	Pelagic	-0.04	0.03			Crockford et al. (2019)
Barite Deposit	Pelagic	0.10	0.03			Crockford et al. (2019)
Barite Deposit	Pelagic	0.04	0.03			Crockford et al. (2019)
Barite Deposit	Pelagic	0.05	0.03			Crockford et al. (2019)
Barite Deposit	Pelagic	0.06	0.03			Crockford et al. (2019)
Barite Deposit	Pelagic	0.09	0.03			Crockford et al. (2019)
Barite Deposit	Pelagic	0.08	0.03			Crockford et al. (2019)
Barite Deposit	Pelagic	-0.03	0.03			Crockford et al. (2019)
Barite Deposit	Pelagic	-0.08	0.03			Crockford et al. (2019)
Barite Deposit	Pelagic	0.01	0.03			Crockford et al. (2019)
Barite Deposit	Pelagic	0.10	0.03			Crockford et al. (2019)
Barite Deposit	Pelagic	0.01	0.03			Crockford et al. (2019)
Barite Deposit	Pelagic	0.04	0.03			Crockford et al. (2019)
Barite Deposit	Pelagic	0.08	0.03			Crockford et al. (2019)
Barite Deposit	Pelagic	-0.04	0.03			Crockford et al. (2019)
Barite Deposit	Pelagic	0.11	0.03			Crockford et al. (2019)
Barite Deposit	Pelagic	-0.02	0.03			Crockford et al. (2019)
Barite Deposit	Pelagic	0.08	0.03			Crockford et al. (2019)
Barite Deposit	Pelagic	0.09	0.03			Crockford et al. (2019)
Barite Deposit	Pelagic	0.10	0.03			Crockford et al. (2019)
Barite Deposit	Pelagic	-0.04	0.03			Crockford et al. (2019)
Barite Deposit	Pelagic	0.05	0.03			Crockford et al. (2019)

Table B.9: $[Ba]$ and $\delta^{138/134}Ba$ data for each input and output flux component of the marine Ba mass balance from literature.

Dataset	Origin (location or depth (mbsl))	$\delta^{138/134}Ba$	$\delta^{138/134}Ba$ error	[Ba]	error	Reference
Barite Deposit	Pelagic	0.11	0.03			Crockford et al. (2019)
Barite Deposit	Pelagic	0.06	0.03			Crockford et al. (2019)
Barite Deposit	Pelagic	0.07	0.03			Crockford et al. (2019)
Barite Deposit	Pelagic	0.10	0.03			Crockford et al. (2019)
Barite Deposit	Pelagic	0.07	0.03			Crockford et al. (2019)
Barite Deposit	Pelagic	0.09	0.03			Crockford et al. (2019)
Barite Deposit	Pelagic	0.07	0.03			Crockford et al. (2019)
Barite Deposit	Pelagic	0.09	0.03			Crockford et al. (2019)
Barite Deposit	Pelagic	0.07	0.03			Crockford et al. (2019)
Barite Deposit	Pelagic	0.04	0.03			Crockford et al. (2019)
Barite Deposit	Pelagic	0.09	0.03			Crockford et al. (2019)
Barite Deposit	Pelagic	0.07	0.03			Crockford et al. (2019)
Barite Deposit	Pelagic	0.00	0.03			Crockford et al. (2019)
Barite Deposit	Pelagic	-0.03	0.03			Crockford et al. (2019)
Barite Deposit	Pelagic	0.13	0.03			Crockford et al. (2019)
Barite Deposit	Pelagic	-0.07	0.03			Crockford et al. (2019)
Barite Deposit	Pelagic	0.12	0.03			Crockford et al. (2019)
Barite Deposit	Pelagic	0.08	0.03			Crockford et al. (2019)
Barite Deposit	Pelagic	0.04	0.03			Crockford et al. (2019)
Barite Deposit	Pelagic	0.11	0.03			Crockford et al. (2019)
Barite Deposit	Pelagic	0.06	0.03			Crockford et al. (2019)
Barite Deposit	Pelagic	-0.02	0.03			Crockford et al. (2019)
Barite Deposit	Pelagic	-0.21	0.03			Crockford et al. (2019)
Barite Deposit	Pelagic	-0.01	0.03			Crockford et al. (2019)
Barite Deposit	Pelagic	-0.06	0.03			Crockford et al. (2019)
Barite Deposit	Pelagic	-0.09	0.03			Crockford et al. (2019)
Barite Deposit	Pelagic	0.03	0.03			Crockford et al. (2019)
Barite Deposit	Pelagic	0.04	0.03			Crockford et al. (2019)
Barite Deposit	Pelagic	-0.02	0.03			Crockford et al. (2019)
Barite Deposit	Pelagic	0.09	0.03			Crockford et al. (2019)
Barite Deposit	Pelagic	0.10	0.03			Crockford et al. (2019)
Barite Deposit	Pelagic	0.07	0.03			Crockford et al. (2019)

Table B.9: $[Ba]$ and $\delta^{138/134}Ba$ data for each input and output flux component of the marine Ba mass balance from literature.

Dataset	Origin (location or depth (mbsl))	$\delta^{138/134}Ba$	$\delta^{138/134}Ba$ error	[Ba]	error	Reference
Barite Deposit	Pelagic	0.08	0.03			Crockford et al. (2019)
Downwelling	0	0.61	0.03	40.5		Zhang et al. (2023)
Downwelling	0	0.29	0.05	75.5		Zhang et al. (2023)
Downwelling	0	0.58	0.05	41		Zhang et al. (2023)
Downwelling	0	0.61	0.03	41.9		Zhang et al. (2023)
Downwelling	0	0.35	0.03	61.7		Zhang et al. (2023)
Downwelling	0	0.19	0.05	92.2		Zhang et al. (2023)
Downwelling	0	0.16	0.01	92.7		Zhang et al. (2023)
Downwelling	0	0.2	0.06	92.6		Zhang et al. (2023)
Downwelling	0	0.52	0.01	49.5		Zhang et al. (2023)
Downwelling	0	0.48	0.02	51.7		Zhang et al. (2023)
Downwelling	0	0.51	0.05	50.7		Zhang et al. (2023)
Downwelling	0	0.47	0.01	48.6		Zhang et al. (2023)
Downwelling	0	0.46	0.05	48.8		Zhang et al. (2023)
Downwelling	0	0.53	0.04	48.2		Zhang et al. (2023)
Downwelling	0	0.6	0.03	40.6		Zhang et al. (2023)
Downwelling	0	0.55	0.01	42.2		Zhang et al. (2023)
Downwelling	0	0.61	0.06	38.9		Zhang et al. (2023)
Downwelling	0	0.61	0.02	38.4		Zhang et al. (2023)
Downwelling	0	0.6	0.03	41		Zhang et al. (2023)
Downwelling	0	0.6	0.04	40.7		Zhang et al. (2023)
Downwelling	0	0.26	0.03	74.7		Zhang et al. (2023)
Downwelling	0	0.23	0.06	94		Zhang et al. (2023)
Downwelling	0	0.22	0.05	93.8		Zhang et al. (2023)
Downwelling	0	0.17	0.01	101.8		Zhang et al. (2023)
Downwelling	0	0.42	0.06	53		Zhang et al. (2023)
Downwelling	0	0.48	0.05	51		Zhang et al. (2023)
Downwelling	0	0.49	0.06	45.6		Zhang et al. (2023)
Downwelling	0	0.53	0.03	46.4		Zhang et al. (2023)
Downwelling	0	0.6	0.02	42.3		Zhang et al. (2023)
Downwelling	0	0.59	0.02	41.6		Zhang et al. (2023)
Downwelling	0	0.59	0.05	41.5		Zhang et al. (2023)

Table B.9: $[Ba]$ and $\delta^{138/134}Ba$ data for each input and output flux component of the marine Ba mass balance from literature.

Dataset	Origin (location or depth (mbsl))	$\delta^{138/134}Ba$	$\delta^{138/134}Ba$ error	[Ba]	error	Reference
Downwelling	0	0.44	0.03	68.8		Hemsing et al. (2018)
Downwelling	3.1	0.59	0.14	33.5		Cao et al. (2020)
Downwelling	5	0.29	0.05	76.5		Hsieh and Henderson (2017)
Downwelling	5	0.37	0.03	69.3		Hsieh and Henderson (2017)
Downwelling	5	0.41	0.02	51.6		Hsieh and Henderson (2017)
Downwelling	5	0.4	0.02	64.9		Hsieh and Henderson (2017)
Downwelling	5	0.5	0.03	55.2		Hemsing et al. (2018)
Downwelling	5	0.58	0.03	43.6		Horner et al. (2015)
Downwelling	5	0.606	0.02	39.85	0.5	Geyman et al. (2019)
Downwelling	5.1	0.64	0.01	34.9		Cao et al. (2020)
Downwelling	5.6	0.57	0.07	34.5		Cao et al. (2020)
Downwelling	5.9	0.6	0.04	33.4		Cao et al. (2020)
Downwelling	6.2	0.63	0.02	36.2		Cao et al. (2020)
Downwelling	10	0.49	0.04	52.53		Yu et al. (2022)
Downwelling	10	0.53	0.04	39.89		Yu et al. (2022)
Downwelling	10	0.45	0.04	50.54		Yu et al. (2022)
Downwelling	11	0.52	0.02	44.7		Hsieh and Henderson (2017)
Downwelling	11	0.57	0.04	36.9	1.1	Bates et al. (2017)
Downwelling	14	0.58	0.03	43.5		Hsieh and Henderson (2017)
Downwelling	14	0.42	0.04	59.58		Yu et al. (2022)
Downwelling	15	0.517	0.024	39.89	0.5	Geyman et al. (2019)
Downwelling	15	0.49	0.04	43.96		Yu et al. (2022)
Downwelling	16	0.58	0.02	42		Bridgestock et al. (2018)
Downwelling	16	0.56	0.01	43		Bridgestock et al. (2018)
Downwelling	20	0.62	0.02	34.2		Hsieh and Henderson (2017)
Downwelling	20	0.61	0.02	34.3		Hsieh and Henderson (2017)
Downwelling	20	0.56	0.06	33	2	Middleton et al. (2023a)
Downwelling	20	0.65	0.07	31	2	Middleton et al. (2023a)
Downwelling	20	0.59	0.05	31	2	Middleton et al. (2023a)
Downwelling	20	0.53	0.04	43.71		Yu et al. (2022)
Downwelling	23	0.59	0.03	43.7		Horner et al. (2015)
Downwelling	24	0.56	0.02	42		Bridgestock et al. (2018)

Table B.9: $[Ba]$ and $\delta^{138/134}Ba$ data for each input and output flux component of the marine Ba mass balance from literature.

Dataset	Origin (location or depth (mbsl))	$\delta^{138/134}Ba$	$\delta^{138/134}Ba$ error	[Ba]	error	Reference
Downwelling	24.2	0.61	0.02	33.3		Cao et al. (2020)
Downwelling	25	0.64	0.03	32.6		Hsieh and Henderson (2017)
Downwelling	25	0.62	0.04	34.7		Cao et al. (2020)
Downwelling	25	0.605	0.015	35.04	0.44	Geyman et al. (2019)
Downwelling	25	0.63	0.04	29.38		Yu et al. (2022)
Downwelling	25.1	0.59	0.02	34.8		Cao et al. (2020)
Downwelling	25.2	0.61	0.1	36		Cao et al. (2020)
Downwelling	25.4	0.52	0.08	33.2		Cao et al. (2020)
Downwelling	29	0.63	0.03	40.7		Zhang et al. (2023)
Downwelling	30	0.31	0.03	84.8		Hsieh and Henderson (2017)
Downwelling	35	0.32	0.02	85.2		Hsieh and Henderson (2017)
Downwelling	35	0.49	0.04	46.34		Yu et al. (2022)
Downwelling	39	0.62	0.02	41.1		Zhang et al. (2023)
Downwelling	39	0.49	0.04	44.47		Yu et al. (2022)
Downwelling	40	0.57	0.06	30	2	Middleton et al. (2023a)
Downwelling	41	0.57	0.02	43		Bridgestock et al. (2018)
Downwelling	43	0.59	0.03	40.7		Zhang et al. (2023)
Downwelling	43	0.62	0.05	40.1		Zhang et al. (2023)
Downwelling	47	0.57	0.03	43.7		Horner et al. (2015)
Downwelling	48	0.509	0.035	46.99	0.59	Geyman et al. (2019)
Downwelling	50	0.34	0.03	85.3		Hsieh and Henderson (2017)
Downwelling	50	0.5	0.03	57.6		Hemsing et al. (2018)
Downwelling	50	0.49	0.04	52.35		Yu et al. (2022)
Downwelling	51	0.53	0.04	43.02		Yu et al. (2022)
Downwelling	51	0.53	0.02	44.3		Hsieh and Henderson (2017)
Downwelling	51	0.57	0.02	45		Bridgestock et al. (2018)
Downwelling	51.2	0.57	0.05	35.3		Cao et al. (2020)
Downwelling	51.9	0.57	0.09	33.1		Cao et al. (2020)
Downwelling	52	0.61	0.04	41.3		Zhang et al. (2023)
Downwelling	55	0.31	0.01	85.4		Hsieh and Henderson (2017)
Downwelling	55	0.57	0.07	36	1.1	Bates et al. (2017)
Downwelling	69	0.62	0.05	31	2	Middleton et al. (2023a)

Table B.9: $[Ba]$ and $\delta^{138/134}Ba$ data for each input and output flux component of the marine Ba mass balance from literature.

Dataset	Origin (location or depth (mbsl))	$\delta^{138/134}Ba$	$\delta^{138/134}Ba$ error	[Ba]	error	Reference
Downwelling	70	0.59	0.05	33	2	Middleton et al. (2023a)
Downwelling	73	0.53	0.02	31.9		Cao et al. (2020)
Downwelling	73.3	0.62	0.05	34.1		Cao et al. (2020)
Downwelling	74.8	0.62	0.08	34.4		Cao et al. (2020)
Downwelling	75	0.577	0.015	37.75	0.47	Geyman et al. (2019)
Downwelling	75.6	0.63	0.1	34		Cao et al. (2020)
Downwelling	75.8	0.63	0.07	34.8		Cao et al. (2020)
Downwelling	76	0.50	0.04	44.43		Yu et al. (2022)
Downwelling	93	0.59	0.01	43.6		Hsieh and Henderson (2017)
Downwelling	93	0.60	0.01	40		Bridgestock et al. (2018)
Downwelling	95	0.571	0.027	44.19	0.55	Geyman et al. (2019)
Downwelling	96	0.59	0.02	42		Bridgestock et al. (2018)
Downwelling	96	0.58	0.07	33.8		Cao et al. (2020)
Downwelling	96	0.55	0.01	46		Bridgestock et al. (2018)
Downwelling	97	0.6	0.02	40.2		Zhang et al. (2023)
Downwelling	98	0.6	0.04	40.4		Zhang et al. (2023)
Downwelling	98	0.61	0.03	40.2		Zhang et al. (2023)
Downwelling	98	0.6	0.03	44.1		Horner et al. (2015)
Downwelling	99			39.4		Zhang et al. (2023)
Downwelling	99			38.7		Zhang et al. (2023)
Downwelling	99	0.6	0.06	32.9		Cao et al. (2020)
Downwelling	99	0.52	0.04	44.56		Yu et al. (2022)
Downwelling	100	0.59	0.03	40.3		Zhang et al. (2023)
Downwelling	100	0.52	0.02	44.9		Hsieh and Henderson (2017)
Downwelling	100	0.62	0.07	32	2	Middleton et al. (2023a)
Downwelling	100	0.34	0.04	88.80		Yu et al. (2022)
Downwelling	100	0.64	0.04	32.78		Yu et al. (2022)
Downwelling	100	0.53	0.04	52.49		Yu et al. (2022)
Downwelling	100.7	0.59	0.03	33.9		Cao et al. (2020)
Downwelling	101	0.52	0.04	43.80		Yu et al. (2022)
Downwelling	109	0.59	0.05	32	2	Middleton et al. (2023a)
Downwelling	110	0.6	0.05	33	2	Middleton et al. (2023a)

Table B.9: $[Ba]$ and $\delta^{138/134}Ba$ data for each input and output flux component of the marine Ba mass balance from literature.

Dataset	Origin (location or depth (mbsl))	$\delta^{138/134}Ba$	$\delta^{138/134}Ba$ error	[Ba]	error	Reference
Downwelling	110	0.591	0.021	34.96	0.44	Geyman et al. (2019)
Downwelling	118	0.553	0.025	42.85	0.54	Geyman et al. (2019)
Downwelling	119	0.6	0.07	36	2	Middleton et al. (2023a)
Downwelling	120	0.29	0.01	88.2		Hsieh and Henderson (2017)
Downwelling	120	0.65	0.02	33.2		Hsieh and Henderson (2017)
Downwelling	122.9	0.55	0.05	34.5		Cao et al. (2020)
Downwelling	123.8	0.56	0.01	34.8		Cao et al. (2020)
Downwelling	125	0.59	0.03	34.5		Cao et al. (2020)
Downwelling	125	0.63	0.04	32.24		Yu et al. (2022)
Downwelling	140	0.3	0.02	98.6		Hsieh and Henderson (2017)
Downwelling	140	0.6	0.05	34	2	Middleton et al. (2023a)
Downwelling	147	0.57	0.02	44		Bridgestock et al. (2018)
Downwelling	148	0.61	0.03	40		Bridgestock et al. (2018)
Downwelling	148.1	0.55	0.03	36.4		Cao et al. (2020)
Downwelling	149	0.61	0.03	40.6		Zhang et al. (2023)
Downwelling	149	0.63	0.05	32	2	Middleton et al. (2023a)
Downwelling	149.5	0.58	0.04	34.3		Cao et al. (2020)
Downwelling	150	0.58	0.04	38	3	Middleton et al. (2023a)
Downwelling	150	0.617	0.021	35.32	0.44	Geyman et al. (2019)
Downwelling	150.1	0.6	0.03	34.4		Cao et al. (2020)
Downwelling	150.4	0.53	0.03	37.5		Cao et al. (2020)
Downwelling	174	0.59	0.01	40.7		Zhang et al. (2023)
Downwelling	180	0.57	0.05	38	3	Middleton et al. (2023a)
Downwelling	192	0.56	0.03	43.1		Hsieh and Henderson (2017)
Downwelling	195	0.62	0.02	40.9		Zhang et al. (2023)
Downwelling	197	0.62	0.01	39.7		Zhang et al. (2023)
Downwelling	197.9	0.55	0.06	40.4		Cao et al. (2020)
Downwelling	198	0.59	0.03	44.3		Horner et al. (2015)
Downwelling	198.6	0.54	0.03	36.6		Cao et al. (2020)
Downwelling	199	0.54	0.02	44.6		Hsieh and Henderson (2017)
Downwelling	199	0.53	0.03	51		Bridgestock et al. (2018)
Downwelling	199	0.50	0.02	52		Bridgestock et al. (2018)

Table B.9: $[Ba]$ and $\delta^{138/134}Ba$ data for each input and output flux component of the marine Ba mass balance from literature.

Dataset	Origin (location or depth (mbsl))	$\delta^{138/134}Ba$	$\delta^{138/134}Ba$ error	[Ba]	error	Reference
Downwelling	199	0.60	0.01	40		Bridgestock et al. (2018)
Downwelling	200	0.62	0.03	39.3		Zhang et al. (2023)
Downwelling	200	0.49	0.03	58.9		Hemsing et al. (2018)
Downwelling	200	0.56	0.05	38	3	Middleton et al. (2023a)
Downwelling	200	0.58	0.05	39	3	Middleton et al. (2023a)
Downwelling	200	0.63	0.07	36	3	Middleton et al. (2023a)
Downwelling	200	0.596	0.015	37.08	0.46	Geyman et al. (2019)
Downwelling	200	0.31	0.04	85.25		Yu et al. (2022)
Downwelling	200	0.27	0.04	90.38		Yu et al. (2022)
Downwelling	200	0.44	0.04	67.98		Yu et al. (2022)
Upwelling	202	0.54	0.04	43.43		Yu et al. (2022)
Upwelling	203	0.52	0.04	42.34		Yu et al. (2022)
Upwelling	203	0.56	0.04	42.81		Yu et al. (2022)
Upwelling	238	0.51	0.03	49.3		Hemsing et al. (2018)
Upwelling	249	0.63	0.02	35.2		Hsieh and Henderson (2017)
Upwelling	249	0.57	0.06	38	3	Middleton et al. (2023a)
Upwelling	250	0.54	0.05	39	3	Middleton et al. (2023a)
Upwelling	250	0.517	0.022	37.47	0.47	Geyman et al. (2019)
Upwelling	257	0.559	0.02	46.97	0.59	Geyman et al. (2019)
Upwelling	282	0.6	0.01	42.5		Zhang et al. (2023)
Upwelling	298	0.61	0.03	43.9		Zhang et al. (2023)
Upwelling	298	0.49	0.02	54		Bridgestock et al. (2018)
Upwelling	298	0.58	0.02	44		Bridgestock et al. (2018)
Upwelling	298	0.58	0.02	41		Bridgestock et al. (2018)
Upwelling	299.7	0.42	0.03	47.8		Cao et al. (2020)
Upwelling	300	0.29	0.02	95.1		Hsieh and Henderson (2017)
Upwelling	300	0.5	0.03	60.8		Hemsing et al. (2018)
Upwelling	300	0.51	0.03	51.3		Hemsing et al. (2018)
Upwelling	300	0.41	0.03	71.7		Hemsing et al. (2018)
Upwelling	300	0.56	0.05	40	3	Middleton et al. (2023a)
Upwelling	300	0.6	0.05	41	3	Middleton et al. (2023a)
Upwelling	300	0.51	0.11	49.9		Cao et al. (2020)

Table B.9: $[Ba]$ and $\delta^{138/134}Ba$ data for each input and output flux component of the marine Ba mass balance from literature.

Dataset	Origin (location or depth (mbsl))	$\delta^{138/134}Ba$	$\delta^{138/134}Ba$ error	[Ba]	error	Reference
Upwelling	300	0.566	0.015	39.4	0.49	Geyman et al. (2019)
Upwelling	300	0.57	0.04	38.53		Yu et al. (2022)
Upwelling	300	0.44	0.04	68.49		Yu et al. (2022)
Upwelling	300.2	0.42	0.04	56.2		Cao et al. (2020)
Upwelling	301	0.55	0.02	44.6		Hsieh and Henderson (2017)
Upwelling	338	0.52	0.03	51.6		Hemsing et al. (2018)
Upwelling	346	0.58	0.02	45.7		Zhang et al. (2023)
Upwelling	350	0.48	0.05	44	3	Middleton et al. (2023a)
Upwelling	350	0.5	0.05	45	3	Middleton et al. (2023a)
Upwelling	350	0.484	0.018	43.48	0.54	Geyman et al. (2019)
Upwelling	350	0.512	0.018	43.68	0.55	Geyman et al. (2019)
Upwelling	350	0.508	0.016	43.33	0.54	Geyman et al. (2019)
Upwelling	360	0.53	0.03	50.3		Hemsing et al. (2018)
Upwelling	395			47.7		Zhang et al. (2023)
Upwelling	397			46.4		Zhang et al. (2023)
Upwelling	399	0.54	0.03	51.3		Horner et al. (2015)
Upwelling	399	0.55	0.05	48	3	Middleton et al. (2023a)
Upwelling	399	0.54	0.04	45.03		Yu et al. (2022)
Upwelling	400	0.45	0.03	44.6		Hsieh and Henderson (2017)
Upwelling	400	0.57	0.03	46		Bridgestock et al. (2018)
Upwelling	400	0.5	0.04	47	3	Middleton et al. (2023a)
Upwelling	400	0.476	0.016	48.86	0.61	Geyman et al. (2019)
Upwelling	400	0.44	0.04	73.57		Yu et al. (2022)
Upwelling	401	0.55	0.01	43.7		Zhang et al. (2023)
Upwelling	404	0.54	0.04	44.59		Yu et al. (2022)
Upwelling	405	0.52	0.04	44.35		Yu et al. (2022)
Upwelling	405	0.56	0.04	41.7	1.1	Bates et al. (2017)
Upwelling	405	0.54	0.04	42.37		Yu et al. (2022)
Upwelling	488	0.55	0.01	49.4		Zhang et al. (2023)
Upwelling	494	0.54	0.02	49.5		Zhang et al. (2023)
Upwelling	495	0.54	0.02	51		Bridgestock et al. (2018)
Upwelling	495	0.51	0.02	50		Bridgestock et al. (2018)

Table B.9: $[Ba]$ and $\delta^{138/134}Ba$ data for each input and output flux component of the marine Ba mass balance from literature.

Dataset	Origin (location or depth (mbsl))	$\delta^{138/134}Ba$	$\delta^{138/134}Ba$ error	[Ba]	error	Reference
Upwelling	497.5	0.35	0.02	71.9		Cao et al. (2020)
Upwelling	498	0.54	0.02	49.1		Zhang et al. (2023)
Upwelling	498	0.31	0.03	41.6		Hsieh and Henderson (2017)
Upwelling	498	0.53	0.02	46		Bridgestock et al. (2018)
Upwelling	499	0.51	0.02	60		Bridgestock et al. (2018)
Upwelling	499	0.45	0.04	57	4	Middleton et al. (2023a)
Upwelling	500	0.45	0.03	63.8		Hemsing et al. (2018)
Upwelling	500	0.48	0.04	52	4	Middleton et al. (2023a)
Upwelling	500	0.52	0.05	55	4	Middleton et al. (2023a)
Upwelling	500	0.436	0.021	59.44	0.74	Geyman et al. (2019)
Upwelling	500	0.446	0.015	69.93	0.87	Geyman et al. (2019)
Upwelling	500	0.29	0.04	90.21		Yu et al. (2022)
Upwelling	500	0.27	0.04	92.36		Yu et al. (2022)
Upwelling	500	0.44	0.04	54.15		Yu et al. (2022)
Upwelling	500	0.48	0.04	56.65		Yu et al. (2022)
Upwelling	500	0.39	0.04	82.16		Yu et al. (2022)
Upwelling	500	0.35	0.04	84.91		Yu et al. (2022)
Upwelling	507	0.51	0.04	43.45		Yu et al. (2022)
Upwelling	550	0.25	0.05	85.8		Hsieh and Henderson (2017)
Upwelling	550	0.41	0.04	55	4	Middleton et al. (2023a)
Upwelling	598	0.47	0.02	52		Bridgestock et al. (2018)
Upwelling	598	0.37	0.04	60	4	Middleton et al. (2023a)
Upwelling	598	0.44	0.04	57	4	Middleton et al. (2023a)
Upwelling	599	0.38	0.04	67	5	Middleton et al. (2023a)
Upwelling	600	0.52	0.03	58.5		Horner et al. (2015)
Upwelling	600	0.417	0.015	68.29	0.85	Geyman et al. (2019)
Upwelling	600	0.38	0.04	85.35		Yu et al. (2022)
Upwelling	608	0.53	0.04	43.14		Yu et al. (2022)
Upwelling	608	0.50	0.05	42.85		Yu et al. (2022)
Upwelling	650	0.34	0.03	83.6		Hemsing et al. (2018)
Upwelling	680	0.52	0.03	51.4		Hemsing et al. (2018)
Upwelling	680	0.52	0.03	52.9		Hemsing et al. (2018)

Table B.9: $[Ba]$ and $\delta^{138/134}Ba$ data for each input and output flux component of the marine Ba mass balance from literature.

Dataset	Origin (location or depth (mbsl))	$\delta^{138/134}Ba$	$\delta^{138/134}Ba$ error	[Ba]	error	Reference
Upwelling	680	0.51	0.03	51.8		Hemsing et al. (2018)
Upwelling	698	0.53	0.04	45.03		Yu et al. (2022)
Upwelling	700	0.45	0.04	59	4	Middleton et al. (2023a)
Upwelling	700	0.38	0.03	65	5	Middleton et al. (2023a)
Upwelling	700	0.396	0.015	77.9	0.97	Geyman et al. (2019)
Upwelling	701	0.52	0.04	44.7		Hsieh and Henderson (2017)
Upwelling	705	0.49	0.04	48.4	1.1	Bates et al. (2017)
Upwelling	706	0.43	0.06	59.9		Zhang et al. (2023)
Upwelling	741	0.38	0.04	59.6		Hsieh and Henderson (2017)
Upwelling	747	0.48	0.02	58		Bridgestock et al. (2018)
Upwelling	747	0.49	0.02	58		Bridgestock et al. (2018)
Upwelling	748	0.47	0.02	57		Bridgestock et al. (2018)
Upwelling	750	0.386	0.015	88.31	1.1	Geyman et al. (2019)
Upwelling	756	0.51	0.04	45.00		Yu et al. (2022)
Upwelling	759			60.8		Zhang et al. (2023)
Upwelling	795			59.5		Zhang et al. (2023)
Upwelling	799	0.35	0.04	70	5	Middleton et al. (2023a)
Upwelling	799.3	0.35	0.03	85.3		Cao et al. (2020)
Upwelling	800	0.43	0.03	71.4		Hemsing et al. (2018)
Upwelling	800	0.37	0.03	85		Hemsing et al. (2018)
Upwelling	800	0.41	0.03	71	5	Middleton et al. (2023a)
Upwelling	801	0.34	0.02	85.8		Hsieh and Henderson (2017)
Upwelling	801	0.31	0.05	86.9		Cao et al. (2020)
Upwelling	810	0.49	0.04	46.06		Yu et al. (2022)
Upwelling	850	0.338	0.015	89.39	1.12	Geyman et al. (2019)
Upwelling	881	0.49	0.02	62.5		Zhang et al. (2023)
Upwelling	890	0.42	0.02	64		Hsieh and Henderson (2017)
Upwelling	899	0.3	0.04	78	5	Middleton et al. (2023a)
Upwelling	989	0.49	0.04	62.9		Zhang et al. (2023)
Upwelling	992	0.42	0.02	66		Bridgestock et al. (2018)
Upwelling	995	0.38	0.01	73		Bridgestock et al. (2018)
Upwelling	997	0.38	0.03	64		Bridgestock et al. (2018)

Table B.9: $[Ba]$ and $\delta^{138/134}Ba$ data for each input and output flux component of the marine Ba mass balance from literature.

Dataset	Origin (location or depth (mbsl))	$\delta^{138/134}Ba$	$\delta^{138/134}Ba$ error	[Ba]	error	Reference
Upwelling	998	0.44	0.03	72.9		Horner et al. (2015)
Upwelling	998.9	0.31	0.03	99.6		Cao et al. (2020)
Upwelling	999	0.34	0.04	84	6	Middleton et al. (2023a)
Upwelling	999	0.37	0.04	88	6	Middleton et al. (2023a)
Upwelling	999	0.34	0.04	77	5	Middleton et al. (2023a)
Upwelling	1000	0.49	0.01	49.2		Hsieh and Henderson (2017)
Upwelling	1000	0.27	0.02	99.5		Hsieh and Henderson (2017)
Upwelling	1000	0.27	0.02	99.6		Hsieh and Henderson (2017)
Upwelling	1000	0.32	0.03	98.5		Hemsing et al. (2018)
Upwelling	1000	0.329	0.015	98.1	1.23	Geyman et al. (2019)
Upwelling	1000	0.371	0.015	114.53	1.43	Geyman et al. (2019)
Upwelling	1000	0.27	0.04	94.10		Yu et al. (2022)
Upwelling	1000	0.26	0.04	96.50		Yu et al. (2022)
Upwelling	1000	0.25	0.04	96.38		Yu et al. (2022)
Upwelling	1000	0.33	0.09	95.98		Yu et al. (2022)
Upwelling	1000	0.31	0.04	84.47		Yu et al. (2022)
Upwelling	1000	0.35	0.04	88.83		Yu et al. (2022)
Upwelling	1000	0.33	0.04	104.16		Yu et al. (2022)
Upwelling	1000	0.31	0.04	106.67		Yu et al. (2022)
Upwelling	1000	0.32	0.04	106.60		Yu et al. (2022)
Upwelling	1000.8	0.32	0.03	102.5		Cao et al. (2020)
Upwelling	1005	0.43	0.03	55.9	1.2	Bates et al. (2017)
Upwelling	1011	0.47	0.05	62.8		Zhang et al. (2023)
Upwelling	1013	0.51	0.04	44.35		Yu et al. (2022)
Upwelling	1014	0.53	0.04	49.93		Yu et al. (2022)
Upwelling	1014	0.52	0.04	45.68		Yu et al. (2022)
Upwelling	1099	0.47	0.04	45.61		Yu et al. (2022)
Upwelling	1240	0.4	0.02	71.8		Hsieh and Henderson (2017)
Upwelling	1246			60.6		Zhang et al. (2023)
Upwelling	1247			59.8		Zhang et al. (2023)
Upwelling	1248	0.43	0.04	58.7		Zhang et al. (2023)
Upwelling	1249	0.26	0.03	93	6	Middleton et al. (2023a)

Table B.9: $[Ba]$ and $\delta^{138/134}Ba$ data for each input and output flux component of the marine Ba mass balance from literature.

Dataset	Origin (location or depth (mbsl))	$\delta^{138/134}Ba$	$\delta^{138/134}Ba$ error	[Ba]	error	Reference
Upwelling	1250	0.28	0.04	99	7	Middleton et al. (2023a)
Upwelling	1250	0.301	0.015	112.18	1.4	Geyman et al. (2019)
Upwelling	1250	0.329	0.015	114.98	1.44	Geyman et al. (2019)
Upwelling	1300	0.29	0.03	96		Hemsing et al. (2018)
Upwelling	1332	0.49	0.05	46.13		Yu et al. (2022)
Upwelling	1349	0.49	0.02	46.21		Yu et al. (2022)
Upwelling	1368	0.51	0.05	49.64		Yu et al. (2022)
Upwelling	1400	0.48	0.01	50.2		Hsieh and Henderson (2017)
Upwelling	1400	0.26	0.02	113.4		Hsieh and Henderson (2017)
Upwelling	1400	0.32	0.03	90.6		Hemsing et al. (2018)
Upwelling	1491	0.38	0.03	77		Bridgestock et al. (2018)
Upwelling	1491	0.35	0.02	78		Bridgestock et al. (2018)
Upwelling	1493	0.36	0.02	76		Bridgestock et al. (2018)
Upwelling	1494	0.34	0.02	81		Bridgestock et al. (2018)
Upwelling	1498	0.38	0.03	76.9		Horner et al. (2015)
Upwelling	1498	0.3	0.03	114	8	Middleton et al. (2023a)
Upwelling	1500	0.32	0.03	95.8		Hemsing et al. (2018)
Upwelling	1500	0.31	0.03	112	8	Middleton et al. (2023a)
Upwelling	1500	0.289	0.015	125.61	1.57	Geyman et al. (2019)
Upwelling	1500	0.297	0.015	127.22	1.59	Geyman et al. (2019)
Upwelling	1500	0.27	0.04	105.05		Yu et al. (2022)
Upwelling	1500	0.29	0.04	112.98		Yu et al. (2022)
Upwelling	1502	0.41	0.03	54.7	1.2	Bates et al. (2017)
Upwelling	1507	0.49	0.04	47.08		Yu et al. (2022)
Upwelling	1573	0.50	0.04	45.69		Yu et al. (2022)
Upwelling	1699	0.47	0.04	48.23		Yu et al. (2022)
Upwelling	1745	0.35	0.02	82		Bridgestock et al. (2018)
Upwelling	1750	0.28	0.03	99.2		Hemsing et al. (2018)
Upwelling	1908	0.49	0.04	47.68		Yu et al. (2022)
Upwelling	1988	0.36	0.02	67.8		Hsieh and Henderson (2017)
Upwelling	1991	0.33	0.01	76		Bridgestock et al. (2018)
Upwelling	1995	0.41	0.04	60.6		Zhang et al. (2023)

Table B.9: $[Ba]$ and $\delta^{138/134}Ba$ data for each input and output flux component of the marine Ba mass balance from literature.

Dataset	Origin (location or depth (mbsl))	$\delta^{138/134}Ba$	$\delta^{138/134}Ba$ error	[Ba]	error	Reference
Upwelling	1995			59.5		Zhang et al. (2023)
Upwelling	1999			60.7		Zhang et al. (2023)
Upwelling	1999	0.45	0.02	51.6		Hsieh and Henderson (2017)
Upwelling	1999	0.4	0.03	76.8		Horner et al. (2015)
Upwelling	1999	0.25	0.03	128	9	Middleton et al. (2023a)
Upwelling	1999	0.49	0.04	47.72		Yu et al. (2022)
Upwelling	2000	0.22	0.03	128	9	Middleton et al. (2023a)
Upwelling	2000	0.234	0.015	139.99	1.75	Geyman et al. (2019)
Upwelling	2000	0.26	0.04	93.20		Yu et al. (2022)
Upwelling	2000	0.26	0.04	93.44		Yu et al. (2022)
Upwelling	2000	0.25	0.04	98.49		Yu et al. (2022)
Upwelling	2000	0.27	0.06	98.17		Yu et al. (2022)
Upwelling	2000	0.27	0.04	129.24		Yu et al. (2022)
Upwelling	2000	0.25	0.04	132.60		Yu et al. (2022)
Upwelling	2002	0.42	0.04	58.6	1.2	Bates et al. (2017)
Upwelling	2031	0.48	0.04	48.87		Yu et al. (2022)
Upwelling	2150	0.26	0.03	96.8		Hsieh and Henderson (2017)
Upwelling	2241	0.46	0.04	48.27		Yu et al. (2022)
Upwelling	2243	0.36	0.01	73		Bridgestock et al. (2018)
Upwelling	2250	0.25	0.03	102		Hemsing et al. (2018)
Upwelling	2302	0.46	0.04	49.04		Yu et al. (2022)
Upwelling	2409	0.46	0.04	49.27		Yu et al. (2022)
Upwelling	2488	0.39	0.02	75.9		Hsieh and Henderson (2017)
Upwelling	2492	0.43	0.02	61		Bridgestock et al. (2018)
Upwelling	2498	0.47	0.04	49.66		Yu et al. (2022)
Upwelling	2499	0.26	0.03	139	10	Middleton et al. (2023a)
Upwelling	2500	0.25	0.03	128	9	Middleton et al. (2023a)
Upwelling	2500	0.236	0.015	145.72	1.82	Geyman et al. (2019)
Upwelling	2500	0.22	0.04	136.11		Yu et al. (2022)
Upwelling	2560	0.26	0.04	96.04		Yu et al. (2022)
Upwelling	2567	0.26	0.04	93.73		Yu et al. (2022)
Upwelling	2568	0.46	0.04	49.37		Yu et al. (2022)

Table B.9: $[Ba]$ and $\delta^{138/134}Ba$ data for each input and output flux component of the marine Ba mass balance from literature.

Dataset	Origin (location or depth (mbsl))	$\delta^{138/134}Ba$	$\delta^{138/134}Ba$ error	[Ba]	error	Reference
Upwelling	2600	0.41	0.01	58.5		Hsieh and Henderson (2017)
Upwelling	2646	0.49	0.04	49.87		Yu et al. (2022)
Upwelling	2740	0.34	0.02	79		Bridgestock et al. (2018)
Upwelling	2740	0.37	0.01	79		Bridgestock et al. (2018)
Upwelling	2800	0.39	0.04	66.3	1.4	Bates et al. (2017)
Upwelling	2894	0.49	0.04	47.78		Yu et al. (2022)
Upwelling	2985	0.37	0.02	77		Bridgestock et al. (2018)
Upwelling	2991	0.29	0.02	90		Bridgestock et al. (2018)
Upwelling	2992	0.30	0.02	84		Bridgestock et al. (2018)
Upwelling	2993	0.38	0.02	67.3		Hsieh and Henderson (2017)
Upwelling	2995			77.9		Zhang et al. (2023)
Upwelling	2996	0.36	0.04	77.2		Zhang et al. (2023)
Upwelling	2996			77.1		Zhang et al. (2023)
Upwelling	2998	0.43	0.01	58.9		Hsieh and Henderson (2017)
Upwelling	2998	0.38	0.03	82.6		Horner et al. (2015)
Upwelling	2998	0.45	0.04	54.08		Yu et al. (2022)
Upwelling	2999	0.24	0.03	138	10	Middleton et al. (2023a)
Upwelling	2999	0.48	0.06	50.85		Yu et al. (2022)
Upwelling	3000	0.246	0.015	156.95	1.96	Geyman et al. (2019)
Upwelling	3000	0.26	0.015	153.28	1.92	Geyman et al. (2019)
Upwelling	3000	0.248	0.015	152.21	1.9	Geyman et al. (2019)
Upwelling	3000	0.24	0.04	98.26		Yu et al. (2022)
Upwelling	3000	0.28	0.04	96.15		Yu et al. (2022)
Upwelling	3000	0.26	0.04	129.05		Yu et al. (2022)
Upwelling	3050	0.24	0.01	99.3		Hsieh and Henderson (2017)
Upwelling	3136	0.26	0.02	95		Bridgestock et al. (2018)
Upwelling	3487	0.26	0.03	89.9		Hsieh and Henderson (2017)
Upwelling	3499	0.22	0.04	147	10	Middleton et al. (2023a)
Upwelling	3499	0.46	0.04	52.81		Yu et al. (2022)
Upwelling	3500	0.235	0.015	151.18	1.89	Geyman et al. (2019)
Upwelling	3500	0.24	0.04	99.71		Yu et al. (2022)
Upwelling	3500	0.26	0.05	97.90		Yu et al. (2022)

Table B.9: $[Ba]$ and $\delta^{138/134}Ba$ data for each input and output flux component of the marine Ba mass balance from literature.

Dataset	Origin (location or depth (mbsl))	$\delta^{138/134}Ba$	$\delta^{138/134}Ba$ error	[Ba]	error	Reference
Upwelling	3500	0.24	0.04	134.92		Yu et al. (2022)
Upwelling	3500	0.24	0.04	138.94		Yu et al. (2022)
Upwelling	3500	0.22	0.04	137.82		Yu et al. (2022)
Upwelling	3600	0.37	0.04	72.3	1.5	Bates et al. (2017)
Upwelling	3800	0.26	0.04	101.22		Yu et al. (2022)
Upwelling	3840	0.25	0.02	99.8		Hsieh and Henderson (2017)
Upwelling	3988	0.31	0.03	99		Hsieh and Henderson (2017)
Upwelling	3992	0.25	0.02	102		Bridgestock et al. (2018)
Upwelling	3996	0.36	0.03	89.3		Zhang et al. (2023)
Upwelling	3996			86.4		Zhang et al. (2023)
Upwelling	3998			85		Zhang et al. (2023)
Upwelling	4000	0.29	0.03	99.9		Horner et al. (2015)
Upwelling	4000	0.27	0.03	138	10	Middleton et al. (2023a)
Upwelling	4000	0.2	0.03	138	10	Middleton et al. (2023a)
Upwelling	4000	0.226	0.015	157.52	1.97	Geyman et al. (2019)
Upwelling	4001			81.5		Zhang et al. (2023)
Upwelling	4146	0.34	0.02	93.8		Zhang et al. (2023)
Upwelling	4167	0.47	0.04	50.04		Yu et al. (2022)
Upwelling	4200	0.26	0.04	99.53		Yu et al. (2022)
Upwelling	4241	0.35	0.03	138	10	Middleton et al. (2023a)
Upwelling	4265	0.24	0.03	122	9	Middleton et al. (2023a)
Upwelling	4295	0.19	0.04	135	9	Middleton et al. (2023a)
Upwelling	4299	0.31	0.04	73.6	1.5	Bates et al. (2017)
Upwelling	4364			85.8		Zhang et al. (2023)
Upwelling	4417			85.2		Zhang et al. (2023)
Upwelling	4431	0.25	0.03	134	9	Middleton et al. (2023a)
Upwelling	4445			83.8		Zhang et al. (2023)
Upwelling	4485			88.1		Zhang et al. (2023)
Upwelling	4500	0.216	0.015	158.24	1.98	Geyman et al. (2019)
Upwelling	4500	0.28	0.04	118.78		Yu et al. (2022)
Upwelling	4501	0.31	0.03	98		Horner et al. (2015)
Upwelling	4512	0.43	0.04	82.3	1.7	Bates et al. (2017)

Table B.9: $[Ba]$ and $\delta^{138/134}Ba$ data for each input and output flux component of the marine Ba mass balance from literature.

Dataset	Origin (location or depth (mbsl))	$\delta^{138/134}Ba$	$\delta^{138/134}Ba$ error	[Ba]	error	Reference
Upwelling	4550	0.27	0.04	102.25		Yu et al. (2022)
Upwelling	4654	0.25	0.05	103.40		Yu et al. (2022)
Upwelling	4986	0.28	0.01	107		Bridgestock et al. (2018)
Upwelling	5000	0.23	0.04	136.96		Yu et al. (2022)
Upwelling	5300	0.28	0.04	113.38		Yu et al. (2022)
Upwelling	5375	0.23	0.04	139.02		Yu et al. (2022)
Suspended particulate measurements	5.8	-0.145	0.033			Horner et al. (2017)
Suspended particulate measurements	12.1	-0.128	0.036	127.85	6.06	Horner et al. (2017)
Suspended particulate measurements	16	-0.208	0.027	177.24	10.1	Horner et al. (2017)
Suspended particulate measurements	18	-0.156	0.022	210.32	10.59	Horner et al. (2017)
Suspended particulate measurements	22.1	-0.054	0.027	131.48	5.26	Horner et al. (2017)
Suspended particulate measurements	30.1	-0.129	0.036	98.88	3.96	Horner et al. (2017)
Suspended particulate measurements	48.1	-0.159	0.032	82.7	3.31	Horner et al. (2017)
Suspended particulate measurements	70.9	-0.21	0.034	102.8	4.11	Horner et al. (2017)
Suspended particulate measurements	97.2	-0.181	0.03	101.47	14.74	Horner et al. (2017)
Suspended particulate measurements	120.1	0.004	0.02	102.56	4.1	Horner et al. (2017)
Suspended particulate measurements	142	0.02	0.02	232.46	9.3	Horner et al. (2017)
Suspended particulate measurements	8	-0.009	0.031			Horner et al. (2017)
Suspended particulate measurements	18.2	-0.135	0.032			Horner et al. (2017)
Suspended particulate measurements	27.9	-0.035	0.032	83.77	4.19	Horner et al. (2017)
Suspended particulate measurements	34.9	-0.214	0.053	82.17	3.29	Horner et al. (2017)
Suspended particulate measurements	50	-0.06	0.035	65.58	2.62	Horner et al. (2017)
Suspended particulate measurements	69.9	0.046	0.03	65.37	3.28	Horner et al. (2017)
Suspended particulate measurements	95	-0.003	0.037	60.64	2.65	Horner et al. (2017)
Suspended particulate measurements	120	0.004	0.03	65.8	2.63	Horner et al. (2017)
Suspended particulate measurements	140.1	0.064	0.03	82.29	5.41	Horner et al. (2017)
Suspended particulate measurements	160.2	-0.021	0.03	120.46	5.63	Horner et al. (2017)
Suspended particulate measurements	178.6	0.031	0.03	131.65	5.72	Horner et al. (2017)
Suspended particulate measurements	25	0.19	0.05	351		Cao et al. (2020)
Suspended particulate measurements	25	0.12		644		Cao et al. (2020)
Suspended particulate measurements	75	0.11	0.09	809		Cao et al. (2020)
Suspended particulate measurements	125	0.05	0.1	579		Cao et al. (2020)

Table B.9: $[Ba]$ and $\delta^{138/134}Ba$ data for each input and output flux component of the marine Ba mass balance from literature.

Dataset	Origin (location or depth (mbsl))	$\delta^{138/134}Ba$	$\delta^{138/134}Ba$ error	[Ba]	error	Reference
Suspended particulate measurements	5	0.21	0.21	374		Cao et al. (2020)
Suspended particulate measurements	25	0.21	0.05	297		Cao et al. (2020)
Suspended particulate measurements	50	0.15	0.1	411		Cao et al. (2020)
Suspended particulate measurements	75	0.15	0.1	920		Cao et al. (2020)
Suspended particulate measurements	100	0.1		508		Cao et al. (2020)
Suspended particulate measurements	125	0.06	0.05	695		Cao et al. (2020)
Suspended particulate measurements	150	0.04	0.07	926		Cao et al. (2020)
Suspended particulate measurements	25	0.12	0.04	690		Cao et al. (2020)
Suspended particulate measurements	75	0.11	0.12	754		Cao et al. (2020)
Suspended particulate measurements	150	0.07		964		Cao et al. (2020)
Suspended particulate measurements	5	0.17	0.07	363		Cao et al. (2020)
Suspended particulate measurements	25	0.21	0.03	305		Cao et al. (2020)
Suspended particulate measurements	50	0.21	0.11	380		Cao et al. (2020)
Suspended particulate measurements	75	0.18	0.07	378		Cao et al. (2020)
Suspended particulate measurements	100	0.09	0.01	649		Cao et al. (2020)
Suspended particulate measurements	150	0.06	0.06	1056		Cao et al. (2020)

B.3 Calculation of propagated error

The isotopic composition of the total input fluxes, $\delta^{138/134}Ba \approx +0.16 \pm 0.98‰$ ($\pm 2\sigma$)) is calculated using Equation 14 where the associated error has been calculated using the general formula for propagation of error.

The result of the isotopic composition of the total input fluxes (R) is a function of multiple independent variables $(x_1, x_2, x_3, ..., x_n)$. In this case these are the average individual isotopic compositions and respective fluxes of each Ba input to the marine Ba mass balance i.e. effective river input, groundwater discharge, and hydrothermal fluid (Table 3.1). The uncertainty of R (σ_R) can be approximated (assuming small errors and linear approximations) using the following formula (Equation 19):

$$\sigma_{\mathrm{R}} = \sqrt{\left(\frac{\partial \mathrm{R}}{\partial \mathrm{x}_1} \cdot \sigma_{\mathrm{x}_1}\right)^2 + \left(\frac{\partial \mathrm{R}}{\partial \mathrm{x}_2} \cdot \sigma_{\mathrm{x}_2}\right)^2 + \cdots + \left(\frac{\partial \mathrm{R}}{\partial \mathrm{x}_\mathrm{n}} \cdot \sigma_{\mathrm{x}_\mathrm{n}}\right)^2} \qquad \{19\}$$

where $\frac{\partial R}{\partial x_i}$ is the partial derivative of the function R with respect to the variable x_i and σ_{x_i} is the uncertainty (2SE) in the variable x_i, also listed in Table 3.1.

Appendix C

Appendix For Chapter 4

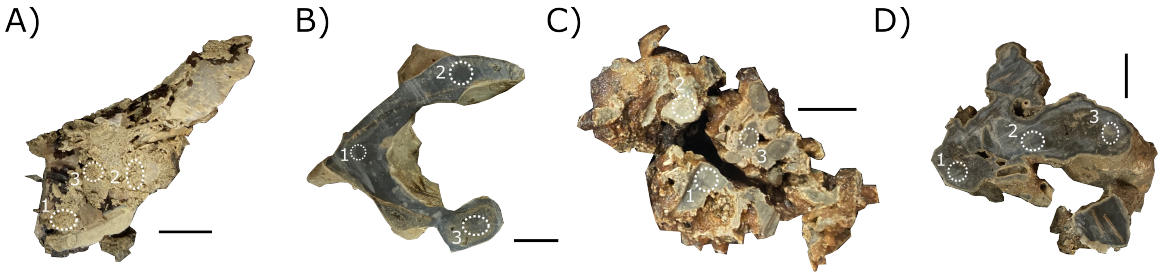

Figure C.1: Scanned images of the split, polished authigenic carbonate samples collected at Regab Pockmark on the WACS cruise. The sampling location is indicated by a dashed white sample for sample a) PL-424-CC1, b) PL-426-CC1, c) PL-429-CC1, and d) PL-429-CC2. All scale bars are 10 mm.

Site	Depth (mbsl)	Altitude (m)	Latitude	Longitude	Type	$[Ca]$ (mol)	$[Ba]$ (nM)	$\delta^{138/134}Ba$	$\delta^{138/134}Ba$ error	n
Reference Site	3095	50	-5.797283	9.719917	Seawater		81.6	0.31	0.09	3
Reference Site	3125	20	-5.797283	9.719917	Seawater		83.2	0.24	0.05	2
Reference Site	3135	10	-5.797283	9.719917	Seawater		83.0	0.27	0.10	2
Reference Site	3140	5	-5.797283	9.719917	Seawater		84.4	0.25	0.05	2
Reference Site	3144	1	-5.797283	9.719917	Seawater		158	-0.03	0.11	2
Bubble Site	3116	40	-5.797700	9.711467	Seawater		90.7	0.23	0.05	2
Bubble Site	3136	20	-5.797700	9.711467	Seawater		87.8	0.31	0.05	2
Bubble Site	3146	10	-5.797700	9.711467	Seawater		90.1	0.30	0.05	3
Bubble Site	3151	5	-5.797700	9.711467	Seawater		88.9	0.27	0.05	2
Bubble Site	3155	1	-5.797700	9.711467	Seawater		92.1	0.25	0.03	1
East Pockmark	3088	62	-5.796800	9.714200	Seawater		84.3	0.28	0.05	2
East Pockmark	3130	20	-5.796800	9.714200	Seawater		84.5	0.28	0.05	2
East Pockmark	3135	15	-5.796800	9.714200	Seawater		83.3	0.31	0.14	2
East Pockmark	3149	1	-5.796800	9.714200	Seawater		80.2	0.42	0.06	3
Mussel 1	3151	1	-5.797567	9.711267	Seawater		86.0	0.35	0.07	3
Clams 1	3153	1	-5.797617	9.711250	Seawater		83.9	0.34	0.05	1
Microbial mats	3152	1	-5.798650	9.709217	Seawater		83.2	0.29	0.05	3
Baboon (Congo Margin)	1		-4.760000	9.943056	Seawater		61.6	0.46	0.08	2
Guiness (Gabon Margin)	1		-1.628611	8.550556	Seawater		47.7	0.55	0.05	2
PL-424-CC1 (1)	3154		-5.797583	9.711322	Carbonate	0.0429	352	-0.24	0.05	3
PL-424-CC1 (2)	3154		-5.797583	9.711322	Carbonate	0.0443	443	-0.05	0.05	4
PL-424-CC1 (3)	3154		-5.797583	9.711322	Carbonate	0.0320	354	-0.27	0.07	4
PL-426-CC1 (1)	3154		-5.797592	9.71131	Carbonate	0.0397	3820	0.27	0.05	2
PL-426-CC1 (2)	3154		-5.797592	9.71131	Carbonate	0.0389	6401	0.25	0.05	3
PL-426-CC1 (3)	3154		-5.797592	9.71131	Carbonate	0.0433	4751	-0.06	0.05	2
PL-429-CC1 (1)	3152		-5.796753	9.714098	Carbonate	0.0401	5421	0.03	0.08	2
PL-429-CC1 (2)	3152		-5.796753	9.714098	Carbonate	0.0409	9133	0.03	0.07	3
PL-429-CC1 (3)	3152		-5.796753	9.714098	Carbonate	0.0617	8368	0.12	0.07	2
PL-429-CC2 (1)	3155		-5.79684	9.713267	Carbonate	0.0367	24404	0.18	0.05	2
PL-429-CC2 (2)	3155		-5.79684	9.713267	Carbonate	0.0385	21758	-0.05	0.09	2
PL-429-CC2 (3)	3155		-5.79684	9.713267	Carbonate	0.0390	24808	-0.05	0.10	3

Table C.1: Location and Ba concentration and $\delta^{138/134}Ba$ values measured along the Congo margin for seawater and carbonate samples used in Chapter 4.

Table C.2: SRM NIST 3104a and NBS-127 data generated in this study, Chapter 4.

Count	Standard	Date Measured	$\delta^{138/134}Ba$	$\delta^{138/134}Ba$ error	Average	2SD
1	NIST 1.01	22/11/2023	0.06	0.06		
2	NIST 1.02	22/11/2023	0.00	0.05		
3	NIST 1.03	22/11/2023	0.07	0.06		
4	NIST 1.04	22/11/2023	0.00	0.06		
5	NIST 1.05	22/11/2023	0.07	0.06		
6	NIST 1.06	22/11/2023	0.04	0.05		
7	NIST 1.07	22/11/2023	0.04	0.04		
8	NIST 1.08	22/11/2023	0.01	0.05	0.04	0.07
9	NIST 1.09	22/11/2023	0.11	0.07		
10	NIST 1.10	22/11/2023	0.03	0.05		
11	NIST 1.11	22/11/2023	0.05	0.05		
12	NIST 1.12	22/11/2023	0.05	0.05		
13	NIST 1.13	22/11/2023	-0.01	0.05		
14	NIST 1.14	22/11/2023	0.00	0.05		
15	NIST 1.15	22/11/2023	0.08	0.05		
1	NBS 1.01	03/11/2023	-0.17	0.05		
2	NBS 1.02	03/11/2023	-0.20	0.08		
3	NBS 1.03	22/11/2023	-0.31	0.05		
4	NBS 1.04	22/11/2023	-0.29	0.05		

Table C.2: SRM NIST 3104a and NBS-127 data generated in this study.

Count	Standard	Date Measured	$\delta^{138/134}Ba$	$\delta^{138/134}Ba$ error	Average	2SD
5	NBS 1.05	22/11/2023	-0.26	0.06		
6	NBS 1.06	22/11/2023	-0.30	0.05		
7	NBS 1.07	22/11/2023	-0.28	0.05	-0.26	0.04
8	NBS 1.08	16/01/2024	-0.28	0.08		
9	NBS 1.09	16/01/2024	-0.31	0.05		
10	NBS 1.10	16/01/2024	-0.24	0.04		
11	NBS 1.11	17/01/2024	-0.22	0.05		
12	NBS 1.12	17/01/2024	-0.24	0.05		
13	NBS 1.13	17/01/2024	-0.27	0.04		

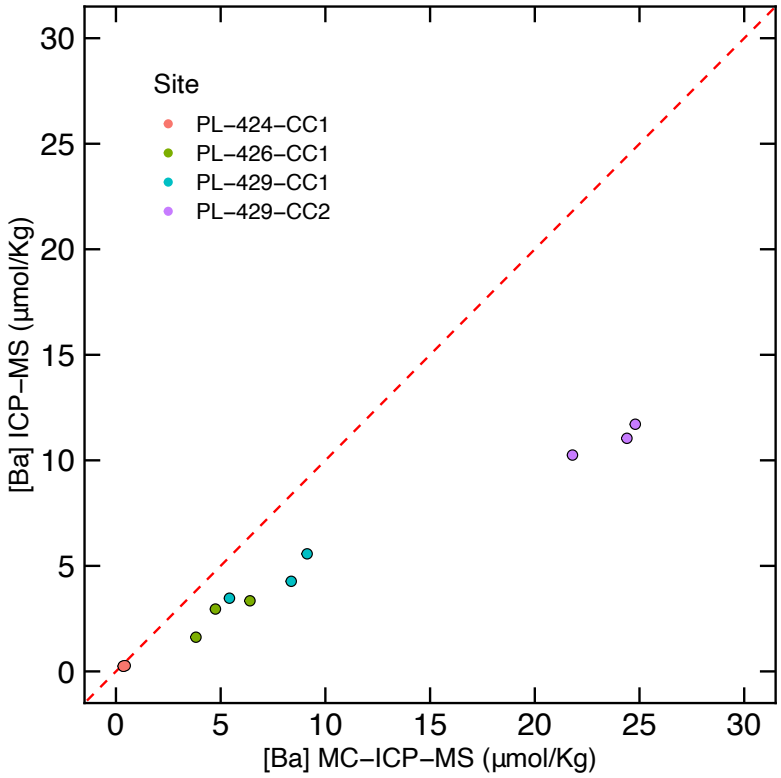

Figure C.2: Authigenic carbonate phase $[Ba]$ instrumental variations. The $[Ba]$ of all sub-samples of the authigenic carbonate was measured at two separate laboratories on different instruments: the quadrupole X-Series II ICP-MS at Academica Sinica, Taipei and on the MC-ICP-MS at NTU. Sample PL-424-CC1 measured by both methods are within 0.67% of each other whereas all other sub-samples recorded 45% higher $[Ba]$ measured on the MC-ICP-MS. The red dashed line is 1:1.

ID	Date	Sample Type	DS conc (ppb)	DS amount (ml)	Blank (ng)	Blank contribution (%)
1	02/11/2023	Seawater	n/a	0.0516	13.51	5.4
2	20/11/2023	Seawater	n/a	0.0516	4.98	2
3	17/01/2024	Seawater	n/a	0.05	3.5	1.4
4	17/01/2024	Carbonate	n/a	0.07	0.58	0.23

Table C.3: Procedural blank data generated in this study, Chapter 4. Aliquots of the seawater and digested carbonate solutions containing ∼250 ng of Ba were taken forward for spiking resulting in the calculated maximum percentage blank contribution.

C.1 TIMS methodology

The $[Ba]$ and isotope composition of the bubble site sample at 1 m altitude was determined using thermal ionisation mass spectrometry (TIMS; TRITON instrument, Thermo Scientific) at the University of Oxford, utilising a previously described double spike technique of a ^{137}Ba–^{135}Ba spike solution to correct for instrumental mass bias (Hsieh and Henderson, 2017).

The same methodology in sample processing and Ba purification as those measured at NTU occurred. A double Re filament assembly was used for sample measurement. The double filaments were outgassed before sample loading. The purified Ba was loaded onto the evaporation filament in 2M HCl without an activator gel and was then loaded into the TIMS instrument on the sample wheel. Once samples were loaded and positioned, and near instrumental vacuum conditions achieved, each sample was run consecutively. The samples were heated until Ba ionisation was achieved and typical beam size of ∼10 V for ^{138}Ba was recorded. This corresponded to applying currents of ∼ 2200 - 2500 mA to the ionisation filament and 50 - 300 mA to the evaporation filament. Once a stable beam at the desired beam size was achieved, the sample underwent 54 blocks of analysis, with 10 measurements in each block. Before starting the analysis, peak centring and baseline monitoring was performed. Throughout the run, the resulting ion beams were monitored using Faraday cups that are equipped with 10^{11} ohm resistors. The raw isotopic ratios were processed offline to correct for instrumental mass bias and finally, data are reported in the δ-notation (‰) ($\delta^{138/134}Ba$) relative to the National Institute of Standards and Technology (NIST) 3104a standard (Equation 16).

Due to limited sample availability the exact same sample was not able to be run using both methodologies at the separate laboratories however all bubble site samples

can be compared together to ascertain if data measured fits in context. The bubble site at 1 m altitude is similar to the rest of the bubble site samples in both $\delta^{138/134}Ba$ and $[Ba]$ ($\delta^{138/134}Ba_{1m} \approx +0.25 \pm 0.03‰$, $\delta^{138/134}Ba_{bubble} \approx 0.28 \pm 0.05‰$; $[Ba]_{1m} = 12.65\ nmol.kg^{-1}$, $[Ba]_{bubble} = 12.28\ nmol.kg^{-1}$) and therefore is assumed to confirm validity of generated results via MC-ICP-MS methods (Figure 4.2).

Bibliography

Abrahams, A., Schlegel, R. W., and Smit, A. J. (2021). Variation and Change of Upwelling Dynamics Detected in the World's Eastern Boundary Upwelling Systems. *Frontiers in Marine Science*, 8:626411.

Abshire, M. L., Romaniello, S. J., Kuzminov, A. M., Cofrancesco, J., Severmann, S., and Riedinger, N. (2020). Uranium isotopes as a proxy for primary depositional redox conditions in organic-rich marine systems. *Earth and Planetary Science Letters*, 529:115878.

Adekola, S. A. and Akinlua, A. (2013). Petrography and stable isotope geochemistry of Cretaceous sandstones, Orange Basin, South Africa. *Journal of Petroleum Exploration and Production Technology*, 3:69–83.

Aditiawati, P. and Pujobroto, A. (2013). Effect of Stimulants on Biogenic Methane Formation and Dynamics of Bacterial Population. *J. Math. Fund. Sci*, 45:274–285.

Akam, S. A., Swanner, E. D., Hongming, Y., Hong, W.-L., and Peckmann, J. (2023). Methane-derived authigenic carbonates; a case for a globally relevant marine carbonate factory. *Earth-science reviews*, 243:104487.

Allison, P. A., Hesselbo, S. P., and Brett, C. E. (2008). Methane seeps on an Early Jurassic dysoxic seafloor. *Palaeogeography, Palaeoclimatology, Palaeoecology*, 270:230–238.

Aloisi, G., Wallmann, K., Bollwerk, S. M., Derkachev, A., Bohrmann, G., and Suess, E. (2004). The effect of dissolved barium on biogeochemical processes at cold seeps. *Geochimica et Cosmochimica Acta*, 68:1735–1748.

Alves, T., Fetter, M., Busby, C., Gontijo, R., Cunha, T. A., and Mattos, N. H. (2020). A tectono-stratigraphic review of continental breakup on intraplate continental margins and its impact on resultant hydrocarbon systems. *Marine and petroleum geology*, 117:104341.

Andresen, K. J. (2012). Fluid flow features in hydrocarbon plumbing systems: What do they tell us about the basin evolution? *Marine Geology*, 332-334:89–108.

Anka, Z., Berndt, C., and Gay, A. (2012). Hydrocarbon leakage through focused fluid flow systems in continental margins. *Marine Geology*, 332-334:1–3.

Aplin, A. C., Fleet, A. J., Macquaker, J. H. S., Aplin, A. C., Fleet, A. J., and Macquaker, J. H. S. (1999). Muds and mudstones; physical and fluid-flow properties. *Geological Society Special Publications - Muds and Mudstones: Physical and Fluid Flow Properties, eds: Aplin, A. C., Fleet, A. J. Macquaker, J. H. S.*, 158:1–8.

Aquilina, L., Dia, A. N., Boulegue, J., Fouillac, A. M., Suess, E., von Breymann, M., Bourgois, J., and Anonymous (1992). Geochemistry of barite and carbonate deposits associated with fluid vents in the Peru convergent margin off Paita. *Eos (Washington, D.C.)*, 73:153.

Araujo-Rodrigues, L. and Luís-Sauer, I. (2015). Exploratory assessment of the economic gains of a pre-salt oil field in Brazil. *Energy Policy*, 87:486–495.

Ashe, D. (2018). Trace Metal Distribution in Redeposited Organic Carbon-Rich Sediments in a Modern Upwelling System. *Boone Pickens School of Geology, Oklahoma State University, Stillwater*, Thesis:1–58.

Awo, F. M., Rouault, M., Ostrowski, M., Tomety, F. S., Da-Allada, C. Y., and Jouanno, J. (2022). Seasonal Cycle of Sea Surface Salinity in the Angola Upwelling System. *Journal of Geophysical Research: Oceans*, 127:1–13.

Azambuja, N. C., Mello, M., Bender, A. A., Schmitt, P., and Swanson, B. (2010). Petroleum System of Deep-Water Offshore Namibia. *AAPG Search and Discovery*, 90108:1–1.

Babonneau, N., Savoye, B., Cremer, M., and Klein, B. (2002). Morphology and architecture of the present canyon and channel system of the Zaire deep-sea fan. *Marine and Petroleum Geology*, 19:445–467.

Baby, G., Guillocheau, F., Braun, J., Robin, C., and Dall'Asta, M. (2020). Solid sedimentation rates history of the Southern African continental margins: Implications for the uplift history of the South African Plateau. *Terra Nova*, 32:53–65.

Baby, G., Guillocheau, F., Morin, J., Ressouche, J., Robin, C., Broucke, O., and Dall'Asta, M. (2018). Post-rift stratigraphic evolution of the Atlantic margin of Namibia and South Africa: Implications for the vertical movements of the margin and the uplift history of the South African Plateau. *Marine and Petroleum Geology*, 97:169–191.

Bagguley, J. and Prosser, S. (1999). The interpretation of passive margin depositional processes using seismic stratigraphy: examples from offshore Namibia. *Geological Society Special Publication - The Oil and Gas Habitats of the South Atlantic, eds: Cameron, N. R., Bate, R. H. Clure, V. S.*, 153:321–344.

Barlow, R., Lamont, T., Mitchell-Innes, B., Lucas, M., and Thomalla, S. (2009). Primary production in the Benguela ecosystem, 1999–2002. *African Journal of Marine Science*, 31:97–101.

Bates, S. L., Hendry, K. R., Pryer, H. V., Kinsley, C. W., Pyle, K. M., Woodward, E. M. S., and Horner, T. J. (2017). Barium isotopes reveal role of ocean circulation on barium cycling in the Atlantic. *Geochimica et Cosmochimica Acta*, 204:286–299.

Baudin, F., Disnar, J. R., Martinez, P., and Dennielou, B. (2010). Distribution of the organic matter in the channel-levees systems of the Congo mud-rich deep-sea fan (West Africa). Implication for deep offshore petroleum source rocks and global carbon cycle. *Marine and Petroleum Geology*, 27:995–1010.

Baudin, F., Rabouille, C., and Dennielou, B. (2020). Routing of terrestrial organic matter from the Congo River to the ultimate sink in the abyss: a mass balance approach. *Geologica Belgica*, 23:41–52.

Bauer, K., Neben, S., Schreckenberger, B., Emmermann, R., Hinz, K., Fechner, N., Gohl, K., Schulze, A., Trumbull, R. B., and Weber, K. (2000). Deep structure of the Namibia continental margin as derived from integrated geophysical studies. *Journal of Geophysical Research: Solid Earth*, 105:25829–25853.

Bayon, G., Birot, D., Ruffine, L., Caprais, J. C., Ponzevera, E., Bollinger, C., Donval, J. P., Charlou, J. L., Voisset, M., and Grimaud, S. (2011). Evidence for intense REE scavenging at cold seeps from the Niger Delta margin. *Earth and Planetary Science Letters*, 312:443–452.

Bei, K., Xu, T., Shang, S., Wei, Z., Li, J., Cao, Y., and Tian, H. (2020). Numerical study on biogeochemical processes induced by methane leakage and its application in estimating the time of cold seeps formation. *Deep-Sea Research Part I: Oceanographic Research Papers*, 157:103206.

Ben-Avraham, Z., Smith, G., Reshef, M., and Jungslager, E. (2002). Gas hydrate and mud volcanoes on the southwest African continental margin off South Africa. *Geology*, 30:927–930.

Berger, W. H., Lange, C. B., and Wefer, G. (2002a). Upwelling history of the Benguela-Namibia system: A synthesis of Leg 175 results. *Proceedings of the Ocean Drilling Program: Scientific Results*, 175:1–53.

Berger, W. H., Wefer, G., Giraudeau, J., and Christensen, B. A. (2002b). On the reconstruction of upwelling history; Namibia upwelling in context. *Marine geology*, 180:3–28.

Berndt, C. (2005). Focused fluid flow in passive continental margins. *Philosophical Transactions of the Royal Society A: Mathematical, Physical and Engineering Sciences*, 363:2855–2871.

Berndt, C., Planke, S., Zarikian, C. A. A., Frieling, J., Jones, M. T., Millett, J. M., Brinkhuis, H., Bünz, S., Svensen, H. H., Longman, J., Scherer, R. P., Karstens, J., Manton, B., Nelissen, M., Reed, B., Faleide, J. I., Huismans, R. S., Agarwal, A., Andrews, G. D., Betlem, P., Bhattacharya, J., Chatterjee, S., Christopoulou, M., Clementi, V. J., Ferré, E. C., Filina, I. Y., Guo, P., Harper, D. T., Lambart, S., Mohn, G., Nakaoka, R., Tegner, C., Varela, N., Wang, M., Xu, W., and Yager, S. L. (2023). Shallow-water hydrothermal venting linked to the Palaeocene–Eocene Thermal Maximum. *Nature Geoscience*, 16:803–809.

Bhatnagar, G., Chapman, W. G., Dickens, G. R., Dugan, B., and Hirasaki, G. J. (2008). Sulfate-methane transition as a proxy for average methane hydrate saturation in marine sediments. *Geophysical Research Letters*, 35:1–5.

Bhatnagar, G., Chatterjee, S., Chapman, W. G., Dugan, B., Dickens, G. R., and Hirasaki, G. J. (2011). Analytical theory relating the depth of the sulfate-methane transition to gas hydrate distribution and saturation. *Geochemistry, Geophysics, Geosystems*, 12:1–21.

Blamey, L. K., Howard, J. A., Agenbag, J., and Jarre, A. (2012). Regime-shifts in the southern Benguela shelf and inshore region. *Progress in Oceanography*, 106:80–95.

Bograd, S. J., Jacox, M. G., Hazen, E. L., Lovecchio, E., Montes, I., Buil, M. P., Shannon, L. J., Sydeman, W. J., and Rykaczewski, R. R. (2022). Climate Change Impacts on Eastern Boundary Upwelling Systems. *Annual review of marine science*, 15:303–328.

Böning, P., Schnetger, B., Belz, L., Ferdelman, T., Brumsack, H. J., and Pahnke, K. (2020). Sedimentary iron cycling in the Benguela upwelling system off Namibia. *Earth and Planetary Science Letters*, 538:116212.

Borchers, S. L., Schnetger, B., Böning, P., and Brumsack, H. J. (2005). Geochemical signatures of the Namibian diatom belt: Perennial upwelling and intermittent anoxia. *Geochemistry, Geophysics, Geosystems*, 6:Q06006.

Bordbar, M. H., Mohrholz, V., and Schmidt, M. (2021). The Relation of Wind-Driven Coastal and Offshore Upwelling in the Benguela Upwelling System. *Journal of Physical Oceanography*, 51:3117–3133.

Bordbar, M. H., Mohrholz, V., and Schmidt, M. (2023). Low confidence in multi-decadal trends of wind-driven upwelling across the Benguela Upwelling System. *Earth System Dynamics*, 14:1065–1080.

Borowski, W. S., Paull, C. K., and Ussler, W. (1996). Marine pore-water sulfate profiles indicate in situ methane flux from underlying gas hydrate. *Geology*, 24:655–658.

Boswell, R., Collett, T. S., Frye, M., Shedd, W., McConnell, D. R., and Shelander, D. (2012). Subsurface gas hydrates in the northern Gulf of Mexico. *Marine and Petroleum Geology*, 34:4–30.

Böttcher, M. E., Neubert, N., von Allmen, K., Samankassou, E., and Nägler, T. F. (2018). Barium isotope fractionation during the experimental transformation of aragonite to witherite and of gypsum to barite, and the effect of ion (de)solvation. *Isotopes in Environmental and Health Studies*, 54:324–335.

Boudreau, B. P. (1997). *Diagenetic Models and their Implementation: Modelling Transport and Reactions in Aquatic Sediments. Boudreau, B. P. (Eds.)*, volume 1, pages 1-414. Springer, Berlin, Germany, 1st edition.

Brady, R. X., Lovenduski, N. S., Alexander, M. A., Jacox, M., and Gruber, N. (2019). On the role of climate modes in modulating the air-sea CO_2 fluxes in eastern boundary upwelling systems. *Biogeosciences*, 16:329–346.

Brandt, P., Bordbar, M. H., Coelho, P., Koungue, R. A. I., Körner, M., Lamont, T., Lübbecke, J. F., Mohrholz, V., Prigent, A., Roch, M., Schmidt, M., van der Plas, A. K., and Veitch, J. (2024). *Physical Drivers of Southwest African Coastal Upwelling and Its Response to Climate Variability and Change. In Von Maltitz, G., Midgley, G. F., Veitch, J., Brümmer, C., Rötter, R., Viehberg, F. Veste, M. (Eds.), Chapter 9 in Sustainability of Southern African Ecosystems under Global Change*, volume 248, pages 221–259. Springer International Publishing, Cham, Switzerland, 1st edition.

Bremner, J. M. and Willis, J. P. (1993). Mineralogy and geochemistry of the clay fraction of sediments from the Namibian continental margin and the adjacent hinterland. *Marine Geology*, 115:85–116.

Bridgestock, L., Hsieh, Y. T., Porcelli, D., and Henderson, G. M. (2019). Increased export production during recovery from the Paleocene–Eocene Thermal Maximum constrained by sedimentary Ba isotopes. *Earth and Planetary Science Letters*, 510:53–63.

Bridgestock, L., Hsieh, Y. T., Porcelli, D., Homoky, W. B., Bryan, A., and Henderson, G. M. (2018). Controls on the barium isotope compositions of marine sediments. *Earth and Planetary Science Letters*, 481:101–110.

Bridgestock, L., Nathan, J., Hsieh, Y. T., Holdship, P., Porcelli, D., Andersson, P. S., and Henderson, G. M. (2021a). Assessing the utility of barium isotopes to trace Eurasian riverine freshwater inputs to the Arctic Ocean. *Marine Chemistry*, 236:104029.

Bridgestock, L., Nathan, J., Paver, R., Hsieh, Y. T., Porcelli, D., Tanzil, J., Holdship, P., Carrasco, G., Annammala, K. V., Swarzenski, P. W., and Henderson, G. M. (2021b). Estuarine processes modify the isotope composition of dissolved riverine barium fluxes to the ocean. *Chemical Geology*, 579:120340.

Brown, A. R. (1986). *Interpretation of Three-dimensional Seismic Data. Brown, A. R. (Eds.)*, volume 1, pages 1-665. Society of Exploration Geophysicists and the American Association of Petroleum Geologists, Tulsa, USA, 3rd edition.

Brüchert, V., Currie, B., Peard, K. R., Lass, U., Endler, R., Dübecke, A., Julies, E., Leipe, T., and Zitzmann, S. (2006). Biogeochemical and Physical Control on Shelf Anoxia and Water Column Hydrogen Sulphide in the Benguela Coastal Upwelling System Off Namibia. *Past and Present Water Column Anoxia*, 1:161–193.

Brüchert, V., Jørgensen, B. B., Neumann, K., Riechmann, D., Schlösser, M., and Schulz, H. (2003). Regulation of bacterial sulfate reduction and hydrogen sulfide fluxes in the central Namibian coastal upwelling zone. *Geochimica et Cosmochimica Acta*, 67:4505–4518.

Buan, N. R. and Robinson, N. P. (2018). Methanogens: Pushing the boundaries of biology. *Emerging topics in life sciences*, 2:629–646.

Burdige, D. J. and Komada, T. (2020). Iron redox cycling, sediment resuspension and the role of sediments in low oxygen environments as sources of iron to the water column. *Marine Chemistry*, 223:103793.

Calvès, G., Huuse, M., Schwab, A., and Clift, P. (2008). Three-dimensional seismic analysis of high-amplitude anomalies in the shallow subsurface of the northern Indus Fan: Sedimentary and/or fluid origin. *Journal of Geophysical Research: Solid Earth*, 113:B11103.

Campbell, B. L. (2017). Seismic Characterisation of Gas Hydrates in the Lüderitz Basin, Offshore Namibia: Investigating Shallow Heat Flow and Fluid Flow Phenomena. *The Department of Earth and Environmental Sciences, The University of Manchester, Manchester*, Thesis:1–79.

Cande, S. C., Patriat, P., and Dyment, J. (2010). Motion between the Indian, Antarctic and African plates in the early Cenozoic. *Geophysical Journal International*, 183:127–149.

Canet, C., Anadón, P., Alfonso, P., Prol-Ledesma, R. M., Villanueva-Estrada, R. E., and García-Vallès, M. (2013). Gas-seep related carbonate and barite authigenic mineralization in the northern Gulf of California. *Marine and Petroleum Geology*, 43:147–165.

Cao, Z., Li, Y., Rao, X., Yu, Y., Hathorne, E. C., Siebert, C., Dai, M., and Frank, M. (2020). Constraining barium isotope fractionation in the upper water column of the South China Sea. *Geochimica et Cosmochimica Acta*, 288:120–137.

Cao, Z., Rao, X., Li, Y., Hong, Q., Wei, L., Yu, Y., Ehlert, C., Liu, B., Siebert, C., Hathorne, E. C., Zhang, Z., Scholz, F., Kasten, S., and Frank, M. (2023). Stable Barium Isotope Fractionation in Pore Waters of Estuarine Sediments. *Geochemistry, Geophysics, Geosystems*, 24:e2023GC010907.

Cao, Z., Rao, X., Yu, Y., Siebert, C., Hathorne, E. C., Liu, B., Wang, G., Lian, E., Wang, Z., Zhang, R., Gao, L., Wei, G., Yang, S., Dai, M., and Frank, M. (2021). Stable Barium Isotope Dynamics During Estuarine Mixing. *Geophysical Research Letters*, 48:e2021GL095680.

Cao, Z., Siebert, C., Hathorne, E. C., Dai, M., and Frank, M. (2016). Constraining the oceanic barium cycle with stable barium isotopes. *Earth and Planetary Science Letters*, 434:1–9.

Carter, S. C., Paytan, A., and Griffith, E. M. (2020). Toward an improved understanding of the marine barium cycle and the application of marine barite as a paleoproductivity proxy. *Minerals*, 10:1–24.

Cartwright, J., Huuse, M., and Aplin, A. (2007). Seal bypass systems. *AAPG Bulletin*, 91:1141–1166.

Cartwright, J. and Santamarina, C. (2015). Seismic characteristics of fluid escape pipes in sedimentary basins: Implications for pipe genesis. *Marine and Petroleum Geology*, 65:126–140.

Cartwright, J., Swart, R., and Corner, B. (2012). *Conjugate margins of the South Atlantic: Namibia-Pelotas. In Roberts, D. G. Bally, A. W. (Eds.), Chapter 5 in Regional Geology and Tectonics*, pages 202–221. Elsevier, Amsterdam, Netherlands, 1st edition.

Castellini, D. G., Dickens, G. R., Snyder, G. T., and Ruppel, C. D. (2006). Barium cycling in shallow sediment above active mud volcanoes in the Gulf of Mexico. *Chemical Geology*, 226:1–30.

Catuneanu, O., Wopfner, H., Eriksson, P. G., Cairncross, B., Rubidge, B. S., Smith, R. M., and Hancox, P. J. (2005). The Karoo basins of south-central Africa. *Journal of African Earth Sciences*, 43:211–253.

Ceraldi, T. S., Hodgkinson, R., and Backé, G. (2017). The petroleum geology of the West Africa margin: An introduction. *Geological Society Special Publication - Petroleum Geoscience of the West Africa Margin, eds: Sabato Ceraldi, T., Hodgkinson, R. A. Backe, G.*, 438:1–6.

Chapman, P. and Shannon, L. V. (1987). Seasonality in the oxygen minimum layers at the extremities of the Benguela system. *South African Journal of Marine Science*, 5:85–94.

Charlou, J. L., Donval, J. P., Fouquet, Y., Ondreas, H., Knoery, J., Cochonat, P., Levaché, D., Poirier, Y., Jean-Baptiste, P., Fourré, E., and Chazallon, B. (2004). Physical and chemical characterization of gas hydrates and associated methane plumes in the Congo-Angola Basin. *Chemical Geology*, 205:405–425.

Charlou, J. L., Donval, J. P., Zitter, T., Roy, N., Jean-Baptiste, P., Foucher, J. P., and Woodside, J. (2003). Evidence of methane venting and geochemistry of brines on mud volcanoes of the eastern Mediterranean Sea. *Deep-Sea Research Part I: Oceanographic Research Papers*, 50:941–958.

Chauvet, F., Sapin, F., Geoffroy, L., Ringenbach, J. C., and Ferry, J. N. (2021). Conjugate volcanic passive margins in the austral segment of the South Atlantic – Architecture and development. *Earth-Science Reviews*, 212:103461.

Chen, F., Wang, X., Li, N., Cao, J., Bayon, G., Peckmann, J., Hu, Y., Gong, S., Cheng, H., Edwards, R. L., Ning, Y., Jin, M., Huang, H., Wu, C., Sun, Y., Chen, H., Zhou, Y., Chen, D., and Feng, D. (2019). Gas Hydrate Dissociation During Sea-Level Highstand Inferred From U/Th Dating of Seep Carbonate From the South China Sea. *Geophysical Research Letters*, 46:13928–13938.

Chen, X. G., Gledhill, M., Lohan, M. C., Milne, A., and Achterberg, E. P. (2024a). Surface ocean biogeochemistry and deep ocean circulation control relationships between nutrient-type trace metals (Cd, Ni, Cu, and Zn) and nutrients in the South Atlantic Ocean near the subtropical front. *Geochimica et Cosmochimica Acta*, 370:144–160.

Chen, X.-G., Milne, A., Klar, J. K., Gledhill, M., Lohan, M. C., Hsieh, Y.-T., Henderson, G. M., Woodward, E. M. S., and Achterberg, E. P. (2024b). Controls on distributions of aluminium, manganese and cobalt in the South Atlantic Ocean along GEOTRACES transect GA10. *Geochimica et Cosmochimica Acta*, 373:177–196.

Cheng, M., Wei, W., Chen, X., Wang, H., Feng, L., She, Z., Fu, Y., Algeo, T. J., Huang, F., and Li, C. (2024). Active methane release in the early Cambrian seafloor? Clues from Ba isotope. *Palaeogeography, Palaeoclimatology, Palaeoecology*, 653:112399.

Cho, H., Hyun, J. H., You, O. R., Kim, M., Kim, S. H., Choi, D. L., Green, S. J., and Kostka, J. E. (2017). Microbial Community Structure Associated with Biogeochemical Processes in the Sulfate–Methane Transition Zone (SMTZ) of Gas-hydrate-bearing Sediment of the Ulleung Basin, East Sea. *Geomicrobiology Journal*, 34:207–219.

Church, T. M. and Wolgemuth, K. (1972). Marine barite saturation. *Earth and Planetary Science Letters*, 15:35–44.

Claypool, G. E. and Kaplan, I. R. (1974). *The Origin and Distribution of Methane in Marine Sediments. In Kaplan, I. R. (Eds.), Chapter 8 in Natural Gases in Marine Sediments*, volume 3, pages 99–139. Plenum Press, New York, USA, 1st edition.

Claypool, G. E. and Threlkeld, C. N. (1983). Anoxic diagenesis and methane generation in sediments of the Blake Outer Ridge, Deep Sea Drilling Project Site 533, Leg 76. *Initial Reports of the Deep Sea Drilling Project, Washington (U.S. Govt. Printing Office)*, 76:391–402.

Clayton, C. J. (1992). *Source Volumetrics of Biogenic Gas Generation. In Vially, R. (Eds.), Chapter 1 in Bacterial Gas*, volume 1, pages 191–204. Editions Technip, Paris, France, 1st edition.

Clemson, J. (1997). Segmentation of the namibian passive margin. *Imperial College of Science, Technology and Medicine, University of London, London*, Thesis:1–173.

Clemson, J., Cartwright, J., and Booth, J. (1997). Structural segmentation and the influence of basement structure on the Namibian passive margin. *Journal of the Geological Society*, 154:477–482.

Cokar, M., Ford, B., Gieg, L. M., Kallos, M. S., and Gates, I. D. (2013a). Reactive reservoir simulation of biogenic shallow shale gas systems enabled by experimentally determined methane generation rates. *Energy and Fuels*, 27:2413–2421.

Cokar, M., Ford, B., Kallos, M. S., and Gates, I. D. (2013b). New gas material balance to quantify biogenic gas generation rates from shallow organic-matter-rich shales. *Fuel*, 104:443–451.

Colosimo, F., Thomas, R., Lloyd, J. R., Taylor, K. G., Boothman, C., Smith, A. D., Lord, R., and Kalin, R. M. (2016). Biogenic methane in shale gas and coal bed methane: A review of current knowledge and gaps. *International Journal of Coal Geology*, 165:106–120.

Conti, B., de Jesus Perinotto, J. A., Veroslavsky, G., Castillo, M. G., de Santa Ana, H., Soto, M., and Morales, E. (2017). Speculative petroleum systems of the southern Pelotas Basin, offshore Uruguay. *Marine and Petroleum Geology*, 83:1–25.

Corner, B., Cartwright, J., and Swart, R. (2002). Volcanic passive margin of Namibia: A potential fields perspective. *Geological Society of America Special Paper - Volcanic Rifted Margins, eds: Menzies, M. A., Klemperer, S. L., Ebinger, C. J. Baker, J.*, 362:203–220.

Crockford, P. W., Wing, B. A., Paytan, A., Hodgskiss, M. S., Mayfield, K. K., Hayles, J. A., Middleton, J. E., Ahm, A. S. C., Johnston, D. T., Caxito, F., Uhlein, G., Halverson, G. P., Eickmann, B., Torres, M., and Horner, T. J. (2019). Barium-isotopic constraints on the origin of post-Marinoan barites. *Earth and Planetary Science Letters*, 519:234–244.

Cutter, G., Casciotti, K., Croot, P., Geibert, W., Heimbürger, L.-E., Lohan, M., Planquette, H., and van de Flierdt, T. (2017). *Sampling and Sample-handling Protocols for GEOTRACES Cruises. Cutter, G. (Eds.)*, volume 1, pages 1-139. GEOTRACES International Project Office, Toulouse, France, 3rd edition.

Daly, M. C., Chorowicz, J., and Fairhead, J. D. (1989). Rift basin evolution in Africa: The influence of reactivated steep basement shear zones. *Geological Society Special Publication - Inversion Tectonics, eds: Cooper, M. A. Williams, G. D.*, 44:309–334.

Davie, M. K. and Buffett, B. A. (2003). A steady state model for marine hydrate formation: Constraints on methane supply from pore water sulfate profiles. *Journal of Geophysical Research: Solid Earth*, 108:1–13.

Davies, C. P. N. and der Spuy, D. V. (1990). Chemical and optical investigations into the hydrocarbon source potential and thermal maturity of the Kudu 9A-2 and 9A-3 boreholes. in The Kudu Offshore Drilling Project. *Communications Of The Geological Survey Of Namibia*, 6:49–58.

de Groot, T. R., Menoud, M., van Bleijswijk, J., van Leeuwen, S. M., van der Molen, J., Hernando-Morales, V., Czerski, H., Maazallahi, H., Walter, S., Rush, D., Röckmann, T., and Niemann, H. (2024). Tidal and seasonal influence on cold seep activity and methanotroph efficiency in the North Sea. *Communications Earth Environment*, 5:368.

de Vera, J., Granado, P., and McClay, K. (2010). Structural evolution of the Orange Basin gravity-driven system, offshore Namibia. *Marine and Petroleum Geology*, 27:223–237.

Dean, W. E., Gardner, J. V., and Piper, D. Z. (1997). Inorganic geochemical indicators of glacial-interglacial changes in productivity and anoxia on the California continental margin. *Geochimica et cosmochimica acta*, 61:4507–4518.

Dehairs, F., Chesselet, R., and Jedwab, J. (1980). Discrete suspended particles of barite and the barium cycle in the open ocean. *Earth and Planetary Science Letters*, 49:528–550.

Delvaux, D. (1991). The Karoo to Recent rifting in the western branch of the East-African rift system: A bibliographical synthesis. *Mus. roy. Afr. centr., Tervuren (Belg.), Dept. Geol. Min*, 1:63–82.

Demarcq, H. (2009). Trends in primary production, sea surface temperature and wind in upwelling systems (1998-2007). *Progress in Oceanography*, 83:376–385.

Desboeufs, K., Formenti, P., Torres-Sánchez, R., Schepanski, K., Chaboureau, J. P., Andersen, H., Cermak, J., Feuerstein, S., Laurent, B., Klopper, D., Namwoonde, A., Cazaunau, M., Chevaillier, S., Feron, A., Mirande-Bret, C., Triquet, S., and Piketh, S. J. (2024). Fractional solubility of iron in mineral dust aerosols over coastal Namibia: a link to marine biogenic emissions? *Atmospheric Chemistry and Physics*, 24:1525–1541.

Dia, A. N., Aquilina, L., Boulegue, J., Bourgois, J., Suess, E., and Torres, M. (1993). Origin of fluids and related barite deposits at vent sites along the Peru convergent margin. *Geology (Boulder)*, 21:1099–1102.

Díaz-Ochoa, J. A., Pantoja, S., Lange, G. J. D., Lange, C. B., Sánchez, G. E., Acuña, V. R., Muñoz, P., and Vargas, G. (2011). Oxygenation variability in Mejillones Bay, off northern Chile, during the last two centuries. *Biogeosciences*, 8:137–146.

Dickens, G. R. (2001). Sulfate profiles and barium fronts in sediment on the Blake Ridge: Present and past methane fluxes through a large as hydrate reservoir. *Geochimica et Cosmochimica Acta*, 65:529–543.

Dickens, G. R., Fewless, T., Thomas, E., and Bralower, T. J. (2003). Excess barite accumulation during the Paleocene-Eocene Thermal Maximum: Massive input of dissolved barium from seafloor gas hydrate reservoirs. *Geological Society of America Special Paper - Causes and Consequences of Globally Warm Climates in the Early Paleogene, eds: Wing, S. L., Gingerich, P. D., Schmitz, B. Thomas, E.*, 369:11–23.

Dickens, G. R. and Quinby-Hunt, M. S. (1994). Methane hydrate stability in seawater. *Geophysical Research Letters*, 21:2115–2118.

Dingle, R. V. (1973). The geology of the continental shelf between Lüderitz and Cape Town (Southwest Africa), with special reference to Tertiary strata. *Journal of the Geological Society*, 129:337–363.

Dingle, R. V. and Nelson, G. (1993). Sea-bottom temperature, salinity and dissolved oxygen on the continental margin off South-Western Africa. *South African Journal of Marine Science*, 13:33–49.

Dowsett, H., Barron, J., and Poore, R. (1996). Middle Pliocene sea surface temperatures: A global reconstruction. *Marine Micropaleontology*, 27:13–25.

Dullien, F. A. L. (1992). *Porous Media: Fluid Transport and Pore Structure. Dullien, F. A. L (Eds.)*, volume 1, pages 1-574. Academic Press, San Diego, USA, 2nd edition.

Duperron, S., Gaudron, S. M., Lemaitre, N., and Bayon, G. (2014). A microbiological and biogeochemical investigation of the cold seep tubeworm Escarpia Southwardae (Annelida: Siboglinidae): Symbiosis and trace element composition of the tube. *Deep-Sea Research Part I: Oceanographic Research Papers*, 90:105–114.

Dymond, J., Suess, E., and Lyle, M. (1992). Barium in Deep-Sea Sediment: A Geochemical Proxy for Paleoproductivity. *Paleoceanography*, 7:163–181.

Eagle, M., Paytan, A., Arrigo, K. R., van Dijken, G., and Murray, R. W. (2003). A comparison between excess barium and barite as indicators of carbon export. *Paleoceanography*, 18:1–13.

Eagles, G. (2007). New angles on South Atlantic opening. *Geophysical Journal International*, 168:353–361.

Eastwell, D., Hodgson, N., and Rodriguez, K. (2018). Source rock characterization in frontier basins - A global approach. *First Break*, 36:53–60.

Eickmann, B., Thorseth, I. H., Peters, M., Strauss, H., Bröcker, M., and Pedersen, R. B. (2014). Barite in hydrothermal environments as a recorder of subseafloor processes: A multiple-isotope study from the Loki's Castle vent field. *Geobiology*, 12:308–321.

Emeis, K., Eggert, A., Flohr, A., Lahajnar, N., Nausch, G., Neumann, A., Rixen, T., Schmidt, M., der Plas, A. V., and Wasmund, N. (2018). Biogeochemical processes and turnover rates in the Northern Benguela Upwelling System. *Journal of Marine Systems*, 188:63–80.

Emeis, K. C., Brüchert, V., Currie, B., Endler, R., Ferdelman, T., Kiessling, A., Leipe, T., Noli-Peard, K., Struck, U., and Vogt, T. (2004). Shallow gas in shelf sediments of the Namibian coastal upwelling ecosystem. *Continental Shelf Research*, 24:627–642.

Emeis, K. C., Struck, U., Leipe, T., and Ferdelman, T. G. (2009). Variability in upwelling intensity and nutrient regime in the coastal upwelling system offshore Namibia: Results from sediment archives. *International Journal of Earth Sciences*, 98:309–326.

England, W. A., Mackenzie, A. S., Mann, D. M., and Quigley, T. M. (1987). The movement and entrapment of petroleum fluids in the subsurface. *Journal of the Geological Society*, 144:327–347.

Eruteya, O. E., Reshef, M., Ben-Avraham, Z., and Waldmann, N. (2018). Gas escape along the Palmachim disturbance in the Levant Basin, offshore Israel. *Marine and Petroleum Geology*, 92:868–879.

Feng, D., Qiu, J. W., Hu, Y., Peckmann, J., Guan, H., Tong, H., Chen, C., Chen, J., Gong, S., Li, N., and Chen, D. (2018). Cold seep systems in the South China Sea: An overview. *Journal of Asian Earth Sciences*, 168:3–16.

Feng, D. and Roberts, H. H. (2011). Geochemical characteristics of the barite deposits at cold seeps from the northern Gulf of Mexico continental slope. *Earth and Planetary Science Letters*, 309:89–99.

Flemings, P. B., Phillips, S. C., Boswell, R., Collett, T. S., Cook, A. E., Dong, T., Frye, M., Goldberg, D. S., Guerin, G., Holland, M. E., Jang, J., Meazell, K., Morrison, J., O'Connell, J. I., Petrou, E. G., Pettigrew, T., Polito, P. J., Portnov, A., Santra, M., Schultheiss, P. J., Seol, Y., Shedd, W., Solomon, E. A., Thomas, C. M., Waite, W. F., and You, K. (2020). Pressure coring a Gulf of Mexico deep-water turbidite gas hydrate reservoir: Initial results from the University of Texas-Gulf of Mexico 2-1 (UT-GOM2-1) Hydrate Pressure Coring Expedition. *AAPG Bulletin*, 104:1847–1876.

Fohrmann, M. and Pecher, I. A. (2012). Analysing sand-dominated channel systems for potential gas-hydrate-reservoirs using an AVO seismic inversion technique on the Southern Hikurangi Margin, New Zealand. *Marine and Petroleum Geology*, 38:19–34.

Foschi, M. and Cartwright, J. (2016). South Malvinas/Falkland Basin: Hydrocarbon migration and petroleum system. *Marine and Petroleum Geology*, 77:124–140.

Foster, D. A., Staubwasser, M., and Henderson, G. M. (2004). 226Ra and Ba concentrations in the Ross Sea measured with multicollector ICP mass spectrometry. *Marine Chemistry*, 87:59–71.

Frieling, J., Peterse, F., Lunt, D. J., Bohaty, S. M., Damsté, J. S. S., Reichart, G. J., and Sluijs, A. (2019). Widespread Warming Before and Elevated Barium Burial During the Paleocene-Eocene Thermal Maximum: Evidence for Methane Hydrate Release? *Paleoceanography and Paleoclimatology*, 34:546–566.

Frieling, J., Svensen, H. H., Planke, S., Cramwinckel, M. J., Selnes, H., and Sluijs, A. (2016). Thermogenic methane release as a cause for the long duration of the PETM. *Proceedings of the National Academy of Sciences of the United States of America*, 113:12059–12064.

Gallego-Torres, D., Martínez-Ruiz, F., Paytan, A., Jiménez-Espejo, F. J., and Ortega-Huertas, M. (2007). Pliocene-Holocene evolution of depositional conditions in the eastern Mediterranean: Role of anoxia vs. productivity at time of sapropel deposition. *Palaeogeography, Palaeoclimatology, Palaeoecology*, 246:424–439.

Gäng, F., Böning, P., Brüchert, V., Lahajnar, N., and Pahnke, K. (2023). Critical assessment of U, Ba and Ni as redox and productivity proxies in organic-rich sediments underneath dynamic, highly productive waters. *Geochimica et Cosmochimica Acta*, 348:206–220.

García-Reyes, M., Koval, G., Sydeman, W. J., Palacios, D., Bedriñana-Romano, L., DeForest, K., Silva, C. M., Sepúlveda, M., and Hines, E. (2023). Most eastern boundary upwelling regions represent thermal refugia in the age of climate change. *Frontiers in Marine Science*, 10:1158472.

García-Reyes, M. and Largier, J. (2010). Observations of increased wind-driven coastal upwelling off Central California. *Journal of Geophysical Research: Oceans*, 115:C04011.

Garzanti, E., Andò, S., Vezzoli, G., Lustrino, M., Boni, M., and Vermeesch, P. (2012). Petrology of the Namib Sand Sea: Long-distance transport and compositional variability in the wind-displaced Orange Delta. *Earth-Science Reviews*, 112:173–189.

Gaudio, A. V. D., Avery, A., Auer, G., Piller, W. E., and Kurz, W. (2024). Planktonic foraminiferal assemblages as tracers of paleoceanographic changes within the Northern Benguela current system since the Early Pleistocene. *Climate of the Past Discussions*, 3:1–57.

Gay, A., Lopez, M., Berndt, C., and Séranne, M. (2007). Geological controls on focused fluid flow associated with seafloor seeps in the Lower Congo Basin. *Marine Geology*, 244:68–92.

Gay, A., Lopez, M., Cochonat, R., Sultan, N., Cauquil, E., and Brigaud, E. (2003). Sinuous pockmark belt as indicator of a shallow buried turbiditic channel on the lower slope of the Congo basin, West African margin. *Geological Society, London, Special Publications - Subsurface Sediment Mobilization, eds: Van Rensbergen, P., Hillis, R. R., Maltman, A.J., Morley, C.K.*, 216:173–189.

Gay, A., Lopez, M., Ondreas, H., Charlou, J. L., Sermondadaz, G., and Cochonat, P. (2006). Seafloor facies related to upward methane flux within a Giant Pockmark of the Lower Congo Basin. *Marine Geology*, 226:81–95.

Geyman, B. M., Ptacek, J. L., LaVigne, M., and Horner, T. J. (2019). Barium in deep-sea bamboo corals: Phase associations, barium stable isotopes, prospects for paleoceanography. *Earth and Planetary Science Letters*, 525:115751.

Gingele, F. (1992). Zur klimaabhängigen Bildung biogener und terrigener Sedimente und ihrer Veränderung durch die Frühdiagenese im zentralen und östlichen Südatlantik. *Department of Geosciences, University of Bremen, Bremen*, Thesis:1–202.

Gingele, F. and Dahmke, A. (1994). Discrete barite particles and barium as tracers of paleoproductivity in South Atlantic sediments. *Paleoceanography*, 9:151–168.

Gingele, F. X., Zabel, M., Kasten, S., Bonn, W. J., and Nürnberg, C. C. (1999). *Biogenic Barium as a Proxy for Paleoproductivity: Methods and Limitations of Application. In Fischer G. Wefer G. (Eds.), Chapter 13 in Use of Proxies in Paleoceanography: Examples from the South Atlantic*, pages 345–364. Springer, Berlin-Heidelberg, Germany, 1st edition.

Glud, R. N., Gundersen, J. K., Jørgensen, B. B., Revsbech, N. P., and Schulz, H. D. (1994). Diffusive and total oxygen uptake of deep-sea sediments in the eastern South Atlantic Ocean: in situ and laboratory measurements. *Deep-Sea Research Part I*, 41:1767–1788.

Goldhammer, T., Brunner, B., Bernasconi, S. M., Ferdelman, T. G., and Zabel, M. (2011). Phosphate oxygen isotopes: Insights into sedimentary phosphorus cycling from the Benguela upwelling system. *Geochimica et Cosmochimica Acta*, 75:3741–3756.

Gong, Y., Zeng, Z., Cheng, W., Lu, Y., Zhang, L., Yu, H., and Huang, F. (2020). Barium isotopic fractionation during strong weathering of basalt in a tropical climate. *Environment International*, 143:105896.

Greinert, J., Bollwerk, S. M., Derkachev, A., Bohrmann, G., and Suess, E. (2002). Massive barite deposits and carbonate mineralization in the Derugin Basin, Sea of Okhotsk; precipitation processes at cold seep sites. *Earth and planetary science letters*, 203:165–180.

Griffith, E. M. and Paytan, A. (2012). Barite in the ocean - occurrence, geochemistry and palaeoceanographic applications. *Sedimentology*, 59:1817–1835.

Griffith, E. M., Thomas, E., Lewis, A. R., Penman, D. E., Westerhold, T., and Winguth, A. M. (2021). Bentho-Pelagic Decoupling: The Marine Biological Carbon Pump During Eocene Hyperthermals. *Paleoceanography and Paleoclimatology*, 36:e2020PA004053.

Guillon, E., Menot, L., Decker, C., Krylova, E., and Olu, K. (2017). The vesicomyid bivalve habitat at cold seeps supports heterogeneous and dynamic macrofaunal assemblages. *Deep-Sea Research Part I: Oceanographic Research Papers*, 120:1–13.

Guiraud, R., Bosworth, W., Thierry, J., and Delplanque, A. (2005). Phanerozoic geological evolution of Northern and Central Africa: An overview. *Journal of African Earth Sciences*, 43:83–143.

Haese, R. R., Petermann, H., Dittert, L., and Schulz, H. D. (1998). The early diagenesis of iron in pelagic sediments: a multidisciplinary approach. *Earth and Planetary Science Letters*, 157:233–248.

Hage, S., Baker, M. L., Babonneau, N., Soulet, G., Dennielou, B., Jacinto, R. S., Hilton, R. G., Galy, V., Baudin, F., Rabouille, C., Vic, C., Sahin, S., Açikalin, S., and Talling, P. J. (2024). How is particulate organic carbon transported through the river-fed Congo Submarine Canyon to the deep-sea? *EGU Sphere*, 900:1–40.

Hanor, J. S. and Mercer, J. A. (2011). *Spatial variations in the salinity of pore waters in northern deep water Gulf of Mexico sediments; implications for pathways and mechanisms of solute transport. In Yardley, B., Manning, C. Garven G. (Eds.), Chapter 13 in Frontiers in Geofluids*, volume 10, pages 83–93. Wiley-Blackwell, Oxford, UK, 1st edition.

Haq, B. U., Hardenbol, J., and Vail, P. R. (1987). Chronology of Fluctuating Sea Levels since the Triassic. *The American Association for the Advancement of Science*, 235:1156–1167.

Hayes, C. T., Costa, K. M., Anderson, R. F., Calvo, E., Chase, Z., Demina, L. L., Dutay, J. C., German, C. R., Heimbürger-Boavida, L. E., Jaccard, S. L., Jacobel, A., Kohfeld, K. E., Kravchishina, M. D., Lippold, J., Mekik, F., Missiaen, L., Pavia, F. J., Paytan, A., Pedrosa-Pamies, R., Petrova, M. V., Rahman, S., Robinson, L. F., Roy-Barman, M., Sanchez-Vidal, A., Shiller, A., Tagliabue, A., Tessin, A. C., van Hulten, M., and Zhang, J. (2021). Global Ocean Sediment Composition and Burial Flux in the Deep Sea. *Global Biogeochemical Cycles*, 35:e2020GB006769.

Haynes, L. L. and Hönisch, B. (2020). The seawater carbon inventory at the Paleocene–Eocene Thermal Maximum. *Proceedings of the National Academy of Sciences - PNAS*, 117:24088–24095.

He, Z., Archer, C., Yang, S., and Vance, D. (2023). Sedimentary cycling of zinc and nickel and their isotopes on an upwelling margin: Implications for oceanic budgets and paleoenvironment proxies. *Geochimica et Cosmochimica Acta*, 343:84–97.

He, Z., Clarkson, M. O., Andersen, M. B., Archer, C., Sweere, T. C., Kraal, P., Guthauser, A., Huang, F., and Vance, D. (2021). Temporally and spatially dynamic redox conditions on an upwelling margin: The impact on coupled sedimentary Mo and U isotope systematics, and implications for the Mo-U paleoredox proxy. *Geochimica et Cosmochimica Acta*, 309:251–271.

Heggland, R. (2004). Definition of geohazards in exploration 3-D seismic data using attributes and neural-network analysis. *AAPG Bulletin*, 88:857–868.

Hein, J. R., Zierenberg, R. A., Maynard, J. B., and Hannington, M. D. (2007). Barite-forming environments along a rifted continental margin, Southern California Borderland. *Deep-Sea Research Part II: Topical Studies in Oceanography*, 54:1327–1349.

Heins, W. A. (2022). Probing the frontier in Namibia. *First Break*, 40:51–57.

Hemsing, F., Hsieh, Y. T., Bridgestock, L., Spooner, P. T., Robinson, L. F., Frank, N., and Henderson, G. M. (2018). Barium isotopes in cold-water corals. *Earth and Planetary Science Letters*, 491:183–192.

Henkel, S., Mogollón, J. M., Nöthen, K., Franke, C., Bogus, K., Robin, E., Bahr, A., Blumenberg, M., Pape, T., Seifert, R., März, C., de Lange, G. J., and Kasten, S. (2012). Diagenetic barium cycling in Black Sea sediments - A case study for anoxic marine environments. *Geochimica et Cosmochimica Acta*, 88:88–105.

Hensen, C. (1996). Frühdiagenetische Prozesse und Quantifizierung benthischer Stoff-Flüsse in Oberflächensedimenten des Südatlantiks. *Department of Geosciences, University of Bremen, Bremen*, Thesis:1–132.

Hensen, C., Landenberger, H., Zabel, M., Gundersen, J. K., Glud, R. N., and Schulz, H. D. (1997). Simulation of early diagenetic processes in continental slope sediments off southwest Africa: The computer model CoTAM tested. *Marine Geology*, 144:191–210.

Hensen, C., Zabel, M., Pfeifer, K., Schwenk, T., Kasten, S., Riedinger, N., Schulz, H. D., and Boetius, A. (2003). Control of sulfate pore-water profiles by sedimentary events and the significance of anaerobic oxidation of methane for the burial of sulfur in marine sediments. *Geochimica et Cosmochimica Acta*, 67:2631–2647.

Heuer, V. (2002). Spurenelemente in Sedimenten Des Südatlantik. Primärer Eintrag Und Frühdiagenetische überprägung. *Department of Geosciences, University of Bremen, Bremen*, Thesis:1–136.

Ho, S., Cartwright, J. A., and Imbert, P. (2012). Vertical evolution of fluid venting structures in relation to gas flux, in the Neogene-Quaternary of the Lower Congo Basin, Offshore Angola. *Marine Geology*, 332-334:40–55.

Hodgson, N., Intawong, A., Rodriguez, K., and Huuse, M. (2014). A seismic tool to reduce source maturity risk in unexplored basins. *First Break*, 32:103–108.

Hodgson, N., Rodriguez, K., and Davies, J. (2021). South Africa poised for exploration greatness. *Geo ExPro*, 18:1–5.

Hodgson, N., Rodriguez, K., and Found, S. L. (2024). Seismic Foldout: Namibia's Orange Basin and the holey slope mystery. *Geo ExPro*, 22:1–5.

Hong, W. L., Solomon, E. A., and Torres, M. E. (2014a). A kinetic-model approach to quantify the effect of mass transport deposits on pore water profiles in the Krishna-Godavari Basin, Bay of Bengal. *Marine and Petroleum Geology*, 58:223–232.

Hong, W. L., Torres, M. E., Kim, J. H., Choi, J., and Bahk, J. J. (2013). Carbon cycling within the sulfate-methane-transition-zone in marine sediments from the Ulleung Basin. *Biogeochemistry*, 115:129–148.

Hong, W. L., Torres, M. E., Kim, J. H., Choi, J., and Bahk, J. J. (2014b). Towards quantifying the reaction network around the sulfate-methane-transition-zone in the Ulleung Basin, East Sea, with a kinetic modeling approach. *Geochimica et Cosmochimica Acta*, 140:127–141.

Hopkins, A. and Cartwright, J. (2021). Large scale excavation of outer shelf sediments by bottom currents during the Late Miocene in the SE Atlantic. *Geo-Marine Letters*, 41:1–15.

Hopkins, A. E. (2006). Seismic stratigraphic interpretation of contourite systems. *School of Earth and Environmental Sciences, University of Cardiff, Cardiff*, Thesis:1–132.

Horner, T. J. and Crockford, P. W. (2021). *Barium Isotopes: drivers, dependencies, and distributions through space and time. Lyons T., Turchyn, A. Reinhard, C. (Eds.)*, volume 1, pages 1-34. Cambridge University Press, Cambridge, UK, 1st edition.

Horner, T. J., Kinsley, C. W., and Nielsen, S. G. (2015). Barium-isotopic fractionation in seawater mediated by barite cycling and oceanic circulation. *Earth and Planetary Science Letters*, 430:511–522.

Horner, T. J., Little, S. H., Conway, T. M., Farmer, J. R., Hertzberg, J. E., Janssen, D. J., Lough, A. J., McKay, J. L., Tessin, A., Galer, S. J., Jaccard, S. L., Lacan, F., Paytan, A., and Wuttig, K. (2021). Bioactive Trace Metals and Their Isotopes as Paleoproductivity Proxies: An Assessment Using GEOTRACES-Era Data. *Global Biogeochemical Cycles*, 35:e2020GB006814.

Horner, T. J., Pryer, H. V., Nielsen, S. G., Crockford, P. W., Gauglitz, J. M., Wing, B. A., and Ricketts, R. D. (2017). Pelagic barite precipitation at micromolar ambient sulfate. *Nature Communications*, 8:1342.

Horsthemke, E., Ledendecker, S., and Porada, H. (1990). Depositional environments and stratigraphic correlation of the Karoo Sequence in northwestern Damaraland. *Communications Of The Geological Survey Of Namibia*, 6:67–77.

House, B. M. and Norris, R. D. (2020). Unlocking the barite paleoproductivity proxy: A new high-throughput method for quantifying barite in marine sediments. *Chemical Geology*, 552:119664.

Hsieh, Y. T., Bridgestock, L., Scheuermann, P. P., Seyfried, W. E., and Henderson, G. M. (2021). Barium isotopes in mid-ocean ridge hydrothermal vent fluids: A source of isotopically heavy Ba to the ocean. *Geochimica et Cosmochimica Acta*, 292:348–363.

Hsieh, Y. T. and Henderson, G. M. (2017). Barium stable isotopes in the global ocean: Tracer of Ba inputs and utilization. *Earth and Planetary Science Letters*, 473:269–278.

Hsieh, Y. T., Paver, R., Tanzil, J. T., Bridgestock, L., Lee, J. N., and Henderson, G. M. (2022). Multi-colony calibration of barium isotopes between shallow-water coral skeletons and in-situ seawater: Implications for paleo proxies. *Earth and Planetary Science Letters*, 580:117369.

Hu, Y., Luo, M., Chen, L., Liang, Q., Feng, D., Tao, J., Yang, S., and Chen, D. (2018). Methane source linked to gas hydrate system at hydrate drilling areas of the South China Sea: Porewater geochemistry and numerical model constraints. *Journal of Asian Earth Sciences*, 168:87–95.

Huenerlage, K. and Buchholz, F. (2013). Krill of the northern Benguela Current and the Angola-Benguela frontal zone compared: Physiological performance and short-term starvation in Euphausia hanseni. *Journal of Plankton Research*, 35:337–351.

Hunt, H. R., Summers, B. A., Sieber, M., Krisch, S., Al-Hashem, A., Hopwood, M., Achterberg, E. P., and Conway, T. M. (2022). Distinguishing the influence of sediments, the Congo River, and water-mass mixing on the distribution of iron and its isotopes in the Southeast Atlantic Ocean. *Marine Chemistry*, 247:104181.

Hunter, S. J., Goldobin, D. S., Haywood, A. M., Ridgwell, A., and Rees, J. G. (2013). Sensitivity of the global submarine hydrate inventory to scenarios of future climate change. *Earth and Planetary Science Letters*, 367:105–115.

Hussain, A. and Al-Ramadan, K. (2022). Organic Matter Burial in Deep-Sea Fans: A Depositional Process-Based Perspective. *Journal of Marine Science and Engineering*, 10:682.

Hustoft, S., Bünz, S., Mienert, J., and Chand, S. (2009). Gas hydrate reservoir and active methane-venting province in sediments on < 20 Ma young oceanic crust in the Fram Strait, offshore NW-Svalbard. *Earth and Planetary Science Letters*, 284:12–24.

Hustoft, S., Mienert, J., Bünz, S., and Nouzé, H. (2007). High-resolution 3D-seismic data indicate focussed fluid migration pathways above polygonal fault systems of the mid-Norwegian margin. *Marine Geology*, 245:89–106.

Hutchings, L., van der Lingen, C. D., Shannon, L. J., Crawford, R. J., Verheye, H. M., Bartholomae, C. H., van der Plas, A. K., Louw, D., Kreiner, A., Ostrowski, M., Fidel, Q., Barlow, R. G., Lamont, T., Coetzee, J., Shillington, F., Veitch, J., Currie, J. C., and Monteiro, P. M. (2009). The Benguela Current: An ecosystem of four components. *Progress in Oceanography*, 83:15–32.

Inglis, G. N., Rohrssen, M., Kennedy, E. M., Crouch, E. M., Raine, J. I., Strogen, D. P., Naafs, B. D. A., Collinson, M. E., and Pancost, R. D. (2021). Terrestrial methane cycle perturbations during the onset of the Paleocene-Eocene Thermal Maximum. *Geology*, 49:520–524.

Intawong, A., Huuse, M., Rodriguez, K., and Hodgson, N. (2015). De-Risking Source Rock Maturity in the Lüderitz Basin using Near-Surface Geotherm Estimates and Basin Modelling. *First Break*, 33:2–5.

Inthorn, M., Wagner, T., Scheeder, G., and Zabel, M. (2006). Lateral transport controls distribution, quality, and burial of organic matter along continental slopes in high-productivity areas. *Geology*, 34:205–208.

Jacobs, Z. L., Jebri, F., Raitsos, D. E., Popova, E., Srokosz, M., Painter, S. C., Nencioli, F., Roberts, M., Kamau, J., Palmer, M., and Wihsgott, J. (2020). Shelf-Break Upwelling and Productivity Over the North Kenya Banks: The Importance of Large-Scale Ocean Dynamics. *Journal of Geophysical Research: Oceans*, 125:e2019JC015519.

James, R. H., Bousquet, P., Bussmann, I., Haeckel, M., Kipfer, R., Leifer, I., Niemann, H., Ostrovsky, I., Piskozub, J., Rehder, G., Treude, T., Vielstädte, L., and Greinert, J. (2016). Effects of climate change on methane emissions from seafloor sediments in the Arctic Ocean: A review. *Limnology and Oceanography*, 61:S283–S299.

Jamieson, J. W., Hannington, M. D., Tivey, M. K., Hansteen, T., Williamson, N. M., Stewart, M., Fietzke, J., Butterfield, D., Frische, M., Allen, L., Cousens, B., and Langer, J. (2016). Precipitation and growth of barite within hydrothermal vent deposits from the Endeavour Segment, Juan de Fuca Ridge. *Geochimica et Cosmochimica Acta*, 173:64–85.

Jørgensen, B. B. and Kasten, S. (2006). *Sulfur Cycling and Methane Oxidation. In Schulz, H. D. Zabel M. (Eds.), Chapter 8 in Marine Geochemistry*, volume 1, pages 271–309. Springer, Berlin-Heidelberg, Germany, 2nd edition.

Jørgensen, B. B., Weber, A., and Zopfi, J. (2001). Sulphate reduction and anaerobic oxidation in Black Sea sediments. *Deep-Sea Res. I*, 48:2097–2120.

Jourdan, F., Féraud, G., Bertrand, H., Kampunzu, A. B., Tshoso, G., Watkeys, M. K., and Gall, B. L. (2005). Karoo large igneous province: Brevity, origin, and relation to mass extinction questioned by new 40Ar/39Ar age data. *Geology*, 33:745–748.

Judd, A. and Hovland, M. (2007). *Seabed Fluid Flow: The Impact of Geology, Biology, and the Marine Environment. Hovland M. (Eds.)*, volume 1, pages 1-475. Cambridge University Press, Cambridge, UK, 1st edition.

Jungslager, E. H. (1999). Petroleum habitats of the Atlantic margin of South Africa. *Geological Society Special Publication - The Oil and Gas Habitats of the South Atlantic, eds - Cameron, N. R., Bate, R. H. Clure, V. S.*, 153:153–168.

Kasten, S., Nöthen, K., Hensen, C., Spieß, V., Blumenberg, M., and Schneider, R. R. (2012). Gas hydrate decomposition recorded by authigenic barite at pockmark sites of the northern Congo Fan. *Geo-Marine Letters*, 32:515–524.

Kirkpatrick, L. H., Green, A. N., and Pether, J. (2019a). The seismic stratigraphy of the inner shelf of southern Namibia: The development of an unusual nearshore shelf stratigraphy. *Marine Geology*, 408:18–35.

Kirkpatrick, L. H., Jacob, J., and Green, A. N. (2019b). Beaches and bedrock: How geological framework controls coastal morphology and the relative grade of a Southern Namibian diamond placer deposit. *Ore Geology Reviews*, 107:853–862.

Knight, A. C., Tipper, E. T., Bradbury, H. J., Turchyn, A. V., Andermann, C., Freymuth, H., Elliot, T., and Bridgestock, L. (2024). Experimental constraints on barium isotope fractionation during adsorption–desorption reactions: Implications for weathering and erosion tracer applications. *Geochimica et Cosmochimica Acta*, 384:194–212.

Koch, C., Greenhalgh, J., and Mathew, F. (2013). Petroleum Prospectivity in the Namibe Basin, offshore Angola. *Society of Exploration Geophysicists International Exposition and 83rd Annual Meeting, SEG 2013: Expanding Geophysical Frontiers*, 1:1284–1287.

Koltermann, C. E. and Gorelick, S. M. (1995). Fractional packing model for hydraulic conductivity derived from sediment mixtures. *Water Resources Research*, 31:3283–3297.

Kopte, R., Brandt, P., Dengler, M., Tchipalanga, P. C., Macuéria, M., and Ostrowski, M. (2017). The Angola Current: Flow and hydrographic characteristics as observed at 11°S. *Journal of Geophysical Research: Oceans*, 122:1177–1189.

Körner, M., Brandt, P., Illig, S., Dengler, M., Subramaniam, A., Bachèlery, M.-L., and Krahmann, G. (2024). Coastal trapped waves and tidal mixing control primary production in the tropical Angolan upwelling system. *Science Advances - Oceanography*, 10:eadj6686.

Koseki, S., Giordani, H., and Goubanova, K. (2019). Frontogenesis of the Angola-Benguela Frontal Zone. *Ocean Science*, 15:83–96.

Kossack, M., Scholz, F., Anderson, C. H., Vosteen, P., Su, C. C., Mohrholz, V., and Zabel, M. (2023). Sedimentary molybdenum and uranium cycling under seasonally contrasting redox conditions on the Namibian Shelf. *Geochimica et Cosmochimica Acta*, 358:174–191.

Kravchishina, M. D., Lein, A. Y., Flint, M. V., Baranov, B. V., Miroshnikov, A. Y., Dubinina, E. O., Dara, O. M., Boev, A. G., and Savvichev, A. S. (2021). Methane-Derived Authigenic Carbonates on the Seafloor of the Laptev Sea Shelf. *Frontiers in Marine Science*, 8:690304.

Kunath, P., Chi, W. C., Berndt, C., Chen, L., Liu, C. S., Kläschen, D., and Muff, S. (2020). A Shallow Seabed Dynamic Gas Hydrate System off SW Taiwan: Results From 3-D Seismic, Thermal, and Fluid Migration Analyses. *Journal of Geophysical Research: Solid Earth*, 125:e2019JB019245-T.

Lamontagne, R. A., Swinnerton, J. W., Linnenbom, V. J., and Smith, W. D. (1973). Methane concentrations in various marine environments. *Journal of Geophysical Research*, 78:5317–5324.

Lamotte, D. F. D., Fourdan, B., Leleu, S., Leparmentier, F., and Clarens, P. D. (2015). Style of rifting and the stages of Pangea breakup. *Tectonics*, 34:1009–1029.

Lan, Z., Roberts, N. M., Zhou, Y., Zhang, S., Li, Z., and Zhao, T. (2022). Application of in situ U-Pb carbonate geochronology to Stenian-Tonian successions of North China. *Precambrian Research*, 370:106551.

Lemaitre, N., Bayon, G., Ondréas, H., Caprais, J. C., Freslon, N., Bollinger, C., Rouget, M. L., de Prunelé, A., Ruffine, L., Roy, K. O.-L., and Sarthou, G. (2014). Trace element behaviour at cold seeps and the potential export of dissolved iron to the ocean. *Earth and Planetary Science Letters*, 404:376–388.

Li, A., Wu, N., Wan, Z., Li, Q., Sun, Z., Cai, F., and Feng, D. (2024). Lateral migration of methane at a cold seep: Evidence from U–Th dating of methane-derived authigenic carbonate in the Middle Okinawa Trough. *Marine and Petroleum Geology*, 163:106778.

Li, J., Li, L., Bai, S., Ta, K., Xu, H., Chen, S., Pan, J., Li, M., Du, M., and Peng, X. (2019). New insight into the biogeochemical cycling of methane, S and Fe above the Sulfate-Methane Transition Zone in methane hydrate-bearing sediments: A case study in the Dongsha area, South China Sea. *Deep-Sea Research Part I: Oceanographic Research Papers*, 145:97–108.

Li, N., Feng, D., Chen, L., Wang, H., and Chen, D. (2016). Using sediment geochemistry to infer temporal variation of methane flux at a cold seep in the South China Sea. *Marine and Petroleum Geology*, 77:835–845.

Light, M. P., Maslanyj, M. P., Greenwood, R. J., and Banks, N. L. (1993). Seismic sequence stratigraphy and tectonics offshore Namibia. *Geological Society Special Publication - Tectonics and Seismic Sequence Stratigraphy, eds: Williams, G. D. Dobb, A.*, 71:163–191.

Lin, Y. B., Wei, H. Z., Zhang, F., Hohl, S. V., Wei, G. Y., Li, T., Xiong, G. L., Li, N., and Jiang, S. Y. (2022). Evaluation of shallow-water corals and associated carbonate sediments as seawater Ba isotope archives in the South China Sea. *Palaeogeography, Palaeoclimatology, Palaeoecology*, 605:111196.

Lin, Y. S., Heuer, V. B., Goldhammer, T., Kellermann, M. Y., Zabel, M., and Hinrichs, K. U. (2012). Towards constraining H2 concentration in subseafloor sediment: A proposal for combined analysis by two distinct approaches. *Geochimica et Cosmochimica Acta*, 77:186–201.

Liu, T., Krisch, S., Xie, R. C., Hopwood, M. J., Dengler, M., and Achterberg, E. P. (2022). Sediment Release in the Benguela Upwelling System Dominates Trace Metal Input to the Shelf and Eastern South Atlantic Ocean. *Global Biogeochemical Cycles*, 36:e2022GB007466.

Liu, Y., Li, X., Zeng, Z., Yu, H. M., Huang, F., Felis, T., and Shen, C. C. (2019). Annually-resolved coral skeletal δ138/134Ba records: A new proxy for oceanic Ba cycling. *Geochimica et Cosmochimica Acta*, 247:27–39.

Locarnini, R., Mishonov, A., Antonov, J., Boyer, T., Garcia, H., Baranova, O., Zweng, M., and Johnson, D. (2010). NOAA Atlas NESDIS 68 WORLD OCEAN ATLAS 2009 Volume 1: Temperature. *World*, 2:182.

Lopez, M., Cochonat, P., Sermondadaz, G., Levaché, D., Gay, A., and Séranne, M. (2005). Isolated seafloor pockmarks linked to BSRs, fluid chimneys, polygonal faults and stacked Oligocene–Miocene turbiditic palaeochannels in the Lower Congo Basin. *Marine Geology*, 226:25–40.

Løseth, H., Gading, M., and Wensaas, L. (2009). Hydrocarbon leakage interpreted on seismic data. *Marine and Petroleum Geology*, 26:1304–1319.

Løseth, H., Wensaas, L., Arntsen, B., Hanken, N. M., Basire, C., and Graue, K. (2011). 1000 m long gas blow-out pipes. *Marine and Petroleum Geology*, 28:1047–1060.

Lovecchio, E., Henson, S., Carvalho, F., and Briggs, N. (2022). Oxygen Variability in the Offshore Northern Benguela Upwelling System From Glider Data. *Journal of Geophysical Research: Oceans*, 127:e2022JC019063.

Loyd, S. J. and Smirnoff, M. N. (2022). Progressive formation of authigenic carbonate with depth in siliciclastic marine sediments including substantial formation in sediments experiencing methanogenesis. *Chemical Geology*, 594:120775.

Lu, Y., Yang, H., Huang, B., Liu, Y., and Lu, H. (2023). Foraminifera associated with cold seeps in marine sediments. *Frontiers in Marine Science*, 10:1157879.

Marchesi, J. R., Weightman, A. J., Cragg, B. A., Parkes, R. J., and Fry, J. C. (2006). Methanogen and bacterial diversity and distribution in deep gas hydrate sediments from the Cascadia Margin as revealed by 16S rRNA molecular analysis. *FEMS Microbiology Ecology*, 34:221–228.

Marcon, Y., Ondréas, H., Sahling, H., Bohrmann, G., and Olu, K. (2014). Fluid flow regimes and growth of a giant pockmark. *Geology*, 42:63–66.

Martinez-Ruiz, F., Jroundi, F., Paytan, A., Guerra-Tschuschke, I., Abad, M. D. M., and González-Muñoz, M. T. (2018). Barium bioaccumulation by bacterial biofilms and implications for Ba cycling and use of Ba proxies. *Nature Communications*, 9:1–9.

Martinez-Ruiz, F., Kastner, M., Gallego-Torres, D., Rodrigo-Gámiz, M., Nieto-Moreno, V., and Ortega-Huertas, M. (2015). Paleoclimate and paleoceanography over the past 20,000yr in the Mediterranean Sea Basins as indicated by sediment elemental proxies. *Quaternary Science Reviews*, 107:25–46.

Martins, M. S. and Stammer, D. (2022). Interannual Variability of the Congo River Plume-Induced Sea Surface Salinity. *Remote Sensing*, 14:1013.

Maslanyj, M. P., Light, M. P., Greenwood, R. J., and Banks, N. L. (1992). Extension tectonics offshore Namibia and evidence for passive rifting in the South Atlantic. *Marine and Petroleum Geology*, 9:590–601.

Mayfield, K. K., Eisenhauer, A., Ramos, D. P. S., Higgins, J. A., Horner, T. J., Auro, M., Magna, T., Moosdorf, N., Charette, M. A., Gonneea, M. E., Brady, C. E., Komar, N., Peucker-Ehrenbrink, B., and Paytan, A. (2021). Groundwater discharge impacts marine isotope budgets of Li, Mg, Ca, Sr, and Ba. *Nature Communications*, 12:1–9.

McManus, J., Berelson, W. M., Hammond, D. E., and Klinkhammer, G. P. (1999). Barium cycling in the North Pacific: Implications for the utility of Ba as a paleoproductivity and paleoalkalinity proxy. *Paleoceanography*, 14:53–61.

McManus, J., Berelson, W. M., Klinkhammer, G. P., Johnson, K. S., Coale, K. H., Anderson, R. F., Kumar, N., Burdige, D. J., Hammond, D. E., Brumsack, H. J., McCorkle, D. C., and Rushdi, A. (1998). Geochemistry of barium in marine sediments: Implications for its use as a paleoproxy. *Geochimica et Cosmochimica Acta*, 62:3453–3473.

McManus, J., Berelson, W. M., Klinkhammer, G. P., Kilgore, T. E., and Hammond, D. E. (1994). Remobilization of barium in continental margin sediments. *Geochimica et Cosmochimica Acta*, 58:4899–4907.

Mcmillan, I. K., Brink, G. I., Broad, D. S., and Maier, J. J. (1997). Late Mesozoic Sedimentary Basins Off the South Coast of South Africa. *Sedimentary Basins of the World*, 3:319–376.

McQuay, E. L., Torres, M. E., Collier, R. W., Huh, C. A., and McManus, J. (2008). Contribution of cold seep barite to the barium geochemical budget of a marginal basin. *Deep-Sea Research Part I: Oceanographic Research Papers*, 55:801–811.

Mello, M. R., Filho, N. C. D. A., Bender, A. A., Barbanti, S. M., Mohriak, W., Schmitt, P., and Jesus, C. L. C. D. (2013). The Namibian and Brazilian southern South Atlantic petroleum systems: Are they comparable analogues? *Geological Society Special Publication - Conjugate Divergent Margins, eds: Mohriak, W. U., Danforth, A., Post, P. J., Brown, D. E., Tari, G. C., Nemčok, M. Sinha, S. T.*, 369:249–266.

Mete, Ö. Z., Subhas, A. V., Kim, H. H., Dunlea, A. G., Whitmore, L. M., Shiller, A. M., Gilbert, M., Leavitt, W. D., and Horner, T. J. (2023). Barium in seawater: dissolved distribution, relationship to silicon, and barite saturation state determined using machine learning. *Earth System Science Data*, 15:4023–4045.

Middag, R., Zitoun, R., and Conway, T. (2023). *Trace Metals. In Blasco, J. Tovar-Sánchez, A. (Eds.), Chapter 3 in Marine Analytical Chemistry*, volume 1, pages 103–198. Springer International Publishing, Cham, Switzerland, 1st edition.

Middleton, J., Paytan, A., Auro, M., Saito, M., and Horner, T. (2023a). Barium isotope signatures of barite–fluid ion exchange in Equatorial Pacific sediments. *Earth and Planetary Science Letters*, 612:118150.

Middleton, J. T., Hong, W. L., Paytan, A., Auro, M. E., Griffith, E. M., and Horner, T. J. (2023b). Barium isotope fractionation in barite–fluid systems at chemical equilibrium. *Chemical Geology*, 627:121453.

Miyajima, Y., Araoka, D., Yoshimura, T., Ota, Y., Suzuki, A., Yoshioka, H., Suzumura, M., Smrzka, D., Peckmann, J., and Bohrmann, G. (2023). Lithium isotope systematics of methane-seep carbonates as an archive of fluid origins and flow rates. *Geochimica et Cosmochimica Acta*, 361:152–170.

Miyazaki, T., Yasukawa, K., Tanaka, E., Vaglarov, B. S., and Yoshida, K. (2023). Ba stable isotope excursions induced by multiple hyperthermal events: A potential new index for transient global warming. *Geochemical Journal*, 57:E1–E8.

Mohrholz, V., Bartholomae, C. H., van der Plas, A. K., and Lass, H. U. (2008). The seasonal variability of the northern Benguela undercurrent and its relation to the oxygen budget on the shelf. *Continental Shelf Research*, 28:424–441.

Monnin, C. (1999). A thermodynamic model for the solubility of barite and celestite in electrolyte solutions and seawater to 200°C and to 1 kbar. *Chemical Geology*, 153:187–209.

Monnin, C., Jeandel, C., Cattaldo, T., and Dehairs, F. (1999). The marine barite saturation state of the world's oceans. *Marine Chemistry*, 65:253–261.

Monnin, C., Wheat, C. G., Dupre, B., Elderfield, H., and Mottl, M. M. (2001). Barium geochemistry in sediment pore waters and formation waters of the oceanic crust on the eastern flank of the Juan de Fuca Ridge (ODP Leg 168). *Geochemistry, Geophysics, Geosystems*, 2:2000GC000073.

Monteiro, P. M. S. (2010). *The Benguela Current System. In Liu, K., Atkinson, L., Quiniones, R. Talue-McManus, L. (Eds.), Chapter 1 in Carbon and Nutrient Fluxes in Continental Margins: A Global Synthesis*, volume 2, pages 65–78. Springer-Verlag, 1st edition.

Moore, W. S. (1997). High fluxes of radium and barium from the mouth of the Ganges-Brahmaputra River during low river discharge suggest a large groundwater source. *Earth and Planetary Science Letters*, 150:4–150.

Moore, W. S. and Shaw, T. J. (1998). Chemical signals from submarine fluid advection onto the continental shelf. *Journal of Geophysical Research: Oceans*, 103:21543–21552.

Moore, W. S. and Shaw, T. J. (2008). Fluxes and behavior of radium isotopes, barium, and uranium in seven Southeastern US rivers and estuaries. *Marine Chemistry*, 108:236–254.

Moss, J. L. (2010). The spatial and temporal distribution of pipe and pockmark formation. *School of Earth and Environmental Sciences, University of Cardiff, Cardiff*, Thesis:1–314.

Moss, J. L. and Cartwright, J. (2010a). 3D seismic expression of km-scale fluid escape pipes from offshore Namibia. *Basin Research*, 22:481–501.

Moss, J. L. and Cartwright, J. (2010b). The spatial and temporal distribution of pipe formation, offshore Namibia. *Marine and Petroleum Geology*, 27:1216–1234.

Moss, J. L., Cartwright, J., Cartwright, A., and Moore, R. (2012). The spatial pattern and drainage cell characteristics of a pockmark field, Nile Deep Sea Fan. *Marine and Petroleum Geology*, 35:321–336.

Müller, P. J. (2003). Density and water content of sediment cores in the South Atlantic Ocean. *Department of Geosciences, Bremen University, Pangaea*, 1:1.

Müller, P. J. (2004). Density and water content of sediment cores in the South Atlantic Ocean. *Department of Geosciences, Bremen University, Pangaea*, 1:1.

Muntingh, A. (1993). Geology, prospects in Orange Basin offshore western South Africa. *Oil Gas Journal*, 91:106–109.

Muntingh, A. and Brown, L. (1993). *Sequence Stratigraphy of Petroleum Plays, Post-Rift Cretaceous Rocks (Lower Aptian to Upper Maastrichtian), Orange Basin, Western Offshore, South Africa. In Spencer, A. (Eds.), Chapter 4 in AAPG Memoir 58: Generation, Accumulation and Production of Europe's Hydrocarbons III*, volume 1, pages 219–231. Springer, 1st edition.

Nan, X., Wu, F., Zhang, Z., Hou, Z., Huang, F., and Yu, H. (2015). High-precision barium isotope measurements by MC-ICP-MS. *Journal of Analytical Atomic Spectrometry*, 30:2307–2315.

Nardini, P., Böttinger, M., Scheuermann, G., Siegfried, L., Schmidt, M., Mohrholz, V., and Pogrzeba, H. (2019). The tropical-subtropical coupling in the Southeast Atlantic from the perspective of the northern Benguela upwelling system. *PLoS ONE*, 14:e0210083.

Nelson, G. (1992). Equatorward wind and atmospheric pressure spectra as metrics for primary productivity in the Benguela system. *South African Journal of Marine Science*, 12:19–28.

Niewöhner, C., Hensen, C., Kasten, S., Zabel, M., Schulz, H. D., and OIew, C. N. (1998). Deep sulfate reduction completely mediated by anaerobic methane oxidation in sediments of the upwelling area off Namibia. *Geochimica et Cosmochimica Acta*, 62:455–464.

Noble, A. E., Lamborg, C. H., Ohnemus, D. C., Lam, P. J., Goepfert, T. J., Measures, C. I., Frame, C. H., Casciotti, K. L., DiTullio, G. R., Jennings, J., and Saito, M. A. (2012). Basin-scale inputs of cobalt, iron, and manganese from the Benguela-Angola front to the South Atlantic Ocean. *Limnology and Oceanography*, 57:989–1010.

Nöthen, K. and Kasten, S. (2011). Reconstructing changes in seep activity by means of pore water and solid phase Sr/Ca and Mg/Ca ratios in pockmark sediments of the Northern Congo Fan. *Marine Geology*, 287:1–13.

Núñez-Useche, F., Canet, C., Liebetrau, V., Puig, T. P., Ponciano, A. C., Alfonso, P., Berndt, C., Hensen, C., Mortera-Gutierrez, C., and Rodríguez-Díaz, A. A. (2018). Redox conditions and authigenic mineralization related to cold seeps in central Guaymas Basin, Gulf of California. *Marine and Petroleum Geology*, 95:1–15.

Nürnberg, C. C., Bohrmann, G., Schlüter, M., and Frank, M. (1997). Barium accumulation in the Atlantic sector of the Southern Ocean: Results from 190,000-year records. *Paleoceanography*, 12:594–603.

Ohnemus, D. C. and Lam, P. J. (2015). Cycling of lithogenic marine particles in the US GEOTRACES North Atlantic transect. *Deep-Sea Research Part II: Topical Studies in Oceanography*, 116:283–302.

Olu, K. (2011). WACS cruise, RV Pourquoi pas ? *https://doi.org/10.17600/11030010*.

Olu, K., Caprais, J. C., Galéron, J., Causse, R., von Cosel, R., Budzinski, H., Ménach, K. L., Roux, C. L., Levaché, D., Khripounoff, A., and Sibuet, M. (2009). Influence of seep emission on the non-symbiont-bearing fauna and vagrant species at an active giant pockmark in the Gulf of Guinea (Congo-Angola margin). *Deep-Sea Research Part II: Topical Studies in Oceanography*, 56:2380–2393.

Ondréas, H., Olu, K., Fouquet, Y., Charlou, J. L., Gay, A., Dennielou, B., Donval, J. P., Fifis, A., Nadalig, T., Cochonat, P., Cauquil, E., Bourillet, J. F., Moigne, M. L., and Sibuet, M. (2005). ROV study of a giant pockmark on the Gabon continental margin. *Geo-Marine Letters*, 25:281–292.

Orange, D. L., Yun, J., Maher, N., Barry, J., and Greene, G. (2002). Tracking California seafloor seeps with bathymetry, backscatter and ROVs. *Continental Shelf Research*, 22:2273–2290.

Ostanin, I., Anka, Z., di Primio, R., and Bernal, A. (2013). Hydrocarbon plumbing systems above the Snøhvit gas field: Structural control and implications for thermogenic methane leakage in the Hammerfest Basin, SW Barents Sea. *Marine and Petroleum Geology*, 43:127–146.

Paparazzo, F. E., Martinez, R. P., Fabro, E., Gonçalves, R. J., Crespi-Abril, A. C., Soria, G. R., Barbieri, E. A., and Almandoz, G. O. (2021). Relevance of sporadic upwelling events on primary productivity: The key role of nitrogen in a gulf of SW Atlantic Ocean. *Estuarine, Coastal and Shelf Science*, 249:107123.

Paton, D. A., di Primio, R., Kuhlmann, G., van der Spuy, D., and Horsfield, B. (2007). Insights into the Petroleum System Evolution of the southern Orange Basin, South Africa. *South African Journal of Geology*, 110:261–274.

Pau, M., Hammer, O., and Chand, S. (2014). Constraints on the dynamics of pockmarks in the SW Barents Sea: Evidence from gravity coring and high-resolution, shallow seismic profiles. *Marine Geology*, 355:330–345.

Paytan, A., Averyt, K., Faul, K., Gray, E., and Thomas, E. (2007). Barite accumulation, ocean productivity, and Sr/Ba in barite across the Paleocene-Eocene Thermal Maximum. *Geology*, 35:1139–1142.

Paytan, A. and Griffith, E. M. (2007). Marine barite: Recorder of variations in ocean export productivity. *Deep-Sea Research Part II: Topical Studies in Oceanography*, 54:687–705.

Paytan, A. and Kastner, M. (1996). Benthic Ba fluxes in the central equatorial pacific, implications for the oceanic Ba cycle. *Earth and Planetary Science Letters*, 142:439–450.

Peketi, A., Mazumdar, A., Joshi, R. K., Patil, D. J., Srinivas, P. L., and Dayal, A. M. (2012). Tracing the Paleo sulfate-methane transition zones and H2S seepage events in marine sediments: An application of C-S-Mo systematics. *Geochemistry, Geophysics, Geosystems*, 13:1–11.

Pérez-Gussinyé, M., Collier, J. S., Armitage, J. J., Hopper, J. R., Sun, Z., and Ranero, C. R. (2023). Towards a process-based understanding of rifted continental margins. *Nature Reviews Earth and Environment*, 4:166–184.

Pfeifer, K., Kasten, S., Hensen, C., and Schulz, H. D. (2001). Reconstruction of primary productivity from the barium contents in surface sediments of the South Atlantic Ocean. *Marine Geology*, 177:13–24.

Pichel, L. M., Legeay, E., Ringenbach, J. C., and Callot, J. P. (2023). The West African salt-bearing rifted margin—Regional structural variability and salt tectonics between Gabon and Namibe. *Basin Research*, 35:2217–2248.

Pierre, C., Blanc-Valleron, M. M., Demange, J., Boudouma, O., Foucher, J. P., Pape, T., Himmler, T., Fekete, N., and Spiess, V. (2012). Authigenic carbonates from active methane seeps offshore southwest Africa. *Geo-Marine Letters*, 32:501–513.

Pierre, C. and Fouquet, Y. (2007). Authigenic carbonates from methane seeps of the Congo deep-sea fan. *Geo-Marine Letters*, 27:249–257.

Pitcher, G. C., Probyn, T. A., Randt, A. D., Lucas, A. J., Bernard, S., Evers-King, H., Lamont, T., and Hutchings, L. (2014). Dynamics of oxygen depletion in the nearshore of a coastal embayment of the southern Benguela upwelling system. *Journal of Geophysical Research: Oceans*, 119:2183–2200.

Polonsky, A. B. and Serebrennikov, A. N. (2022). What is the Reason for the Multiyear Trends of Variability in the Benguela Upwelling? *Izvestiya - Atmospheric and Ocean Physics*, 58:1450–1457.

Polus, A., Kopinski, D., and Tycholiz, W. (2015). Ready or not: Namibia as a potentially successful oil producer. *Africa Spectrum*, 50:31–55.

Poole, R. and Tomczak, M. (1999). Optimum multiparameter analysis of the water mass structure in the Atlantic Ocean thermocline. *Deep-sea research. Part I, Oceanographic research papers*, 46:1895–1921.

Pretet, C., Zuilen, K., Nägler, T. F., Reynaud, S., Böttcher, M. E., and Samankassou, E. (2015). Constraints on barium isotope fractionation during aragonite precipitation by corals. *The Depositional Record*, 1:118–129.

Rabinowitz, P. D. and Labrecque, J. (1979). The Mesozoic South Atlantic ocean and evolution of its continental margins. *Journal of Geophysical Research*, 84:5973–6002.

Rabouille, C., Baudin, F., Dennielou, B., and Olu, K. (2017). Organic carbon transfer and ecosystem functioning in the terminal lobes of the Congo deep-sea fan: outcomes of the Congolobe project. *Deep-Sea Research Part II: Topical Studies in Oceanography*, 142:1–6.

Rahman, S., Shiller, A. M., Anderson, R. F., Charette, M. A., Hayes, C. T., Gilbert, M., Grissom, K. R., Lam, P. J., Ohnemus, D. C., Pavia, F. J., Twining, B. S., and Vivancos, S. M. (2022). Dissolved and Particulate Barium Distributions Along the US GEOTRACES North Atlantic and East Pacific Zonal Transects (GA03 and GP16): Global Implications for the Marine Barium Cycle. *Global Biogeochemical Cycles*, 36:e2022GB007330.

Rathee, D. and Tewari, S. (2024). The Next Oil Frontier: Namibia's Promising Hydrocarbon Plays. *EAGE Sub-Saharan Africa Energy Forum*, 2024:1–3.

Reitz, A., Pfeifer, K., Lange, G. J. D., and Klump, J. (2004). Biogenic barium and the detrital Ba/Al ratio: A comparison of their direct and indirect determination. *Marine Geology*, 204:289–300.

Renne, P. R., Ernesto, M., Pacca, I. G., Coe, R. S., Glen, J. M., Prévot, M., and Perrin, M. (1992). The Age of Paraná Flood Volcanism, Rifting of Gondwanaland, and the Jurassic-Cretaceous Boundary. *Science (American Association for the Advancement of Science)*, 258:975–979.

Renne, P. R., Glen, J. M., Milner, S. C., and Duncan, A. R. (1996). Age of Etendeka flood volcanism and associated intrusions in southwestern Africa. *Geology*, 24:659–662.

Rice, D. D. (1993). Biogenic gas: Controls, habitats, and resource potential. *United States Geological Survey, Professional Paper - The Future of Energy Gases, eds: D.G. Howell*, 1570:583–606.

Riedinger, N., Kasten, S., Gröger, J., Franke, C., and Pfeifer, K. (2006). Active and buried authigenic barite fronts in sediments from the Eastern Cape Basin. *Earth and Planetary Science Letters*, 241:876–887.

Ristova, P. P., Wenzhöfer, F., Ramette, A., Zabel, M., Fischer, D., Kasten, S., and Boetius, A. (2012). Bacterial diversity and biogeochemistry of different chemosynthetic habitats of the REGAB cold seep (West African margin, 3160 m water depth). *Biogeosciences*, 9:5031–5048.

Rixen, T., Lahajnar, N., Lamont, T., Koppelmann, R., Martin, B., van Beusekom, J. E., Siddiqui, C., Pillay, K., and Meiritz, L. (2021). Oxygen and Nutrient Trapping in the Southern Benguela Upwelling System. *Frontiers in Marine Science*, 8:730591.

Rochelle-Bates, N., Huuse, M., Schröder, S., and Pritchard, G. (2017). Seismic Characterisation of "Prospect B": A Possible Carbonate Build-Up From the Late Syn-Rift (Barremian) of the Lüderitz Basin, Namibia. *AAPG Annual Convention and Exhibition*, 108:261–283.

Rogers, J. and Bremner, J. M. (1991). *The Benguela Ecosystem. Part VII. Marine-Geological Aspects. Barnes M. (Eds.)*, volume 29, pages 1-85. Aberdeen University Press, Aberdeen, UK, 1st edition.

Roy, K. O.-L., Caprais, J. C., Fifis, A., Fabri, M. C., Galéron, J., Budzinsky, H., Ménach, K. L., Khripounoff, A., Ondréas, H., and Sibuet, M. (2007). Cold-seep assemblages on a giant pockmark off West Africa: Spatial patterns and environmental control. *Marine Ecology*, 28:115–130.

Ruban, A., Rudmin, M., Dudarev, O., and Mazurov, A. (2020). The formation of authigenic carbonates at a methane seep site in the northern part of the Laptev Sea. *Minerals*, 10:1–14.

Rutsch, H. J., Mangini, A., Bonani, G., Dittrich-Hannen, B., Kubik, P. W., Suter, M., and Segl, M. (1995). 10Be and Ba concentrations in West African sediments trace productivity in the past. *Earth and Planetary Science Letters*, 133:129–143.

Sager, W., Hoernle, K., Höfig, T., Avery, A., Bhutani, R., Buchs, D., Carvallo, C., Class, C., Dai, Y., Valle, G. D., Gaudio, A. D., Fielding, S., Gaastra, K., Han, S., Homrighausen, S., Kubota, Y., Li, C.-F., Nelson, W., Petrou, E., Potter, K., Pujatti, S., Scholpp, J., Shervais, J., Thoram, S., Tikoo-Schantz, S., Tshiningayamwe, M., Wang, X.-J., and Widdowson, M. (2023). Expedition 391 summary. *Proceedings of the International Ocean Discovery Program*, 391:1–101.

Sahling, H., Bohrmann, G., Spiess, V., Bialas, J., Breitzke, M., Ivanov, M., Kasten, S., Krastel, S., and Schneider, R. (2008). Pockmarks in the Northern Congo Fan area, SW Africa: Complex seafloor features shaped by fluid flow. *Marine Geology*, 249:206–225.

Said, M. H., Wangui, W. B., and Muthumbi, A. (2023). Influence of Oxygen Minimum Zone on Macrobenthic Community Structure in the Northern Benguela Upwelling System: A Macro-Nematode Perspective 2. *EGU Biogeoscience Discussions*, 151:1–35.

Santos, F., Gomez-Gesteira, M., deCastro, M., and Alvarez, I. (2012). Differences in coastal and oceanic SST trends due to the strengthening of coastal upwelling along the Benguela current system. *Continental Shelf Research*, 34:79–86.

Savoye, B., Cochonat, P., Apprioual, R., Bain, O., Baltzer, A., Bellec, V., Beuzart, P., Bourillet, J.-F., Cagna, R., Cremer, M., Crusson, A., Dennielou, B., Diebler, D., Droz, L., Ennes, J.-C., Floch, G., Guiomar, M., Harmegnies, F., Kerbrat, R., Klein, B., Kuhn, H., Landuré, J.-Y., Lasnier, C., Drezen, E. L., Formal, J.-P. L., Lopez, M., Loubrieu, B., Marsset, T., Migeon, S., Normand, A., Nouzé, H., Ondréas, H., Pelleau, P., Saget, P., Séranne, M., Sibuet, J.-C., Tofani, R., Voisset, M., Par, P., and Pichon, X. L. (2000). Structure et évolution récente de l'éventail turbiditique du Zaïre : premiers résultats scientifiques des missions d'exploration Zaïango 1 2 (marge Congo-Angola) Abridged version. *Earth and Planetary Sciences*, 331:211–220.

Scarselli, N., McClay, K., and Elders, C. (2016). Seismic geomorphology of Cretaceous megaslides offshore Namibia (Orange Basin): Insights into segmentation and degradation of gravity-driven linked systems. *Marine and Petroleum Geology*, 75:151–180.

Schenau, S. J., Prins, M. A., Lange, G. J. D., and Monnin, C. (2001). Barium accumulation in the Arabian Sea: Controls on barite preservation in marine sediments. *Geochimica et Cosmochimica Acta*, 65:1545–1556.

Schenau, S. J., Reichart, G. J., and Lange, G. J. D. (2002). Oxygen minimum zone controlled Mn redistribution in Arabian Sea sediments during the late Quaternary. *Paleoceanography*, 17:1058.

Schlitzer, R., Anderson, R. F., Dodas, E. M., Lohan, M., Geibert, W., Tagliabue, A., Bowie, A., Jeandel, C., Maldonado, M. T., Landing, W. M., Cockwell, D., Abadie, C., Abouchami, W., Achterberg, E. P., Agather, A., Aguliar-Islas, A., van Aken, H. M., Andersen, M., Archer, C., Auro, M., de Baar, H. J., Baars, O., Baker, A. R., Bakker, K., Basak, C., Baskaran, M., Bates, N. R., Bauch, D., van Beek, P., Behrens, M. K., Black, E., Bluhm, K., Bopp, L., Bouman, H., Bowman, K., Bown, J., Boyd, P., Boye, M., Boyle, E. A., Branellec, P., Bridgestock, L., Brissebrat, G., Browning, T., Bruland, K. W., Brumsack, H. J., Brzezinski, M., Buck, C. S., Buck, K. N., Buesseler, K., Bull, A., Butler, E., Cai, P., Mor, P. C., Cardinal, D., Carlson, C., Carrasco, G., Casacuberta, N., Casciotti, K. L., Castrillejo, M., Chamizo, E., Chance, R., Charette, M. A., Chaves, J. E., Cheng, H., Chever, F., Christl, M., Church, T. M., Closset, I., Colman, A., Conway, T. M., Cossa, D., Croot, P., Cullen, J. T., Cutter, G. A., Daniels, C., Dehairs, F., Deng, F., Dieu, H. T., Duggan, B., Dulaquais, G., Dumousseaud, C., Echegoyen-Sanz, Y., Edwards, R. L., Ellwood, M., Fahrbach, E., Fitzsimmons, J. N., Flegal, A. R., Fleisher, M. Q., van de Flierdt, T., Frank, M., Friedrich, J., Fripiat, F., Fröllje, H., Galer, S. J., Gamo, T., Ganeshram, R. S., Garcia-Orellana, J., Garcia-Solsona, E., Gault-Ringold, M., George, E., Gerringa, L. J., Gilbert, M., Godoy, J. M., Goldstein, S. L., Gonzalez, S. R., Grissom, K., Hammerschmidt, C., Hartman, A., Hassler, C. S., Hathorne, E. C., Hatta, M., Hawco, N., Hayes, C. T., Heimbürger, L. E., Helgoe, J., Heller, M., Henderson, G. M., Henderson, P. B., van Heuven, S., Ho, P., Horner, T. J., Hsieh, Y. T., Huang, K. F., Humphreys, M. P., Isshiki, K., Jacquot, J. E., Janssen, D. J., Jenkins, W. J., John, S., Jones, E. M., Jones, J. L., Kadko, D. C., Kayser, R., Kenna, T. C., Khondoker, R., Kim, T., Kipp, L., Klar, J. K., Klunder, M., Kretschmer, S., Kumamoto, Y., Laan, P., Labatut, M., Lacan, F., Lam, P. J., Lambelet, M., Lamborg, C. H., Moigne, F. A. L., Roy, E. L., Lechtenfeld, O. J., Lee, J. M., Lherminier, P., Little, S., López-Lora, M., Lu, Y., Masque, P., Mawji, E., Mcclain, C. R., Measures, C., Mehic, S., Barraqueta, J. L. M., van der Merwe, P., Middag, R., Mieruch, S., Milne, A., Minami, T., Moffett, J. W., Moncoiffe, G., Moore, W. S., Morris, P. J., Morton, P. L., Nakaguchi, Y., Nakayama, N., Niedermiller, J., Nishioka, J., Nishiuchi, A., Noble, A., Obata, H., Ober, S., Ohnemus, D. C., van Ooijen, J., O'Sullivan, J., Owens, S., Pahnke, K., Paul, M., Pavia, F., Pena, L. D., Peters, B., Planchon, F., Planquette, H., Pradoux, C., Puigcorbé, V., Quay, P., Queroue, F., Radic, A., Rauschenberg, S., Rehkämper, M., Rember, R., Remenyi, T., Resing, J. A., Rickli, J., Rigaud, S., Rijkenberg, M. J., Rintoul, S., Robinson, L. F., Roca-Martí, M., Rodellas, V., Roeske, T., Rolison, J. M., Rosenberg, M., Roshan, S., van der Loeff, M. M. R., Ryabenko, E., Saito, M. A., Salt, L. A., Sanial, V., Sarthou, G., Schallenberg, C., Schauer, U., Scher, H., Schlosser, C., Schnetger, B., Scott, P., Sedwick, P. N., Semiletov, I., Shelley, R., Sherrell, R. M., Shiller, A. M., Sigman, D. M., Singh, S. K., Slagter, H. A., Slater, E., Smethie, W. M., Snaith, H., Sohrin, Y., Sohst, B., Sonke, J. E., Speich, S., Steinfeldt, R., Stewart, G., Stichel, T., Stirling, C. H., Stutsman, J., Swarr, G. J., Swift, J. H., Thomas, A., Thorne, K., Till, C. P., Till, R., Townsend, A. T., Townsend, E., Tuerena, R., Twining, B. S., Vance, D., Velazquez, S., Venchiarutti, C., Villa-Alfageme, M., Vivancos, S. M., Voelker, A. H., Wake, B., Warner, M. J., Watson, R., van Weerlee, E., Weigand, M. A., Weinstein, Y., Weiss, D., Wisotzki, A., Woodward, E. M. S., Wu, J., Wu, Y., Wuttig, K., Wyatt, N., Xiang, Y., Xie, R. C., Xue, Z., Yoshikawa, H., Zhang, J., Zhang, P., Zhao, Y., Zheng, L., Zheng, X. Y., Zieringer, M., Zimmer, L. A., Ziveri, P., Zunino, P., and Zurbrick, C. (2018). The GEOTRACES Intermediate Data Product 2017. *Chemical Geology*, 493:210–223.

Schlitzer, R. and Wegener, A. (2000). Electronic Atlas of WOCE Hydrographic and Tracer Data. *Eos*, 81:45–46.

Schmidt, M. and Eggert, A. (2016). Oxygen cycling in the northern Benguela Upwelling System: Modelling oxygen sources and sinks. *Progress in Oceanography*, 149:145–173.

Schmidt, S. (2004). The Petroleum Potential of the Passive Continental Margin of South-Western Africa-A Basin Modelling Study. *Georessourcen und Materialtechnik, Rheinisch-Westfälischen Technischen Hochschule, Aachen*, Thesis:1–161.

Schneider, R., Müller, P., Ruhland, G., Meinecke, G., Schmidt, H., and Wefer, G. (1996). *Late Quaternary Surface Temperatures and Productivity in the East-Equatorial South Atlantic: Response to Changes in Trade/Monsoon Wind Forcing and Surface Water Advection. In Wefer G., Berger W., Siedler G. Webb, D. (Eds.), Chapter 27 in The South Atlantic: Present and Past Circulation*, volume 1, pages 527–551. Springer Berlin, Heidelberg, 1st edition.

Schnyder, J., Stetten, E., Baudin, F., Pruski, A. M., and Martinez, P. (2017). Palynofacies reveal fresh terrestrial organic matter inputs in the terminal lobes of the Congo deep-sea fan. *Deep-Sea Research Part II: Topical Studies in Oceanography*, 142:91–108.

Scholz, F., Cheng, J., Zhang, Z., Vosteen, P., Siebert, C., and Frank, M. (2023). Benthic-pelagic coupling and isotopic fractionation of barium in Kiel Bight, SW Baltic Sea. *Frontiers in Marine Science*, 10:1101095.

Seabra, R., Varela, R., Santos, A. M., Gómez-Gesteira, M., Meneghesso, C., Wethey, D. S., and Lima, F. P. (2019). Reduced nearshore warming associated with eastern boundary upwelling systems. *Frontiers in Marine Science*, 6:104.

Seton, M., Müller, R. D., Zahirovic, S., Gaina, C., Torsvik, T., Shephard, G., Talsma, A., Gurnis, M., Turner, M., Maus, S., and Chandler, M. (2012). Global continental and ocean basin reconstructions since 200Ma. *Earth-Science Reviews*, 113:212–270.

Shaw, T. J., Moore, W. S., Kloepfer, J., and Sochaski, M. A. (1998). The flux of barium to the coastal waters of the southeastern USA: The importance of submarine groundwater discharge. *Geochimica et cosmochimica acta*, 62:3047–3054.

Sheriff, R. E. (1975). Factors Affecting Seismic Amplitudes. *Geophysical Prospecting*, 23:125–138.

Small, L. F. and Menzies, D. W. (1981). Patterns of primary productivity and biomass in a coastal upwelling region. *Deep-Sea Research*, 28:123–149.

Snyder, G. T., Dickens, G. R., and Castellini, D. G. (2007a). Labile barite contents and dissolved barium concentrations on Blake Ridge: New perspectives on barium cycling above gas hydrate systems. *Journal of Geochemical Exploration*, 95:48–65.

Snyder, G. T., Hiruta, A., Matsumoto, R., Dickens, G. R., Tomaru, H., Takeuchi, R., Komatsubara, J., Ishida, Y., and Yu, H. (2007b). Pore water profiles and authigenic mineralization in shallow marine sediments above the methane-charged system on Umitaka Spur, Japan Sea. *Deep-Sea Research Part II: Topical Studies in Oceanography*, 54:1216–1239.

Stevens, E. W., Bailey, J. V., Flood, B. E., Jones, D. S., Gilhooly, W. P., Joye, S. B., Teske, A., and Mason, O. U. (2015). Barite encrustation of benthic sulfur-oxidizing bacteria at a marine cold seep. *Geobiology*, 13:588–603.

Stolper, D. A., Lawson, M., Davis, C. L., Ferreira, A. A., Neto, E. V. S., Ellis, G. S., Lewan, M. D., Martini, A. M., Tang, Y., Schoell, M., Sessions, A. L., and Eiler, J. M. (2014). Formation temperatures of thermogenic and biogenic methane. *Science*, 344:1500–1503.

Strozyk, F., Back, S., and Kukla, P. A. (2017). Comparison of the rift and post-rift architecture of conjugated salt and salt-free basins offshore Brazil and Angola/Namibia, South Atlantic. *Tectonophysics*, 716:204–224.

Summerhayes, C. P., Kroon, D., Rosell-Melé, A., Jordan, R. W., Schrader, H. J., Hearn, R., Villanueva, J., Grimalt, J. O., and Eglinton, G. (1995). Variability in the Benguela Current upwelling system over the past 70,000 years. *Progress in Oceanography*, 35:207–251.

Sun, Q., Cartwright, J., Foschi, M., Lu, X., and Xie, X. (2021). The interplay of stratal and vertical migration pathways in shallow hydrocarbon plumbing systems. *Basin Research*, 33:2157–2178.

Sun, Q., Wu, S., Cartwright, J., and Dong, D. (2012). Shallow gas and focused fluid flow systems in the Pearl River Mouth Basin, northern South China Sea. *Marine Geology*, 315-318:1–14.

Swart, R. (2009). Hydrate occurrences in the Namibe Basin, offshore Namibia. *Geological Society Special Publication - Sediment-Hosted Gas Hydrates: New Insights on Natural and Synthetic Systems, eds: Long, D., Lovell, M. A., Rees, J. G. Rochelle, C. A.*, 319:73–80.

Tchipalanga, P., Dengler, M., Brandt, P., Kopte, R., Macuéria, M., Coelho, P., Ostrowski, M., and Keenlyside, N. S. (2018). Eastern boundary circulation and hydrography off Angola building Angolan oceanographic capacities. *Bulletin of the American Meteorological Society*, 99:1589–1605.

Thiagarajan, N., Crémière, A., Blättler, C., Lepland, A., Kirsimäe, K., Higgins, J., Brunstad, H., and Eiler, J. (2020). Stable and clumped isotope characterization of authigenic carbonates in methane cold seep environments. *Geochimica et Cosmochimica Acta*, 279:204–219.

Tian, L. L., Zeng, Z., Nan, X. Y., Yu, H. M., and Huang, F. (2019). Determining Ba isotopes of barite using the Na2CO3 exchange reaction and double-spike method by MC-ICP-MS. *Journal of Analytical Atomic Spectrometry*, 34:1459–1467.

Tieman, Z. G., Stewart, B. W., Capo, R. C., Phan, T. T., Lopano, C. L., and Hakala, J. A. (2020). Barium Isotopes Track the Source of Dissolved Solids in Produced Water from the Unconventional Marcellus Shale Gas Play. *Environmental Science and Technology*, 54:4275–4285.

Tim, N., Zorita, E., and Hünicke, B. (2015). Decadal variability and trends of the Benguela upwelling system as simulated in a high-resolution ocean simulation. *Ocean Science*, 11:483–502.

Torres, M., Brumsack, H., Bohrmann, G., and Emeis, K. (1996a). Barite fronts in continental margin sediments: A new look at barium remobilization in the zone of sulfate reduction and formation of heavy barites in diagenetic fronts. *Chemical Geology*, 127:125–139.

Torres, M. E., Bohrmann, G., and Suess, E. (1996b). Authigenic barites and fluxes of barium associated with fluid seeps in the Peru subduction zone. *EPSL Earth and Planetary Science Letters*, 144:469–481.

Torres, M. E., Hong, W. L., Solomon, E. A., Milliken, K., Kim, J. H., Sample, J. C., Teichert, B. M., and Wallmann, K. (2020). Silicate weathering in anoxic marine sediment as a requirement for authigenic carbonate burial. *Earth-Science Reviews*, 200:102960.

Torres, M. E., Mcmanus, J., Huh, C.-A., and Huh, C.-A. (2002). Fluid seepage along the San Clemente Fault scarp: basin-wide impact on barium cycling. *EPSL Earth and Planetary Science Letters*, 203:181–194.

Tyson, R. V. and Pearson, T. H. (1991). Modern and ancient continental shelf anoxia : an overview. *Geological Society special publication - Modern and Ancient Continental Shelf Anoxia, eds: Tyson, R. V. Pearson, T. H.*, 58:1–24.

van Zuilen, K., Harrison, A. L., Stammeier, J. A., Nagler, T. F., and Mavromatis, V. (2023). Barium isotope (re-)equilibration in the barite-fluid system and its implications for marine barite archives. *Earth and Planetary Science Letters*, 618:118280.

Varela, R., Álvarez, I., Santos, F., DeCastro, M., and Gómez-Gesteira, M. (2015). Has upwelling strengthened along worldwide coasts over 1982-2010? *Nature Scientific Reports*, 5:10016–10016.

Vedamati, J., Chan, C., and Moffett, J. W. (2015). Distribution of dissolved manganese in the Peruvian Upwelling and Oxygen Minimum Zone. *Geochimica et Cosmochimica Acta*, 156:222–240.

Verheye, H. M., Lamont, T., Huggett, J. A., Kreiner, A., and Hampton, I. (2016). Plankton productivity of the Benguela Current Large Marine Ecosystem (BCLME). *Environmental Development*, 17:75–92.

Vermeesch, P., Fenton, C. R., Kober, F., Wiggs, G. F., Bristow, C. S., and Xu, S. (2010). Sand residence times of one million years in the Namib Sand Sea from cosmogenic nuclides. *Nature Geoscience*, 3:862–865.

Vermeesch, P., Rittner, M., Petrou, E., Omma, J., Mattinson, C., and Garzanti, E. (2017). High Throughput Petrochronology and Sedimentary Provenance Analysis by Automated Phase Mapping and LAICPMS. *Geochemistry, Geophysics, Geosystems*, 18:4096–4109.

Vollebregt, A., van Helmond, N. A., Pit, S., Kraal, P., and Slomp, C. P. (2023). Trace metals as a redox proxy in Arabian Sea sediments in and below the oxygen minimum zone. *Chemical Geology*, 618:121300.

von Allmen, K., Böttcher, M. E., Samankassou, E., and Nägler, T. F. (2010). Barium isotope fractionation in the global barium cycle: First evidence from barium minerals and precipitation experiments. *Chemical Geology*, 277:70–77.

Wang, D., Gouhier, T. C., Menge, B. A., and Ganguly, A. R. (2015). Intensification and spatial homogenization of coastal upwelling under climate change. *Nature*, 518:390–394.

Wang, W., Wu, Z., and Huang, F. (2021). Equilibrium barium isotope fractionation between minerals and aqueous solution from first-principles calculations. *Geochimica et Cosmochimica Acta*, 292:64–77.

Wefer, G., Berger, W. H., and C., R. (1999). Site 1084. *Proceedings of the Ocean Drilling Program, 177 Initial Reports*, 175:339–384.

Wefer, G., Berger, W. H., and Richter, C. (1998). The Angola-Benguela upwelling system: paleoceanographic synthesis of shipboard results from Leg 175. *Proceedings of the Ocean Drilling Program, Initial Reports, 177 Initial Reports*, 175:505–531.

Wefer, G., Bleil, U., Schulz, H., and Fischer, G. (1997). Geo Bremen South Atlantic 1996 - Cruise M34. *METEOR-Berichte*, 1:1–268.

Wei, J., Wu, T., Zhang, W., Deng, Y., Xie, R., Feng, J., Liang, J., Lai, P., Zhou, J., and Cao, J. (2020). Deeply buried authigenic carbonates in the Qiongdongnan Basin, South China Sea: Implications for ancient cold seep activities. *Minerals*, 10:1–19.

Wenau, S. and Spiess, V. (2018). Active Seafloor Seepage Along Hydraulic Fractures Connected to Lateral Stress From Salt-Related Rafting: Regab Pockmark, Congo Fan. *Journal of Geophysical Research: Solid Earth*, 123:3301–3319.

Wenau, S., Spiess, V., Pape, T., and Fekete, N. (2015). Cold seeps at the salt front in the Lower Congo Basin I: Current methane accumulation and active seepage. *Marine and Petroleum Geology*, 67:894–908.

Werner, T., Huenerlage, K., Verheye, H., and Buchholz, F. (2012). Thermal constraints on the respiration and excretion rates of krill, Euphausia Hanseni and Nematoscelis Megalops, in the northern Benguela upwelling system off Namibia. *African Journal of Marine Science*, 34:391–399.

Whitmore, L. M., Shiller, A. M., Horner, T. J., Xiang, Y., Auro, M. E., Bauch, D., Dehairs, F., Lam, P. J., Li, J., Maldonado, M. T., Mears, C., Newton, R., Pasqualini, A., Planquette, H., Rember, R., and Thomas, H. (2022). Strong Margin Influence on the Arctic Ocean Barium Cycle Revealed by Pan-Arctic Synthesis. *Journal of Geophysical Research: Oceans*, 127:e2021JC017417.

Widess, M. B. (1973). How Thin Is A Thin Bed? *Geophysics*, 38:1176–1180.

Wyatt, N. J., Milne, A., Achterberg, E. P., Browning, T. J., Bouman, H. A., Woodward, E. M. S., and Lohan, M. C. (2021). Seasonal cycling of zinc and cobalt in the south-eastern Atlantic along the GEOTRACES GA10 section. *Biogeosciences*, 18:4265–4280.

Xu, W. and Ruppel, C. (1999). Predicting the Occurrence, Distribution, and Evolution of Methane Gas Hydrate in Porous Marine Sediments. *Earth*, 104:5081–5095.

Yamano, M., Uyeda, S., Aoki, Y., and Shipley, T. H. (1982). Estimates of heat flow derived from gas hydrates. *Geology*, 10:339–343.

Yu, Y., Xie, R. C., Gutjahr, M., Laukert, G., Cao, Z., Hathorne, E., Siebert, C., Patton, G., and Frank, M. (2022). High latitude controls on dissolved barium isotope distributions in the global ocean. *Geochemical Perspectives Letters*, 24:22–26.

Zabel, M., Schneider, R. R., Brüchert, V., and Meteor, L. (2003). The Benguela Upwelling System 2003 Capetown-Dakar. *Meteor Cruise No. 57*, 57:1–181.

Zachos, J., Kroon, D., and Blum, P. (2004). ODP Leg 208 Summary. *Proceedings of the Ocean Drilling Program, Initial Reports*, 208:1–112.

Zhang, L. L., Zhu, D. C., Yang, Y. H., Wang, Q., Xie, J. C., and Zhao, Z. D. (2021). U–pb geochronology of carbonate by laser ablation MC-ICP-MS: Method improvements and geological applications. *Atomic Spectroscopy*, 42:335–348.

Zhang, Z., Yu, Y., Hathorne, E. C., Vieira, L. H., Grasse, P., Siebert, C., Rahlf, P., and Frank, M. (2023). Decoupling of Barium and Silicon at the Congo River-Dominated Southeast Atlantic Margin: Insights From Combined Barium and Silicon Isotopes. *Global Biogeochemical Cycles*, 37:e2022GB007610.

Zhang, Z., Zhou, L., Chen, X.-G., Achterberg, E. P., Yu, Y., Hathorne, E., Steiner, Z., Siebert, C., and Frank, M. (2024). Introduction of isotopically light barium from the Rainbow hydrothermal system into the deep Atlantic Ocean. *Earth and Planetary Science Letters*, 625:118476.

Zhou, X., Li, R., Tang, D., Huang, K. J., Liu, K., and Ding, Y. (2022). Cold seep activity in the early Cambrian: Evidence from the world-class shale-hosted Tianzhu barite deposit, South China. *Sedimentary Geology*, 439:106220.